Annual Research Journal

Electrical Engineering
Research Experience for Undergraduates

Vol. IV

August 2006

National Science Foundation
Grant No. EEC-0244030

Principal Investigators:
Ruyan Guo and Kenneth Jenkins

PENNSTATE

Department of Electrical Engineering
University Park, Pennsylvania

EEREU Annual Research Journal

Ruyan Guo (editor)
W. Kenneth Jenkins (co-editor)

Volume IV
Published in 2006 by
The Department of Electrical Engineering
The Pennsylvania State University
University Park, Pennsylvania, 16802

NSF EE REU Site Program Contact

316 Electrical Engineering East
The Pennsylvania State University
University Park, PA 16802
Telephone (814) 865-0184
Fax (814) 865-7065
E-Mail: eereu@engr.psu.edu
Web Site: http://www.ee.psu.edu/reu/

ISBN 0-913260-06-1

PREFACE

Summer 2006 marks our fourth year hosting the National Science Foundation sponsored Research Experience for Undergraduates (REU) Site program, by Department of Electrical Engineering, Penn State University. Eighteen outstanding young men and women participated in this year's EEREU program at Penn State's University Park Campus. These EEREU scholars, selected from nation-wide applicants, are primarily college sophomores or juniors with outstanding academic backgrounds and intense interests in exploring research in electrical engineering and related areas.

During the nine-week summer program, each REU student was engaged in a research project under the guidance of his or her faculty mentor(s). Eighteen research projects were carried out. Technical reports were written by the EEREU students as the primary authors. Their research experience and findings were also presented at the 2006 Annual *EEREU Symposium,* held at University Park, in July 2006.

We are happy to present the 2006 *Annual Research Journal – Electrical Engineering Research Experience for Undergraduates, Vol. IV.* This volume contains highlights of the EEREU program activities and 18 technical papers with the EEREU scholars as primary authors. These reports document original research and are of value for scientific dissemination and publications.

Besides research activities, the EEREU program organized a *Weekly Scientific Seminar Series* that introduced a broad range of research topics to the REU students. Students also went on *field trips* visiting prominent local and regional industrial and research sites. In addition, they were engaged in debate and analysis of ethical issues in engineering through *Weekly Workshop on Ethics and Professional Development*. For more information about Penn State's Research Experience for Undergraduates Program in Electrical Engineering, please visit our website at: http://www.ee.psu.edu/reu/.

We are confident that this series of EEREU journals showcases the achievement of our EEREU students and demonstrates the effective mentorship provided by the faculty and graduate student mentoring teams. We are also hopeful that this publication may serve as a stepping-stone for our EEREU students at the beginning stage of their research career. In addition, it may stimulate more college students to consider research career and pursue graduate studies in electrical engineering.

Ruyan Guo and W. Kenneth Jenkins
Co-Directors of the NSF EE REU Site Program
Dept. EE, The Pennsylvania State University

July 2006
University Park, Pennsylvania

TABLE OF CONTENTS

Research Articles (* indicates REU student author)

2006 NSF EEREU FACULTY AND STAFF MEMBERS

Faculty Mentors
Prof. Amar Bhalla
Prof. Sven Bilén
Prof. Craig Grimes
Prof. Ruyan Guo, Director
Prof. Heath Hofmann
Prof. Ken Jenkins, Co-Director
Prof. I. C. Khoo
Prof. Mike Lanagan
Prof. Zhiwen Liu
Prof. Theresa Mayer
Prof. John Mitchell, Seminar Chair
Prof. Robert Nickel
Prof. Victor Pasko
Prof. Joan Redwing
Prof. Jeff Schiano
Prof. Srinivas Tadigadapa
Prof. Kenji Uchino

Prof. Andy Lau, Ethics Workshop Chair
Prof. David Salvia, Activities Chair
Ms. Amy Freeman, Director, Multicultural Program

Mrs. Linda Becker, Administration
Mr. Stephen Hall, Assistant Director
Ms. Lana Yezhova, Publicity Chair

2006 EEREU Scholars, Research Topics and Faculty Mentors

2006 EEREU Scholars	Research Topics	Faculty Mentors
Mr. Matthew Thomas Blaisse Physics, Music Lebanon Valley College	Phase Locked Optical Sensing of Two-D Piezoelectric Strain	Prof. Amar Bhalla 187 MATERIALS RES LAB BLDG
Ms. Erica Christensen Engineering Oberlin College	Network Analyzer Based Implementation of Plasma Frequency Probe	Prof. Sven Bilén 213N HAMMOND BLDG
Mr. Andrew David Price Computer Engineering Penn State University	Implementing an IQ Diagram to Determine RF Signal Modulation Classification	
Mr. Kristoffer Lee Greenert Electrical Engineering Penn State University	ESPRIT: Observations of Mesospheric Particles Using In-Situ and Ground-Based Measurements	Prof. John Mitchell 330 ELEC ENGR EAST Prof. Sven Bilén 213N HAMMOND BLDG
Ms. Adriana Kathleen Fitzgerald Electrical Engineering University of Minnesota-Twin Cities	Investigation of the Morphology and Structure of TiO_2 Nanotubes Fabricated in High Dielectric Constant Electrolytes	Prof. Craig Grimes 217 MATERIALS RES LAB BLDG
Mr. Gabriel Adrian Reyes Electrical Engrg / East Asian Language University of Florida	Piezoelectric Resonance Influenced Electrooptic (EO) Effects	Prof. Ruyan Guo 108B RUA, MATERIALS RES LAB
Mr. Grant Matthew Shane Electro-Mechanical Engineering Tech. Penn State University, Altoona	Self-Excited Synchronous Field Winding Machine	Prof. Heath Hofmann 209K ELEC ENGR WEST
Mr. Suman Venkatesh Ravuri Electrical Engineering and Classics Columbia University	A Comparative Study of Pitch Estimation Methods of Voiced Speech	Prof. Ken Jenkins 121 ELEC ENGR EAST Prof. Robert Nickel 111H ELEC ENGR WEST

2006 EEREU Scholars, Research Topics, and Faculty Mentors (Cont.)		
2006 EEREU Scholars	**Research Topics**	**Faculty Mentors**
Mr. Jason Michael Wishnov Electrical & Computer Engineering University of Florida	Terahertz Wave Generation Via Optical Rectification	Prof. Zhiwen Liu 314 ELEC ENGR EAST
Ms. Lana Haru Carnel Electrical Engineering University of Tennessee	Microwave Characterization of Semiconductors	Prof. Mike Lanagan 278 MATERIALS RES LAB BLDG
Mr. Zhenyan Hua Electrical Engineering Penn State University	CARS - Coherent Anti-Stokes Raman Scattering Microscopy	Prof. Zhiwen Liu 314 ELEC ENGR EAST
Mr. Adam Dreibelbis Physics Susquehanna University	Studies of Electromagnetic Fields in the Atmosphere	Prof. Victor Pasko 121 ELEC ENGR EAST
Ms. Whitney Tidwell Physics Rhodes College	Fractal Modeling of Lightning	
Mr. Jason Christopher Mantey Electrical Engineering Wayne State University	An Analysis of the Physical Properties of Silicon Nanowires	Prof. Joan Redwing 108 STEIDLE BLDG
Mr. Thomas Joe Tyson Engineering Physics West Virginia Wesleyan College	Development of Undergraduate Laboratory Modules in Continuous-Wave Quadrupole Resonance Spectroscopy	Prof. Jeff Schiano 227D ELEC ENGR WEST
Mr. David Edward Gagnon Electrical Engineering, Music Virginia Tech	Measurement of Graphene Semiconductors	Prof. Srinivas Tadigadapa 121 ELEC ENGR EAST
Mr. Jay Mathews Physics Colorado State University	Study of absorption isotherms using micromachined quartz crystal gravimetric sensors	
Mr. Haig Stephen Norian Electrical Engineering Villanova University	Energy Harvesting with PVDF Piezoelectric Film	Prof. Kenji Uchino 134 MATERIALS RES LAB BLDG

NSF EE REU 2006 Summer Program
Weekly Scientific Seminar

Department of Electrical Engineering
Pennsylvania State University, University Park, PA 16802

Room 225 E E West, 11:00 – 11:50 AM, Tuesdays (except July 4th)
Lunch: 12:00-12:30 PM

(Followed by **REU Weekly Workshop on Ethics and Professional Development,** 12:40-1:40 PM)

Date	***Topic***	***Speaker***
June 6, 2006	**Topics in Digital Speech Signal Processing**	Robert Nickel
June 13, 2006	**Lightning-related Transient Luminous Events in the Middle Atmosphere**	Victor Pasko
June 20, 2006	**Semiconductor Nanowires: Building Blocks for Nanoscale Devices**	Joan Redwing
June 27, 2006	**Software Defined Radio Applications**	Sven Bilén
July 5, 2006 (Wednesday)	**Sensors Using Micro and Nanoscale Structures**	Srinivas Tadigadapa
July 11, 2006	**Energy Harvesting**	Heath Hofmann
July 18, 2006	**What's Next? Graduate School, of Course!**	Ken Jenkins
July 25, 2006	**(reserved for preparation on symposium presentation)**	
July 27, 2006 (Thursday)	**2006 NSF EEREU Symposium**	REU Students

Suggestions and inquiries: eereu@engr.psu.edu

NSF EE REU 2006 Summer Program
Weekly Workshop on Ethics and Professional Development

Department of Electrical Engineering
Pennsylvania State University, University Park, PA 16802

Room 225 EE West, 12:40 pm –1:40 pm, Tuesdays (except July 4th)
Chair: **Prof. Andrew Lau** (andylau@psu.edu)

Date	***Workshop Topic Addressed***	***Weekly***	***Faculty Leader***
May 31	(Welcome Meeting, 11:00 am)	***Week 1***	Prof. Andy Lau (Chair)
June 6	Introduction; Types of Moral Problems; Academic Integrity	***Week 2***	
June 13	Central Professional Responsibilities of Engineers – Codes of Ethics and Their Application; The Responsible Conduct of Research	***Week 3***	
June 20	Global Environmental Issues: Climate Change, Oil Depletion, Sustainability	***Week 4***	
June 27	(Reserved for Preparation for presentations on Ethical Issue in Research)	***Week 5***	
July 5 (Wed.)	Situation Ethics for University Students	***Week 6***	Prof. Jenkins
July 11	Happy Valley Values - The Game	***Week 7***	Prof. Andy Lau (Chair)
July 18	Student Presentations of Ethical Issues in Their Research – 2 hr. session	***Week 8***	
July 25	(Reserved for preparation symposium presentation)	***Week 9***	
July 27	(2006 EEREU Symposium)	***Week 9***	

Suggestions and inquiries: eereu@engr.psu.edu

2006 NSF EE REU Bi-Weekly Field Trips and Academic/Industrial Sponsors

Nanofabrication National Facility
Penn State University
University Park, Pennsylvania

Sound Technology, Inc.
State College, Pennsylvania

State of The Art, Inc.
State College, Pennsylvania

VertexRSI
State College, Pennsylvania

Department of Electrical Engineering
Materials Research Institute
Penn State University
University Park, Pennsylvania

Applied Research Laboratory
Penn State University
University Park, Pennsylvania

Videon Central, Inc.
State College, Pennsylvania

2006 NSF EE REU SYMPOSIUM

8:30 AM to 4:00 PM, Thursday, July 27, 2006
Room 225 Electrical Engineering West Building
Pennsylvania State University
University Park, PA 16802

Time	Sessions and Topics	Chairs and Speakers
8:30 - 8:55 am	**Symposium Registration (Refreshments Provided)**	**(Linda Becker Stephen Hall)**
8:55 – 9:00 am	**Welcome**	**Jack Mitchell**
9:00 – 10:15 am	**Session I** Session Chairs:	**Bilén/Mitchell/ Pasko**
9:00 – 9:15	ESPRIT: OBSERVATIONS OF GROUND BASED LIDAR AND RADAR FOR SOUNDING ROCKET LAUNCH	Kristoffer Greenert
9:15 – 9:30	NETWORK ANALYZER BASED IMPLEMENTATION OF PLASMA FREQUENCY PROBE	Erica Christensen
9:30 – 9:45	IMPLEMENTING AN IQ DIAGRAM TO DETERMINE RF SIGNAL MODULATION CLASSIFICATION	Andrew Price
9:45 – 10:00	3D FINITE DIFFERENCE TIME-DOMAIN MODELING OF THE SCHUMANN RESONANCES ON EARTH AND MARS	Adam Dreibelbis
10:00 – 10:15	FRACTAL MODELING OF CLOUD-TO-GROUND LIGHTNING	Whitney Tidwell
	10:15 – 10:30 am Coffee Break	
10:30 – 11:45 am	**Session II** Session Chairs:	**Nickel/Schiano/ Hofmann/Redwing/ Grimes**
10:30 – 10:45	PARAMETER ESTIMATION OF A 6-POLE WOUND ROTOR MACHINE	Grant Shane
10:45 – 11:00	DEVELOPMENT OF UNDERGRADUATE LABORATORY MODULES IN CONTINUOUS-WAVE QUADRUPOLE RESONANCE SPECTROSCOPY	Thomas Tyson
11:00 – 11:15	A COMPARATIVE STUDY OF PITCH ESTIMATION METHODS FOR VOICED SPEECH	Suman Ravuri
11:15 – 11:30	ELECTRICAL CHARACTERIZATION OF SI NANOWIRE FET AND CORRELATION TO DEVICE PHYSICAL DIMENSIONS	Jason Mantey
11:30 – 11:45	INVESTIGATION OF THE MORPHOLOGY AND STRUCTURE OF TIO2 NANOTUBES FABRICATED IN HIGH DIELECTRIC CONSTANT ELECTROLYTES	Adriana Fitzgerald
11:45 Noon	**(Group Photo – All invited. Please plan to be available)**	(Lana Yezhova)
	12:00 – 1:15 pm Luncheon (Atherton Hotel)	

2006 NSF EE REU SYMPOSIUM (cont.)

8:55 AM to 3:45 PM, Thursday, July 27, 2006
Room 225 Electrical Engineering West Building
Pennsylvania State University
University Park, PA 16802

Time	Sessions and Topics	Chairs and Speakers
1:30 – 2:30 pm	**Session III** Session Chairs:	**Tadigadapa/ Liu**
1:30 – 1:45	STUDY OF ABSORPTION ISOTHERMS USING MICROMACHINED QUARTZ CRYSTAL GRAVIMETRIC SENSORS	Jay Mathews
1:45 – 2:00	RESISTANCE AND FIELD EFFECT BEHAVIOR OF GRAPHENE FLAKES	David Gagnon
2:00 – 2:15	FEMTOSECOND FIBER LASER FOR CARS MICROSCOPY	Zhenyan Hua
2:15 – 2:30	TERAHERTZ WAVE GENERATION VIA OPTICAL RECTIFICATION	Jason Wishnov
	2:30 – 2:45 pm Coffee Break	
2:45 – 3:45 pm	**Session IV** Session Chairs:	**Lanagan/Bhalla/ Guo/Uchino**
2:45 – 3:00	MICROWAVE CHARACTARIZATION OF METAMATERIALS	Lana Carnel
3:00 – 3:15	PHASE LOCKED OPTICAL SENSING OF TWO-D PIEZOELECTRIC STRAIN	Matthew Blaisse
3:15 – 3:30	DYNAMIC MEASUREMENT AND NUMERICAL SIMULATION IN DETERMINING FREQUENCY DEPENDENCIES OF EO EFFECTS	Gabriel Reyes
3:30 – 3:45	ENERGY HARVESTING WITH PVDF PIEZOELECTRIC FILM	Haig Norian
3:45 – 4:00	**CONGRATULATIONS AND CONCLUDING REMARKS**	**Guo/Mitchell**
	4:00 pm Adjournment	

Picnic at Sunset Park, 5:00 pm – sunset, ALL INVITED

Resource persons:	Stephen Hall and Linda Becker
Special Notes:	Overhead transparency projector, PC, and LCD PC projector are provided. Speakers please upload presentation files to EEREU group web in Angel by July 26 Wed.. It is strongly recommended that speakers test-run presentation files for audio, video, or special applications prior to Thursday presentation. Each presentation is 15 min, chair introduction, question and answer included.

ESPRIT: OBSERVATIONS BY GROUND-BASED LIDAR AND RADAR FOR A SOUNDING ROCKET LAUNCH

K. L. Greenert,* S. G. Bilén,[#] J. D. Mitchell,[#] and C. R. Philbrick[#]

Department of Electrical Engineering
The Pennsylvania State University, University Park, PA 16802

*Undergraduate student of
Department of Electrical Engineering
The Pennsylvania State University
University Park, PA 16802

ABSTRACT

The ESPRIT and HOTPAY-1 sounding rocket campaign at Rocket Range, Norway, presented a scientific objective of studying particle-related phenomena occurring in the high-latltude mesosphere during summer. Between 80 km and 90 km water vapor condenses and freezes into small particles. Under certain geophysical condtions, nanometer-size ice particles present themselves as polar mesospheric summer echoes, PMSEs, and/or noctilucent clouds, NLCs. Coordination with ALOMAR's RMR LIDAR, ALWIN RADAR, and the EISCAT RADAR throughout the campaign launch window determined launch conditions. This paper serves as a record of observations and analyses of the LIDAR and RADAR systems during the launch on 1 July 2006.

[#] Faculty Mentor, The Pennsylvania State University

Annual Research Journal, Vol. IV
Electrical Engineering Research Experience for Undergraduates

ISBN 0-913260-06-1 (http://www.ee.psu.edu/reu/)

INTRODUCTION

Noctilucent Clouds, NLCs, and Polar Mesospheric Summer Echoes, PMSEs, are interesting because of their structure and composition at the altitudes at which they exist. Occurring in the mesosphere, these atmospheric phenomena are quite different than the particle effects observed in tropospheric cloud regions. Due to the high altitude of the particles, little is known of their origin or composition. However, by using sounding rocket payloads and ground based RADARs and LIDARs, more relevant data are coming to light. The Andøya Rocket Range in northern Norway presented the perfect conditions for NLC research. Seated at a latitude of approximately 69°N, it met the requirements set for the existence of NLCs and PMSEs. NLCs and PMSE particles form during appropriate geophysical conditions only at latitudes above 50°. The range also was a perfect location for studying ionospheric phenomenon due to the high probability for aurora.

PAYLOAD DESCRIPTION AND GROUND OBSERVATORIES

The ESPRIT payload hosted seven scientific experiments focused on the detection and characterization of NLCs, PMSEs, and the ionosphere. The payload was launched on a Terrier-Improved Orion rocket supplied by NASA. Figure 1 shows the experiments and their placement within the payload. Table 1 gives a short summary of the scientific experiments. The aerosol detector shown on the forward shaft uses two charged grids to separate plasma ions from the charged dust particle. The charged dust particles then become attracted to a low potential, gold collector plate. The fluctuation in voltage from the collector indicates the amount of charge. Two cylindrical langmuir probes attached at the ends of carbon fiber booms used a swept bias to detect plasma temperature and a fixed bias to determine the plasma electron density. The solid state and X-ray detectors measured the emissions from an X-ray aurora in the ionosphere. An NLC imager was setup on the payload to take still images of NLCs as the payload passed through the mesosphere. Along with the imager, an NLC photometer used ten channels at wavelengths of 420 nm, 340 nm, and 550 nm at two polarization orientations. The plasma frequency probe on the aft shaft swept through frequencies in order to find the resonant frequency of the ionospheric plasma.[1][2]

Annual Research Journal, Vol. IV
Electrical Engineering Research Experience for Undergraduates

ISBN 0-913260-06-1 (http://www.ee.psu.edu/reu/)

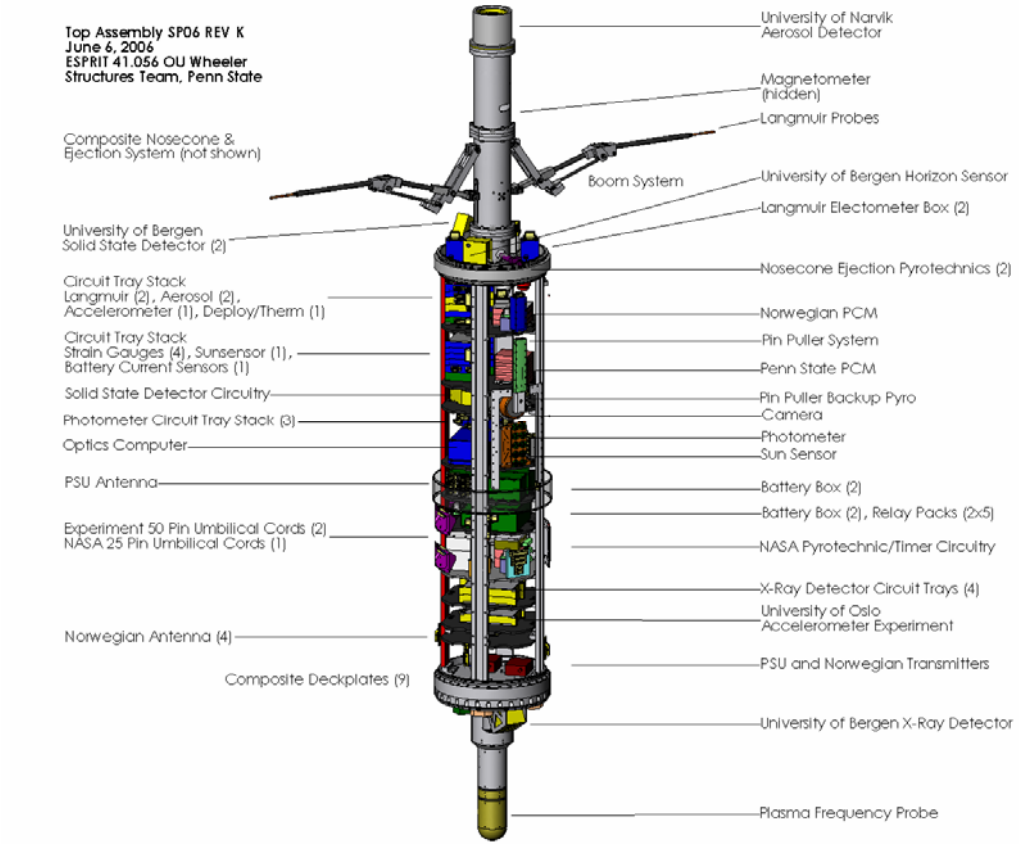

Figure 1: ESPRIT Payload Layout

Table I: ESPRIT Experiments Summary

Summary of Scientific Experiments		
Experiment	Scientific Purpose	University
Aerosol Detector	Electric charge in PMSEs	Narvik
Langmuir Probes	Electron temperature and density	PSU
Solid State Detector	Detect lower X-Ray Aurora	Bergen
NLC Imager	Photograph NLCs	PSU
NLC Photometer	Detect and characterize NLCs	PSU
X-Ray Detector	Detect upper X-Ray Aurora	Bergen
Plasma Frequency Probe	Resonant frequency of atmospheric plasma	PSU

The ALOMAR facility at Andøya Rocket Range utilized its 539-nm RMR LIDAR for remote sensing of NLCs.[3] Detection of PMSEs was done using the 53.5-MHz ALWIN RADAR at the ALOMAR Observatory and the 223-MHz VHF and 933-MHz UHF RADARs of the EISCAT Facility located at Tromsø, Norway.

ISBN 0-913260-06-1 (http://www.ee.psu.edu/reu/)

LAUNCH CONDITIONS

The launch conditions for ESPRIT and HOTPAY-1 at 06:39.00 UTC showed a very strong three-layer PMSE return on the ALWIN RADAR. Figures 2 and 3 show the ALWIN RADAR profiles that indicate high PMSE levels between 80 km and 90 km. The gaps in the PMSE layers suggested the presence of an NLC. The ALOMAR LIDAR measurements confirmed the presence of NLCs. The LIDAR returns in Figures 4 and 5 showed that there was a strong NLC presence at altitudes between 82 km and 87 km. The NLC dropped in altitude and intensity as time progressed. The event eventually pinched off approximately two hours after launch. Table 2 shows a compilation of nominal launch conditions.

Table II: Launch Conditions for ESPRIT

General Launch Information for ESPRIT (Wheeler 51.056)	
Launch	
Date (UTC)	1 July 2006
Time (UTC)	06:39:00
Solar Zenith Angle	59.7°
Azimuth	328.2°
Elevation	84.3°
Time to Apogee (s)	209.35
Apogee Height (km)	169.045
Time to ~80km Upleg (s)	72
Time to ~80km Downleg (s)	346
Payload mass (kg)	194
Payload Length (m)	2.57
Launch Location	
Name	Andøya Rocket Range, Norway
Latitude	69.29°N
Longitude	16.02°E

Annual Research Journal, Vol. IV
Electrical Engineering Research Experience for Undergraduates

ISBN 0-913260-06-1 (http://www.ee.psu.edu/reu/)

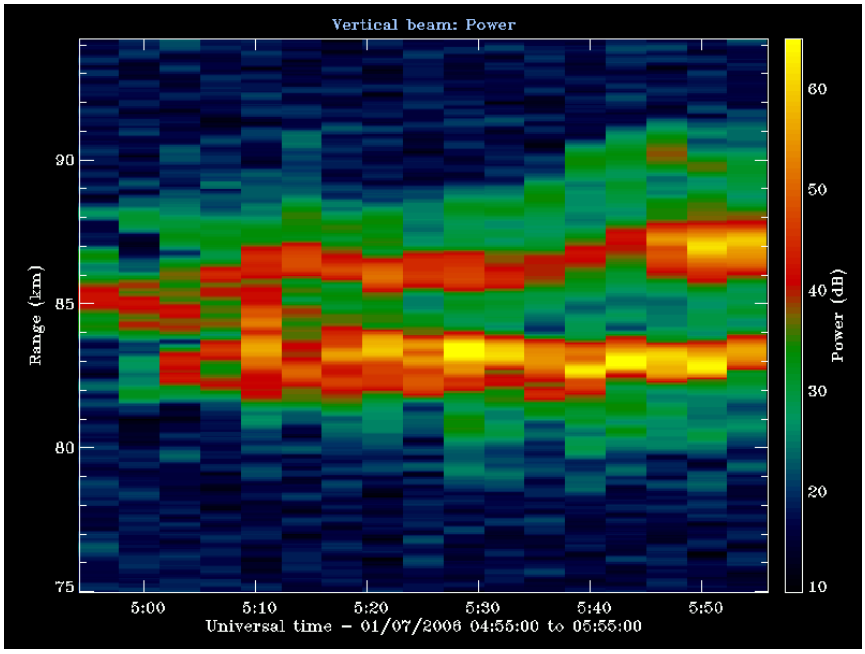

Figure 2: ALWIN Time Averaged RADAR Measurements

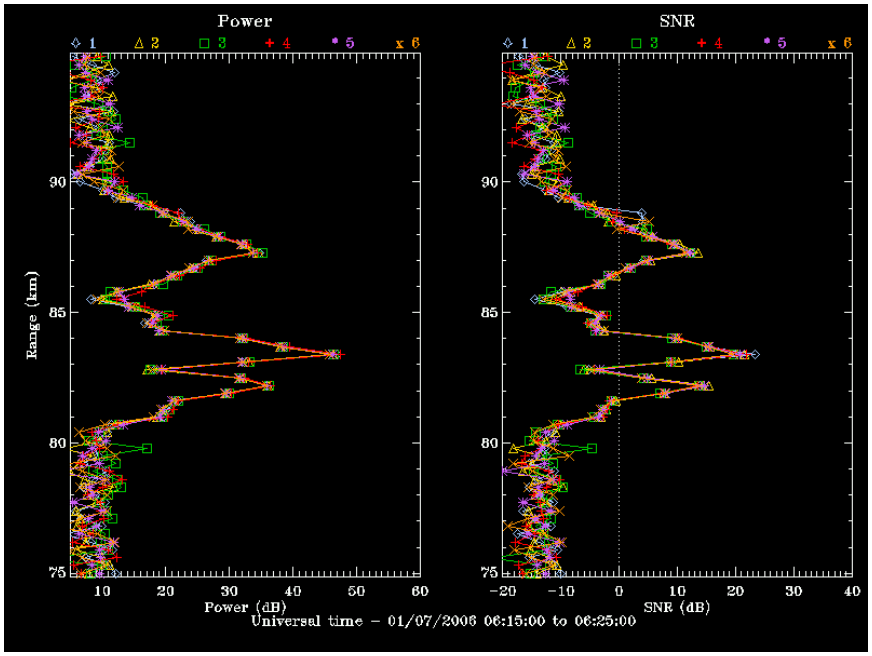

Figure 3: ALWIN RADAR PMSE Profiles

ISBN 0-913260-06-1 (http://www.ee.psu.edu/reu/)

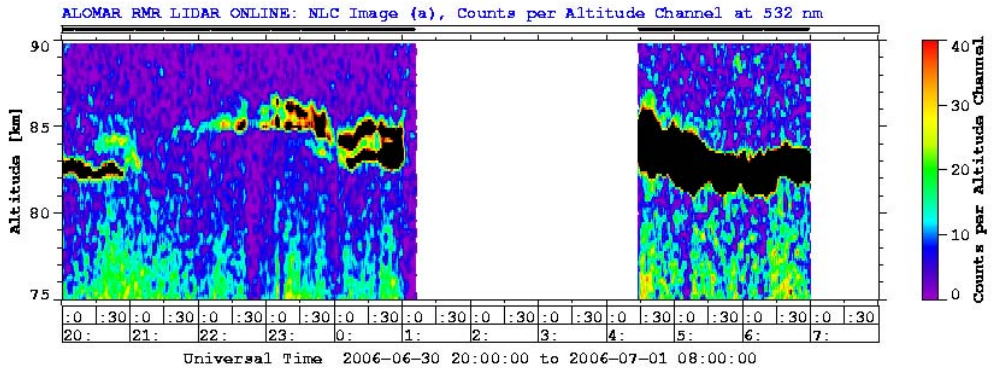

Figure 4: ALOMAR RMR Lidar Measurements of Present NLCs

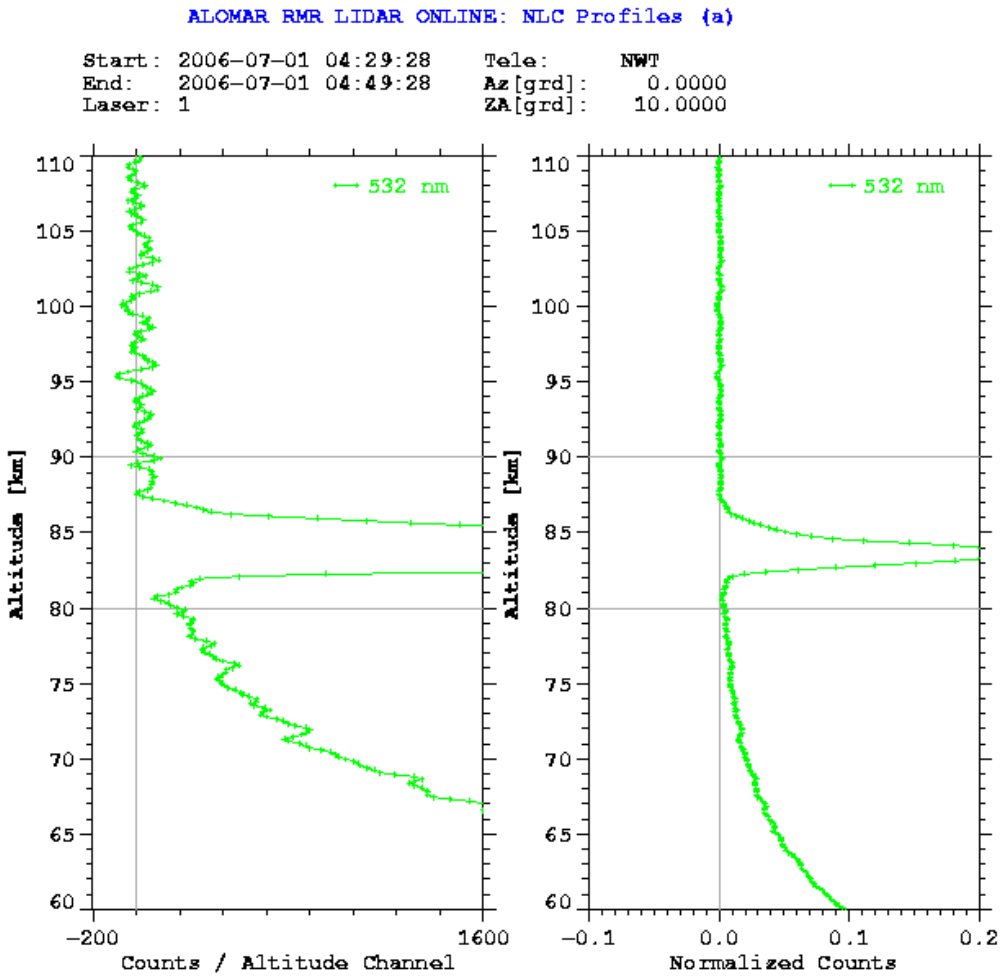

Figure 5: Time Averaged Lidar Power Profiles of Present NLCs

Annual Research Journal, Vol. IV
Electrical Engineering Research Experience for Undergraduates

ISBN 0-913260-06-1 (http://www.ee.psu.edu/reu/)

RESULTS AND DISCUSSION

The signal returns from the LIDAR and RADAR ground-based experiments located at the ALOMAR Facility nearby the Andøya Rocket Range indicated excellent PMSE and NLC conditions for the ESPRIT rocket launch. Launching into the sort of atmosphere shown, gave a high probability for experimental success for the NLC photometer and imager. A quick-look analysis of the photometer and imager showed that indeed they both detected the NLC. Further analysis is underway in order to determine the NLC structure.

The PMSE layers also gave a high probability of success for the aerosol detector. Quick look analysis of the aerosol detector indicated that charged particles from the PMSE were collected into the instrument. Additional analysis will indicate the amount of charge that was accumulated from these particles. Moreover, data from the plasma x-ray experiments is currently under analysis and results will be available in future papers.

SUMMARY AND CONCLUSIONS

ESPRIT was a student-built scientific payload with a mission to study polar upper atmospheric summer phenomena. Launching into high NLC and PMSE layers made for a successful launch. The payload was able to detect NLCs and measure charge from the aerosols of the PMSEs. Plasma density, temperature, and frequency were measured as well. At the present time, it is unclear if x-ray aurora was detected. In conclusion, conditions for the launch were nearly perfect and the payload is deemed a success.

ACKNOWLEDGMENTS

We would like to thank all the members of ESPRIT, past and present, for their hard work and dedication throughout the campaign. A special thanks to Perry Edwards, Adam Escobar, Ken McKeever, and Brian Schratz for their tireless efforts to ensure a successful launch. Also, thanks to Bruce Scott and his team of NSROC engineers and technicians and Mr. Jørgen Ilsted, from the Andøya Rocket Range who provided critical payload support. Moreover, we would like to thank ALOMAR and EISCAT personnel who performed the ground based atmospheric measurements. Furthermore, gratitude to the Pennsylvania Space Grant Consortium, Lockheed Martin, The Pennsylvania State University Department of Electrical Engineering, The Pennsylvania State University Department of Aerospace Engineering, and RTD Embedded Systems for their financial support. Lastly, thanks to the National Science Foundation that supported this work under Grant No. EEC-0244030.

ISBN 0-913260-06-1 (http://www.ee.psu.edu/reu/)

REFERENCES

[1] The Pennsylvania State University, Critical Design Review, 2005

[2] University of Bergen, Technical University of Narvik, University of Oslo, Critical Design Review: Norwegian Systems, 2005

[3] von Zahn, U., G. von Cossart, J. Fiedler, K. H. Fricke, G. Nelke, G. Baumgarten, D. Rees, A. Hauchecorne, K. Adolfsen, The ALOMAR Rayleigh/Mie/Raman lidar: objectives, configurations, and performance, Ann. *Geophysicae,*18, 815-833, 2000

Annual Research Journal, Vol. IV
Electrical Engineering Research Experience for Undergraduates

ISBN 0-913260-06-1 (http://www.ee.psu.edu/reu/)

NETWORK ANALYZER-BASED IMPLEMENTATION OF PLASMA FREQUENCY PROBE

Erica M. Christensen* and Sven G. Bilén[#]

Department of Electrical Engineering
The Pennsylvania State University, University Park, PA 16802

*Undergraduate student of
Oberlin College
Oberlin, OH 44074

ABSTRACT

This project examines the use of a network-analyzer implementation of a plasma frequency probe. A plasma frequency probes works by emitting low radio frequency voltages over a range of frequencies, and then examining the current through the probe-plasma system. When the current is in phase with the emitted voltage, the corresponding frequency is the plasma frequency. In this project, a network analyzer is used to measure the reflection coefficient from a probe-plasma system, from which the impedance of the system can be calculated. The frequency that produces a real impedance, with no inductive or capacitive component, is the plasma frequency.

This paper compares the performance of a high-end network analyzer, which is known to be appropriately accurate, to a more compact and, therefore, more practical network analyzer by comparing their results for several passive devices. The performance of the PFP-network analyzer approach is intended to then be compared to the performance of a conventional Langmuir probe. Both probes will be immersed in an artificially created plasma atmosphere, and the results compared.

[#] Faculty Mentor

Annual Research Journal, Vol. IV
Electrical Engineering Research Experience for Undergraduates

ISBN 0-913260-06-1 (http://www.ee.psu.edu/reu/)

INTRODUCTION

The frequency measured by a plasma frequency probe (PFP) is the upper hybrid frequency. This frequency is the result of two kinds of motion exhibited by the charged particles of the plasma, each having an associated frequency: the frequency of electron-ion interaction, which is referred to as the plasma frequency, and electron cyclotron frequency. Cyclotron frequency is the frequency at which electrons circle around the Earth's magnetic field lines due to the Lorentz force. This frequency is given by

$$\omega_{ce} = \frac{eB}{m_e} \tag{1}$$

where e is the charge on an electron, B is the magnitude of Earth's magnetic field, and m_e is the mass of an electron. Plasma frequency describes the influence of an external field. When an external field is applied to the plasma, the electrons are attracted or repelled from their original positions. When the field is removed, they tend to return to their original positions, but overshoot due to inertia. Thus, when a sinusoidally varying electric field is applied to the plasma, the electrons can be made to oscillate back and forth around their original positions with a frequency that depends on the density of the plasma.[1,4] Both electrons and ions experience these frequencies, but since ions are significantly heavier than electrons, ion frequencies are comparably very low, and the observable frequency can be assumed to be solely due to electron motion.

A PFP works by applying a sinusoidal electric field. It then measures the induced current in the plasma-probe circuit and compares it to the applied voltage. The probe sweeps through a range of different frequencies for the applied field. Previous PFP implementations measured the phase between current and voltage, and the gain as a function of frequency.[3,5] The frequency for which the phase is minimized and the gain maximized is the plasma frequency. The version of the PFP examined in this work uses a network analyzer to instead measure the reflection coefficient of the probe, from which the impedance of the plasma-probe system can be calculated. The frequency that corresponds to a real impedance with no inductive or capacitive component is the upper hybrid frequency.

The probe is able to measure the upper hybrid frequency of the plasma, which is defined as

$$\omega_{uh} = \sqrt{\omega_{pe} + \omega_{ce}} \tag{2}$$

where ω_{pe} is the plasma frequency. In general, the cyclotron frequency remains roughly constant for most measurements, since it depends only on the magnitude of the Earth's magnetic field, which is well characterized. Thus, since the cyclotron frequency is known and constant, the electron-ion interaction frequency

Annual Research Journal, Vol. IV
Electrical Engineering Research Experience for Undergraduates

ISBN 0-913260-06-1 (http://www.ee.psu.edu/reu/)

can be calculated from the upper hybrid frequency. The plasma density is directly dependent on the plasma frequency, which is given by

$$\omega_{pe}^2 = \frac{n_o e^2}{\varepsilon_o m_e} \tag{3}$$

where n_0 is the number of electrons per unit volume of the plasma, and ε_0 is the permittivity of free space.[2]

The Langmuir probe is the oldest and most conventional method for measuring plasma parameters; hence, it is often used as a reference point for newer measurement techniques The Langmuir probe usually consists of one electrode, but sometimes two or three electrodes, which are inserted into the plasma. A constant or time-varying potential is then established between the multiple electrodes or between the single electrode and the wall of the plasma container. The current and potential characteristics of the collected current are then measured, from which plasma properties such as electron temperature, electron density, and plasma potential can be derived.

TESTING OF NETWORK ANALYZER

The network analyzer used in conjunction with the PFP was a Ten-tec Model 6000 Vector Network Analyzer. To test the precision of the Ten-tec, two passive filters were analyzed by both the Ten-tec and a high-end Agilent PNA Series Network Analyzer. The Agilent was assumed to give highly accurate readings, and so the Ten-tec was compared to this standard.

The filters used were a 90-MHz bandpass filter and a BPF single channel bandpass filter (TV channel 2 filter). The Agilent performed a frequency sweep of the range 300kHz to 140 MHz. The Ten-tec performed a sweep of the range 200 kHz to its upper limit of 110 MHz. S11 and S21 parameters were compared.

It can be seen in the plots below that there is fairly good agreement between the two VNAs, particularly in the S21 parameter. See Figs. 1-4. It is particularly important to note that there is very close agreement of the frequencies at which main peaks and valleys occur on the graphs. The Channel 2 filter, when examined by the Agilent VNA, was found to have peak transmittance from port 1 to port 2 at a frequency of 57.214 MHz (4.0 dB). On the Ten-tec NA, this peak was found at a frequency of 57.021 MHz (2.7 dB) (See Fig. 4). The 90-MHz bandpass filter was found by the Agilent VNA to pass frequencies between 83.56 MHz and 99.77 MHz. The Ten-tec NA found this range to be 82.0 MHz to 100.67 MHz (See Fig. 2).

Annual Research Journal, Vol. IV
Electrical Engineering Research Experience for Undergraduates

ISBN 0-913260-06-1 (http://www.ee.psu.edu/reu/)

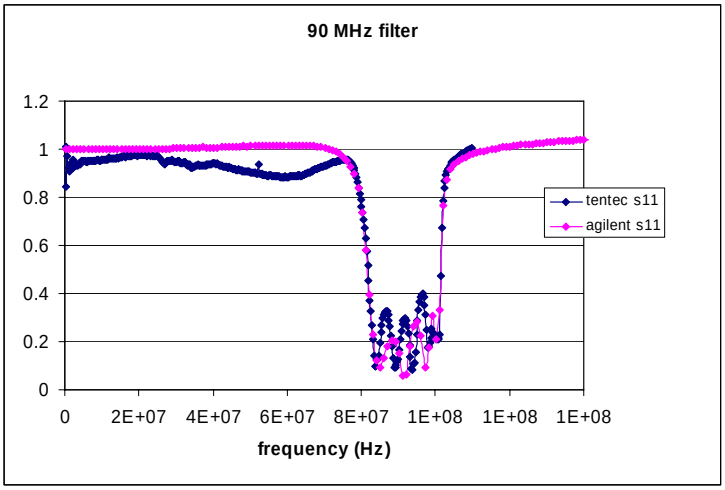

Fig. 1. S11 comparison for 90-MHz filter

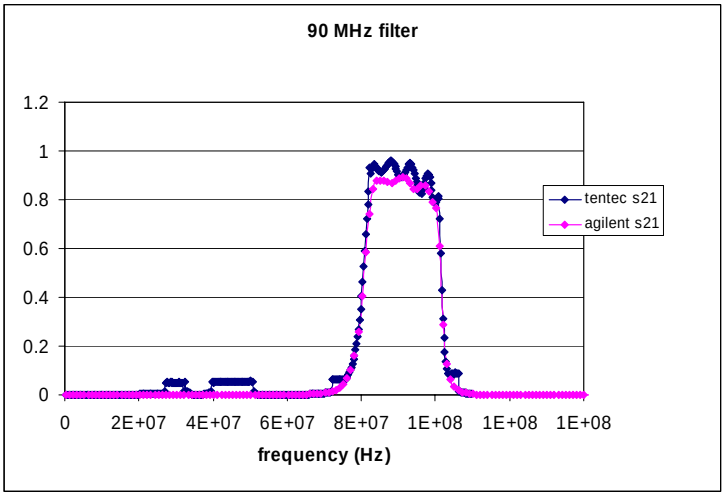

Fig. 2. S21 comparison for 90-MHz filter

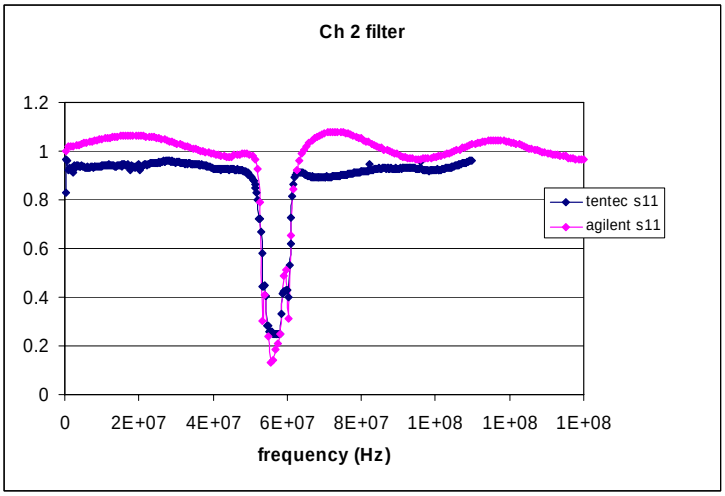

Fig. 3. S11 comparison for Ch. 2 filter

Annual Research Journal, Vol. IV
Electrical Engineering Research Experience for Undergraduates

ISBN 0-913260-06-1 (http://www.ee.psu.edu/reu/)

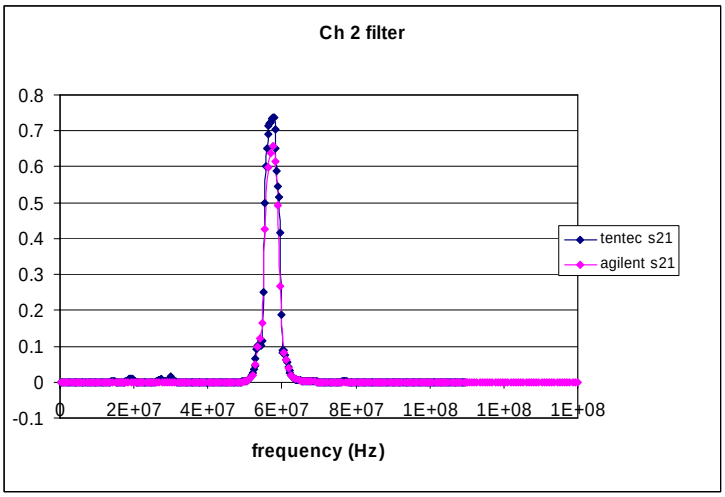

Fig. 4. S21 comparison for Ch. 2 filter

TESTING OF PFP

Probe Construction and Setup

The PFP was constructed from a solid brass rod 0.5 inches in diameter and 1 inch in length. This was attached to a brass barrel of roughly the same size, with a non-conducting tube between the pieces. A female SMA connector was attached to the end of the brass barrel, connected via a wire to the tip of the probe. See Fig. 5 for a schematic of the PFP construction.

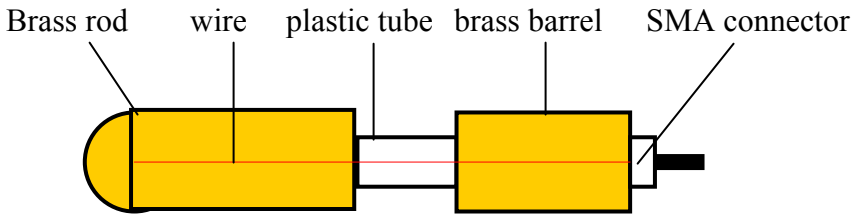

Fig. 5. Block diagram of PFP

After calibration, the PFP was connected to the Tx (transmit) port of the VNA and placed in the plasma chamber. A Langmuir probe was also placed in the chamber in close proximity to the PFP for comparison testing. The two probes were situated roughly equidistant from the side walls of the chamber and five inches from the plasma source. See Figs. 6,7 and 8. The plasma to be used is an argon plasma generated by a hollow cathode.

Annual Research Journal, Vol. IV
Electrical Engineering Research Experience for Undergraduates

ISBN 0-913260-06-1 (http://www.ee.psu.edu/reu/)

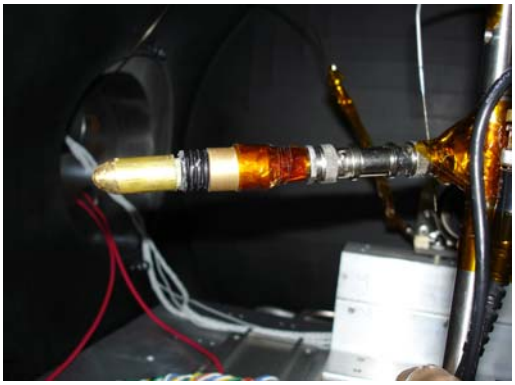

Fig. 6. Plasma Frequency Probe

Fig. 7. Langmuir probe

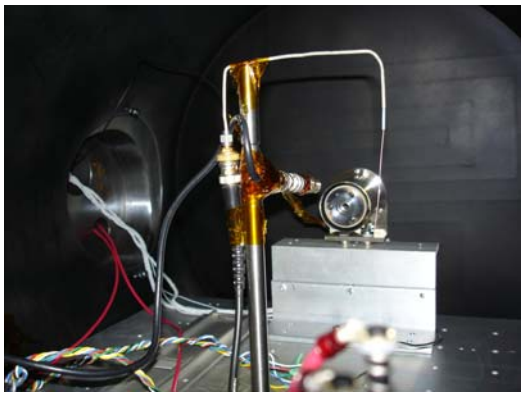

Fig. 8. Setup of PFP and Langmuir probe in vacuum chamber

Unfortunately, at the time of the experiment the plasma source was malfunctioning and no plasma was able to be created in the chamber. The intended experiment was to run a frequency sweep from 200 kHz to 110 MHz through the PFP in order to observe the plasma frequency. This data would be compared with the results of a voltage sweep through the Langmuir probe.

SUMMARY AND FUTURE WORK

The Ten-tec VNA to be used in conjunction with the PFP was tested against the high-end Agilent PNA Series Network Analyzer. It was found that the precision of the Ten-tec VNA will be acceptable for use with the PFP. The PFP itself was built from a brass rod, rounded off, and connected to a female SMA connector. The probe was then connected to the Ten-tec VNA and placed in the plasma chamber. A Langmuir probe was placed along side the PFP for comparison. The authors hoped to run a frequency sweep on the PFP and thus observe the plasma frequency. However, the plasma source malfunctioned, and no plasma was able to be created in the chamber. It is recommended that this experiment be repeated with a more reliable plasma source.

Annual Research Journal, Vol. IV
Electrical Engineering Research Experience for Undergraduates

ISBN 0-913260-06-1 (http://www.ee.psu.edu/reu/)

ACKNOWLEDGEMENT
This material is based upon work supported by the National Science Foundation under Grant No. EEC-0244030.

REFERENCES
[1] Schratz, Brian C., "Design of a Rocket-borne *In Situ* Plasma Frequency Probe," MS Thesis, The Pennsylvania State University, 2006.
[2] Bilén, Sven G., "Pulse Propagation Along Conductors in Low-density, Cold Plasmas as Applied to Electrodynamic Tethers in the Ionosphere," PhD Thesis. The University of Michigan, 1998.
[3] Takayama, K., and H. Ikegami, "Plasma Resonance in a Radio-Frequency Probe," *Physical Review Letters*, Vol. 5, No. 6, September 1960, pp. 238–240.
[4] Bilén, Sven G., James M. Haas, Frank S. Gulczinski III, and Alec D. Gallimore. "Resonance-Probe Measurements of Plasma Densities in Electric-Propulsion Plumes," American Institute of Aeronautics and Astronautics Paper 99-2714.
[5] Harp, R. S., and R. W. Crawford, "Characteristics of the Plasma Resonance Probe," *Journal of Applied Physics*, Vol. 35, No. 12, December 1964, pp. 3436–3446.

Annual Research Journal, Vol. IV
Electrical Engineering Research Experience for Undergraduates

ISBN 0-913260-06-1 (http://www.ee.psu.edu/reu/)

IMPLEMENTING AN IQ DIAGRAM TO DETERMINE RF SIGNAL MODULATION CLASSIFICATION

Andrew D. Price* and Sven G. Bilén#

Department of Electrical Engineering
The Pennsylvania State University, University Park, PA 16802

*Undergraduate Student of
Department of Electrical Engineering
The Pennsylvania State University
University Park, PA 16802

ABSTRACT

This paper details the implementation of a modulation classification (MC) system that utilizes a signal's In-phase and Quadrature (IQ) components to generate a constellation diagram for modulation classification. A survey of current MC techniques is presented to give the reader background on the subject. The goal of the research is to provide a method for classifying the modulation scheme of an unknown signal that is both resource-conservative and robust. This paper focuses on analog modulation types, particularly AM and FM. The MC system is implemented on a Lyrtech SignalWAVe board. Several diagrams of both real-world and simulated signals will be presented in order to analyze the effectiveness of the MC system.

Faculty Mentor

Annual Research Journal, Vol. IV
Electrical Engineering Research Experience for Undergraduates

ISBN 0-913260-06-1 (http://www.ee.psu.edu/reu/)

INTRODUCTION

A software-defined radio (SDR) is a radio communication device that allows for a flexible communication system. Typical radios are built with hardware components that are fixed and cannot change. For example, the AM/FM radio in a car only has the capability to receive AM and FM radio signals. Similarly, a typical US cell phone that uses the CDMA or TDMA standards can only communicate using those standards. As communication standards proliferate, new radio equipment must be designed and installed. In addition, old equipment becomes obsolete, or is not interoperable with new equipment. The solution to this problem is a reconfigurable radio that can be programmed to receive and transmit any radio signal. SDR is precisely this solution.

During the development of SDR technology several definitions have been put forth to help classify an exact radio type. The SDR classification system is broken into five tiers as shown in Table 1 [1].

	Name	Description
Tier 0	Hardware Radio	Typical "electronics store" AM/FM radio; no software
Tier 1	Software-Controlled Radio	Software tunable or controllable; RF hardware
Tier 2	Software-Defined Radio (SDR)	Analog RF front end with all processing done in software
Tier 3	Ideal Software Radio	Only hardware is antenna and anti-aliasing filter
Tier 4	Ultimate Software Radio	Direct sampling of antenna signal; complete software processing

Table 1 – Classifications of SDR technology and basic descriptions

The classification scale of Table 1 ranges from a radio implemented fully via hardware (Tier 0), typical of today's radios, to the ultimate software radio (Tier 4), which is essentially an antenna whose output is directly sampled. Tier 4 is rather impractical in that sampling the output of an antenna directly would require an enormously fast ADC to avoid aliasing. It is, however, used as a benchmark to judge how close to the ideal a given SDR is. Note that, from this point on, SDR will refer to the Tier 2 SDR category, which is defined as a radio that has a minimal analog front end that may consist of amplifiers, filters, etc. with all functionality being defined by software.

With the SDR device described above, which can be programmed to receive AM, FM, or any of the myriad of digitally modulated signals, it is easy to see why this technology is of considerable interest. Cell phone providers could build base stations with SDRs that would simply need to be reprogrammed when a new communication standard emerged. A car radio could ship with basic

Annual Research Journal, Vol. IV
Electrical Engineering Research Experience for Undergraduates

ISBN 0-913260-06-1 (http://www.ee.psu.edu/reu/)

AM/FM functionality and new software could be downloaded if the user desired GPS or Bluetooth capabilities. A not-so-obvious advantage presents itself when the areas of SDR and artificial intelligence (AI) combine. These radios, often called Cognitive Radios (CRs), employ SDR technology and AI to sense their environment and dynamically adjust to improve quality of service and bandwidth utilization [2]. Ideally, the entire process, from signal acquisition to data retrieval, will be handled seamlessly and automatically by the SDR.

In CR, and to an extent in SDR, it becomes clear that a method for signal recognition is needed. To have a fully automated radio, it is necessary to be able to recognize the modulation used on a signal to properly demodulate and process the data, whether it be in a civilian environment to cope with different communication standards, or in a military environment to perform real-time signal interception and efficient jamming [3] [4]. This paper presents an implementation of a modulation classification (MC) system on a SDR platform.

BACKGROUND

SDR Technology

There are many platforms available for the development of SDR technology, but they all share some common features. There is the analog front end, ADC, processor, and DAC (Figure 1). The analog front end primarily consists of an antenna, amplifier, and, perhaps, simple filters. The ADC and DAC are simply used to convert between the analog radio signal and digital data, and vice-versa. These components often dictate how well the SDR can perform since the ADC must be fast enough to sample a signal at the Nyquist rate (although bandpass filtering can alleviate this constraint). The processing is typically done on a general purpose processor (GPP). These range from processors like Intel's Pentium chips to more specialized digital signal processors (DSPs). In either case, they are programmed—usually using a high level language such as C—in order to perform demodulation and any other signal processing that must be done [5].

Annual Research Journal, Vol. IV
Electrical Engineering Research Experience for Undergraduates

ISBN 0-913260-06-1 (http://www.ee.psu.edu/reu/)

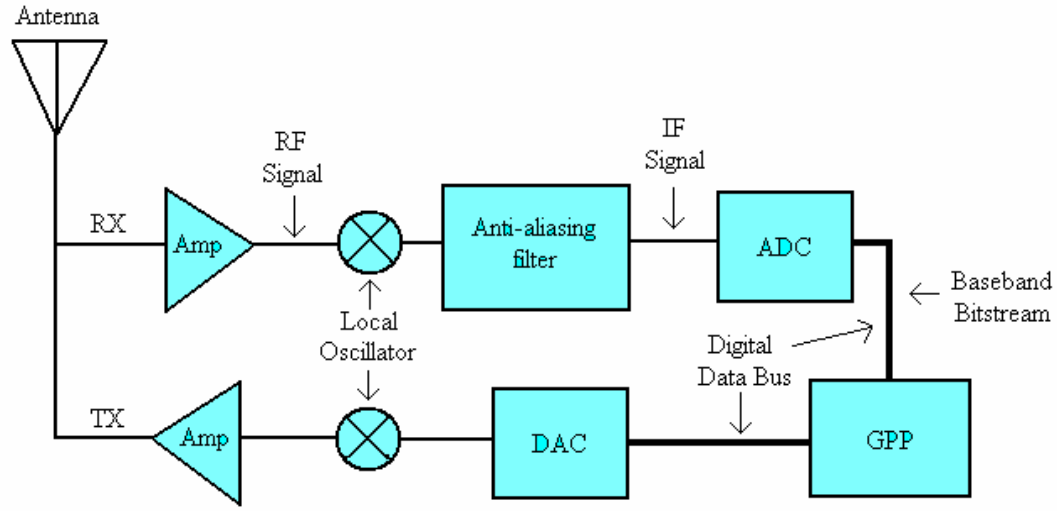

Figure 1 – General SDR block diagram

Modulation

Modulation consists of encoding data onto a carrier signal. There are several practical uses of modulation that make it absolutely essential in today's radio communication environment. Most importantly, modulation allows the frequency spectrum of the message signal to be shifted by an arbitrary amount. This ensures that data can be transmitted by many people without interfering, simply by shifting the spectrum of the data and broadcasting at an available frequency [6]. Unfortunately, the radio spectrum is a limited resource with a seemingly unlimited number of users, all desiring access. As a result, modulation alone is insufficient for efficient spectrum utilization. Another reason modulation is attractive has to do with transmission of radio signals. For efficient transmission of a signal, the antenna size must be on the order of the wavelength of the signal (e.g., half a wavelength for a dipole antenna). Audio frequencies, therefore, would require impractically large antennas [6]. For this reason, radio stations modulate the audio signal to a much higher radio frequency (RF) and then broadcast it.

There are three parameters of a radio signal that can change to produce modulation. They are the signal's amplitude, frequency, and phase. Modulation generally consists of multiplying a message signal, $m(t)$, with a carrier, $c(t)$. The message signal is at a much lower frequency than the carrier and contains the actual data of interest: speech, for example. The carrier is a sinusoid with a frequency equal to the desired transmission frequency. Modulation techniques can fall into the analog or digital categories. Analog modulation, in particular amplitude modulation (AM) and frequency modulation (FM), are perhaps the most widely known and used over-the-air modulation schemes. Due to their abundance and relatively low frequency on the RF spectrum, they are the focus of this research.

Annual Research Journal, Vol. IV
Electrical Engineering Research Experience for Undergraduates

ISBN 0-913260-06-1 (http://www.ee.psu.edu/reu/)

AM modulation uses the message signal to alter the amplitude of the carrier. AM demodulation can be done either by locally generating a signal at the carrier frequency, (coherent demodulation) or by transmitting the carrier along with the message (non-coherent demodulation). The latter approach is used more frequently since it allows for inexpensive and simple receivers. A typical AM signal is given by

$$\varphi_{AM}(t) = A \cdot \cos(\omega_c \cdot t) + m(t) \cdot \cos(\omega_c \cdot t). \quad (1)$$

Note that the carrier is transmitted along with the message signal. The carrier frequency is ω_c and the gain factor A is used to ensure the modulated signal amplitude is greater than 0 for all t.

Demodulation of an AM signal of the type in Equation 1 can be easily accomplished by a technique called envelope detection. Envelope detection is an attractive option for AM demodulation because it requires very simple hardware and is a form of non-coherent demodulation [6]. An envelope detector works by locating the signal peaks and reconstructing the message signal (Figure 2).

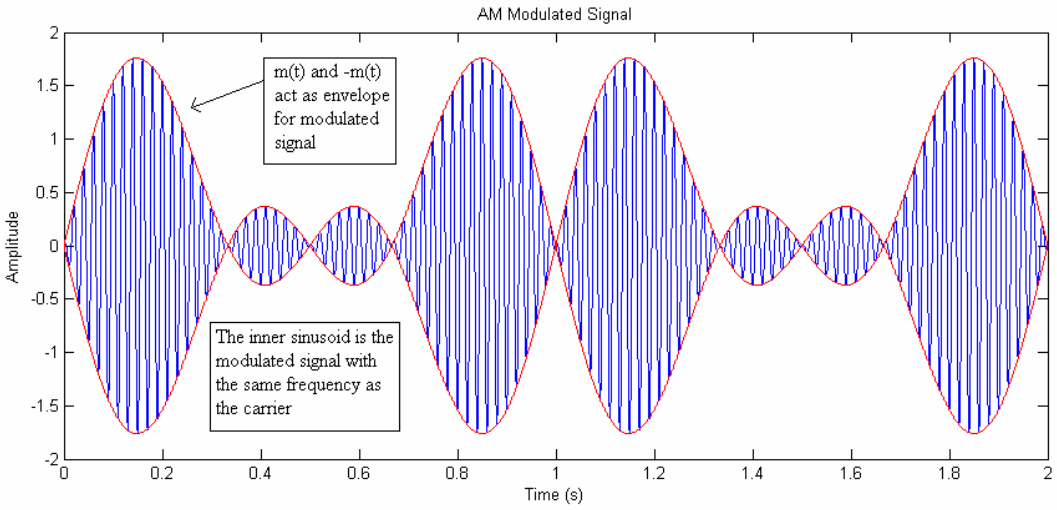

Figure 2 – Time domain view of AM modulation

FM modulation uses the message signal to vary the frequency of a constant amplitude carrier. The equation

$$\varphi_{FM}(t) = A \cdot \cos\left[\omega_c \cdot t + k_f \cdot \int_{-\infty}^{t} m(\alpha) \cdot d\alpha\right] \quad (2)$$

illustrates a typical FM signal. Once again, the carrier frequency is ω_c and k_f is a constant. In the case of FM, we can see that the instantaneous frequency of the FM signal is varied linearly with the modulating signal, $m(t)$ (Figure 3). Demodulation of a FM signal is typically done using a phase-locked loop (PLL). FM is the preferred method of analog modulation because it is much less susceptible to noise than AM is and it requires a lower transmission power to achieve the same quality [6]. Both of these advantages stem from the fact that a

Annual Research Journal, Vol. IV
Electrical Engineering Research Experience for Undergraduates

ISBN 0-913260-06-1 (http://www.ee.psu.edu/reu/)

FM signal occupies a larger bandwidth than an AM signal. In fact, a commercial AM station has a bandwidth of 20 kHz while a commercial FM station has a bandwidth of 200 kHz.

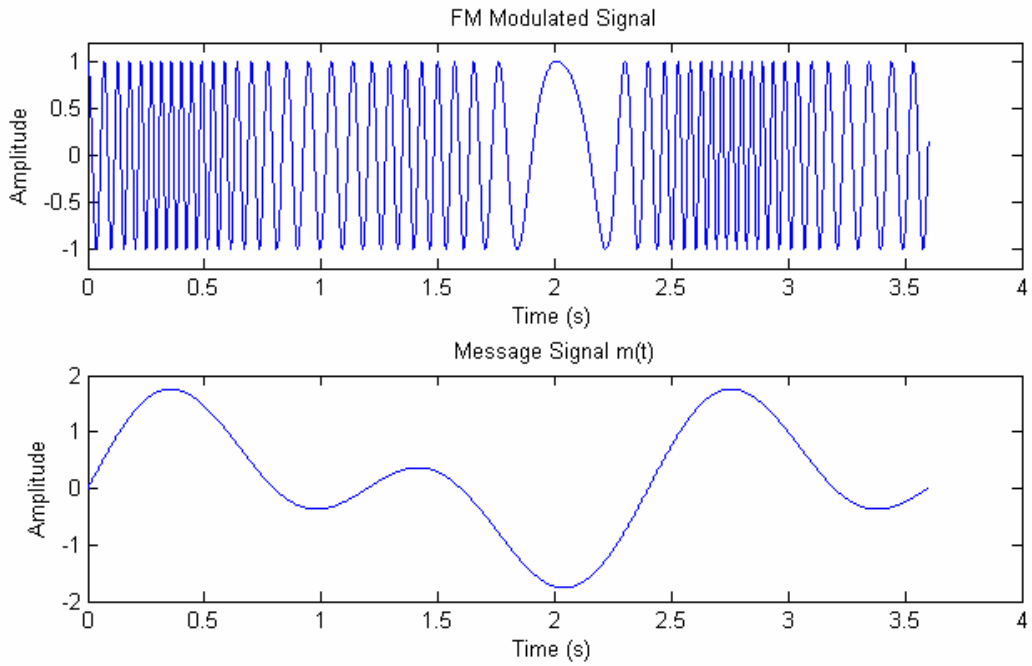

Figure 3 – Time domain view of FM modulation

Digital modulation schemes differ from analog ones primarily in that fact that the signals are converted from analog to digital format before modulation takes place [7]. Most digital modulation techniques use vector modulation or in-phase–quadrature (IQ) modulation. Vector modulation can be thought of as simultaneously changing both amplitude and frequency (or phase) of a signal. The name IQ modulation is fitting since it describes the preferred means of visualizing a vector modulation scheme. An IQ diagram is basically a means of plotting the in-phase (I) and quadrature (Q) components of a signal. The IQ diagram is a complex plane where I corresponds to the real part of the signal and Q to the imaginary part. IQ diagrams are typically used to view digital modulation schemes but they can also be used to understand analog schemes. In a digital scheme, each point on the diagram corresponds to a symbol. In analog schemes, the symbols "blur" into line segments, but they still follow easy-to-understand rules. AM modulation, for example, produces an IQ diagram with constant phase but varying amplitude. FM modulation is the opposite, with constant amplitude and varying phase (Figure 4). Digital modulation is preferred over analog because of its more efficient use of the spectrum and resistance to channel effects such as noise [7]. In digital modulation, data is commonly

Annual Research Journal, Vol. IV
Electrical Engineering Research Experience for Undergraduates

ISBN 0-913260-06-1 (http://www.ee.psu.edu/reu/)

referred to as symbols, and the number of symbols in a particular scheme corresponds to the number of bits per symbol. The symbols can be easily viewed on an IQ diagram (Figure 5). Some common types of digital modulation include QPSK for cellular phones (CDMA) and 256-QAM for digital television (in the US) [8].

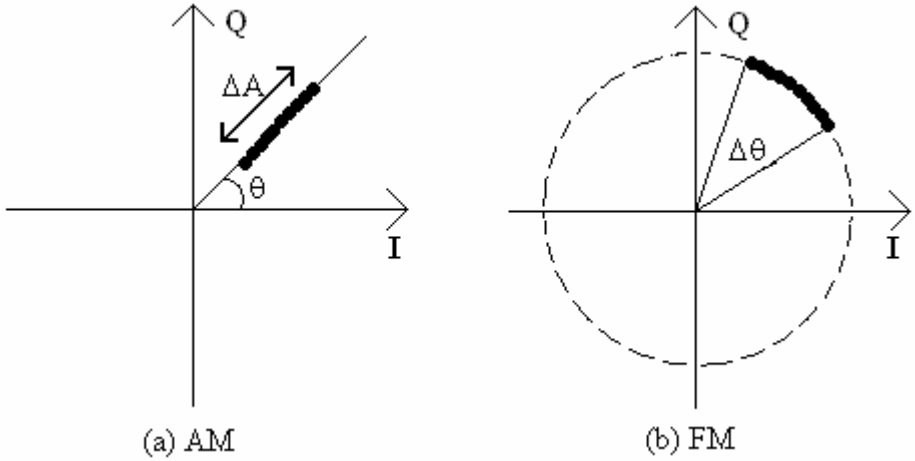

Figure 4 – Typical IQ diagrams for (a) AM signal and (b) FM signal

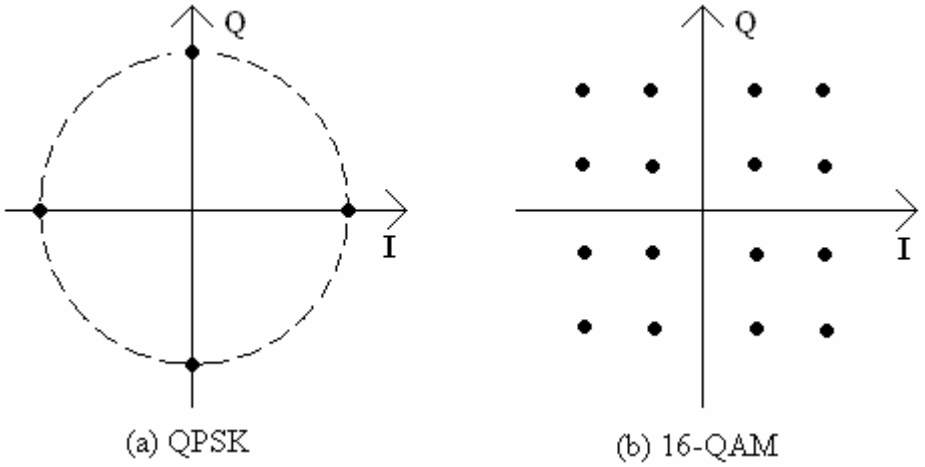

Figure 5 – Typical IQ diagrams for (a) QPSK signal and (b) 16-QAM signal

Modulation Classification

The field of modulation classification (MC) has been around since the mid 1980s, well before the advent of SDR. Techniques have been developed that examine the signal in the time domain, frequency domain, and vector space. Algorithms for modulation classification can be separated in two categories, likelihood based (LB) and feature based (FB) [4]. Most methods proceed with signal classification by first extracting a set of features, and then applying a classification algorithm to the extracted features.

Annual Research Journal, Vol. IV
Electrical Engineering Research Experience for Undergraduates

ISBN 0-913260-06-1 (http://www.ee.psu.edu/reu/)

The feature set can be comprised of time domain, frequency domain, or vector space aspects of the signal, and can include carrier frequency estimation, symbol timing, power spectral density (PSD), constellation shape, and various statistical measurements. Signal preprocessing, such as noise reduction, is often performed prior to feature extraction [4].

The algorithms used for modulation classification vary greatly. In the LB category, a likelihood function computes a likelihood value for a given signal and compares it to some threshold value. Based on the value, the modulation scheme can be determined. The FB methods use several signal features and base the classification on the signal's feature values [4]. Although LB approaches usually have better performance in terms of correct classification percentage, they are computationally complex and, therefore, not a viable option in most real-time scenarios [4]. FB methods can come close to meeting the performance of LB approaches when the features are carefully chosen. Since our interest is in real-time classification, we will only examine some of the more prominent FB classification schemes in this paper. For a more complete survey of automatic modulation classification schemes see Dobre *et al.* [4].

When features are extracted from a signal and compared to a set of "ideal" features to determine the modulation scheme of an incoming signal, the problem essentially becomes one of pattern matching. The goal is to find a feature pattern from a library of patterns that matches the feature pattern of the unknown signal. Several approaches to this pattern matching problem have been researched. Some of the earlier work by Aisbett used a feature set based on time-domain signal parameters and attempted to isolate features that were not strongly influenced by Gaussian noise [9]. This work concentrated solely on analog modulation schemes. More recent work has included research on digital modulation schemes. Neural networks are of interest due to their ability to recognize patterns, and be trained. Work by Le *et al.* [2], and Nandi and Azzouz [10], use neural networks to classify modulation schemes of unknown signals. One benefit of neural networks is that they can be designed to be fairly computationally simple, and have the potential to work in real-time systems. Nandi and Azzouz [10] also worked on the decision theoretic approach to pattern matching, which is hailed by many as the current state-of-the-art method for modulation classification [11] [12]. The decision theoretic approach can be modeled with a flowchart. Signal features are compared to some threshold value at each node of the flowchart and branches are followed until the end is reached and the modulation scheme is determined.

Another popular area of research is in using constellation diagrams to determine the modulation scheme. Many claim that a constellation diagram serves as a unique signature, and is more immune to poor channel effects (e.g., noise) than other signal features [11–14] [17]. Hero and Hadinejad–Mahram worked on a system that would convert constellation data into gray scale images, and then use image processing techniques to evaluate the constellation and determine the modulation scheme [15]. The image processing system performed

Annual Research Journal, Vol. IV
Electrical Engineering Research Experience for Undergraduates

ISBN 0-913260-06-1 (http://www.ee.psu.edu/reu/)

well; however, it was complex and could not be done in real-time [16]. Another method of assessing constellation similarity is by using a fuzzy c-means (FCM) algorithm to find constellation points. FCM is a clustering algorithm that allows data points to belong to two or more clusters. A simple difference measurement can then be used to compute the probability of a match [11] [13] [14]. Shahmohammadi and Nikoofar devised a mathematical method for determining the similarity between the constellation diagram of a received signal and the geometric pattern of a candidate modulation constellation. This approach led to a system that required far fewer computations than with decision theoretic algorithms [12].

EXPERIMENTAL DESCRIPTION

The following section describes the SDR platform that was used to implement the IQ modulation classification system.

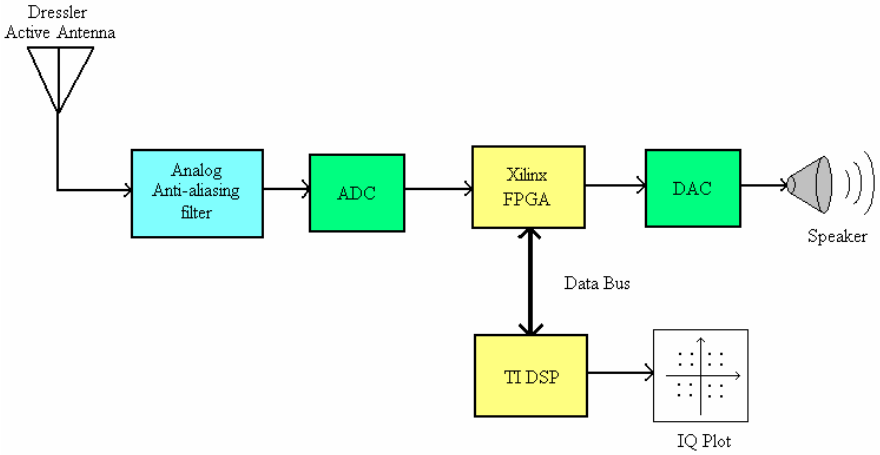

Figure 6 – SDR Platform

The system consists of hardware and software components. The hardware consists of an analog front end (for acquiring real-world signals), a simple signal generator (for test signals), and the Lyrtech SignalWAVe board. Software consists of Simulink models created to run on the board's DSP and FPGA.

Test signals are generated with a Fluke 6060B signal generator capable of modulating an RF signal (freq range 0.01–1050 MHz) with a 400-Hz or 1-kHz tone using either AM or FM. Real-world signals are acquired via an antenna and consist of AM and FM radio stations in State College, PA. The analog front end consists of an active antenna and a simple filter. The antenna used is a Dressler ARA-60 active antenna, chosen for its ability to pick up a large range of frequencies; 40 kHz to 60 MHz (although with a slightly reduced gain of 2–3 dB the frequency range can be extended to ~100 MHz to include the FM band). The filter depends on what type of signal is being monitored. A Mini-Circuits 1.9-

Annual Research Journal, Vol. IV
Electrical Engineering Research Experience for Undergraduates

ISBN 0-913260-06-1 (http://www.ee.psu.edu/reu/)

MHz lowpass filter is used to tune into AM stations while a FM bandpass filter is used to tune into FM stations.

The board used is a Lyrtech SignalWAVe board that has an integrated DSP and FPGA. The DSP is a Texas Instruments TMS320C6713. The DSP has a 225-MHz clock and access to 32 MB of onboard shared memory. The FPGA is a Xilinx Virtex II XC2V3000. The FPGA has 3 million gates and access to 32 MB of onboard shared memory. The SignalWAVe board also contains an ADC (Analog Devices' AD6644) capable of 65 MSPS with 14-bit resolution and a DAC (Analog Devices' AD9754) capable of 125 MSPS with 14-bit resolution.

Programming the board consisted of using MATLAB and Simulink to build models using block sets provided by Lyrtech. Several pieces of software were required to build and test models on the SignalWAVe board. Table 2 gives a list of all the software as well as version numbers. MATLAB makes use of Code Composer Studio to generate the C code that runs on the DSP while Xilinx Foundation ISE is used to generate the VHDL code for the FPGA. For more detailed instructions on the installation and configuration of the SignalWAVe board see the Lyrtech documentation [18].

In addition to the setup above, a Tektronix RSA 3303A Signal Analyzer was used during development of the system to monitor signals and generate IQ diagrams.

Package	Sub-Packages	Version
MATLAB	Main Program	7.0.4.365 (R14) SP 2
	Simulink	6.2
	Communications Blockset	3.1
	Signal Processing Blockset	6.1
Texas Instruments Code Composer Studio	Main Program	2.20.00 (or 3.0.0.21)
Xilinx Foundation ISE	Main Program	7.1.04i
	System Generator	7.1

Table 2 – Software Requirements for SDR Platform

The functionality of the design is split between the FPGA and DSP. The FPGA, which is capable or running at a much higher clock rate than the DSP, is used to separate the incoming signal into I and Q components (Figure 7). The sampled signal is sent through a Hilbert transformer that keeps the signal intact while shifting its phase by 90 degrees. The two components (I and Q) are appropriately scaled and packed so they can be sent over the DSP/FPGA bus.

Annual Research Journal, Vol. IV
Electrical Engineering Research Experience for Undergraduates

ISBN 0-913260-06-1 (http://www.ee.psu.edu/reu/)

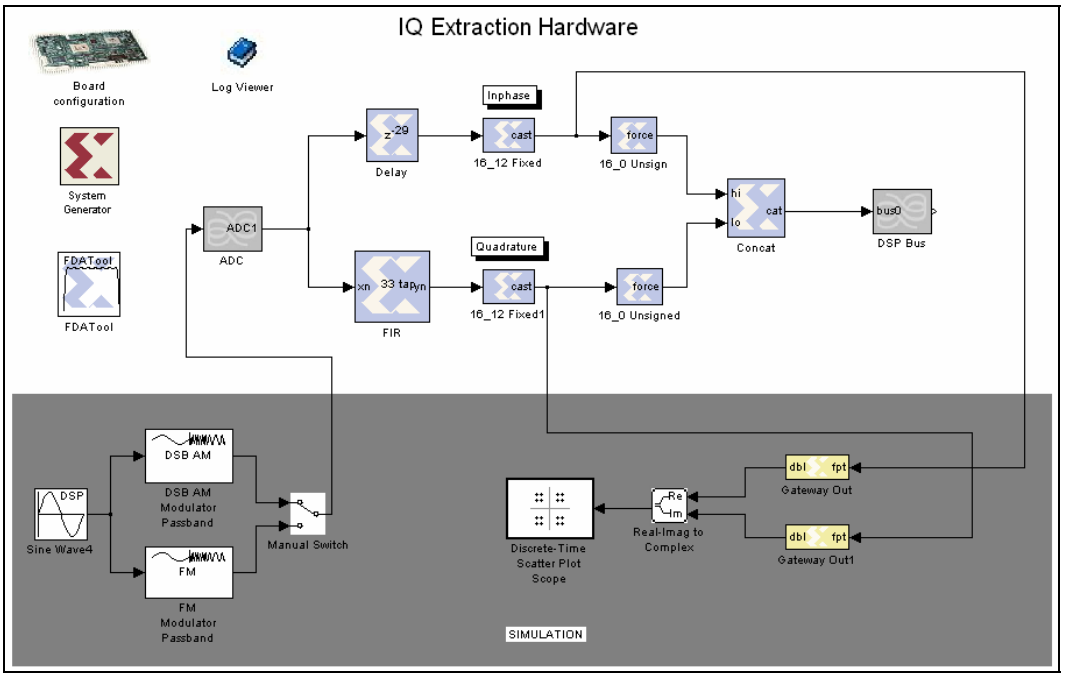

Figure 7 – FPGA Design

The DSP receives the signal's I and Q components and implements the algorithm to determine the modulation scheme (Figure 8). As of the writing of this paper, this algorithm has not yet been implemented. Currently, the I and Q components are simply displayed on a graph in real-time.

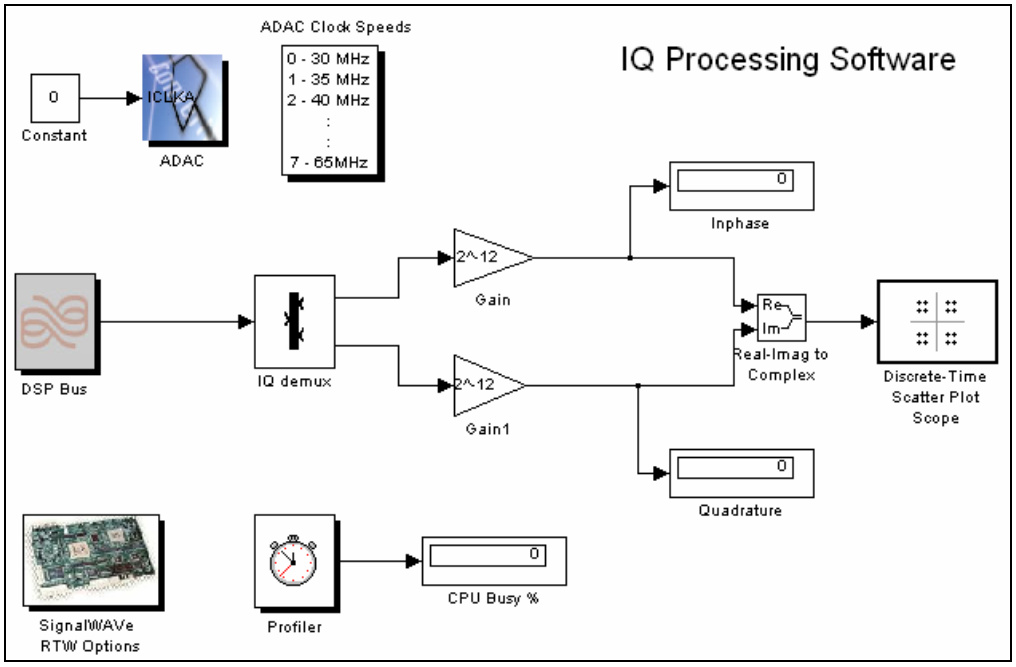

Figure 8 – DSP Design

Annual Research Journal, Vol. IV
Electrical Engineering Research Experience for Undergraduates

ISBN 0-913260-06-1 (http://www.ee.psu.edu/reu/)

Hilbert Transformer

The Hilbert transformer in the FPGA portion of the design is a crucial component of the MC system. This filter creates a signal that is orthogonal to the incoming signal. The Hilbert transformer ideally leaves the magnitude of the signal unchanged, but shifts the phase by 90 degrees. The effects of the Hilbert transformer can best be viewed by examining the frequency response of the filter. From

$$H(\omega) = -j \cdot \mathrm{sgn}(\omega) \tag{3}$$

it is easy to see that all negative frequencies receive a phase shift of −90 degrees and all positive frequencies receive a phase shift of +90 degrees.

The actual Hilbert transformer implemented in our design differs from the ideal in a few ways. First, it is impossible to have a completely flat magnitude response. Second, the filter's cutoff frequencies cannot be "brick walls"; there must be some transition region between the passband and stopband. When designing an FIR filter, the number of filter coefficients must be finite—and the number of filter coefficients determines the delay of the filter. It is desirable to have a high accuracy filter (many coefficients) with a low delay (few coefficients). These competing factors must be weighed in the design of the filter. Fewer filter coefficients means that the filter will have either a large transition region or significant passband/stopband ripple (i.e., non-uniform magnitude response).

We used the Simulink FDATool block to design our Hilbert transformer. By specifying the transition region and the desired number of coefficients, the block automatically produced the filter coefficients. Our Hilbert transformer contained 33 taps, or coefficients. This allows a relatively constant magnitude response and a tolerable delay. In our case, at a sampling rate of 30 MHz, the filter delay is

$$\frac{33}{30\ \mathrm{MHz}} = 1.1\ \mu\mathrm{s}.$$

RESULTS/DISCUSSION

Designing and implementing the MC system turned out to be a fairly involved process. The original goal for my eight-week project was to design a complete MC system; however, this turned out to be slightly ambitious. From a high-level view, the project consists of a hardware portion that runs on the FPGA, and a software portion that runs on the DSP. The FPGA portion of the design takes the input signal and separates it into I and Q components. These components are correctly scaled and then packed together and sent over the bus to the DSP. The DSP portion of the design unpacks and scales the data from the FPGA and implements the algorithm that, ultimately, will perform the modulation classification based on the I and Q data from the DSP. At the conclusion the eight weeks, the FPGA portion is complete but the DSP portion still needs a fair

Annual Research Journal, Vol. IV
Electrical Engineering Research Experience for Undergraduates

ISBN 0-913260-06-1 (http://www.ee.psu.edu/reu/)

amount of work. In its current state, the MC system can take an incoming signal, separate it into I and Q components and send these data to the DSP. The DSP simply displays the data on a scatter plot, essentially generating an IQ diagram in real-time. No automatic classification is performed, however.

Due to the incomplete nature of the system, the testing that could be done was somewhat limited. The FPGA design was verified through simulation. A sinusoidal signal was modulated with AM and FM and passed through the FPGA design. The simulation blocks appear in the gray box in the FPGA model (Figure 7). The IQ diagrams obtained suggested that the design was working properly. It was easy to tell from the different IQ diagrams when the incoming signal was AM or FM (Figure 9). Independently, the DSP model was tested to make sure that data was correctly being passed between the FPGA and DSP. This was verified to work correctly. Unfortunately, there was insufficient time to do real-world signal testing.

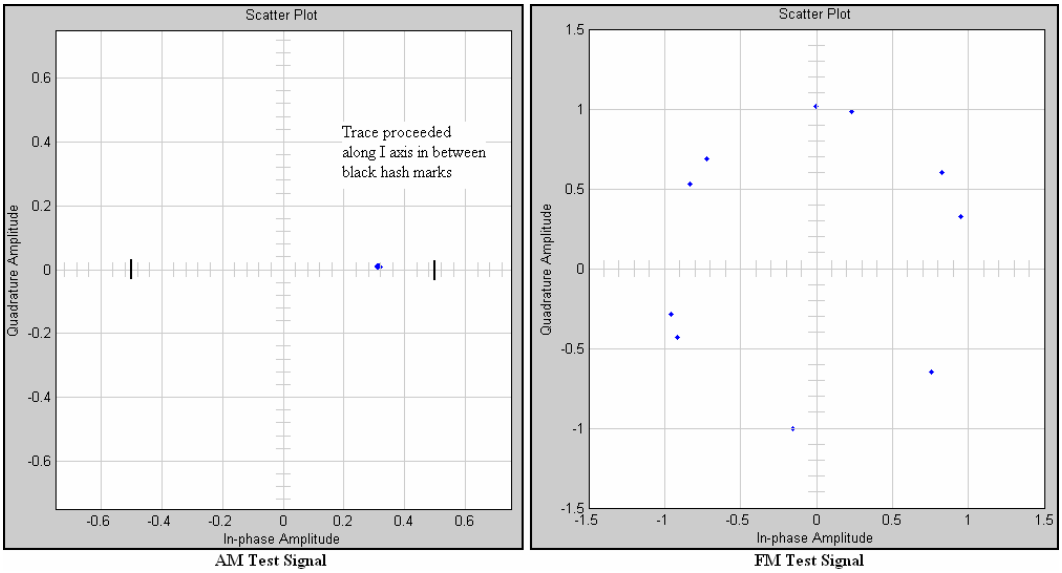

Figure 9 – FPGA Test Results

Although the project is far from complete, the results obtained so far are encouraging. We have shown through simulation that, at least for AM and FM, an IQ diagram can be used as a unique signature to determine modulation classification. In addition, the integration of the DSP and FPGA allowed us to create a system that utilized each component in such a way as to minimize the system footprint. In other words, the project goal of creating a resource-conservative system was realized. Approximately 10% of the available FPGA resource was used, leaving plenty of room for demodulation hardware. On the DSP side, the unpacking and displaying of IQ signals utilized approximately 6% of the DSP's processing power, again, leaving plenty of processing power for the classification algorithm.

Annual Research Journal, Vol. IV
Electrical Engineering Research Experience for Undergraduates

ISBN 0-913260-06-1 (http://www.ee.psu.edu/reu/)

CONCLUSIONS/FUTURE WORK

The project set out to create a completely automated MC system. Although it has not yet been completed, significant progress towards creating the MC system has been made. Initial testing shows that the design is feasible and that it has good potential to meet the original goal of a resource-conservative system. The IQ diagrams produced from simulated signals show that they can be used as unique signatures to classify modulation types.

While these initial strides provide a foundation for completing the project, there are still a number of issues that need to be addressed. Initially, the complete design (DSP and FPGA) will need to be verified with real-world AM and FM signals. Afterwards the design can proceed along different paths.

To have a truly robust system, we must be able to classify not only analog modulation types, but digital ones as well. The system can be tested with various digital modulation types to see if they generate unique signatures as well. This may be a challenging problem since digital IQ diagrams are often more complex than analog ones. In addition, IQ diagrams of digital modulation schemes often require knowledge of the symbol rate to plot correctly.

An equally challenging problem is to create the MC algorithm that will run on the DSP. In the current system, this algorithm will most likely need to be written in C to ensure efficiency and allow flexibility. While the Simulink block-building approach allows for quick design and prototyping, it does not allow the flexibility that will most likely be required for a MC algorithm. In addition to flexibility, efficiency is also desired. To ensure the most efficient design the C code will probably have to be written by hand as opposed to generated by MATLAB. The specific design of this algorithm is fairly flexible. A number of potential candidates for MC algorithms were presented in the background section of this paper. Among the most attractive are neural network approaches. They are not computationally intensive (a must for the limited computational power of the DSP), they are fairly simple to implement, and they have been shown to perform well as MC algorithms.

ACKNOWLEDGEMENTS

Throughout my research experience I received help and guidance from several people. My mentor, Dr. Sven Bilén, provided suggestions for how to go about accomplishing the project goals. He was always able to answer questions I had and provide valuable advice. Ricardo Jímenez, a graduate student who worked in my lab, was also very helpful and answered several general questions I had about the platform we used. Another person who proved to be a valuable technical support resource was Dany Jaques of Lyrtech. He answered the more complicated questions I had concerning my design. Finally, I would like to thank the REU program supported by the National Science Foundation (under Grant Number EEC-0244030) for providing me with this opportunity.

Annual Research Journal, Vol. IV
Electrical Engineering Research Experience for Undergraduates

ISBN 0-913260-06-1 (http://www.ee.psu.edu/reu/)

REFERENCES

[1] J. Taudien, *Using Software Defined Radio Techniques to Monitor the Radio Spectrum and Demodulate AM and FM Signals*, pp.74, Thesis (B.S.)--Pennsylvania State University, 2005.

[2] B. Le, et al., *Modulation Identification Using Neural Networks for Cognitive Radios*, Department of Engineering, Virginia Tech, 2005.

[3] O.A. Dobre, et al., "Blind Modulation Classification: A Concept Whose Time Has Come," in 2005 IEEE/Sarnoff Symposium, April 18—19, 2005, pp. 223-228.

[4] O.A. Dobre, et al., "A Survey of Automatic Modulation Classification Techniques: Classical Approaches and New Trends," to be published in IEEE Proc. Commun., 2006.

[5] K.E. Nolan, et al., "Modulation Scheme Classification for 4G Software Radio Wireless Networks," in SPPRA 2002, June 25—28, 2002, Crete, Greece, pp. 25—31.

[6] B.P. Lathi, *Signal Processing and Linear Systems*, Oxford, NY: Oxford University Press, 1998, pp. 277—300.

[7] "An Introduction to Digital and Vector Modulation," Aeroflex, 2005.

[8] "Digital Modulation in Communications Systems—An Introduction," Agilent Technologies, 2001.

[9] J. Aisbett, "Automatic Modulation Recognition Using Time Domain Parameters," Signal Processing, vol. 13, pp. 323—328, 1987.

[10] A.K. Nandi, and E.E. Azzouz, "Algorithms for Automatic Modulation Recognition of Communication Signals," *IEEE Transactions on Communications*, vol. 46, no. 4, April 1998.

[11] B.G. Mobasseri, *Constellation Shape as a Robust Signature for Digital Modulation Recognition*, ECE Department, Villanova University, 1999.

[12] M. Shahmohammadi, and H.R. Nikoofar, "Modulation Classification for QAM/PSK Using A Soft Clustering Algorithm," in ISIT 2002, Lausanne, Switzerland, June 30—July 5, 2002, pp. 19.

[13] P.C. Pinto, S.B. Silva, and H.C. Miranda, "An Adaptive Software Radio Receiver Architecture for Linear Bidimensional Modulations," in Sixth Baiona Workshop on Signal Processing in Communications, September, 2003, Baiona, Spain.

[14] B. Mobasseri, *Digital Modulation classification using constellation shape*, ECE Department, Villanova University, 1997.

[15] A.O. Hero III, and H. Hadinejad-Mahram, "Digital Modulation Classification Using Power Moment Matrices," *IEEE*, 1998.

[16] K.E. Nolan, et al., "Modulation Scheme Recognition Techniques for Software Radio on a General Purpose Processor Platform," in First Joint IEI/IEE Symposium on Telecommunications System Research, November 27, 2001, Dublin, Ireland, pp. 5.

[17] C. Narduzzi, and M. Bertocoo, *Conformance and Performance*, Dipartimento di Elettronica e Informatica, Università di Padova, 2004.

[18] "SignalWAVe Quick Start Guide," Lyrtech Inc.

Annual Research Journal, Vol. IV
Electrical Engineering Research Experience for Undergraduates

ISBN 0-913260-06-1 (http://www.ee.psu.edu/reu/)

THREE-DIMENSIONAL FINITE DIFFERENCE TIME-DOMAIN MODELING OF THE SCHUMANN RESONANCES ON EARTH AND MARS

Adam R. Dreibelbis[*], Heng Yang[+], and Victor P. Pasko[#]

Department of Electrical Engineering
The Pennsylvania State University, University Park, PA 16802

[*]Undergraduate student of
Department of Physics
Susquehanna University
Selinsgrove, PA 17870

ABSTRACT

The three-dimensional (3-D) finite difference time domain (FDTD) modeling technique developed by Yang and Pasko [1] has been shown to be useful for solution of realistic Schumann resonance (SR) problems. In this paper we use this technique to calculate the Schumann resonance frequencies on Earth using two different atmospheric conductivity profiles, and on Mars both for normal ionospheric conditions and during solar flares. The Martian conductivity profile is derived from realistic measurements of electron densities conducted by the Mars Global Surveyor (MGS) mission and from data published in previous literature[2]. Comparison of results from the 3D FDTD model with those from previous investigations reporting parameters for Martian Schumann resonances[2] demonstrates the potential and applicability of the FDTD technique for studies of realistic SR problems on the planets in the solar system.

1. INTRODUCTION

The highly conducting Earth's surface and ionosphere create a cavity through which the extremely low frequency (ELF) electromagnetic waves can propagate

[+] Graduate Mentor
[#] Faculty Mentor

Annual Research Journal, Vol. IV
Electrical Engineering Research Experience for Undergraduates

ISBN 0-913260-06-1 (http://www.ee.psu.edu/reu/)

around the globe. The resonant waves of this cavity, called Schumann resonances (SR) were first theorized by W. O. Schumann in 1952 [3]. In an ideal cavity, the frequencies for SR can be calculated by the following equation:

$$f_n = \frac{c}{2\pi a}\sqrt{n(n+1)} \tag{1}$$

where n is the mode number, c is the speed of light in a vacuum, and a is the radius of the planet. It has since been proven that these ELF waves can be applied in many remote sensing applications on a global scale[4,5,6]. Schumann resonance frequencies have been shown to be related to the global lightning activity and the electromagnetic properties of the lower ionosphere[5,6]. Research has also shown a correlation between global temperature patterns and SR parameters[4,7]. Some previous studies have also discussed the response of SR to x-ray bursts and solar proton events (SPEs). It is shown that x-ray bursts increase the SR frequencies, and SPEs decrease the SR frequencies, due to the conductivity perturbations at difference altitudes associated with these two events[1,8,9].

The correlation of Schumann resonances and lightning activity has recently led to interest in studying the possibility of the existence of lightning discharges on other planets and moons in the solar system. The Mars Global Surveyor Mission as well as the Cassini-Huygens Mission to Saturn and Titan are partially interested in finding lightning activity on Mars and Titan. The existence of SR will strongly support the existence of the electrical discharges in the atmosphere on these celestial bodies.

The FDTD technique[10] provides a flexible means for solving electromagnetic problems in a medium with arbitrary inhomogeneities, and recently, it has been successfully applied to solve VLF/ELF propagation problems in the Earth-ionosphere cavity [1,11,12].

2. MODEL FORMULATION

2.1 The 3-Dimesional Finite Difference Time-Domain Model

The 3-D FDTD model[1] numerically solves Maxwell's equations (2) and (3) in spherical coordinates:

$$\nabla \times \vec{E} = -\mu_0 \frac{\partial \vec{H}}{\partial t} \tag{2}$$

$$\nabla \times \vec{H} = \varepsilon_0 \frac{\partial \vec{E}}{\partial t} + \sigma \vec{E} \tag{3}$$

The simulation domain is assumed to be between two perfectly conducting spheres. For the Earth, an inner radius of 6400 km was used with an additional 100 km altitude for the ionosphere, and for Mars, an inner radius of 3400 km with the same 100 km separation between surfaces of the conducting spheres. The

Annual Research Journal, Vol. IV
Electrical Engineering Research Experience for Undergraduates

ISBN 0-913260-06-1 (http://www.ee.psu.edu/reu/)

cavity formed by the concentric spheres is divided into small cells, with 10, 20, and 40 divisions in the r, θ, and ϕ directions, respectively. A model lightning strike, 10 km in length with a current rise time of 500 μs and exponential fall of time scale 5 ms provides the excitation for the cavity. This excitation source is located at 0ºN, 0ºE, with a receiver placed at 18ºN, 0ºE. The algorithm returns a time dependent electric field value. This time domain data is converted to frequency domain data using fast Fourier transformation (FFT). The SR frequencies we report in this paper are from the peaks of the E_r power spectrum curve, or the peak frequencies. The first five peak frequencies are derived from the E_r power spectrum for each of the cases we modeled, e.g., Earth with the single exponential profile and "knee" model, Mars with normal ionospheric conditions, and Mars during solar flares. The related conductivity (σ) distributions between the two surfaces forming the cavity are defined in the next section.

2.2 Conductivity profiles

Several approximations of the Earth's conductivity profile have been employed through previous research [13,14,15]. The single exponential approximation and "knee" model play important roles in the development of the SR theory. Figure 1[1], shows a single exponential conductivity profile from Sentman[14] and a "knee" profile from Mushtak and Williams [15]. The conductivity profiles for the single exponential (Eq. 4) and "knee" model (Eqs. 5a and 5b) approximations are given by:

$$\sigma(z) = 10^{-16} \exp\left(\frac{z}{3.1}\right) \tag{4}$$

$$\sigma(z) = \sigma_{kn} \exp[(z - h_{kn})/\varsigma_b] \quad \text{for } z < h_{kn} \tag{5a}$$

$$\sigma(z) = \sigma_{kn} \exp[(z - h_{kn})/\varsigma_a] \quad \text{for } z \geq h_{kn} \tag{5b}$$

where $h_{kn} = 55$ km, $\varsigma_a = 2.9$km, $\varsigma_b = 8.3$ km, and $\sigma_{kn} = 5.56 \times 10^{-10}$S/m.

The accuracy of the FDTD model is verified using these types of profiles for the Earth-ionosphere cavity and comparing the FDTD results to previous results obtained by different models using the same profiles.

An accurate conductivity profile for Mars can be derived from the following equation:

$$\sigma_e = \frac{N_e q_e^2}{m_e \nu_e} \tag{6}$$

where N_e is the electron number density, q_e and m_e are the charge and mass of an electron, respectively, and ν_e is the frequency of collisions between electrons and neutral particles. This collision frequency was obtained using the equation:

Annual Research Journal, Vol. IV
Electrical Engineering Research Experience for Undergraduates

ISBN 0-913260-06-1 (http://www.ee.psu.edu/reu/)

$$\nu_e = N_n \overline{\sigma v} \tag{7}$$

where N_n is the neutral gas density and $\overline{\sigma v}$ is the average of the product of the total collision cross section and the velocity, which is calculated using a Maxwellian velocity distribution. More detail on the calculation of the collision frequency can

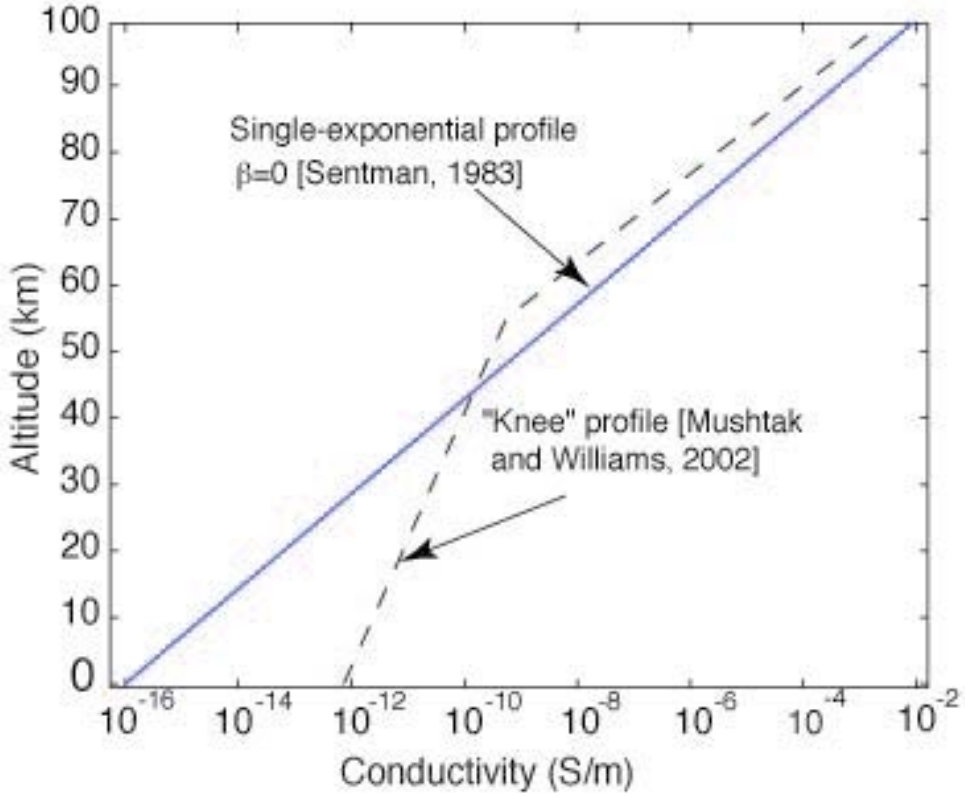

Figure 1. The modeling conductivity profiles in the Earth-ionosphere cavity.

found in the book written by Banks and Kockarts[16]. Figure 4 shows the calculated collision frequencies for Earth and Mars. The cross section data for the neutral gas particles in Earth's and Mars' atmospheres were taken from http://jilawww.colorado.edu/www/research/colldata.html. Despite the large difference in neutral gas density between the Earth and Mars as seen in Figure 3, their collision frequencies are relatively similar, because the Martian atmosphere is comprised mostly of carbon dioxide. The peak of carbon dioxide's cross-section curve occurs at low energy, which is close to the velocity of the peak of the Maxwellian energy distribution. Therefore, the larger values of $\overline{\sigma v}$ on Mars compensate for lower neutral gas density on this planet, allowing the Martian collision frequency to be very similar to Earth's. The Martian temperature profile shown in Figure 2 was derived from previous literature[17].

Annual Research Journal, Vol. IV
Electrical Engineering Research Experience for Undergraduates

ISBN 0-913260-06-1 (http://www.ee.psu.edu/reu/)

The Martian conductivity profiles (shown in Figure 5) are derived from realistic measurements of electron density and related data documented in previous literature. A public database from the Mars Global Surveyor (MGS) mission[18] provided information for the upper atmosphere (from ~70 km to ~200 km). The dashed line in Figure 5 indicates the conductivity profile derived from MGS data for April 15, 2001, a day Mars experienced a solar flare[19], and the solid line represents the Martian conductivity for normal conditions. The data for lower level of the atmosphere (from 0 km to ~70 km) was obtained from previous publications that estimated the SR for Mars [2]. This model used Eq. 5a with h_{kn} = 53 km, ς_b= 6.0 km, and $\sigma_{kn} = 7.5 \times 10^{-10}$ S/m. The data available from the MGS

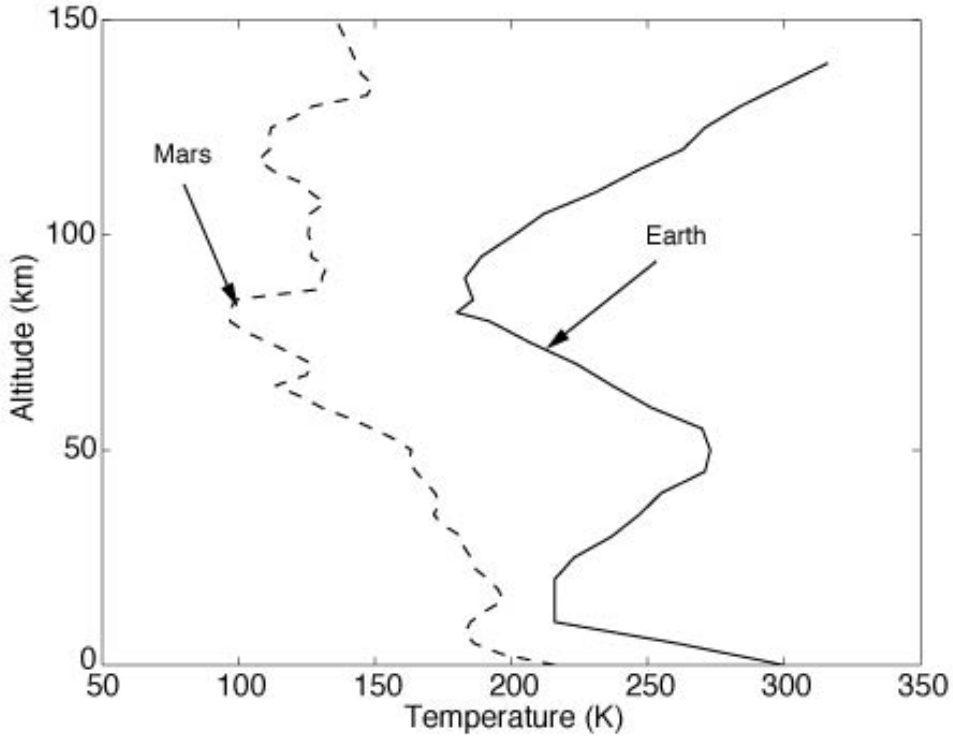

Figure 2. Temperature profiles for both Earth and Mars.

Annual Research Journal, Vol. IV
Electrical Engineering Research Experience for Undergraduates

ISBN 0-913260-06-1 (http://www.ee.psu.edu/reu/)

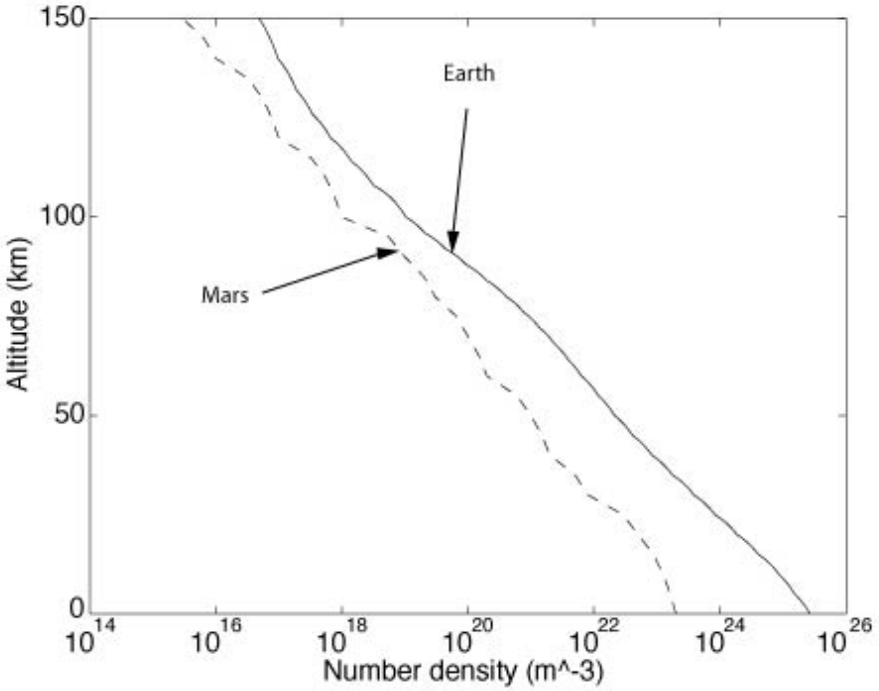

Figure 3. Neutral gas density profile for Earth and Mars.

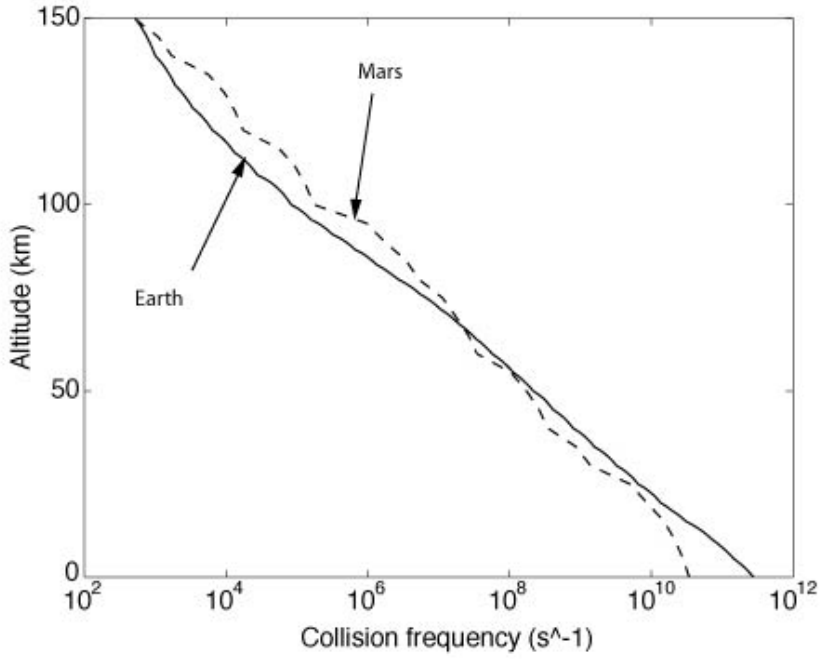

Figure 4. Collision frequency between electrons and neutral particles for Earth and Mars.

Annual Research Journal, Vol. IV
Electrical Engineering Research Experience for Undergraduates

ISBN 0-913260-06-1 (http://www.ee.psu.edu/reu/)

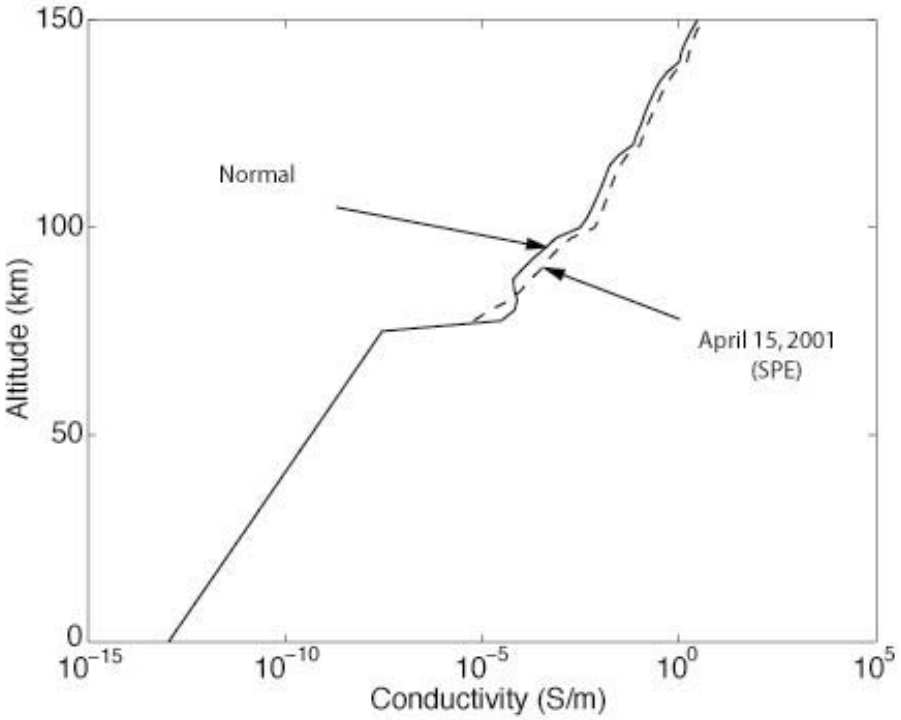

Figure 5. Martian conductivity profile for both a normal case, and during a solar flare on April 15, 2001.

public database all were taken at times and locations that corresponded to near sunrise or sunset, so a spherically uniform profile is employed in our simulations for Mars without solar flares. To account for the ionospheric perturbation produced by solar flares, half Mars is covered by the disturbed conductivity profile shown by the dashed line in Figure 5.

3. RESULTS AND DISCUSSION

Figures 6 and 7 show the E_r spectra for the Earth-ionosphere cavity obtained from the 3-D FDTD model for a single exponential conductivity profile and a "knee" model approximation profile, respectively. As is from Table I, the results obtained by the FDTD method are very close to the previous analytical results[1,20].

Annual Research Journal, Vol. IV
Electrical Engineering Research Experience for Undergraduates

ISBN 0-913260-06-1 (http://www.ee.psu.edu/reu/)

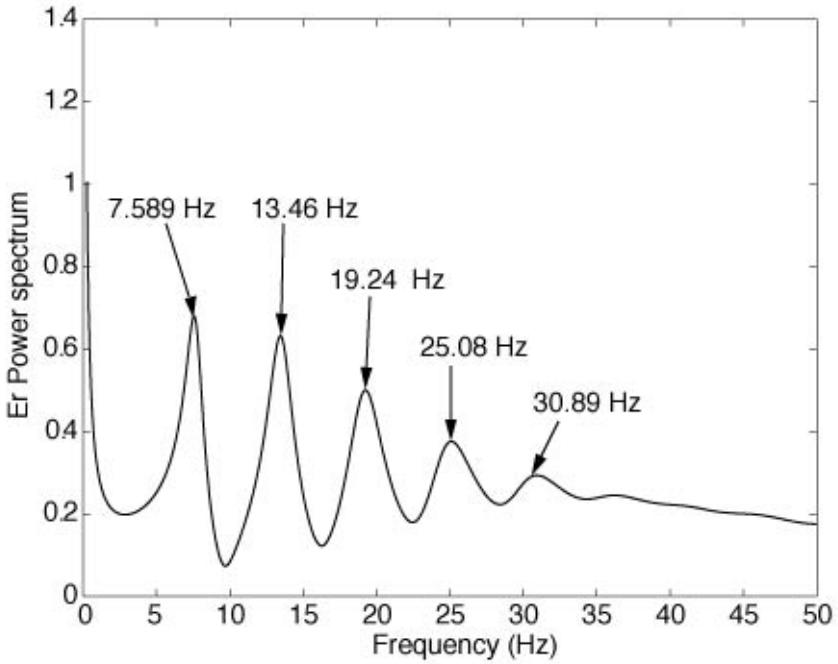

Figure 6. E_r spectrum for Earth obtained from 3-D FDTD modeling method with a single exponential conductivity profile.

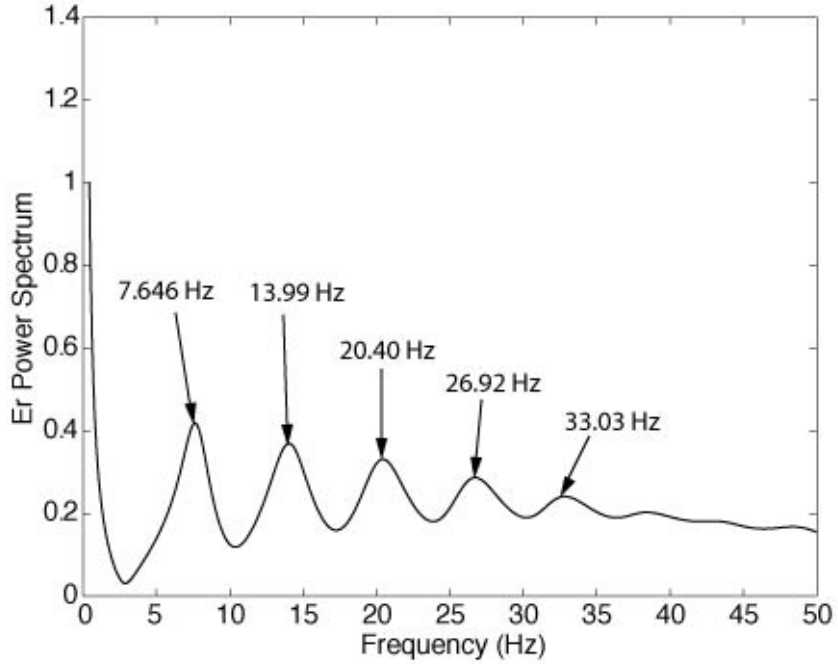

Figure 7. E_r spectrum for Earth obtained from 3-D FDTD modeling method with a "knee" model conductivity profile.

Annual Research Journal, Vol. IV
Electrical Engineering Research Experience for Undergraduates

ISBN 0-913260-06-1 (http://www.ee.psu.edu/reu/)

The largest difference for the single exponential profile was 1.6% and the largest difference for the knee model was 1.9%.

Figure 8 shows the 3-D FDTD E_r spectrum output for the conductivity profiles shown in Figure 5. The solid line is the E_r spectrum on Mars during normal conditions. The SR frequencies for the normal Mars-ionosphere cavity are 15.2 Hz, 28.3 Hz, 41.5 Hz, 54.7 Hz, and 67.8 Hz, respectively, for the first five modes. These values are close to those reported by Sukhorukov,[2] because the lower half of the conductivity profile is the same for both cases. The respective values for all of the Martian SR frequencies are approximately twice that of their terrestrial analogs. This result can be easily explained by direct inspection of equation (1). The radius of Mars is approximately half of Earth's, so this equation should yield a result approximately twice as large. Meanwhile, the conductivity profile is also an important parameter to determine the SR frequencies in a global resonant cavity.

The dashed line in Figure 8 is the E_r spectrum on Mars during the solar flare on April 15, 2001. The SR for the first five modes for this case are 15.0 Hz, 27.7 Hz, 40.7 Hz, 53.7 Hz, and 66.4 Hz respectively. The solar flare did not change the SR for Mars in the same way that they affect the Earth[9]. The SR frequency variation is much less noticeable on Mars, a change of only about 1% for the first mode, as opposed to about 5% for the first mode on Earth[1]. Such small frequency variation can be explained by the little difference in the conductivity profiles on Mars during normal ionospheric conditions and the solar flares [19] shown in Figure 5. The perturbation of the conductivity profile employed in previous studies to account for the SPEs is as much as 1000 times[1] of the normal ionospheric condition in the Earth-ionosphere cavity, yet for Mars, the perturbation is only about 200-300%, which accounts for relatively small changes in resonant frequencies shown in Table II.

Table I. Comparison of the first five Schumann resonance modes for Earth with different conductivity profiles and different modeling methods.

Mode Number	Earth with Single Exponential profile (FDTD)	Single Exponential [Yang and Pasko, 2005]	Earth with "Knee" model (FDTD)	"Knee" model [Pechony and Price, 2004, Table 2]
n	f, Hz	f, Hz	f, Hz	f, Hz
1	7.6	7.54	7.6	7.7
2	13.5	13.4	14.0	14.0
3	19.2	19.2	20.4	20.2
4	25.1	24.8	26.9	26.4
5	30.9	30.4	33.0	32.6

ISBN 0-913260-06-1 (http://www.ee.psu.edu/reu/)

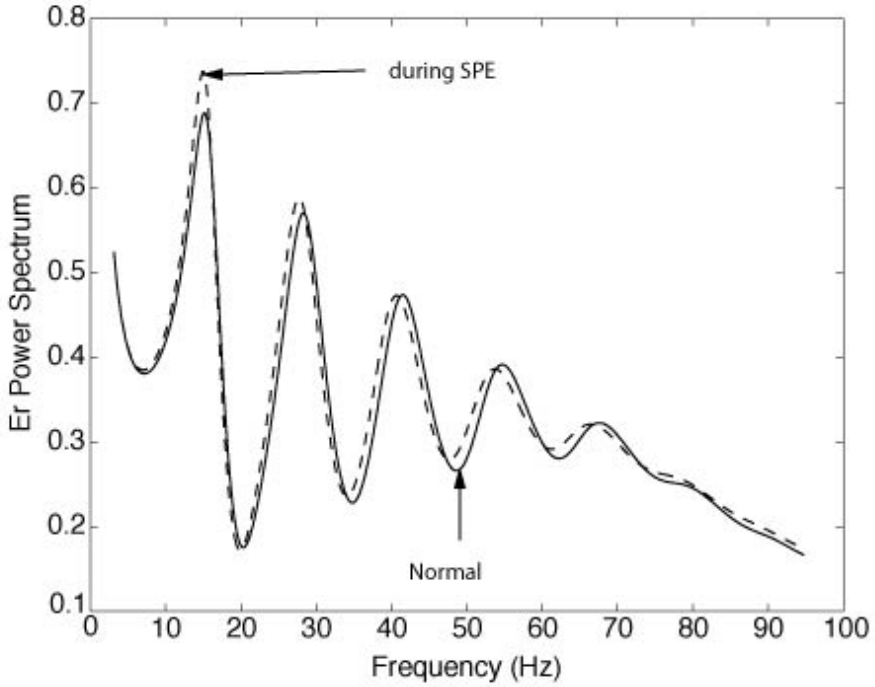

Figure 8. E_r spectrum for the Mars-ionosphere cavity using the 3-D FDTD modeling method.

Table II. Schumann resonance results for Mars.

Mode Number	[Sukhorukov, 1991]	FDTD Mars with normal conditions	FDTD Mars with Solar Proton Event	% Difference (normal and SPE)
n	f, Hz	f, Hz	f, Hz	%
1	13-14	15.2	15.0	1.06
2	24-25	28.3	27.7	2.01
3	35-37	41.5	40.7	1.98
4	--	54.7	53.7	1.79
5	--	67.8	66.4	1.93

The real data from the MGS mission being only available down to about 70 km forced us to use other approximation methods for the atmospheric conductivity below 70 km. However, the SR parameters are also strongly dependent on the conductivity distribution in this region. Therefore, we believe that the results derived from the conductivity profiles shown in Figure 5 are preliminary and additional research work is needed for accurate estimation of the conductivity perturbation in the Martian cavity below 70 km during SPEs.

Annual Research Journal, Vol. IV
Electrical Engineering Research Experience for Undergraduates

ISBN 0-913260-06-1 (http://www.ee.psu.edu/reu/)

4. CONCLUSIONS

The agreement between the FDTD results for the Earth-ionosphere cavity and the previous results[1,20] shows that the FDTD modeling method is a very good method to solving SR problems. The FDTD method can be applied to the Mars-ionosphere cavity with a derived conductivity profile. The first five frequencies for the Mars-ionosphere cavity are 15.2 Hz, 28.3 Hz, 41.5 Hz, 54.7 Hz, and 67.8 Hz respectively. We have found that solar flares can change the frequency of SR on Mars, but the change in frequency is much smaller for Mars (~1.0 %) than on Earth (~5.0 %), because the perturbation of Mars' ionosphere is much smaller than it is on Earth. The conductivity profile that can be derived from current Mars global Surveyor (MGS) data is not enough for an accurate calculation of SR parameters. If more accurate calculations of Martian Schumann resonances are to be made in the future using this method, a more detailed and accurate conductivity profile must be attained.

5. ACKNOWLEDGEMENTS

This material is based upon work supported by the National Science Foundation under Grant No. EEC-0244030 and by NSF ATM-0134838 grant to Penn State University.

REFERENCES

[1] Yang, H. and V. P. Pasko, "Three-dimensional finite difference time domain modeling of the Earth-ionosphere cavity resonances," *Geophys. Res. Lett.*, **32** L03114 (2005).

[2] Sukhorukov, A. I., "On the Schumann Resonances on Mars," *Planet. Space Sci.,* **39,** (12), 1673-1676 (1991).

[3] Schumann, W. O., "Uber die strahlungslosen eigenschwingungen einer leitenden Kugel die von einer Luftschicht und einer Ionospharenhulle umgeben ist," *Z. Naturforsch.,* **7a,** 149, (1952).

[4] Williams, E. R., "The Schumann Resonance: A Global Tropical Thermometer," *Science,* **256,** (5060), 1184-1187 (1992).

[5] Cummer, S.A., "Modeling Electromagnetic Propagation in the Earth-Ionosphere Waveguide," *IEEE Trans. Antennas Propagat.*, **45,** 837, (2000).

[6] Roldugin, V.C., Y.P. Maltsev, A.N. Vasiljev, A.Y. Schokotov, and G.G. Belyajev, "Schumann resonance frequency increase during solar proton X-ray bursts," *J. Geophys. Res.,* **109,** A01216, (2004).

[7] Williams, E. R., "Lightning and climate: A review," *Atmos. Res.* **76,** 272-287 (2005).

[8] Sátori, G., E. Williams, and V. Mushtak, "Response of the Earth-ionosphere cavity resonator to the 11-year solar cycle in X-radiation," *J. Atmos. Sol. Terr. Phys.,* **67,** 553-562, (2005).

[9] Roldugin, V.C., Y.P. Maltsev, A.N. Vasiljev, A.V. Shvets, and A.P. Nikolaenko, "Changes on Schumann resonance parameters during the solar

ISBN 0-913260-06-1 (http://www.ee.psu.edu/reu/)

proton event of 14 July 2000," *J. Geophys. Res.,* **108,** (A3), 1103, (2003).
[10] Taflove, A. and S.C. Hagness, *Computational Electrodynamics: The Finite-Difference Time-Domain Method,* Artech House, Norwood, Mass., 2000.
[11] Pasko, V.P., U.S. Inan, T.F. Bell, and S.C. Reising, "Mechanism of ELF radiation from sprites," *Geophys. Res. Lett.,* **25,** 3493 (1998).
[12] Simpson, J.J., and A. Taflove, "Two-dimesional FDTD model of antipodal ELF propagation about the earth-sphere," *Antennas Wireless Propag. Lett.,* **1,** 53, (2002).
[13] Thèvenot, M., J.P. Bérenger, T. Mondière, F. Jecko, "A FDTD scheme for the computation of VLF-ELF propagation in the anisotropic earth-ionosphere waveguide," *Annales Des Télécommunications,* **54,** (5-6), 297-310 (1999).
[14] Sentman, D.D., "Schumann resonance effects of electrical conductivity perturbaqtions in an exponential atmospheric/ionospheric profile," *J. Atmos. Sol. Terr. Phys.* **45,** (1), 55-65, (1983).
[15] Mushtak, V.C. and Williams E.R., "ELF propagation parameters for uniform models of the Earth-ionosphere waveguide," *J. Atmos. Sol. Terr. Phys.* **64,** (18), 1989-2001, (2002).
[16] Banks, P.M. and G. Kockarts, "Chapter 9: Collision Processes," *Aeronomy: Part A,* Academic Press, New York, 1973.
[17] Magalhães, J.A., J.T. Schofield, and A. Seiff, "Results of the Mars Pathfinder atmospheric structure investigation," *J. Geophys. Res.,* **104,** (E4), 8943-8955, (1999).
[18] Twicken, J., and D. Hinson. "Public Access to Mars Global Surveyor Radio Science Standard Electron Density Profiles." STAR Lab. 21 Apr. 2006. Stanford University. June 2006 <http://nova.stanford.edu/projects/mod/eds-public.html>.
[19] Mendillo, M., P. Withers, D. Hinson, H. Rishbeth, B. Reinisch, "Effects of Solar Flares on the Ionosphere of Mars," *Science,* **311,** 1135-1138, (2006).
[20] Pechony, O., and C. Price, "Schumann resonance parameters calculated with a partially uniform knee model on Earth, Venus, Mars, and Titan," *Radio Sci.*, **39** (5), RS5007 (2004).

Annual Research Journal, Vol. IV
Electrical Engineering Research Experience for Undergraduates

ISBN 0-913260-06-1 (http://www.ee.psu.edu/reu/)

FRACTAL MODELING OF CLOUD-TO-GROUND LIGHTNING

Whitney Tidwell*, Jérémy A. Riousset†, and Victor P. Pasko‡

CSSL Laboratory, Department of Electrical Engineering
The Pennsylvania State University, University Park, PA 16802

*Undergraduate student of
Department of Physics
Rhodes College, Memphis, TN 38112

ABSTRACT

Marshall and Stolzenburg[1] hypothesized following discussion by Kasemir[2] that lightning, as a mover of charge within the thundercloud[3, 4], is responsible for decreases in the total electrostatic energy of a thunderstorm. Therefore, understanding the mechanisms of lightning propagation can lead to a better understanding of the redistribution of charge within the thundercloud. Niemeyer *et al.*[5] suggested that gas discharges can be modeled using a probabilistic approach based on Mandelbrot's[6] fractal theory. Following this description, several fractal models of lightning discharge have been developed[7–9]. The results presented in this paper are obtained using the three-dimensional fractal model of lightning discharge discussed by Riousset *et al.*[10] and Riousset[11]. This model combines the Niemeyer et al. hypothesis with the assumption put forth by Kasemir[2] that lightning discharges are equipotential and overall neutral. We apply this model to investigate cloud-to-ground discharges and related cloud charge configurations leading to this types of discharge. Results are compared with measurements of actual events similar to those reported in Coleman *et al.*[12] obtained using the Lightning Mapping Array (LMA) observing lightning discharges over Langmuir Laboratory, New Mexico.

---

†Graduate Mentor
‡Faculty Mentor

Annual Research Journal, Vol. IV
Electrical Engineering Research Experience for Undergraduates

ISBN 0-913260-06-1 (http://www.ee.psu.edu/reu/)

INTRODUCTION

The search for a theoretical model to describe lightning propagation began in the 1950s[2]. In particular, Kasemir[2] hypothesized that the lightning channel is both equipotential and overall neutral. This idea follows from the description of the lightning channel as a plasma wave of mainly leader nature, which had been established as early as the 1930s by Schonland, Malan, and their co-workers during their photographic studies of the initiation and propagation of cloud-to-ground lightning in South Africa[13]. However, an understanding of the leader process is still far from complete[14–16]. Leaders, due to their high conductivity, are analogous to an equipotential metallic wire that becomes polarized when placed in a non-zero electric field. Hence, charge accumulates at the tip of the leader and enhances the surrounding electric field above the threshold required for the initiation of streamers. As a result, a streamer zone develops around the leader tip. In the streamer zone, streamers are generated at a frequency of about $10^9\ \mathrm{s}^{-1}$. Consequently, the sum of these numerous streamer channel currents leads to heating of the region ahead of the leader tip, leading in turn to an increase of the conductivity of the heated region, which eventually allows further leader propagation[10]. It should be noted that processes occurring in the streamer zone are not fully understood at present, therefore, most existing models do not attempt to model them directly.

Interest in lightning modeling was recently renewed by the potential hazards posed by lightning strokes to aircraft, spacecraft, and installations using solid-state electronics. Also, major advances in lightning modeling were made possible by the development of computer science in the 1970s and 1980s. Some early computer models of lightning focused on the interaction between the lightning channel and the surrounding thunderstorm electric field[17, 18], while others focused on only bulk effects of the discharge[19]. In most of these early models, the lightning channel propagates along electric field lines and does not exhibit the highly branched behavior of the lightning channel that is often observed in nature. Figure 1 shows a cloud-to-ground flash that took place over Arecibo, Puerto Rico. It should be noted that the flash initiation occurs in the lower part of the cloud, where the channel appears brightest. The channel develops branches that propagate both downward toward the ground and upward into the cloud (not visible in this picture but measured by the Lightning Mapping Array (LMA), see Figure 2 and further discussion in this paper for details).

At present, a lightning model based on a microphysical approach to the mechanisms governing lightning initiation and propagation is not possible due to both the lack of a complete theory of the involved processes and of computational power to model these processes. Therefore, Niemeyer *et al.*[20] attempted to model gas discharges on a macroscopic scale. To overcome the limitations of the earlier deterministic models, they developed a probabilistic model based on Mandelbrot's[6]

Annual Research Journal, Vol. IV
Electrical Engineering Research Experience for Undergraduates

ISBN 0-913260-06-1 (http://www.ee.psu.edu/reu/)

Figure 1: A cloud-to-ground flash over Arecibo, Puerto Rico. The flash initiates in the lower part of the cloud where the channel appears brightest and develops channels that propagate in the downward and upward directions.

fractal theory. The model discharge propagates in two dimensions, and the probability for a path to be chosen is calculated based on both the ambient electric potential and the electric potential along the existing discharge channel. A path is then randomly chosen among all the candidate links for propagation. Later, more lightning-specific models such as Petrov and Petrova[21] were developed, which revisited the fractal model and applied it to intracloud discharges, cloud-to-ground discharges and ground-to-cloud discharges. Other fractal models of lightning were introduced in the context of the cloud electrification model[8], or were applied to investigate the probability of a strike to a structure[9]. However, none of these models ensured overall neutrality of the discharge by adequately shifting the channel potential. Therefore, Riousset *et al.*[10] recently applied a three-dimensional fractal model to simulate intracloud discharges. This model combines Niemeyer *et al.*'s[20] fractal approach and Kasemir's[2] hypotheses to create a model of lightning that is stochastic, equipotential, and overall neutral.

The goal of this paper is to apply Riousset *et al.*'s[10] three-dimensional fractal model in order to investigate cloud-to-ground discharges and cloud charge configurations leading to this type of discharge. Cloud charge configurations are based on the common tripole hypothesis[4, 22], which is discussed and detailed further in this paper. Results will be compared with measurements of an actual event by Coleman *et al.*[12] obtained using the Lightning Mapping Array (LMA) operating over Langmuir Laboratory, New Mexico (Figure 2) and with other relevant data available in the referred literature.

Annual Research Journal, Vol. IV
Electrical Engineering Research Experience for Undergraduates

ISBN 0-913260-06-1 (http://www.ee.psu.edu/reu/)

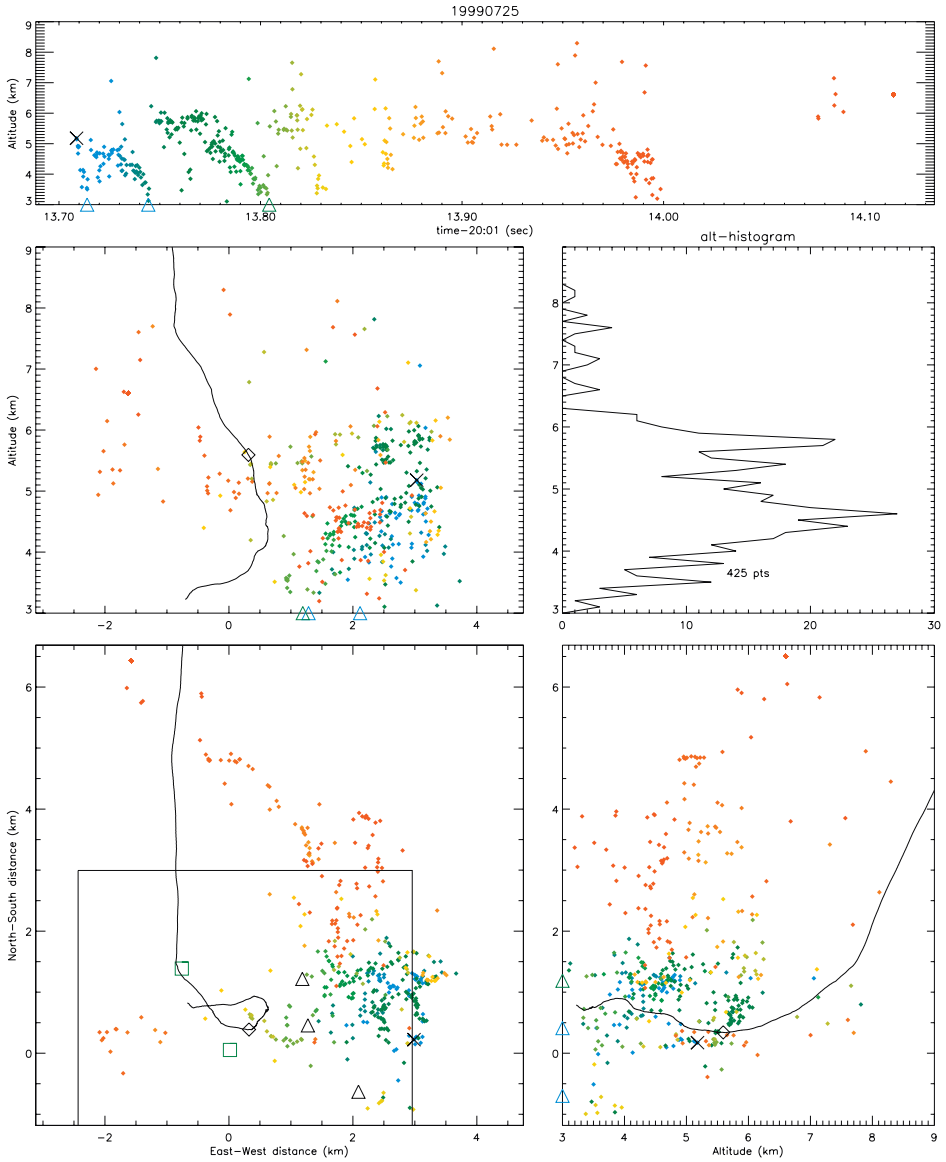

Figure 2: Flash F from Coleman *et al.*[12]. This cloud-to-ground flash occurred at 2001:13 UT on July 25 1999. From the altitude of initiation, it can be guessed that this flash is of negative polarity. In the original figure, the occurrence of radiation sources which trace the lightning path[23] are color-coded with the first sources colored blue and the last sources colored red. Shown are five different graphs (clockwise from the top): altitude versus time, altitude histogram of the sources in 100-m bins, a projection onto the north-south vertical plane, a horizontal projection of the sources, and a projection onto the west-east vertical plane. The cross denotes the position of the first Lightning Mapping Array (LMA) source. Triangles indicate three ground strike locations detected by the National Lightning Detection Network. The path of an instrumented balloon is shown in the projections; the diamonds show the location of the balloon at the time of the flash.

Annual Research Journal, Vol. IV
Electrical Engineering Research Experience for Undergraduates

ISBN 0-913260-06-1 (http://www.ee.psu.edu/reu/)

MODEL FORMULATION

The lightning channel and thundercloud are modeled in a three-dimensional Cartesian coordinate system whose exact dimensions are discussed at the end of this section. The cloud electrical structure used for this model is based on the classical tripole structure[4, 22], the validity of which has since been confirmed by several authors[12, 19, 24]. The core of the tripole model consists of two main charge layers: a dominant central negative charge layer below (N), and an upper positive layer of charge (P) with similar and opposite charge content[22]. Below the main charge layers exists a layer of positive charge (LP) of lesser magnitude than the upper layers, completing the tripole. A negative screening layer is sometimes added above the upper positive charge layer[19], but is not implemented in this study. Assuming that the ground is a perfect electrical conductor, three additional image charges must be accounted for. The ambient electric field of the thunderstorm can be solved numerically using the successive overrelaxation (SOR) method[10].

It has been hypothesized that different cloud charge configurations lead to cloud-to-ground lightning of different polarity[3]. Negative cloud-to-ground lightning can be produced from a tripole structure whose charge layers are centered on the same vertical axis[4]. The charge configuration used to reproduce negative cloud-to-ground lightning for this model represents a non-uniform charge configuration which was approximated by a Gaussian distribution with parameters summarized in Table I. The values for the upper positive layer, the central negative layer, and the lower positive layer were respectively 50 C, -60 C, and 13 C (also shown in Table I). These values were based on experimental data found and presented by Krehbiel *et al.*[19]. Figure 3 shows the charge density and the electric field lines produced by this cloud charge configuration. The tripole structure can clearly be seen in this plot: light shading indicates regions of positive charge while dark shading represents regions of negative charge. The black arrows represent electric field lines.

Less is known about the production of positive cloud-to-ground lightning. Jursa's[3] diagram of the typical charge distribution and lightning patterns of a mid-latitude thunderstorm pictures a tripole structure in which the upper positive charge layer is extended significantly out over the ground, forming a tilted electrical structure. Such a structure is thought to allow positive cloud-to-ground strikes to bypass the negative and lower positive charge layers and go straight to the ground. Positive polarity lightning may also be produced by a charge configuration in which all three charge layers are aligned, but the negative charge layer has been depleted, as during the final stages of a thunderstorm's life[4, 25, 26]. The model of positive cloud-to-ground lightning presented in this paper combines these two hypotheses. The cloud charge layers are represented by a non-uniform charge configuration which was approximated using Gaussian distributions with parameters given in Table I.

Annual Research Journal, Vol. IV
Electrical Engineering Research Experience for Undergraduates

ISBN 0-913260-06-1 (http://www.ee.psu.edu/reu/)

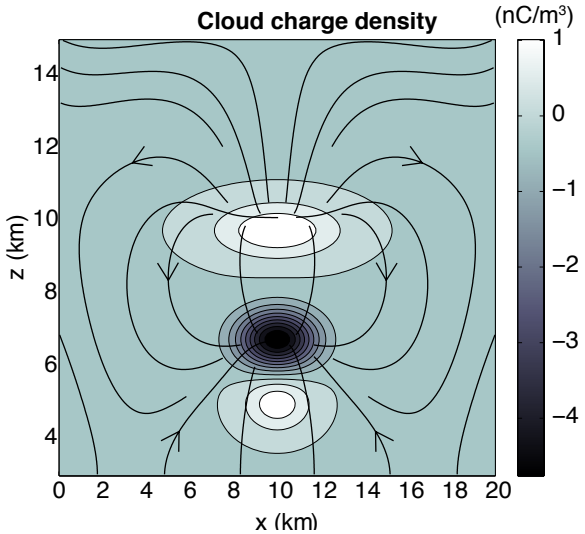

Figure 3: Cloud charge density and electric field lines produced by a cloud charge configuration leading to negative cloud-to-ground lightning. Light shading indicates regions of positive charge while dark shading represents regions of negative charge. The black arrows represent electric field lines.

All three layers were centered in the y-z plane, but the center of the upper positive charge layer was displaced by 8 km in the x-direction. The net charges contained in the upper positive, central negative, and lower positive layers were respectively 60 C, -40 C, and 8 C (also shown in Table I). Figure 4 shows the charge density and electric field lines produced by this cloud charge configuration.

The field and potential distributions induced by cloud charges are derived assuming open boundary conditions at the side and top boundaries of the simulation domain. The bottom boundary represents the ground and is assumed to be a perfect conductor with zero potential. The potential at the boundaries is found using the following equation[27]:

$$\phi(\vec{r}) = \phi_{amb}(\vec{r}) = \frac{1}{4\pi\epsilon_0}\iiint_{V'}\frac{\rho_{amb}(\vec{r'})}{|\vec{r}-\vec{r'}|}dV' + \frac{1}{4\pi\epsilon_0}\iiint_{V'}\frac{\rho^i_{amb}(\vec{r'_i})}{|\vec{r}-\vec{r'_i}|}dV' \quad (1)$$

where $\vec{r}$ represents the coordinate vector of a point on the boundary and $\phi_{amb}(\vec{r})$ the potential at this point. $\rho_{amb}(\vec{r'})$ represents the ambient charge density at a point $\vec{r'}$, and $\rho^i_{amb}(\vec{r'})$ represents the charge density of the image charges at point $\vec{r'}$. After the potential at the boundaries is found, the ambient potential is derived by solving Poisson's equation $\nabla^2\phi_{amb} = -\rho_{amb}/\varepsilon_0$ using the SOR algorithm, and the electric field is obtained by finite differentiation[10].

The exact value for lightning initiation and propagation threshold has yet to be accurately determined, therefore we assume the initiation and propagation thresh-

Annual Research Journal, Vol. IV
Electrical Engineering Research Experience for Undergraduates

ISBN 0-913260-06-1 (http://www.ee.psu.edu/reu/)

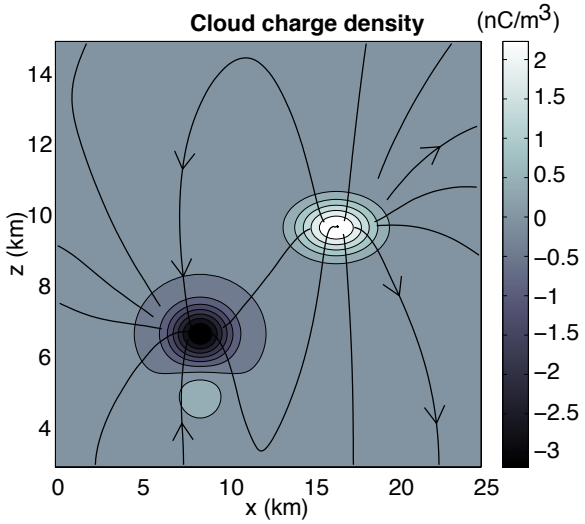

Figure 4: Cloud charge density and electric field lines produced by a cloud charge configuration leading to positive cloud-to-ground lightning. Light shading indicates regions of positive charge while dark shading represents regions of negative charge. The black arrows represent electric field lines.

Table I: Parameters of the charge layers. Adapted from Krehbiel *et al.*[19].

Layer	$x_Q\,(\mathrm{km})^a$	$y_Q\,(\mathrm{km})^a$	$z_Q\,(\mathrm{km})^{a,d}$	$a_x\,(\mathrm{km})^b$	$a_y\,(\mathrm{km})^b$	$a_z\,(\mathrm{km})^a$	$Q\,(\mathrm{C})^c$
For negative cloud-to-ground discharge							
LP	10.0	10.0	5.00	1.50	1.50	0.75	13.0
N	10.0	10.0	6.75	1.73	1.73	0.75	−60.0
P	10.0	10.0	9.75	2.82	2.82	0.75	40.0
For positive cloud-to-ground discharge							
LP	4.5	12.5	5.00	1.50	1.50	0.75	8.0
N	4.5	12.5	6.75	1.73	1.73	0.75	−40.0
P	20.5	12.5	9.75	2.30	2.30	0.75	60.0

[a] Coordinates of the charge center
[b] Space scales of the Gaussian distribution
[c] Charge values
[d] Measured above sea level

Annual Research Journal, Vol. IV
Electrical Engineering Research Experience for Undergraduates

ISBN 0-913260-06-1 (http://www.ee.psu.edu/reu/)

olds to be $E_{init} = E_{th}^{\pm} = \pm 2.16\ \mathrm{kV/cm}$ at sea level[28]. In addition, we know that these threshold values change with altitude[14]. Thus, the model uses the following expression to derive the initiation and propagation thresholds:

$$E_{init}(z) = E_{th}^{\pm}(z) = \pm 2.16 \frac{N(z + z_{gnd})}{N_0} [\mathrm{kV/cm}] \tag{2}$$

where z is the altitude above the ground, z_{gnd} is the altitude of the ground plane, N is the value of the neutral charge density, and N_0 is the value of N at sea level[10, 11].

The initiation point is chosen from regions of high electric field (i.e., exceeding the initiation threshold) at altitudes corresponding to the altitude of initiation of positive or negative cloud-to-ground discharges. From the initiation point, the lightning channel begins to propagate. Only one link is added at each step and the potential ϕ_0 along the channel is recalculated after each step to ensure neutrality of the channel[10]. First, the new candidates for propagation are identified. Any point within one grid step of the channel that is not at any boundary and that possesses a potential difference between its ends that exceeds the threshold for propagation is a viable candidate for the next stage of development. The difference in potential for each candidate link is calculated as $E_i = (\phi^{start} - \phi^{end})/l$, where ϕ^{start} and ϕ^{end} are the potentials at either end of the candidate link and l is its length.

The probability for a candidate being chosen for propagation is then calculated by[29]:

$$p_i = \frac{|E_i - E_{th}^{\pm}|^{\eta}}{\sum_i |E_i - E_{th}^{\pm}|^{\eta}} \tag{3}$$

where η describes the sensitivity of the probability to the field strength[7]. Following Niemeyer and Wiesmann[30] and Mansell *et al.*[8], η is chosen equal to 1. The next link defining discharge propagation is randomly chosen among the candidate links, accounting for their respective probabilities. The process is illustrated in a two-dimensional plane in Figure 5. The extension to three dimensions is straightforward. The solid lines in Figure 5a represent the existing channel, and the dashed lines represent candidate links. In Figure 5b, the probabilities for each candidate link are represented on a unit length segment, and a random point is chosen between 0 and 1. The candidate link corresponding to the section of the segment from which the random point is chosen will become the new section of the channel.

For further propagation to take place, the electric potential must be recalculated for every point within the domain to ensure the overall neutrality of the discharge. This is done using a procedure based on the bisection method and described by Riousset *et al.*[10] and Riousset[11].

This step-wise process continues until either a boundary is reached or the ambient electric field no longer exceeds the threshold field anywhere in the simulation domain. (It is important to note that the simulation will stop when the channel first reaches the ground, which corresponds only to the part of Figure 2 up to the first

Annual Research Journal, Vol. IV
Electrical Engineering Research Experience for Undergraduates

ISBN 0-913260-06-1 (http://www.ee.psu.edu/reu/)

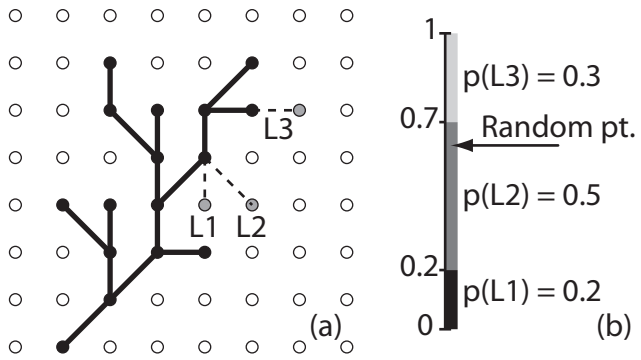

Figure 5: Channel extension in a 2-D geometry[10, 11]. (a) Channel links (solid lines) and link candidates (dashed lines); (b) Probability associated with each link. (The values of the probabilities given on this plot are arbitrary and are shown only for two representative points on the existing discharge tree for the purposes of illustration. Real values are derived based on the analysis of potential differences involving all grid points of the existing discharge tree–see text for details.)

return stroke around 20:01.13.71 UT. Therefore, subsequent strokes will not appear in the simulation results.)

For the negative cloud-to-ground discharge, the simulation domain is divided using rectangular grids with dimensions 0.5 km $\times$ 0.5 km $\times$ 0.15 km. Thus, the steps taken in the horizontal direction are of length 0.5 km while the steps taken in the vertical direction are of length 0.15 km. The size of the simulation domain in this case is 20 km $\times$ 20 km $\times$ 12 km. For the positive cloud-to-ground discharge, the simulation domain is discretized using 1.25 km long grid steps in the x- and y-directions and 0.3 km grid steps in the z-direction. The simulation domain extends to 25 km in the x- and y-directions and 12 km in the z-direction.

RESULTS

In this section, we present two simulation runs. First we discuss the model negative cloud-to-ground discharge, then we present the results for the model positive cloud-to-ground discharge.

Figure 6 shows a representative example of a model negative cloud-to-ground discharge leading up to the first stroke to ground. The steps are color-coded with the first steps colored dark grey and the last steps colored light grey. Panel (a) represents the altitude of each newly added link. Figure 6 also shows three views of the discharge tree: a projection in the x-z plane (panel (b)), x-y plane (panel (d)), and y-z plane (panel (e)). The figure shows a histogram of the number of grid points occupied by a link as a function of altitude (panel (c)). A triangle indicates the

Annual Research Journal, Vol. IV
Electrical Engineering Research Experience for Undergraduates

ISBN 0-913260-06-1 (http://www.ee.psu.edu/reu/)

point at which the stroke reaches the ground. The initiation point of this discharge is marked by a cross and is beneath the central negative layer at an altitude of 6 km above sea level (the ground has been set at an altitude of 3 km above sea level to simulate conditions over Langmuir Laboratory in New Mexico). Two sets of branches develops from the initiation point . The upper set of branches propagates horizontally within the central negative layer. The lower set of branches propagates rather horizontally between 4 km and 6 km through the lower positive charge layer before going straight to the ground.

Figure 7 shows that before the first stroke to the ground takes place the initiation and propagation thresholds are exceeded by $\sim$80% between the altitudes of 6.5 km and 9 km, which corresponds to the possible initiation of intracloud discharges, and at $\sim$6 km by $\sim$45%, which corresponds to the initiation of negative cloud-to-ground discharges. Strong field reduction is observed in the lower part of the plot in regions where the discharge propagated.

The total charge transferred by the channel was 23.3 C, and the total length of the channel was 17.2 km, thus the linear charge density of the channel was 1.35 mC/m.

Figure 8 shows a model positive cloud-to-ground discharge using the same formatting as in Figure 6. The discharge initiates at 9 km above sea level and propagates vertically to the ground with very little horizontal propagation tortuosity or branching.

The total charge transferred by the channel was 27.8 C and the total length of the channel was 8.75 km, thus the linear charge density of the channel was $\sim$3.2 mC/m.

DISCUSSION

It has been reported that in North America, the average ratio of cloud lightning to cloud-to-ground lightning is between 2.5 and 3[4], and of all cloud-to-ground lightning, about 90 percent is negative and about 10 percent is positive[4]. These statistics indicate that the occurrence of cloud-to-ground lightning of any polarity is not as frequent as the occurrence of intracloud discharges and the instance of a positive cloud-to-ground discharge is rare. The relative rarity of cloud-to-ground discharges compared to intracloud flashes becomes more meaningful when considering that both intracloud and cloud-to-ground discharges may originate from the same cloud charge structure[19]. Indeed, we found that the cloud configurations used in the model were usually capable of producing more than one type of discharge. For example, Figure 7 shows that this charge configuration can lead to both intracloud and negative cloud-to-ground discharges, consistent with Krehbiel *et al.*'s[19] study. Similarly, a closer look at the configuration shown in Figure 4 reveals that both negative cloud-to-ground and positive cloud-to-ground flashes are likely to occur.

Further investigation revealed that both positive and negative cloud-to-ground

Annual Research Journal, Vol. IV
Electrical Engineering Research Experience for Undergraduates

ISBN 0-913260-06-1 (http://www.ee.psu.edu/reu/)

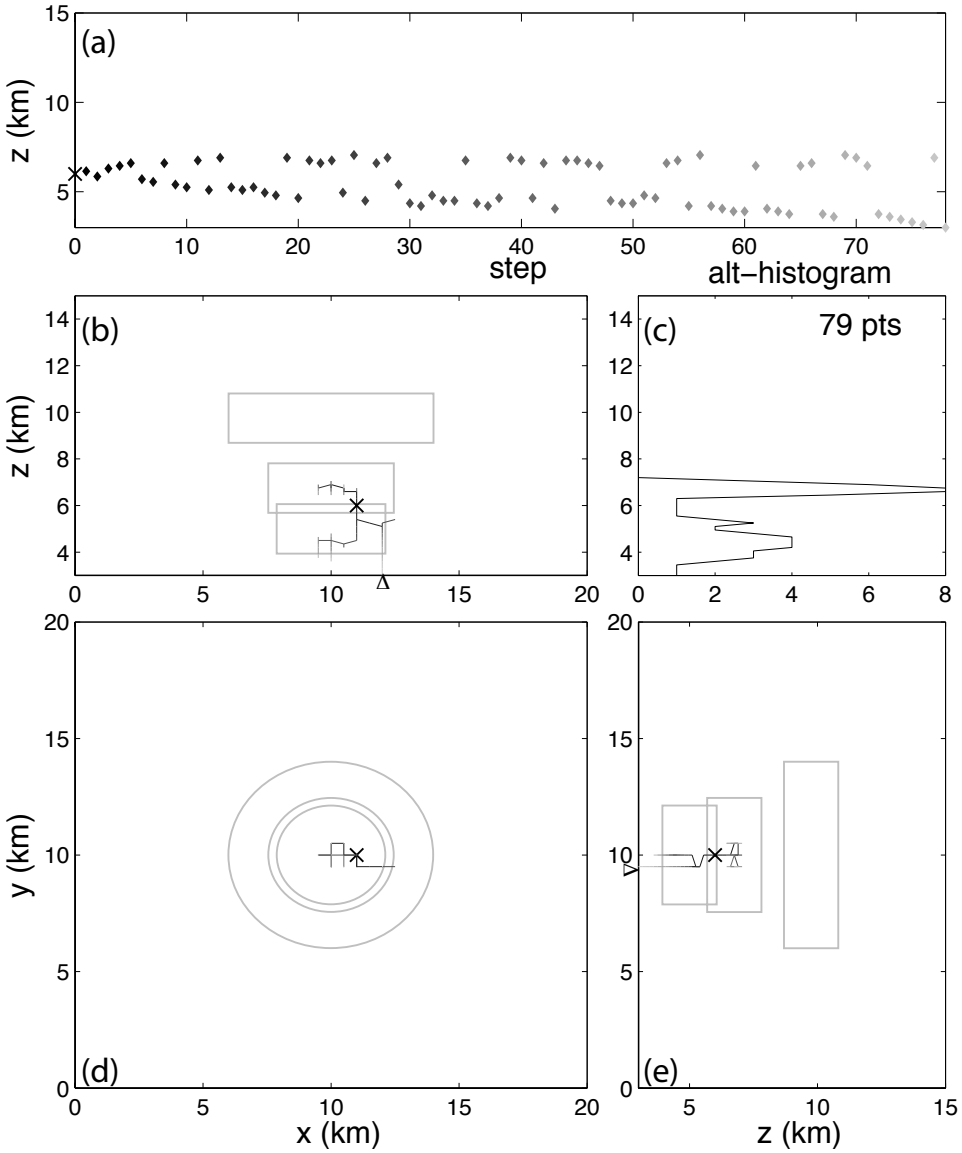

Figure 6: An example of a model negative cloud-to-ground discharge leading to the first stroke to ground. The steps are color-coded with the first steps colored dark grey and the last steps colored light grey. Panel (a) represents the altitude of each newly added link. Shown are three views of the discharge tree: a perspective from (b) the x-z plane, (d) the x-y plane, (e) the y-z plane. (c) shows a histogram of the grid point occupied by a channel link taken as a function of altitude. The upper positive, central negative, and lower positive charge layers are shown as cylinders with diameter $2a_x$ and depth $2a_z$ outlined in grey. The initiation point of this discharge is beneath the upper positive layer and is marked by a cross. A triangle indicates the point at which the lightning tree reaches the ground.

Annual Research Journal, Vol. IV
Electrical Engineering Research Experience for Undergraduates

ISBN 0-913260-06-1 (http://www.ee.psu.edu/reu/)

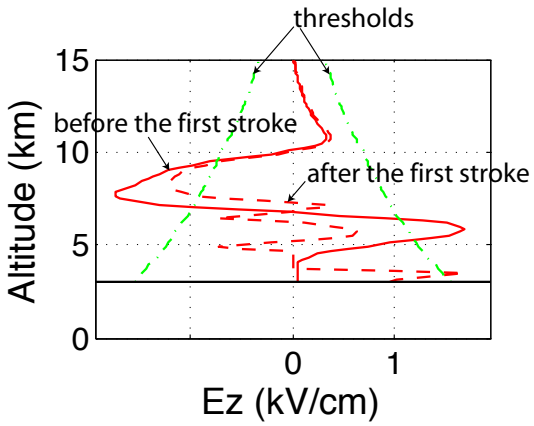

Figure 7: Electric field profiles measured on the central axis of the simulation domain before and after the occurrence of the negative model's first stroke to the ground. The dot-dashed lines represent the propagation thresholds. The solid line represents the total electric field before the first stroke to the ground and the dashed line represents the total electric field after the first stroke to the ground.

flashes were more readily produced by non-uniform charge layers than by disk-shaped layers of uniformly distributed charge. Thus, a Gaussian representation of the charge layers was chosen. In general, the uniform charge layers required about twice as much charge as the non-uniform layers to exceed the initiation and propagation thresholds. For the same net charge, the use of a Gaussian distribution creates regions of higher charge density and lower charge density. In the former, the electric field can be sufficiently high to initiate the discharge, but the field will fade rapidly in the region of lower density. Physically, it is expected that lightning discharges are initiated in such small regions of high electric field[11].

A quantification of the performance of the model can be achieved by comparing the channel parameters (in particular altitude of initiation, charge transfer, length, and linear charge density) with measurements available from the available literature.

A comparison of Figures 2 and 6 shows similar altitudes of initiation of $\sim$6 km (i.e., below the main negative charge center) for a negative cloud-to-ground stroke. Williams *et al.*[31] first showed that a leader channel of positive or negative polarity will propagate in a region of negative or positive charge, respectively. This behavior has also been observed for actual intracloud discharges[12] and modeled using numerical simulation[10]. Therefore, it is expected that lightning leaders propagate in regions of opposite polarity. Consistent with the above discussion and Figure 2, the portion of the negative cloud-to-ground discharge developing in the negative charge layer is positive and the lower part which reaches the ground is negative.

Annual Research Journal, Vol. IV
Electrical Engineering Research Experience for Undergraduates

ISBN 0-913260-06-1 (http://www.ee.psu.edu/reu/)

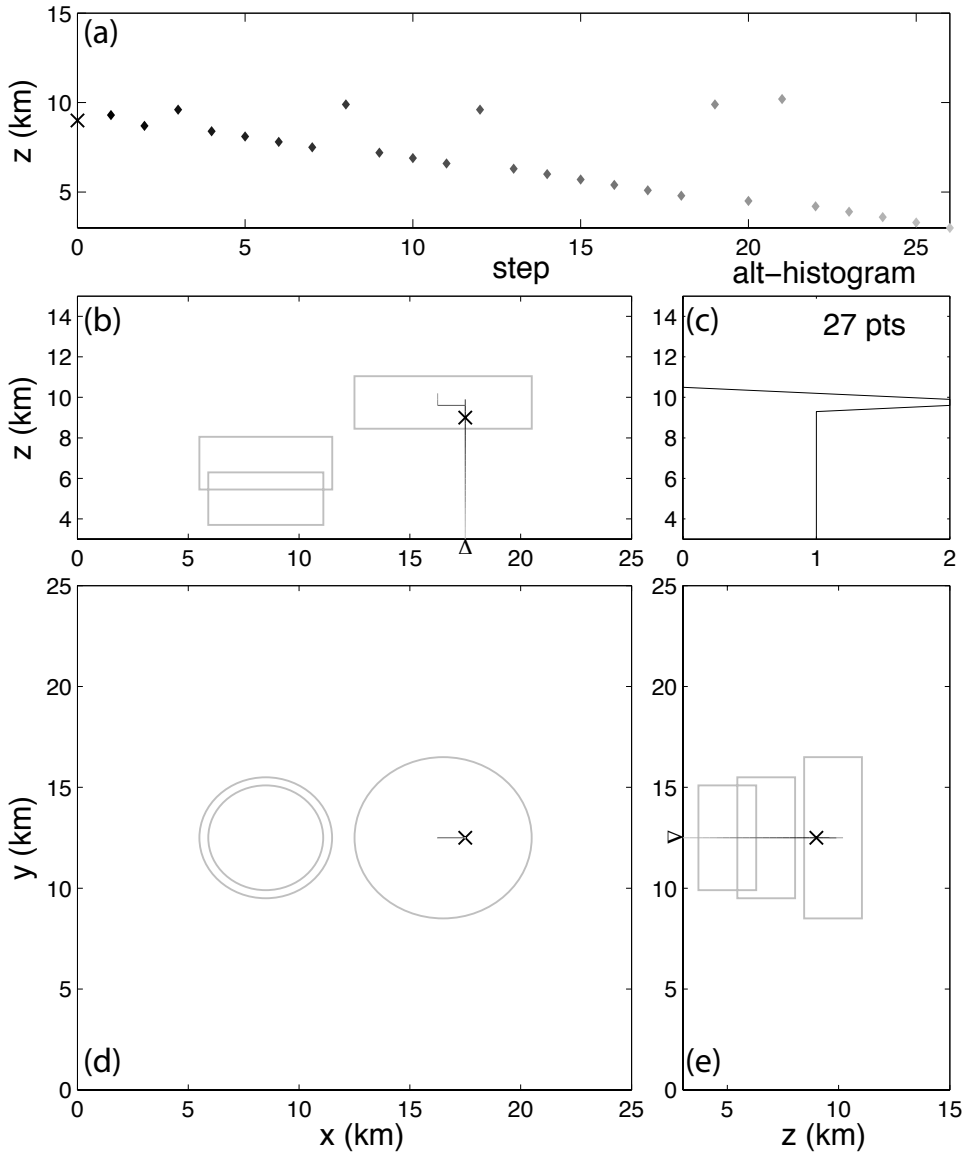

Figure 8: An example of a model positive cloud-to-ground discharge leading to the first stroke to ground. The steps are color-coded with the first steps colored dark grey and the last steps colored light grey. Panel (a) represents the altitude of each newly added link. Shown are three views of the discharge tree: a perspective from (b) the x-z plane, (d) the x-y plane, (e) the y-z plane. (c) shows a histogram of the grid point occupied by a channel link taken as a function of altitude. The upper positive, central negative, and lower positive charge layers are shown as cylinders with diameter $2a_x$ and depth $2a_z$ outlined in grey. The initiation point of this discharge is beneath the upper positive layer and is marked by a cross. A triangle indicates the point at which the lightning tree reaches the ground.

Annual Research Journal, Vol. IV
Electrical Engineering Research Experience for Undergraduates

ISBN 0-913260-06-1 (http://www.ee.psu.edu/reu/)

(Note that similar conclusions can be drawn for Figure 8: the portion of the positive cloud-to-ground discharge that develops in the positive charge layer is negative and the lower part which reaches the ground is positive.) However, a comparison of the behavior between the flashes from Figures 2 and 6 is quite tedious since Figure 2 also shows subsequent discharges to the ground. Nevertheless, it can be noted that in both cases, the propagation is essentially vertical, unlike the intracloud charges measured by Rison *et al.*[23] and modeled by Riousset *et al.*[10]. No LMA data are available for positive cloud-to-ground discharges, however, it can be noted that the altitude of initiation of the model at $\sim$9 km is in good agreement with measurements[32].

Rakov and Uman[4] reviews values of charge transfer due to the first stroke to the ground of both positive and negative cloud-to-ground discharges. In particular, negative cloud-to-ground discharges are measured to transfer 1.1 C to 24 C in the first stroke to ground. From our model we estimate a charge transfer of $\sim$11.6 C, which is consistent with previously cited values. Similarly, Rakov and Uman[4] cite values between 20 C to 80 C for the typical charge transfer corresponding to positive cloud-to-ground discharges. From the simulation results, we infer a charge transfer of $\sim$13.92 C, which is lower that the referred range, but still in reasonable agreement.

The linear charge density of the discharge channel can also be derived as $(|Q^+_{cha}| + |Q^-_{cha}|)/l$ (where Q^+_{cha} and Q^-_{cha} are the net charges carried by the positive and negative leaders, respectively), and compared to measurements. The linear charge density of the model negative cloud-to-ground channel is derived as $\sim$1.35 mC/m, which lies in the lower part of the scale (0.7 mC/m to 8.7 mC/m) quoted by Rakov and Uman[4]. The same derivation applied to the model positive cloud-to-ground channel yields a linear charge density of $\sim$3.2 mC/m. This value is comparable to the average linear charge density for leaders of $\sim$1 mC/m found by Helsdon *et al.*[18]. Although this value is not specific to positive cloud-to-ground discharges, it is a reasonable comparison considering the absence of available information on this issue.

Finally, we notice that Figure 7 shows a net field reduction of approximately 65% induced by the negative cloud-to-ground discharge, which is consistent with the previous modeling of intracloud discharges by Riousset *et al.*[10] and data reported by Winn and Byerley[33].

CONCLUSIONS

This paper makes several contributions to the fields of atmospheric electricity and gas discharge modeling, which can be summarized as follows:

- The ability of the lightning model described in Riousset *et al.*[10] to simulate both negative and positive cloud-to-ground discharges has been demonstrated by comparisons of simulation results to LMA data and other relevant data available in the referred literature.

Annual Research Journal, Vol. IV
Electrical Engineering Research Experience for Undergraduates

ISBN 0-913260-06-1 (http://www.ee.psu.edu/reu/)

- The initiation of cloud-to-ground discharges has been shown to be easier with configurations involving layers of non-uniform Gaussian charge density rather than with configurations employing disks of uniform charge density for the same amount of net charges in each layer.

ACKNOWLEDGMENTS

This material is based upon work supported by the National Science Foundation under Grants No. EEC-0244030 and ATM-0134838 to the Pennsylvania State University.

REFERENCES

[1] T. C. Marshall and M. Stolzenburg, "Electrical energy constraints on lightning," *J. Geophys. Res.*, **107** (D7) 4052, doi:10.1029/2000JD000024 (2002).

[2] H. W. Kasemir, "A contribution to the electrostatic theory of a lightning discharge," *J. Geophys. Res.*, **65** (7) 1,873–1,878 (1960).

[3] A. S. Jursa, ed., Handbook of Geophysics and the Space Environment, US Air Force Geophysics Lab., Springfield, VA, 1985.

[4] V. A. Rakov and M. A. Uman, Lightning Physics and Effects, Cambridge Univ. Press, New York, NY, 2003.

[5] L. Niemeyer, L. Ullrich and N. Wiegart, "The mechanism of leader breakdown in electronegative gases," *IEEE Trans. on Electr. Insul.*, **24** (2) 309–324, doi: 10.1109/14.90289 (1989).

[6] B. B. Mandelbrot, The Fractal Geometry of Nature, updated and augmented ed., W. H. Freeman, New York, NY, 1983.

[7] N. I. Petrov and G. N. Petrova, "Physical mechanisms for intracloud lightning discharges," *Techn. Phys.*, **38** (4) 287–290 (1993).

[8] E. R. Mansell, D. R. MacGorman, C. L. Ziegler and J. M. Straka, "Simulated three-dimensional branched lightning in a numerical thunderstorm model," *J. Geophys. Res.*, **107** (D9) 4075, doi:10.1029/2000JD000244 (2002).

[9] D. P. Agoris, V. P. Charalambakos, E. Pyrgloti and S. Grzybowski, "A computational approach on the study of Franklin rod height impact on striking distance using a stochastic model," *J. El. Stat.*, **60** (2–4) 175–181, doi: 10.1016/j.elstat.2004.01.020 (2004).

[10] J. A. Riousset, V. P. Pasko, P. R. Krehbiel, R. J. Thomas and W. Rison, "Three-dimensional fractal modeling of intracloud lightning discharge in a New Mexico

Annual Research Journal, Vol. IV
Electrical Engineering Research Experience for Undergraduates

ISBN 0-913260-06-1 (http://www.ee.psu.edu/reu/)

thunderstorm and comparison with lightning mapping observations," *J. Geophys. Res.*, doi:10.1088/xxx-xxxx, In review (2006).

[11] J. A. Riousset, Fractal modeling of lightning, Master's thesis, The Pennsylvania State University, University Park, PA (2006).

[12] L. M. Coleman, T. C. Marshall, M. Stolzenburg, T. Hamlin, P. R. Krehbiel, W. Rison and R. J. Thomas, "Effects of charge and electrostatic potential on lightning propagation," *J. Geophys. Res.*, **108** (D9) 4298, doi: 10.1029/2002JD002718 (2003).

[13] M. A. Uman, Lightning, reprint ed., Dover, Mineola, NY, 1984.

[14] V. P. Pasko, "Theoretical modeling of sprites and jets," in: M. Füllekrug, E. A. Mareev and M. J. Rycroft, ed., "Sprites, Elves and Intense Lightning Discharges," vol. 225 of *NATO Science Series II: Mathematics, Physics and Chemistry*, pp. 253–311, Springer, Heidleberg, Germany, 2006.

[15] E. M. Bazelyan and Y. P. Raizer, Lightning Physics and Lightning Protection, IoP, Philadelphia, PA, 2000.

[16] I. Gallimberti, G. Bacchiega, A. Bondiou-Clergerie and P. Lalande, "Fundamental processes in long air gap discharges," *C. R. Physique*, **3** (10) 1,335–1,359, doi:10.1016/S1631-0705(02)01414-7 (2002).

[17] V. Mazur and L. H. Ruhnke, "Model of electric charges in thunderstorms and associated lightning," *J. Geophys. Res.*, **103** (D18) 23,299–23,308 (1998).

[18] J. H. Helsdon, Jr., G. Wu and R. D. Farley, "An intracloud lightning parameterization scheme for a storm electrification model," *J. Geophys. Res.*, **97** (D5) 5,865–5,884 (1992).

[19] P. Krehbiel, W. Rison, R. Thomas, T. Marshall, M. Stolzenburg, W. Winn and S. Hunyady, "Thunderstorm charge studies using a simple cylindrical charge model, electric field measurements, and lightning mapping observations," *Eos Trans. AGU*, **85** (47), Fall Meet. Suppl., Abstract AE23A-0843 (2004).

[20] L. Niemeyer, L. Pietrono and H. J. Wiesmann, "Fractal dimension of dielectric breakdown," *Phys. Rev. Lett.*, **52** (12) 1,033–1,036, doi: 10.1103/PhysRevLett.52.1033 (1984).

[21] N. I. Petrov and G. N. Petrova, "Simulation of the branching and bending of breakdown channels in dielectrics," *Tech. Phys. Lett.*, **18** (2) 65–67 (1992).

[22] E. R. Williams, "The tripolar structure of thunderstorms," *J. Geophys. Res.*, **94** (D11) 13,151–13,167 (1989).

Annual Research Journal, Vol. IV
Electrical Engineering Research Experience for Undergraduates

ISBN 0-913260-06-1 (http://www.ee.psu.edu/reu/)

[23] W. Rison, R. J. Thomas, P. R. Krehbiel, T. Hamlin and J. Harlin, "A GPS-based three-dimensional lightning mapping system: Initial observations in central New Mexico," *Geophys. Res. Lett.*, **26** (23) 3,573–3,576, doi:10.1029/1999GL010856 (1999).

[24] T. C. Marshall, M. Stolzenburg, C. R. Maggio, L. M. Coleman, P. R. Krehbiel, T. Hamlin, R. J. Thomas and W. Rison, "Observed electric fields associated with lightning initiation," *Geophys. Res. Lett.*, **32** L03813, doi: 10.1029/2004GL021802 (2005).

[25] D. R. MacGorman and W. D. Rust, The Electrical Nature of Storms, Oxford Univ. Press, New York, NY, 1998.

[26] V. A. Rakov, "A Review of Positive and Bipolar Lightning Discharges," *Bulletin of the American Meterological Society*, **84** (96) 767–776, doi:10.1175/BAMS-84-6-767 (2003).

[27] N. Liu and V. P. Pasko, "Effects of photoionization on propagation and branching of positive and negative streamers in sprites," *J. Geophys. Res.*, **109** A04301, doi:10.1029/2003JA010064 (2004).

[28] V. P. Pasko and J. J. George, "Three-dimensional modeling of blue jets and blue starters," *J. Geophys. Res.*, **107** (A12) 1458, doi:10.1029/2002JA009473 (2002).

[29] N. Femia, L. Niemeyer and V. Tucci, "Fractal characteristics of electrical discharges: experiments and simulation," *J. Phys D: Appl. Phys.*, **26** (4) 619–627, doi:10.1088/0022-3727/26/4/014 (1993).

[30] L. Niemeyer and H. J. Wiesmann, "Modeling of leader branching in electronegative gases," pp. 134–139, Gaseous Dielectrics V: Proceedings of the Fifth International Symposium on Gaseous Dielectrics: Knoxville, TN, 3-7 May (1987).

[31] E. R. Williams, C. M. Cooke and K. A. Wright, "Electrical discharge propagation in and around space charge clouds," *J. Geophys. Res.*, **90** (D4) 6,059–6,070 (1985).

[32] M. A. Uman, The Lightning Discharge, unabridged ed., Dover, Mineola, NY, 2001.

[33] W. P. Winn and I. Byerley, L. G., "Electric field growth in thunderclouds," *Quart. J. R. Met. Soc.*, **101** 979–994 (1975).

Annual Research Journal, Vol. IV
Electrical Engineering Research Experience for Undergraduates

ISBN 0-913260-06-1 (http://www.ee.psu.edu/reu/)

PARAMETER ESTIMATION OF A 6-POLE WOUND ROTOR MACHINE

Grant M. Shane[*], Alexander J. Rovnan[+], and Heath F. Hofmann[#]

Department of Electrical Engineering
The Pennsylvania State University, University Park, PA 16802

[*]Undergraduate student of
Department of Business and Engineering
The Pennsylvania State University, Altoona Campus
Altoona, PA 16601

ABSTRACT

Overall, the proposed invention is to build a self-excited, brushless synchronous field winding machine to be used for propulsion in hybrid electric vehicles. For such an application the following criteria must be met: low cost, high power density, and the ability to operate efficiently over a wide speed range.

In working toward this particular goal a 6-pole wound rotor machine was used for testing. This machine was used because it was equipped with slip rings; therefore, access to the rotor was possible. Typically the test machine is run as an induction machine but with access to the rotor, synchronous field winding machine operation can be achieved. Testing of the 6-pole wound rotor machine included running it through a series of tests to define its parameters, or equivalent circuit. These tests include: a DC resistance test; two no-load tests, one with an open circuit rotor and one with a short circuit rotor; and a locked rotor test. Furthermore, new tests were done to determine values that were assumed using the standard tests. These new tests were possible because the rotor windings were accessible. A comparison between the standard and new tests is then made. The characteristics of the test machine can be used in the development of the new type of electric motor since it is similar to the proposed invention.

[+] Graduate Mentor
[#] Faculty Mentor

Annual Research Journal, Vol. IV
Electrical Engineering Research Experience for Undergraduates

ISBN 0-913260-06-1 (http://www.ee.psu.edu/reu/)

INTRODUCTION

Low cost, high power density, and the ability to operate efficiently over a wide speed range are criteria that must be met for electric machines to be used in hybrid electric vehicles. The most actively pursued machine for this particular application is the permanent magnet machine, which lacks in its ability to achieve a wide speed range, high cost, and the overvoltages that arise when faults occur in the system. Another option is to use a synchronous field winding machine which is capable of high power density but has faults in cost, mass, and space due to the associated circuits and slip rings required to generate and regulate the rotor field current. Of the current technologies available for propulsion, all have faults in at least one of these criteria. Therefore, an optimum electric motor has yet to be developed for use in hybrid electric vehicles.

In developing an optimum electric motor for hybrid vehicles a brushless, self-excited synchronous field winding machine is proposed. This machine is a synchronous field winding machine with the exception that the excitation of the rotor current comes from the stator instead of through slip rings as have been previously used. This approach to transferring power from the stator to the rotor field winding is comparable to that of an induction machine. The transfer of power is done through a rotor "transformer" winding and "field" winding oriented specifically according to axes in the rotor reference frame. This design has the advantages of an induction machine where no slip rings causing sparks and wear and no external circuits are required. Also, in using windings on the rotor, the current in the rotor electromagnets can be adjusted to avoid overvoltages.[1]

When developing a new type of electric motor for hybrid electric vehicles it is necessary to compare its performance to that of existing motors to examine strengths and weaknesses. The motor chosen to be compared to was a Century wound rotor polyphase induction motor, model number JC3-5AN, rated at 208 primary line to line volts, 10hp, and 1,150 rpm. This motor was used because it is equipped with slip rings. With access to the rotor windings through the slip rings the test motor can be run as an induction motor or a synchronous field winding motor. Later experiments will compare the operation of the motor as an induction machine versus that of a synchronous field winding machine and eventually to the operation of the new type of electric motor, but first the parameters of the test motor's equivalent circuit must be determined.

In order to gain a better understanding of the properties of an electric machine, in this case a 6-pole wound rotor motor, it is essential that its equivalent circuit be defined. Standard tests such as the DC resistance test, the no-load test, and the locked rotor test are used to define the parameters of the machine's equivalent circuit. In determining the parameters these standard tests were performed along with new procedures for testing to extract as much information as possible. These new procedures were possible because of access to the rotor windings and were done to get around the assumptions made using the standard tests. In the end a comparison is made between the values determined using the

Annual Research Journal, Vol. IV
Electrical Engineering Research Experience for Undergraduates

ISBN 0-913260-06-1 (http://www.ee.psu.edu/reu/)

standard tests and the new procedures. The information from these tests will be invaluable when designing and testing the new type of electric motor.

EXPERIMENTAL DESCRIPTION

Tests were performed to determine the parameters of the motor's equivalent circuit. These tests included the DC standard resistance test, the no-load test, and the locked rotor test. The new procedure for testing included two stator excited tests, one with an open circuit rotor and one with a short circuit rotor, and two rotor excited tests, one with an open circuit stator and one with a short circuit stator.

One phase of the wound rotor motor's equivalent circuit is shown in Figure 1. Of the circuit elements shown, all are fixed, except for the resistance of R_R/s. This resistance value depends on the slip (s) of the motor, which depends on motor speed. Motor slip varies from 1 to 0 as the motor goes from start up to synchronous speed. Therefore, the value of R_R/s varies from R_R to infinity respectively.

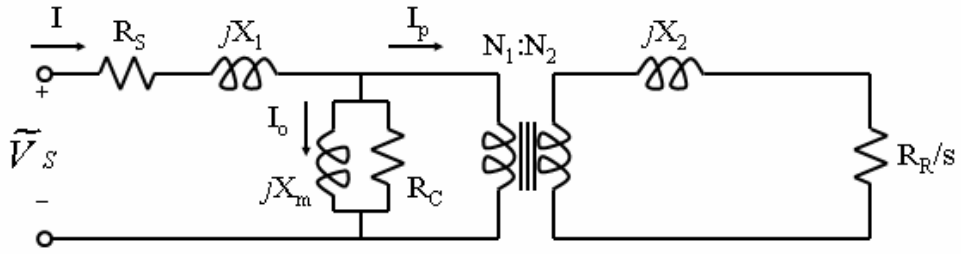

Figure 1: Equivalent circuit of a wound rotor motor.

$\tilde{V}_S$ = voltage source per phase
I = line current
I_0 = exciting current
I_p = primary current
X_m = magnetizing inductance
R_C = core resistance
R_S = stator winding resistance
X_1 = stator leakage reactance
X_2 = rotor leakage reactance
R_R/s = rotor winding resistance in relation to slip
$N_1:N_2$ = effective turns ration of motor

DC Resistance Test

The DC resistance test was used to measure the resistance of the stator and rotor windings, R_S and R_R. This test was performed by connecting a DC power supply to the windings and measuring the voltage between each phase, the current from the DC power supply was set according to the limits of the windings being

Annual Research Journal, Vol. IV
Electrical Engineering Research Experience for Undergraduates

ISBN 0-913260-06-1 (http://www.ee.psu.edu/reu/)

measured. The results of the DC resistance test are shown in Table I. Using Equation 1 the values of the stator and rotor windings can be determined.

$$R_S, R_R = \frac{Vavg}{2 * Iavg} \tag{1}$$

No-Load Test with Short Circuit Rotor

Operating an induction machine at no-load causes its slip to be small; therefore, the value of R_R/s is infinity. With an infinite rotor winding resistance there is no rotor current, therefore no rotor action. With no rotor action the circuit in Figure 1 consists primarily of the magnetizing branch R_c and X_m as shown in Figure 2. The value of $X_m + X_1$ was determined by running the motor at no-load according to its rated voltage and measuring the line to neutral voltage (V_{L-N}) of each phase, the current (I_{NL}), with phase angle θ, and the line to line voltage (V_{NL}) using an oscilloscope. Also, the rotor current was examined to obtain information on motor slip and slot frequency. The measurements from the no-load test are shown in Table II. Equations 2 through 7 were then used to calculate total 3-phase active power (P_{NL}); total apparent power (S_{NL}); total reactive power (Q_{NL}); windage, friction, and iron losses ($P_f + P_v$); resistance corresponding to iron, windage, and friction losses (R_m); and the magnetizing reactance (X_m).[2] Equation 8 was used to calculate the no-load impedance (Z_{NL}) which is equal to $X_m + X_1$. Here it is necessary to note that Equation 7 was only used to compare with the value of X_m determined through the locked rotor test and it is assumed that the effective turns ratio of the motor is 1:1.

$$P_{NL} = \sqrt{3} V_{NL} * I_{NL} * \cos\theta \tag{2}$$

$$S_{NL} = \sqrt{3} V_{NL} * I_{NL} \tag{3}$$

$$Q_{NL} = \sqrt{S_{NL}^2 - P_{NL}^2} \tag{4}$$

$$P_f + P_v = P_{NL} - 3 * I_{NL}^2 * R_S \tag{5}$$

$$R_m = \frac{V_{NL}^2}{P_f + P_v} \tag{6}$$

$$X_m = \frac{V_{NL}^2}{Q_{NL}} \tag{7}$$

$$\left|Z_{NL}\right| = \frac{V_{L-N}}{I_{NL}} = X_m + X_1 \tag{8}$$

Annual Research Journal, Vol. IV
Electrical Engineering Research Experience for Undergraduates

ISBN 0-913260-06-1 (http://www.ee.psu.edu/reu/)

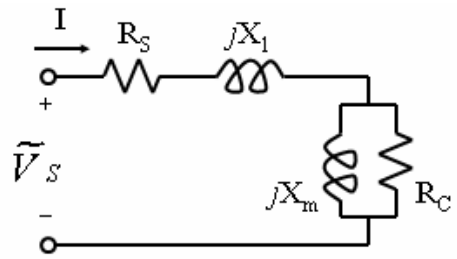

Figure 2: Equivalent circuit of no-load test with short circuit rotor.

The rotor current during no-load operation was examined to determine slip of the motor under these conditions. An oscilloscope was used to measure the rotor current time per cycle (t_{avg}) and slot frequency (f_s) of each phase. The slot frequencies are small oscillations in rotor current that are caused by the slots in the rotor. The rotor current time per cycle and slot frequency are shown in Table III. Using Equation 9 and 10 the rotor current frequency (f_2) and slip (s) of the motor at no-load were determined using the source frequency (f) equal to 60 Hz.

$$f_2 = \frac{1}{t_{avg}} \tag{9}$$

$$s = \frac{f_2}{f} \tag{10}$$

No-Load Test with Open Circuit Rotor

The no-load test with an open circuit rotor was used to approximately determine the turns ratio (N_1:N_2) of the equivalent circuit. The voltage of each phase was measured for both the stator and rotor and Equation 11 was used to estimate the turns ratio. The equivalent circuit for this test is shown in Figure 3.

$$N_1 : N_2 = \frac{\tilde{V}_S}{\tilde{V}_R} \tag{11}$$

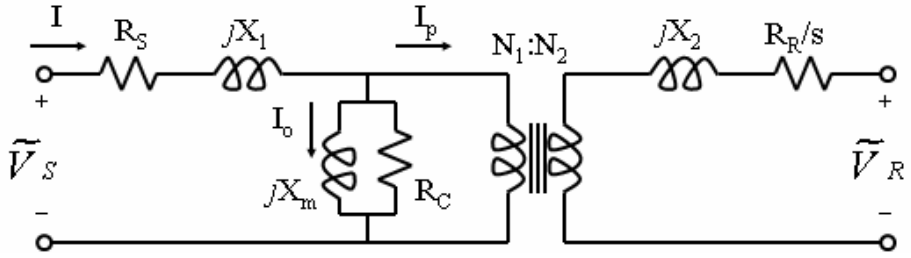

Figure 3: Equivalent circuit of n-load test with open circuit rotor.

Annual Research Journal, Vol. IV
Electrical Engineering Research Experience for Undergraduates

ISBN 0-913260-06-1 (http://www.ee.psu.edu/reu/)

Locked Rotor Test

The locked rotor test was performed by locking the rotor in place so it cannot move and applying a low voltage to the motor at the rated frequency. The stator voltage line to neutral ($V_{L\text{-}N}$) and current (I_{LR}) with phase angle (θ) were measured along with the rotor currents ($\tilde{i}_r$). With the rotor locked in place the slip (s) of the motor is equal to 1 making the rotor resistance R_R/s equal to R_R, a small value. With a small rotor resistance almost all current will flow through X_2 and R_R therefore, the magnetizing branch consisting of X_m and R_C can be ignored.[3] The equivalent circuit during a locked rotor test is shown in Figure 4.

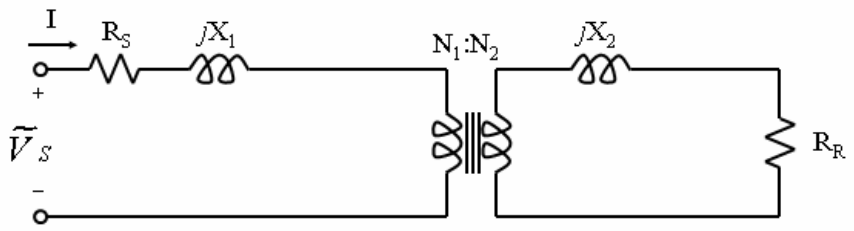

Figure 4: Equivalent circuit of locked rotor test.

The following equations were then used to determine the locked rotor impedance (Z_{LR}), the locked rotor resistance (R_{LR}), the locked rotor reactance (X_{LR}), and the rotor resistance (R_R) to be compared with the measured value from the DC resistance test.

$$|Z_{LR}| = \frac{V_{L-N}}{I_{LR}} \tag{12}$$

$$\begin{aligned} Z_{LR} &= R_{LR} + jX_{LR} \\ &= |Z_{LR}|\cos\theta + j|Z_{LR}|\sin\theta \end{aligned} \tag{13}$$

$$R_{LR} = R_R + R_S \tag{14}$$

$$X_{LR} = X_1 + X_2 \tag{15}$$

In a standard locked rotor test the assumption is made that in a wound rotor induction motor the stator/rotor reactances are equal as shown in Equation 16. Under this assumption Equation 8 can be rearranged to determine the magnetizing reactance (X_m) using the value determined from the no-load test with a short circuit rotor.

Annual Research Journal, Vol. IV
Electrical Engineering Research Experience for Undergraduates

ISBN 0-913260-06-1 (http://www.ee.psu.edu/reu/)

$$X_1 = X_2 = \frac{X_{LR}}{2} \tag{16}$$

The previous tests were performed and values calculated according to the set standards and equations except for the no-load test with an open circuit rotor. This is not a standard test but was done to get an approximation of the turns ratio. The standard tests are used for induction motors where access to the rotor is not possible. Therefore, one doesn't care about the actual rotor current and voltage, since the parameters are only being looked at from the stator side. In working through these tests it is noticed that the core resistance was not determined, the test used to determine the turns ratio is considered inaccurate, and in the locked rotor test it was assumed from experience that for a wound rotor induction motor the stator/rotor reactances are equal. In order to avoid these assumptions new procedures were developed to correctly determine the turns ratio, the core resistance, and the stator/rotor reactances. The following tests were done using a locked rotor: stator excited with short circuit rotor, rotor excited with short circuit stator, stator excited with open circuit rotor, and rotor excited with open circuit stator. Note that the position of the rotor was the same for each test. For each test a voltage of approximately 10 V was applied to either the stator or rotor through a 3 phase variac and the voltage or current was measured on the other end depending on the test performed. The phase angle of the current (θ) was also measured for each test. The equivalent circuit for this new procedure is shown in Figure 5.

Stator Excited with Open Circuit Rotor

For this test the stator voltages ($\tilde{V}_{S1}$) and currents ($\tilde{i}_{s1}$) along with the rotor voltages ($\tilde{V}_{R1}$) were measured per phase. Using Figure 5 a nodal analysis was performed with respect to $\tilde{e}_m$ producing the following equations for this particular setup. Note that G_C represents conductivity which is the inverse of the core resistance (R_C).

$$\tilde{e}_{m1} = [(R_S + jX_1)^{-1} - \frac{j}{X_m} + G_C]^{-1}(R_S + jX_1)\tilde{V}_{S1} \tag{17}$$

$$\tilde{i}_{s1} = \frac{\tilde{V}_{S1} - \tilde{e}_{m1}}{R_S + jX_1} \tag{18}$$

$$\tilde{V}_{R1} = \frac{N_2}{N_1}\tilde{e}_{m1} \tag{19}$$

Annual Research Journal, Vol. IV
Electrical Engineering Research Experience for Undergraduates

ISBN 0-913260-06-1 (http://www.ee.psu.edu/reu/)

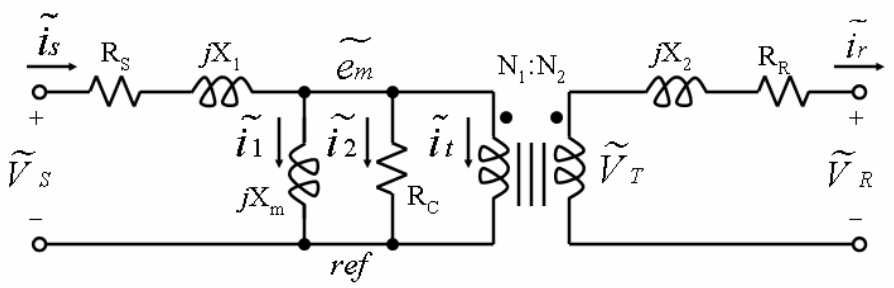

Figure 5: Equivalent circuit for new procedure.

$\tilde{V}_S$ = voltage at the stator
$\tilde{i}_s$ = stator current
R_S = stator winding resistance
X_1 = stator leakage reactance
$\tilde{i}_1$, $\tilde{i}_2$ = current through the branches shown
$\tilde{i}_t$ = current reflected through turns ratio
X_m = magnetizing inductance
$\tilde{e}_m$ = voltage at the node
ref = reference voltage
R_c = core resistance
$N_1:N_2$ = effective turns ratio of motor
$\tilde{V}_T$ = voltage reflected through turns ratio
X_2 = rotor leakage reactance
R_R = rotor winding resistance
$\tilde{i}_r$ = rotor current
$\tilde{V}_R$ = voltage at the rotor

Stator Excited with Short Circuit Rotor

The stator voltages ($\tilde{V}_{S2}$) were measured per phase along with the currents for both the stator ($\tilde{i}_{s2}$) and rotor ($\tilde{i}_{r2}$). Again using Figure 5 the following equations can be derived by performing a nodal analysis with respect to $\tilde{e}_m$.

$$\tilde{e}_{m2} = [(R_S + jX_1)^{-1} - \frac{j}{X_m} + G_C + (\frac{N_2}{N_1})^2 (R_R + jX_2)^{-1}]^{-1} (R_S + jX_1)^{-1} \tilde{V}_{S2} \qquad (20)$$

$$\tilde{i}_{s2} = \frac{\tilde{V}_{S2} - \tilde{e}_{m2}}{R_R + jX_2} \qquad (21)$$

$$\tilde{i}_{r2} = \frac{(\frac{N_2}{N_1})\tilde{e}_{m2}}{R_R + jX_2} \qquad (22)$$

Annual Research Journal, Vol. IV
Electrical Engineering Research Experience for Undergraduates

ISBN 0-913260-06-1 (http://www.ee.psu.edu/reu/)

Rotor Excited with Open Circuit Stator

The rotor voltages ($\tilde{V}_{R3}$) and currents ($\tilde{i}_{r3}$) were measured per phase along with the stator voltages ($\tilde{V}_{S3}$). Again, doing a nodal analysis using Figure 5 produces the following equations.

$$\tilde{e}_{m3} = [\frac{-j}{X_m} + G_C + (\frac{N_2}{N_1})^2 (R_R + jX_2)^{-1}]^{-1} (\frac{N_2}{N_1})(R_R + jX_2)V_{R3} \quad (23)$$

$$\tilde{i}_{r3} = \frac{\tilde{V}_{R3} - (\frac{N_2}{N_1})\tilde{e}_{m3}}{R_R + jX_2} \quad (24)$$

$$\tilde{V}_{S3} = \tilde{e}_{m3} \quad (25)$$

Rotor Excited with Short Circuit Stator

Finally, the last test was performed and the per phase values of the rotor voltages ($\tilde{V}_{R4}$) and currents of both the rotor ($\tilde{i}_{r4}$) and stator ($\tilde{i}_{s4}$) were measured. The nodal analysis produced these equations.

$$\tilde{e}_{m4} = [(R_S + jX_1)^{-1} - \frac{j}{X_m} + G_C + (\frac{N_2}{N_1})^2 (R_R + jX_2)^{-1}]^{-1} (\frac{N_2}{N_1})(R_R + jX_2)^{-1}\tilde{V}_{R4} \quad (26)$$

$$\tilde{i}_{r4} = \frac{\tilde{V}_{R4} - (\frac{N_2}{N_1})\tilde{e}_{m4}}{R_R + jX_2} \quad (27)$$

$$\tilde{i}_{s4} = \frac{\tilde{e}_{m4}}{R_S + jX_1} \quad (28)$$

The final step to determine the values for the equivalent circuit included writing a program using MatLab. A nonlinear Least Squared Error Method was used, see Equation 29. This method involves inputting the following: the equations derived from the different tests (Equations 17 through 28), the measured values from each test, and an estimate of what the parameters might be. The results from the standard tests were used to estimate the parameters. Essentially the program takes the equations and determines values for the parameters that best fit these equations according to the estimated parameters and the actual measurements from the four tests. All measurements are phasors, but since the phase angle relation between stator and rotor variables depends on rotor position, which is not known, only the magnitudes are used when looking at the

Annual Research Journal, Vol. IV
Electrical Engineering Research Experience for Undergraduates

ISBN 0-913260-06-1 (http://www.ee.psu.edu/reu/)

variables on the unexcited side. The code for the MatLab program is shown at the end.

$$y = f(x, B) \tag{29}$$

y = outputs
x = inputs
B = parameters
f = a function relating x and B to y

RESULTS

DC Resistance Test

Table I: Stator and rotor voltages and currents from DC resistance test.

Stator			Rotor		
Phase	**V (Volts) DC**	**I (Amps)**	**Phase**	**V (Volts) DC**	**I (Amps)**
A-B	5.92	30	A-B	6.09	25
A-C	5.81	30	A-C	6.15	25
B-C	5.92	30	B-C	6.22	25
Average	V_{avg} = 5.88	I_{avg} = 30	Average	V_{avg} = 6.15	I_{avg} = 25

Using Equation 1 and Table 1 the values of the stator and rotor windings can be determined where R_S = .0981 ohm and R_R = .1231 ohm.

No-Load Test with Short Circuit Rotor

In analyzing the values in Table II from the no-load test with a short circuit rotor the angles between the currents and voltages are in worst case within 4.7^o of -90^o. Using Equations 2 through 8 and the results in Table II the following parameters were determined: P_{NL}= 616.36 W, S_{NL} = 7685.23 VA, Q_{NL} = 7660.48 vars, $P_f + P_v$ = 483.71 W, $R_m = 90.31\,\Omega$, $X_m = 5.70\,\Omega$, and $X_m + X_l = 5.63\,\Omega$. Note that R_m is nonlinear and varies according to motor operation but was determined for future reference.

Table II: Stator voltages and currents during no-load short circuit rotor test.

Phase	Voltage (Volts @ degrees)	Current (Amps @ degrees)	
A	119.90 @ 0	21.84 @ -85.3	
B	119.15 @ 0	20.14 @ -86.5	
C	119.40 @ 0	21.70 @ -85.6	
Average	V_{L-N} = 119.48 @ 0	I_{NL} = 21.23 @ θ = -85.4	V_{NL} = 209 V

Annual Research Journal, Vol. IV
Electrical Engineering Research Experience for Undergraduates

ISBN 0-913260-06-1 (http://www.ee.psu.edu/reu/)

Equations 9 and 10 along with Table III were used to calculate the slip of the motor at no load where slip (s) = .00189 or .189%. When a motor is operating at no-load the difference between the stator speed and rotor speed is very small as shown by the calculated slip of .00189. The slot frequency (f_s) of 361.737 Hz may be useful in later experiments when comparing this test machine to the proposed design.

Table III: Rotor current frequency and slot frequency.

Phase	Rotor Current (Seconds per cycle)	Slot Frequency (Hertz)
A	9.44	362.32
B	8.52	360.58
C	8.56	362.31
Average	t_{avg} = 8.84	f_s = 361.737

No-Load Test with Open Circuit Rotor

The nameplate on the test motor indicated that the primary voltage (Vp) was equal to 208 V whereas the secondary voltage (Vs) was 180 V. Using Equation 10, the turns ratio (N_1:N_2) of the motor was calculated. Although this calculation may be inaccurate since the ratings on the primary and secondary voltage are due to other factors such as limitations of the windings, this method was used to get an idea of what the turns ratio might be. Using motor specified values the turns ratio was 1.156:1. Also, using Equation 11 with the values in Table IV the turns ratio was calculated to be approximately 1.219:1.

Table IV: Stator and rotor voltages during no-load open circuit rotor test.

Stator		Rotor	
Phase	Voltage (V)	Phase	Voltage (V)
A-B	210.80	A-B	172.90
B-C	210.50	B-C	173.00
A-C	210.90	A-C	172.90
Average (V_S)	210.73	Average (V_R)	172.93

Locked Rotor Test

The results of the locked rotor test are shown in Table V. Using Equation 12 through 15 with the results of this test yield the following values: $Z_{LR} = .85\,\Omega$, $R_{LR} = .3\,\Omega$, and $X_{LR} = .8\,\Omega$. Using R_S from the DC resistance test Equation 14 can used to solve for R_R where $R_R = .2\,\Omega$. The measured value for $R_R = .1231\,\Omega$. This difference of $.07\,\Omega$ is due to some extent from the rounding off of numbers that occurred when calculating these values. Following the assumption that the stator/rotor reactances are equal, as shown in Equation 16, X_1 and X_2 can be

Annual Research Journal, Vol. IV
Electrical Engineering Research Experience for Undergraduates

ISBN 0-913260-06-1 (http://www.ee.psu.edu/reu/)

determined as $X_1 = X_2 = .3957\,\Omega$. Using the results from the no-load test with a short circuit rotor, Equation 8 can then be used to determine $X_{m,}$ which is $5.233\,\Omega$. Using Equation 7, $X_m = 5.70\,\Omega$. The difference between the values of X_m using two different equations is $.467\,\Omega$ which can be considered reasonable since different approaches were used for each. From the standard tests the value of $X_2 = .3957\,\Omega$, but since an estimate of the turns ratio was determined it is possible to reflect this value to its proper side, that being on the rotor. The standard tests transfer X_2 to the stator side where its value is determined, meaning that this value of X_2 contains the turns ratio within it. Typically the turns ratio can't be determined, but in this application it could. Equation 30 is used to reflect impedances between the rotor and stator using the turns ratio where $X_{2R} = .2663\,\Omega$, this being the value of X_2 reflected to the rotor side, its actual value.

$$X_{2R} = X_{2S}\left(\frac{N_2}{N_1}\right)^2 \tag{30}$$

Table V: Stator voltages and stator/rotor currents from locked rotor test.

Stator			Rotor	
Phase	Voltage (Volts @ degrees)	Current (Amps @ degrees)	Phase	Rotor Current (Amps)
A	8.55 @ 0	10.00 @ -69	A	10.34
B	8.31 @ 0	9.80 @ -70	B	10.33
C	8.46 @ 0	10.13 @ -69	C	10.68
Average	$V_{L\text{-}N}$ = 8.44 @ 0	I_{LR} = 9.98 @ -69.33	Average	$\tilde{i}_r$ = 10.45

New Procedure using MatLab

The results from the four different tests are shown in the tables below. In Table VI and VIII the line to neutral (L-N) voltages were calculated from the line to line (L-L) voltages measured. In using the values of the currents with their respected angles they were broken up into real and imaginary parts when entered into the program. The measured values along with Equations 17 through 28 and estimates for each parameter were used in the calculation of each parameter using this method. The estimates used from the standard tests include: $R_S = .0981\,\Omega$, $R_R = .1231\,\Omega$, $X_1 = .3957\,\Omega$, $X_2 = .2663\,\Omega$, $X_m = 5.233\,\Omega$, and $N_1{:}N_2 = 1.219$. A value of $100\,\Omega$ was used as the core resistance (R_C) since it wasn't determined using the standard tests.

The results using MatLab are as follows: $R_S = .1599\,\Omega$, $R_R = .1230\,\Omega$, $X_1 = .4361\,\Omega$, $X_2 = .3002\,\Omega$, $X_m = 6.379\,\Omega$, $N_1{:}N_2 = 1.1184{:}1$, and $G_C = .0164$ S/m, or $R_C = 60.9756\,\Omega$ since R_C is the inverse of G_C.

Annual Research Journal, Vol. IV
Electrical Engineering Research Experience for Undergraduates

ISBN 0-913260-06-1 (http://www.ee.psu.edu/reu/)

Table VI: Stator excited with open circuit rotor.

Stator			Rotor	
	Voltage	Current		Voltage L-L
Phase	(Volts @ degrees)	(Amps @ degrees)	Phase	(Volts rms)
A	9.37 @ 0	1.40 @ -83.0	A-B	13.59
B	9.35 @ 0	1.40 @ -83.0	B-C	13.62
C	9.37 @ 0	1.42 @ -83.5	C-A	13.79
Average	$\tilde{V}_{S1}$ = 9.36 @ 0	$\tilde{i}_{s1}$ = 1.41 @ -83.2	Average	13.67
			$\tilde{V}_{R1}$	7.89 L-N

Table VII: Stator excited with short circuit rotor.

Stator			Rotor	
	Voltage	Current		Current
Phase	(Volts @ degrees)	(Amps @ degrees)	Phase	(Amps)
A	8.55 @ 0	10.00 @ -69.0	A	10.34
B	8.31 @ 0	9.80 @ -70.0	B	10.33
C	8.46 @ 0	10.13 @ -69.0	C	10.68
Average	$\tilde{V}_{S2}$ = 8.44 @ 0	$\tilde{i}_{s2}$ = 9.98 @ -69.33	Average	$\tilde{i}_{r2}$ = 10.45

Table VIII: Rotor excited with open circuit stator.

Rotor			Stator	
	Voltage	Current		Voltage L-L
Phase	(Volts @ degrees)	(Amps @ degrees)	Phase	(Volts rms)
A	9.40 @ 0	1.74 @ -83.0	A-B	17.12
B	9.34 @ 0	1.74 @ -83.0	B-C	17.09
C	9.37 @ 0	1.77 @ -82.0	C-A	17.39
Average	$\tilde{V}_{R3}$ = 9.37 @ 0	$\tilde{i}_{r3}$ = 1.75 @ -82.7	Average	17.2
			$\tilde{V}_{S3}$	9.93 L-N

Annual Research Journal, Vol. IV
Electrical Engineering Research Experience for Undergraduates

ISBN 0-913260-06-1 (http://www.ee.psu.edu/reu/)

Table IX: Rotor excited with short circuit stator.

Rotor			Stator	
Phase	Voltage (Volts @ degrees)	Current (Amps @ degrees)	Phase	Current (Amps)
A	8.28 @ 0	12.10 @ -69.0	A	10.03
B	8.01 @ 0	11.95 @ -70.0	B	10.17
C	8.20 @ 0	12.49 @ -69.0	C	10.35
Average	$\tilde{V}_{R4}$ = 8.16 @ 0	$\tilde{i}_{r4}$ = 12.18 @ -69.33	Average	$\tilde{i}_{s4}$ = 10.18

SUMMARY

The values determined from both methods are shown in Table X. The large percent error for the value of R_S may be due to its order of magnitude, causing it to generate a low absolute error using the Least Squared Error method. The assumption made that $X_1 = X_2$, referred to the stator side, in the standard tests may be responsible for the percent error of X_1. The percent errors when looking at X_2 and N_1:N_2 are likely caused by the no-load test with an open circuit rotor to calculate the turns ratio. Due to machine construction a measurement of the voltage at N_1 is not capable of being made, therefore the voltage used to calculate the turns ratio doesn't take into account the voltage drop across R_S and X_1. If it did, the turns ratio would be lower for the standard tests and more accurate. The value of X_2 is affected also since the turns ratio is used in its calculation. If the value of X_2 is determined being reflected to the stator side using Equation 30, the following values are: $X_2 = .3957\,\Omega$ for standard test, new test $X_2 = .3754\,\Omega$, a percent error of 5.41%. This clearly indicates that the turns ratio that was first determined was inaccurate. Remember that when using the standard tests the turns ratio is not determined since it is not possible. For this particular application it was calculated by a test that isn't a part of the standard tests. The 17.97% error for X_m may be explained due to the fact that different tests were used to calculate its value therefore the level of excitation was different due to saturation of the magnetic core, which might affect the results.

Table X: Values determined using standard test and new procedure

Parameter	Standard Tests	New Procedure	Percent Error
R_S	$0.0981\,\Omega$	$0.1599\,\Omega$	38.65%
R_R	$0.1231\,\Omega$	$0.1230\,\Omega$	.08%
X_1	$0.3957\,\Omega$	$0.4361\,\Omega$	9.26%
X_2	$0.2663\,\Omega$	$0.3001\,\Omega$	11.26%
X_m	$5.233\,\Omega$	$6.379\,\Omega$	17.97%
N_1:N_2	1.219:1	1.1184:1	8.99%
R_C	unknown	$60.9756\,\Omega$	unknown
s	0.189%	not determined	unknown

Annual Research Journal, Vol. IV
Electrical Engineering Research Experience for Undergraduates

ISBN 0-913260-06-1 (http://www.ee.psu.edu/reu/)

Overall, the values determined using the standard tests and those using the MatLab program are for the most part equal, the greatest difference being slightly larger than .06 Ω for resistance and 1 Ω for the magnetizing reactance. The benefits of using the MatLab program are to determine a more accurate turns ratio, find the value of R_C, and to verify the results using the standard tests. From these two approaches in determining the parameters one can conclude that the values obtained accurately represent the parameters in the equivalent circuit. From here these values can be used to compare the test motor machine operation as an induction machine to that of a synchronous field winding machine.

ACKNOWLEDGEMENTS

I would like to thank Dr. Heath Hofmann and Alex Rovnan for their time and input on the work done. The information they supplied was essential to all phases of the project and its completion. This material is based upon work supported by the National Science Foundation under Grant No. EEC-0244030.

REFERENCES

[1] H. Hofmann and A. Rovnan, Invention Disclosure: Brushless, Self-Excited Synchronous Field-Winding Machine. Unpublished Invention Disclosure, Department of Electrical Engineering, The Pennsylvania State University, University Park, PA.

[2] T. Wildi, "Equivalent Circuit of the Induction Motor"; pp. 331-332 in Electrical Machines, Drives, and Power Systems, 5th ed. Edited by S. Helba and A.B. Wolf, Pearson Education Inc., Upper Saddle River, NJ, 2002.

[3] S. J. Chapman, "Determining Circuit Model Parameters"; pp. 337-345 in Electric Machinery and Power System Fundamentals, Edited by S. Director, McGraw-Hill Companies, Inc., New York, NY, 2002.

ISBN 0-913260-06-1 (http://www.ee.psu.edu/reu/)

MatLab Program Code

```
function y=WRInd(beta, x)
%Dependent Parameter Description
% y=[real(ISRotorOC), imag(ISRotorOC), abs(VRRotorOC), real(ISRotorSC),
imag(ISRotorSC), abs(IRRotorSC), real(IRStatorOC)
%imag(ISRotorSC),abs(VSStatorOC),real(IRStatorSC),imag(IRStatorSC),abs(VStatorSC)]
% Measured Values
%y =[0.1673   -1.3960    7.8900    3.5220   -9.3340   10.4500    0.2237   -1.7376
%9.9300    4.3000  -11.3950   10.1800]
%Independent Variable Description
% x=[VSRotorOC VSRotorSC VRStatorOC VRStatorSC]
% x=[9.363, 8.44, 9.370, 8.163];
%Input Parameters
VSRotorOC=x(1);
VSRotorSC=x(2);
VRStatorOC=x(3);
VRStatorSC=x(4);
% Estimated Parameters
% beta=[Rs, Rr, X1, X2, Xm, N2/N1, 1/Rc]
% beta=[.0981, .1231, .3957, .2663, %   5.233, .82062, 1/60];
Rs=beta(1);
Rr=beta(2);
X1=beta(3);
X2=beta(4);
Xm=beta(5);
t_ratio=beta(6);
Gc=beta(7);
%Output Parameters
%Stator Excited, Open Ckt Rotor
ERotorOC=VSRotorOC*(((Rs+j*X1)^-1-j/Xm+Gc)^-1)*(Rs+j*X1)^-1;
ISRotorOC=(VSRotorOC-ERotorOC)/(Rs+j*X1);
VRRotorOC=t_ratio*abs(ERotorOC);
%Stator Excited, Short Ckt Rotor
ERotorSC=VSRotorSC*(((Rs+j*X1)^-1-j/Xm+Gc+t_ratio^2*(Rr+j*X2)^-1)^-1)*(Rs+j*X1)^-1;
ISRotorSC=(VSRotorSC-ERotorSC)/(Rs+j*X1);
IRRotorSC=t_ratio*abs(ERotorSC/(Rr+j*X2));
%Rotor Excited, Open Ckt Stator
EStatorOC=VRStatorOC*((-j/Xm+Gc+t_ratio^2*(Rr+j*X2)^-1)^-1)*t_ratio*(Rr+j*X2)^-1;
IRStatorOC=(VRStatorOC-t_ratio*EStatorOC)/(Rr+j*X2);
VSStatorOC=abs(EStatorOC);
%Rotor Excited, Short Ckt Stator
EStatorSC=VRStatorSC*(((Rs+j*X1)^-1-j/Xm+Gc+t_ratio^2*(Rr+j*X2)^-1)^-
1)*t_ratio*(Rr+j*X2)^-1;
IRStatorSC=(VRStatorSC-t_ratio*EStatorSC)/(Rr+j*X2);
ISStatorSC=abs(EStatorSC/(Rs+j*X1));
%Convert Phasors to Real / Imaginary
ReISRotorOC=real(ISRotorOC);
ImISRotorOC=imag(ISRotorOC);
ReISRotorSC=real(ISRotorSC);
ImISRotorSC=imag(ISRotorSC);
ReIRStatorOC=real(IRStatorOC);
ImIRStatorOC=imag(IRStatorOC);
ReIRStatorSC=real(IRStatorSC);
ImIRStatorSC=imag(IRStatorSC);
%Returned Output
y(1)=ReISRotorOC;
y(2)=ImISRotorOC;
y(3)=VRRotorOC;
y(4)=ReISRotorSC;
y(5)=ImISRotorSC;
y(6)=IRRotorSC;
y(7)=ReIRStatorOC;
y(8)=ImIRStatorOC;
y(9)=VSStatorOC;
y(10)=ReIRStatorSC;
y(11)=ImIRStatorSC;
y(12)=ISStatorSC;
```


Annual Research Journal, Vol. IV
Electrical Engineering Research Experience for Undergraduates

ISBN 0-913260-06-1 (http://www.ee.psu.edu/reu/)

A COMPARATIVE STUDY OF PITCH ESTIMATION METHODS FOR VOICED SPEECH

Suman Ravuri*, Robert M. Nickel[#] and William K. Jenkins[#]

Department of Electrical Engineering
The Pennsylvania State University, University Park, PA 16802

*Undergraduate Student in the
Department of Electrical Engineering
Columbia University
New York, NY 10027

ABSTRACT

The function of pitch estimation is to determine the frequency of the vibration of the vocal folds from voiced speech. At first glance, pitch estimation may seem to be a rather trivial task. However, irregularities in the speech signal that are (in part) due to changes in the geometry of the vocal tract complicate the situation. The irregularities lead to frequent estimation errors such as pitch-doubling (the measured pitch is twice what it should be) and pitch-halving (the measured F0 is half of what it should be). Furthermore, other problems, such as determining the first formant as the fundamental frequency, may degrade the quality of the pitch estimator.

The goal of this research project is to create a robust pitch estimator that is less prone to the above problems. This study considers a number of traditional methods of pitch extraction and discusses their advantages and disadvantages. Five different methods of pitch estimation are compared: i) temporal autocorrelation, ii) spectral autocorrelation, iii) average magnitude difference function, iv) cepstrum analysis, and v) wavelet analysis. In addition, two hybrid pitch estimators are described and compared to the classical estimators. Relative advantages of each method and a robust pitch estimation method combining different types of pitch estimation is outlined.

[#] Faculty Mentors

Annual Research Journal, Vol. IV
Electrical Engineering Research Experience for Undergraduates

ISBN 0-913260-06-1 (http://www.ee.psu.edu/reu/)

INTRODUCTION

One can classify speech as either noisy or voiced. Noisy speech is generated by the mouth and tends to produce a "noise-like" sound (such as the sounds 'sh' and 'ch'). Voiced speech, on the other hand, is first generated at the vocal folds in the neck. This periodic sound travels through a tube-like filters at the nose and the mouth and generates most of the speech sounds in Western language.

Properly identifying the frequency of vibration of the vocal folds (called the fundamental frequency) after it has passed through the filter of the nose/mouth is the function of pitch detection. A good pitch detection algorithm is very useful in many applications of speech-processing, such as speech recognition, speaker recognition, voice transformation and a number of other speech topics.

While pitch detection seems to be a trivial problem, even after over twenty years of work, no pitch detection algorithm can perfectly determine the fundamental frequency of speech. Pitch detection is complicated by two major issues: the filter of the nose/mouth is constantly changing and the frequency during voiced sections is not completely stationary. Generally, we deal with the former problem by assuming that the filter is static for two pitch periods and the latter problem by assuming that the fundamental frequency (F0) is static for 5ms. Unfortunately, these assumption leads to problems outlined below.

The goal of this research project is to compare some of the classic types of pitch detection: autocorrelation, cepstral, average magnitude difference function, and spectral correlation techniques. The paper seeks to outline the relative strengths and weaknesses of each type of pitch-detection algorithm, and tries to compare some hybrid approaches that lead to better pitch estimation. We also compare these algorithms to a newer and widely available algorithm (the wavelet analysis (with significant post-processing) method called TEMPO[1]) and compare the results to the more classical techniques.

Before we discuss the details of each algorithm it is beneficial to first introduce some notation. We will refer to a sampled speech signal with s(t). A vector $\mathbf{s}_L(t)$ of L sequential speech samples is defined by:

$$\mathbf{s}_L(t) = [\, s(t) \;\; s(t+1) \;\ldots\; s(t+L-1) \,]^{T} . \qquad (1)$$

Autocorrelation

Assuming a discretized speech signal, the short-time autocorrelation function of length L can be defined as:

$$r(i,j) = \mathbf{s}_L(i)^{T}\, \mathbf{s}_L(i+j) \qquad (2)$$

When j is equal to a multiple of the pitch period of a periodic signal, the windowed signal $s_i(t)$ is most similar to $s_j(t)$ and r(i,j) is at a maximum. Hence, the

Annual Research Journal, Vol. IV
Electrical Engineering Research Experience for Undergraduates

ISBN 0-913260-06-1 (http://www.ee.psu.edu/reu/)

distance between peaks is the pitch period P or 1/F0. Not accurately identifying all the peaks of the autocorrelation methods leads to pitch-halving problems (which is more accurately described as fractional pitch problems), since the estimated distance between peaks would be n·P.

A normalized periodicity measure that is similar to autocorrelation is called the normalized inner product. For a speech segment at sample i, we take n-number of samples on either side of the i-th sample (for instance 2), and take the normalized inner product of the resulting two vectors:

$$q(i,n) = \mathbf{s}_n(i)^T \mathbf{s}_n(i-n) \; / \; (\|\mathbf{s}_n(i)\| \, \|\mathbf{s}_n(i-n)\|). \quad (3)$$

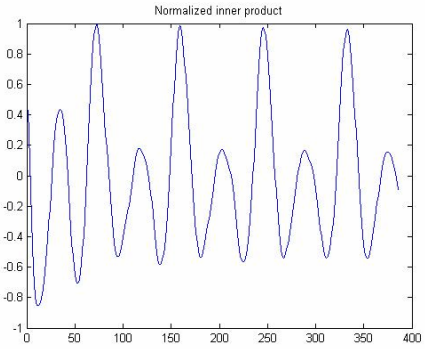

Figure 1: Sample output of Normalized Inner Product at Time t

One subsequently increases the number of samples on either side of i and continues to calculates their normalized inner product.[2] Near pitch periods, the normalized inner products approach their maximum value of 1. This property is quite useful since voiced sections will have similar maximum normalized inner products regardless of the amplitude of speech.

Cepstral Analysis

The real cepstrum is most conveniently defined via MATLAB pseudocode:

$$c[i,n] = \text{ifft}\{ \log\{ \text{abs}\{ \text{fft}\{ \mathbf{s}_L(i) \} \} \} \}. \quad (4)$$

Cepstral analysis is a technique that can be used to linearly deconvolve two signals. For speech signal processing, the output of the mouth s(t) can be thought of as the convolution of the excitation of the vocal folds, v(t), (for voiced speech) and the filter of the nose/mouth, n(t). When transformed into the frequency domain, the spectrum of the speech signal S(w) is merely N(w)*V(w). We can separate out the V(w) linearly by taking log(S(w))= log(N(w))+log(V(w)). By taking the inverse Fourier transform of the signal, we separate the excitation v(t) from the filter n(t) by picking out the peaks in the quefrency domain.

Annual Research Journal, Vol. IV
Electrical Engineering Research Experience for Undergraduates

ISBN 0-913260-06-1 (http://www.ee.psu.edu/reu/)

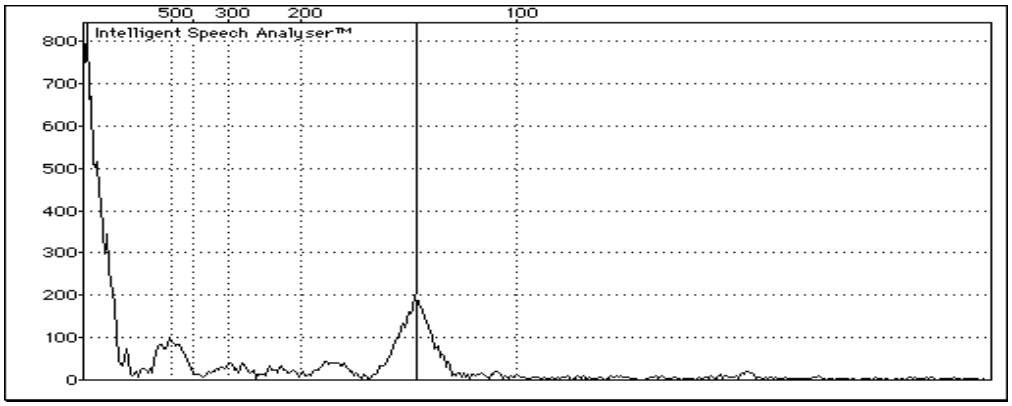

Figure 2: Sample output of a Cepstrum at Time t.

Peaks are not as pronounced as the autocorrelation method, since the peaks are of the amplitude are less than the log of the amplitude of the speech signal.[3]

Average Magnitude Difference Function

The Average Magnitude Difference Function is a very similar measure to the correlation method described above. The AMDF is calculated as:

$$\mathrm{AMDF}(t) = \frac{1}{L}\sum_{i=1}^{L} |s(i) - s(i-t)| \qquad (5)$$

where s(i) : the samples of input speech
s(i)=[s(1),s(2), ... ,s(L)]
s(i- τ) : the samples time shifted

The major difference between the AMDF and correlation method is that AMDF(t) will give local minima at pitch periods, while the correlation methods give local maxima at pitch periods. Also, unlike the normalized inner product, the AMDF function is not necessarily bounded, so voicing decisions cannot be made by using a simple absolute threshold.

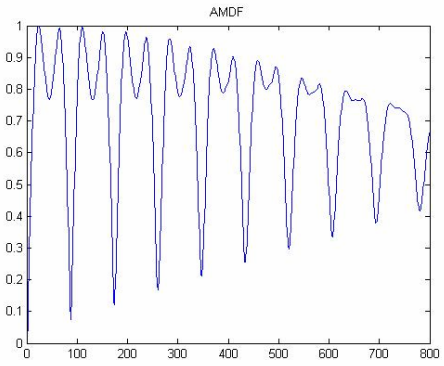

Figure 3: Sample output of the AMDF at Time t.

Annual Research Journal, Vol. IV
Electrical Engineering Research Experience for Undergraduates

ISBN 0-913260-06-1 (http://www.ee.psu.edu/reu/)

Spectral Autocorrelation

Spectral Autocorrelation is a method to determine the pitch of a voiced speech signal in the frequency domain. In theory, one would be able to determine the fundamental frequency in the frequency domain by extracting the spectral peak at F_0. Unfortunately, in practice, this spectral peak is not always present. A more robust method is to determine all the spectral peaks and determine the average distance between spectral peaks. This can be done using a comb filter, as shown below:

$$C(\omega, \omega 0) = W(k\omega 0);\ \omega = k\omega 0,\ k = 1, 2, \ldots \frac{\Omega m}{\omega 0} \tag{6}$$

$$C(\omega, \omega 0) = 0;\ o/w$$

We then correlate the comb filter with the spectrum of the speech signal:

$$Ac(\omega 0) = \frac{\omega 0}{\Omega m} \sum_{k=1}^{\frac{\omega 0}{\Omega m}} S(k\omega 0)\ W(k\omega 0) \tag{7}$$

$$\frac{2\pi}{tmin} \le \omega 0 \le \frac{2\pi}{tmax}$$

Ωm is the max frequency of the speech signal

At $n*\omega_0$, the ACF is at a maximum value. If $Ac(\omega_0)$ misses the first peak, however, pitch estimates will be $N*F_0$.[4]

Hybrid Methods

After stage 1 of the experiment, we discovered that some methods are better at certain parts of pitch detection (the normalized inner product method was very good at determining voiced sections) while other algorithms excelled in other areas (the AMDF function produced minimal pitch halving/doubling errors). We therefore tried some hybrid approaches, such as using the normalized inner product to give voiced section data and have the AMDF or spectral autocorrelation methods determine the fundamental frequency within those sections.

Pitch Halving/Doubling Minimization Algorithm

After stage 2 of the experiment, we found that there is a rather simple technique for minimizing pitch doubling and halving errors by making two assumptions: (1) a person's minimum correct pitch is not a 1/n fraction of the maximum correct pitch, and (2) the pitch estimators correctly identify most pitch decisions. Given these two assumptions, we take the mean of the entire pitch track. Then we perform the following calculation:

Annual Research Journal, Vol. IV
Electrical Engineering Research Experience for Undergraduates

ISBN 0-913260-06-1 (http://www.ee.psu.edu/reu/)

$$E=m-n*F_0(t)\ . \quad (8)$$

where n=1/4,1/3,1/2,1,2,3,4;

E is the error; m is mean pitch; and $F_0(t)$ is F_0 at time t.

The n with the minimum error is the correct multiple by which to multiply the pitch. In this instance, n could be scaled to include more multiples, but 4 seemed to be a sufficient number for the algorithm.

EXPERIMENTAL PROCEDURE

Stage 1

For the experimental procedure, we used MATLAB to implement all of the pitch detection algorithms. In order to assess the accuracy of the pitch detection algorithms, we used the Keele database, which has speech and laryngographic signals as well as manually checked pitch tracks from each of the speakers. The database consists of 10 speakers (5 male and 5 female) reading from a script of the "North Wind Story", a 30-second phonetically balanced clip. We tested the five classic and two hybrid pitch detection algorithms (PDAs) and checked them against the manually checked pitch track. With the exception of the TEMPO, pitch estimates were made at 5ms intervals (TEMPO used 1ms intervals). We determined correct pitch estimates at $\pm$10%, 15% and 20% windows and checked for n-tuple and fractional estimates up to 4. We then checked for voiced estimates in unvoiced sections, unvoiced estimates in voiced sections and other errors.

Stage 2

We then ran the same test by adding four different types of noise: white noise, speech babble, F16 cockpit noise, and machine gun noise. These noises were taken from the Noisex database.[5] They were added at different signal-to-noise ratios (20dB, 10dB, 5dB, -5dB, -10dB) and the estimates were taken again. Every piece of data checked in stage 1 was also checked in state 2.

Stage 3

After stage 2, raw pitch estimates were put through the pitch having/doubling minimization algorithm. These new pitch estimates were again compared to the original pitch tracks and then compared to the pitch tracks that were used in stage 2.

EXPERIMENTAL RESULTS AND DISCUSSION

Stage 1

Tables I, II, and III summarize pitch estimation (Est.) for male and female voices with $\pm$ 10% window.

Annual Research Journal, Vol. IV
Electrical Engineering Research Experience for Undergraduates

ISBN 0-913260-06-1 (http://www.ee.psu.edu/reu/)

Table I: Pitch Estimation for Male and Female Voices with ± 10% window

Pitch Estimation Method	Overall Correct Estimates (%)	Pitch halving errors (%)	Pitch doubling errors (%)	Other Errors (%)	Voiced Est. in Unvoiced Sections (%)	Unvoiced Estimates in Voiced Sections (%)
TEMPO(Wavelet)	81.089	0.60555	0.26153	6.4887	8.8134	2.7422
Autocorrelation	56.16	7.8463	0.064943	24.812	2.5918	8.5249
Cepstral	55.659	2.2305	0.038935	14.994	2.7227	24.356
AMDF	72.768	1.2476	0.1099	4.8142	4.822	16.238
Spectral Autocorrelation	72.354	0.80877	0.51184	5.6602	2.4534	18.212
Hybrid AMDF	77.529	2.0299	0.14948	6.3698	5.8915	8.0298
Hybrid Spectral Autocorrelation	72.836	1.4342	2.383	10.209	4.383	8.7541

Table II: Pitch Estimation for Male Voices with ± 10% window.

Pitch Estimation Method	Overall Correct Estimates (%)	Pitch halving errors (%)	Pitch doubling errors (%)	Other Errors (%)	Voiced Est. in Unvoiced Sections (%)	Unvoiced Estimates in Voiced Sections (%)
TEMPO(Wavelet)	77.958	0.45074	0.11416	9.3631	8.6983	3.4157
Autocorrelation	66.162	4.4294	0.071543	15.824	2.2267	11.287
Cepstral	53.868	1.992	0.027456	10.807	2.5581	30.748
AMDF	65.094	0.58766	0.006734	7.0492	2.2272	25.036
Spectral Autocorrelation	59.534	0.73721	0.42287	7.1327	0.82478	31.348
Hybrid AMDF	73.159	1.4455	0.057879	9.7399	3.6088	11.989
Hybrid Spectral Autocorrelation	61.652	1.7603	3.7539	16.326	2.643	13.865

Table III: Pitch Estimation for Female Voices with ± 10% window

Pitch Estimation Method	Overall Correct Est. (%)	Pitch halving errors (%)	Pitch doubling errors (%)	Other Errors (%)	Voiced Est. in Unvoiced Sections (%)	Unvoiced Est. in Voiced Sections (%)
TEMPO(Wavelet)	84.219	0.76036	0.4089	3.6142	8.9285	2.0688
Auto-correlation	46.159	11.263	0.058342	33.8	2.957	5.7629
Cepstral	57.449	2.469	0.050413	19.18	2.8873	17.964
AMDF	80.442	1.9076	0.21307	2.5792	7.4168	7.4412
Spectral Autocorrelation	85.173	0.88033	0.60081	4.1876	4.082	5.0763
Hybrid AMDF	81.9	2.6144	0.24108	2.9997	8.1743	4.0708
Hybrid Spectral Autocorrelation	84.021	1.108	1.0121	4.0924	6.123	3.6434

Annual Research Journal, Vol. IV
Electrical Engineering Research Experience for Undergraduates

ISBN 0-913260-06-1 (http://www.ee.psu.edu/reu/)

Considering both male and female data, the autocorrelation and cepstral methods performed the most poorly (with around 55% correct estimates), while the wavelet, AMDF and spectral methods performed much better. The wavelet pitch estimator produced pitch tracks which were around 80% correct overall, while the AMDF and spectral estimators derived tracks were roughly 72% correct overall.

The main source of error for the autocorrelation method is its estimates are outside the $\pm$10% window. An explanation for this behavior is that the autocorrelation function is extremely sensitive to amplitude changes. Amplitude changes cause the pitch period of a signal to lag rather than remain constant. Thus, the pitch estimates are lower than what they should be.[6]

What is even more interesting to note that the AMDF and spectral methods performed extremely well for female voices (with 80% and 85% correct respectively), while the two methods had only a mediocre performance on male voices (65% and 59% correct respectively). In fact, the autocorrelation function outperforms both the AMDF and spectral autcorrelation function.

The main source of error for male tracks were the rather large unvoiced estimates in voiced sections (25% for the AMDF and 31% for the spectral autocorrelation). This is in large part due to the fact that the voicing estimator for the AMDF and spectral methods was originally tuned for female speech. The autocorrelation voicing method, on the other hand, was quite a bit better overall than the AMDF and spectral autocorrelation methods (8.5% vs. 16% and 18% respectively) and was much better for male estimates (11% vs. 25% and 31% respectively).

We also tested two hybrid detectors; one by using autocorrelation voicing estimates with the AMDF pitch estimator and the other by using the same autocorrelation voicing estimates with a spectral autocorrelator. The hybrid AMDF performed very well, increasing its overall correct estimates by 5% overall, 8% for male sections and 1.5% for female sections. The hybrid spectral autocorrelator made only a nominal gain (0.5% overall, 2% for male signals and -1% for female signals). While the hybrid spectral autocorrelation method produced roughly half the unvoiced in voiced section errors, the number of other errors (pitch estimates outside the $\pm$10% window) doubled. This suggests that while the AMDF may be able to produce more correct pitch estimates when given voicing decisions from other voicing estimators, the spectral method seems to produce more errors when given different voicing information.

Stage 2

Correct pitch estimates vs. noise

Annual Research Journal, Vol. IV
Electrical Engineering Research Experience for Undergraduates

ISBN 0-913260-06-1 (http://www.ee.psu.edu/reu/)

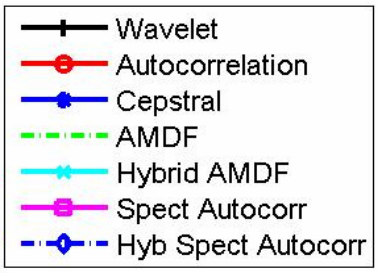

Figure 4: Legend for proceeding graphs

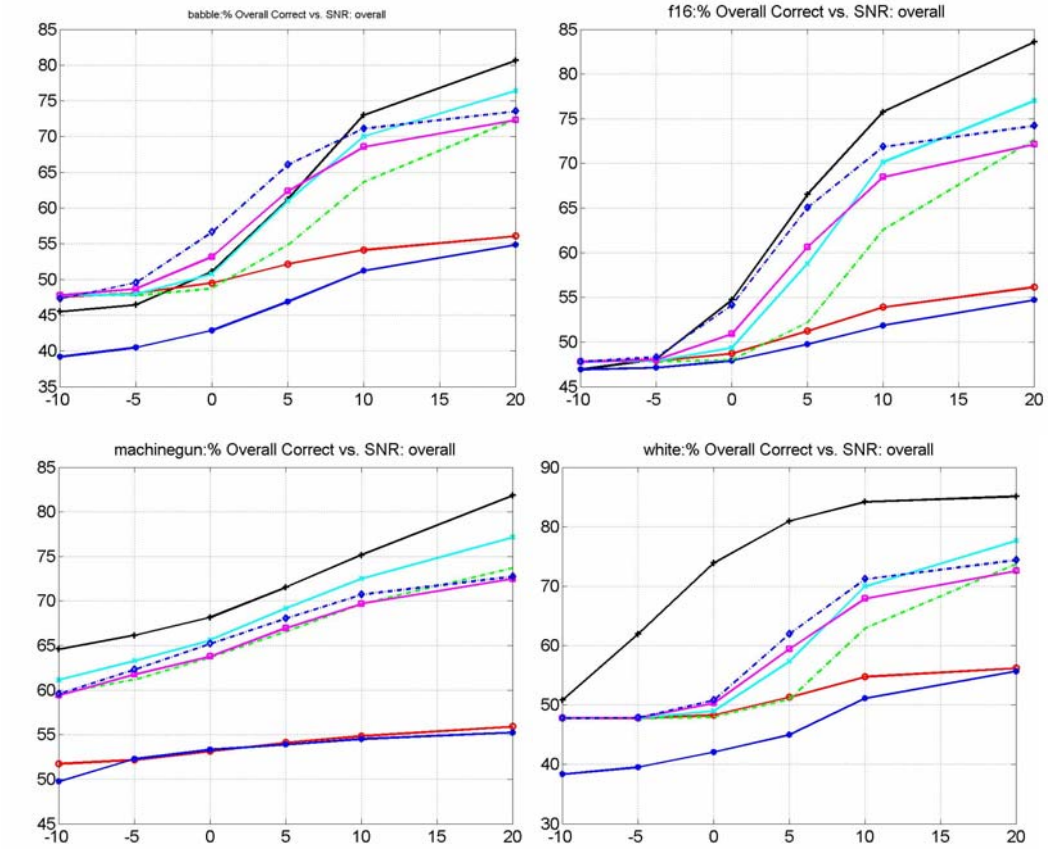

Figure 5: Comparison of percentage of correct pitch estimates in both voiced and unvoiced sections vs. signal-to-noise ratio of babble (top-left) , f16 (top-right), machine gun (bottom-left) and white (bottom-right) noises

Babble noise is perhaps the most damaging noise for a speech signal, since the noise consists of other speech signals. For the babble signal, TEMPO reached above an 80% estimate for 20dB SNR and fell rather precipitously from 10dB to -

Annual Research Journal, Vol. IV
Electrical Engineering Research Experience for Undergraduates

ISBN 0-913260-06-1 (http://www.ee.psu.edu/reu/)

5dB, when the signal levels off again. The AMDF, the hybrid AMDF, the spectral autocorrelator and the hybrid spectral autocorrelator all performed similarly. The hybrid spectral autocorrelator is most resistant to noise compared to all other methods (it even surpasses the wavelet pitch estimator for SNRs under 10dB).

For F16 noise, the classic pitch estimators exhibit the same characteristics as with babble noise. The wavelet analyzer, on the other hand, performs 2-5dB better for every SNR.

Machine gun noise is used since it approximates impulsive noise. It is interesting to note that while the lower SNRs for babble noise and F16 noise cause a precipitous drop in correct estimates, machine gun noise exhibits a more linear drop as the SNR decreases.

For white noise, the TEMPO offers superior estimation compared to all other techniques by a wide margin. While every other method exhibits the same characteristic as with babble and F16 noise, TEMPO is close to 10% better than the best pitch estimator for every SNR.

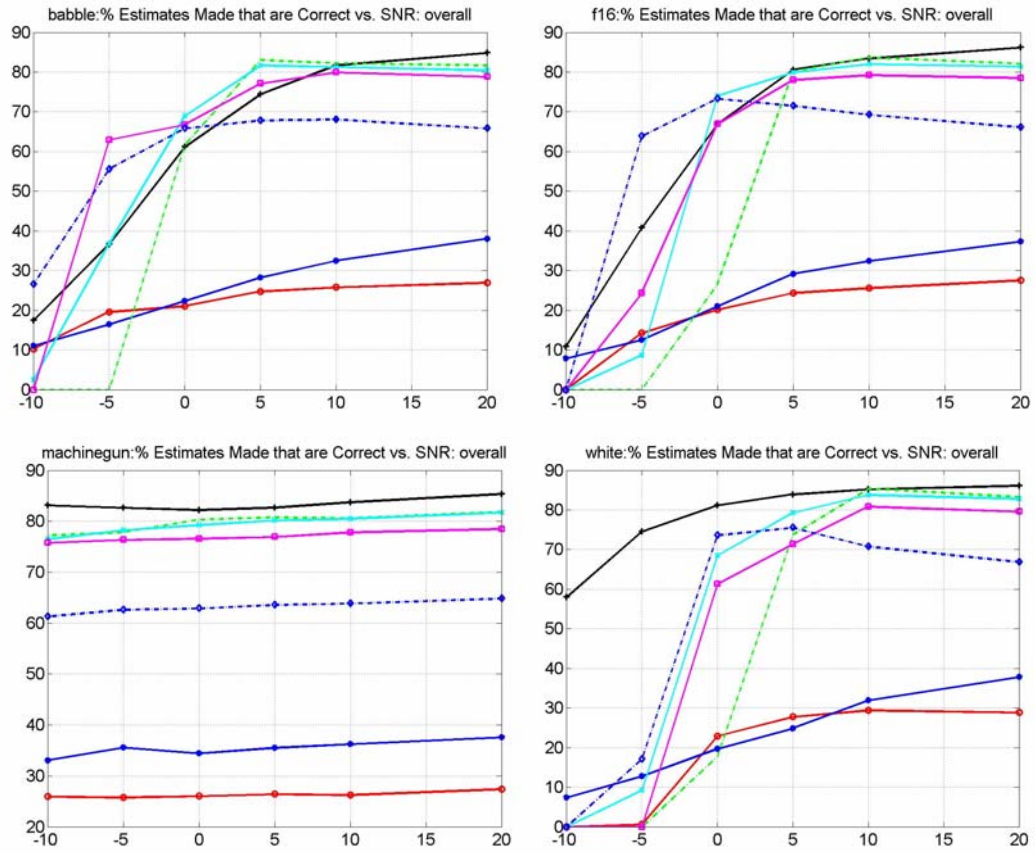

Figure 6: Pitch estimates correct/pitch estimates made (%) vs. SNR of babble (top-left), f16 (top-right), machine gun (bottom-left) and white (bottom-right) noises

Annual Research Journal, Vol. IV
Electrical Engineering Research Experience for Undergraduates

ISBN 0-913260-06-1 (http://www.ee.psu.edu/reu/)

Another metric for pitch estimation is determining what percentage of pitch estimates made is correct. This standard strips the function of how well the pitch estimator acts as a voicing detector and instead judges how well the pitch estimator actually works. By this standard, the AMDF and spectral autocorrelation estimators perform almost as well as TEMPO. Furthermore, for all types of noise except for white noise, the AMDF and spectral estimators are more resistant to bad estimates as the SNR decreases. The autocorrelation and cepstral methods again perform poorly relative to other pitch estimation methods.

From figure 7, we can see that unvoiced errors in voiced sections generally make up the majority of errors for each type of pitch estimator. There are two small exceptions, however. For SNR greater than 8dB, the percentage of other errors exceeds the unvoiced type for the autocorrelation method. Also, around 17dB the wavelet estimator exhibits more types of voiced errors in unvoiced sections and other errors. For every other situation, however, the errors stem from an unvoiced estimate in a voiced section. This seems to indicate that a better voiced section estimator should be used and that one should not rely on the pitch estimator for voiced/unvoiced decisions.

Types of Error

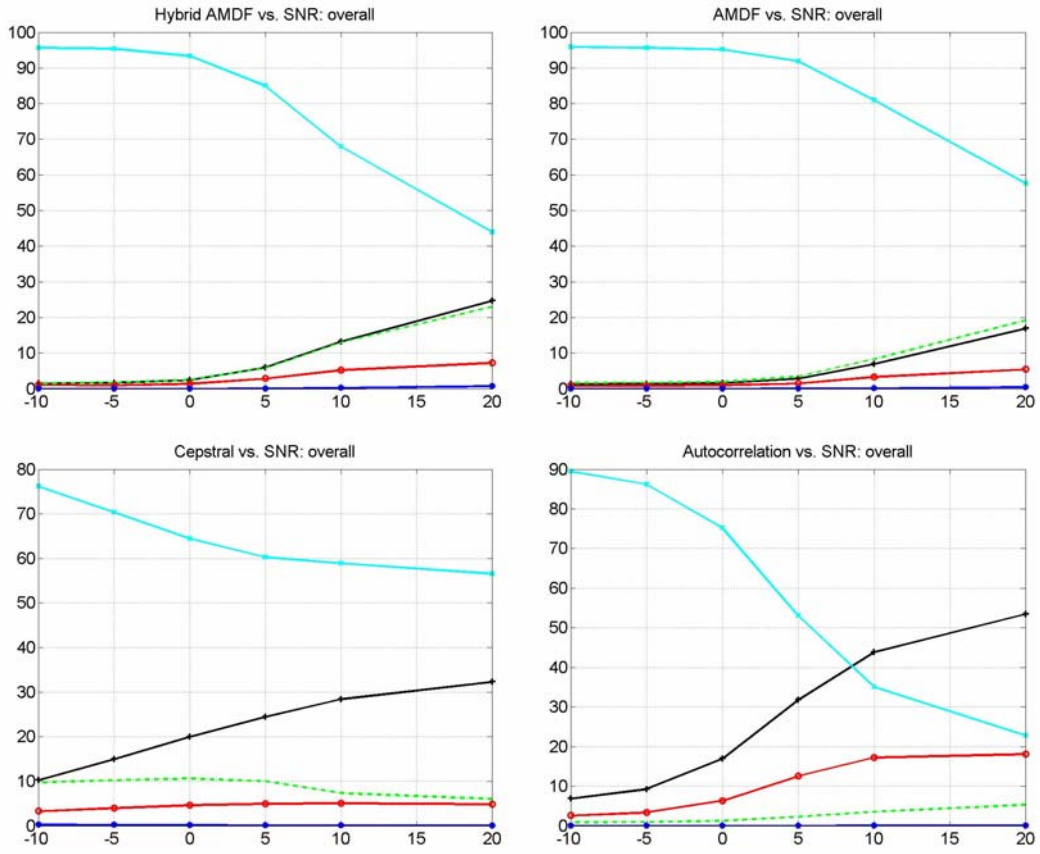

Annual Research Journal, Vol. IV
Electrical Engineering Research Experience for Undergraduates

ISBN 0-913260-06-1 (http://www.ee.psu.edu/reu/)

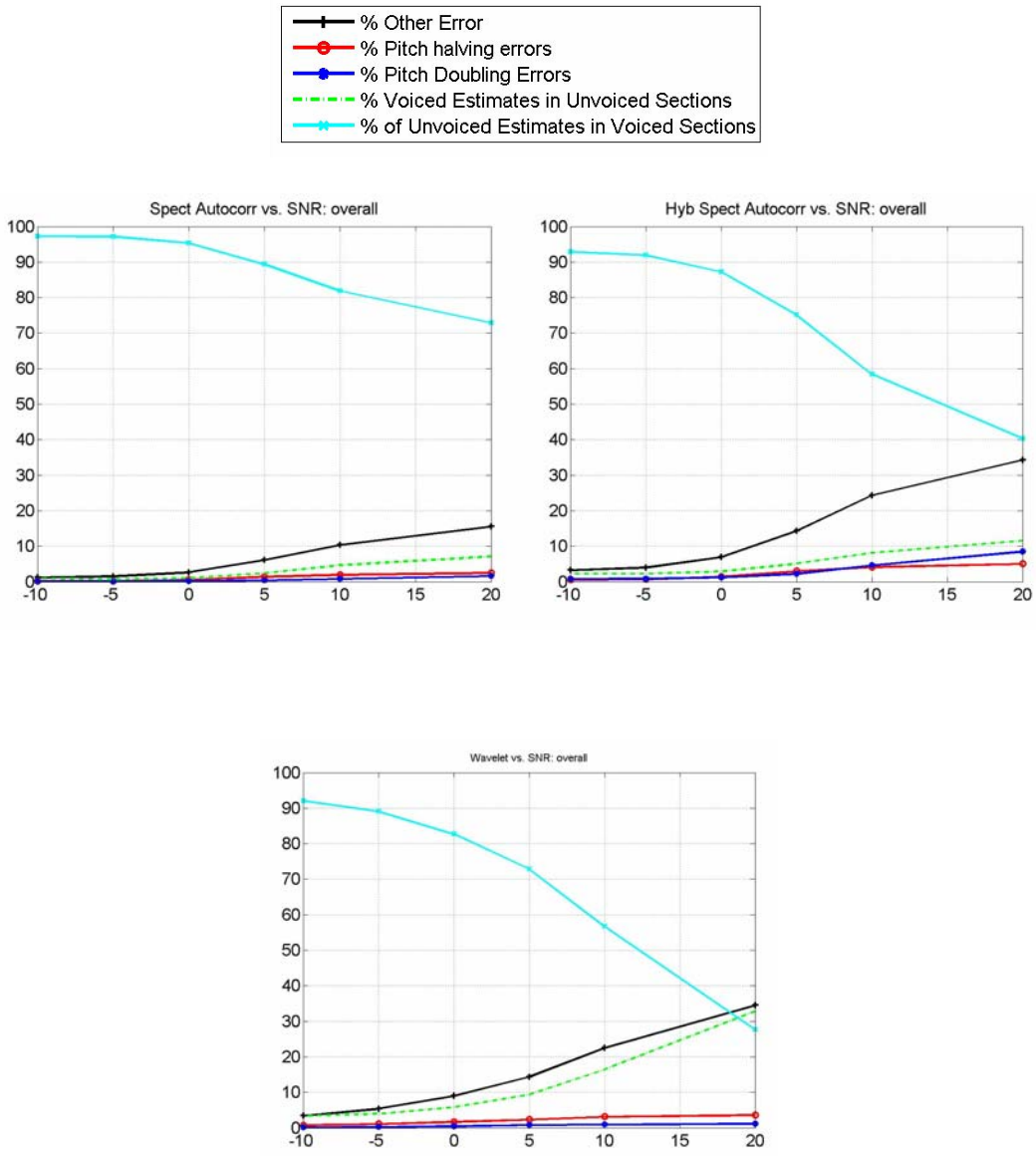

Figure 7: Percentage types of errors vs. SNR for different pitch estimators

Annual Research Journal, Vol. IV
Electrical Engineering Research Experience for Undergraduates

ISBN 0-913260-06-1 (http://www.ee.psu.edu/reu/)

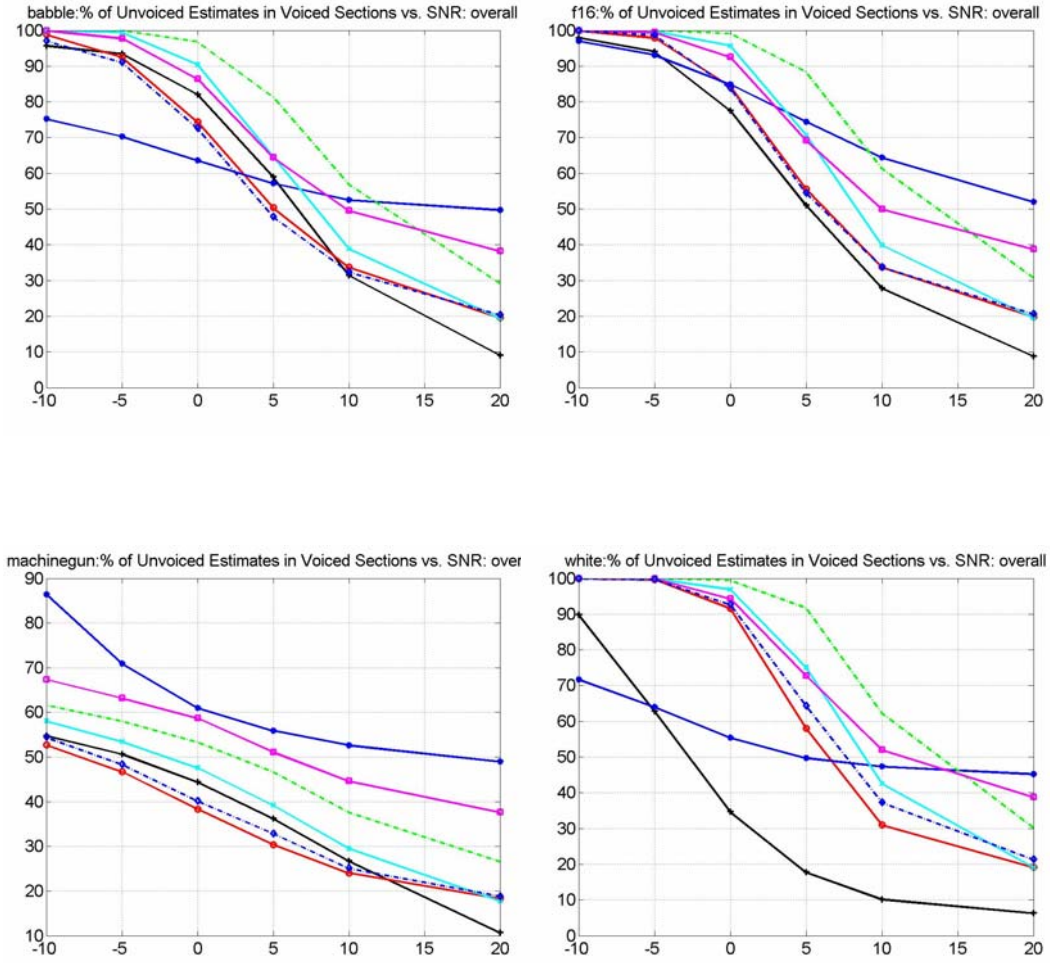

Figure 8: Percentage of Unvoiced Estimates in Voiced Sections vs. SNR of babble (top-left), f16 (top-right), machine gun (bottom-left) and white (bottom-right) noises

With every type of noise, the percentage of unvoiced estimates in voiced section increases as the SNR decreases. With every type of noise except for machine gun noise, this number approaches 100% as the SNR approaches 20dB. Babble, F16 and white noise produce a reverse S-curve characteristic while machine gun noise produces a linear decrease as the SNR rises.

The other interesting thing to note is that the wavelet analyzer is significantly more resistant to white noise compared to the classical methods. Rather than exhibiting a normal S-curve, the wavelet white noise characteristic is more akin to a decreasing exponential.

Annual Research Journal, Vol. IV
Electrical Engineering Research Experience for Undergraduates

ISBN 0-913260-06-1 (http://www.ee.psu.edu/reu/)

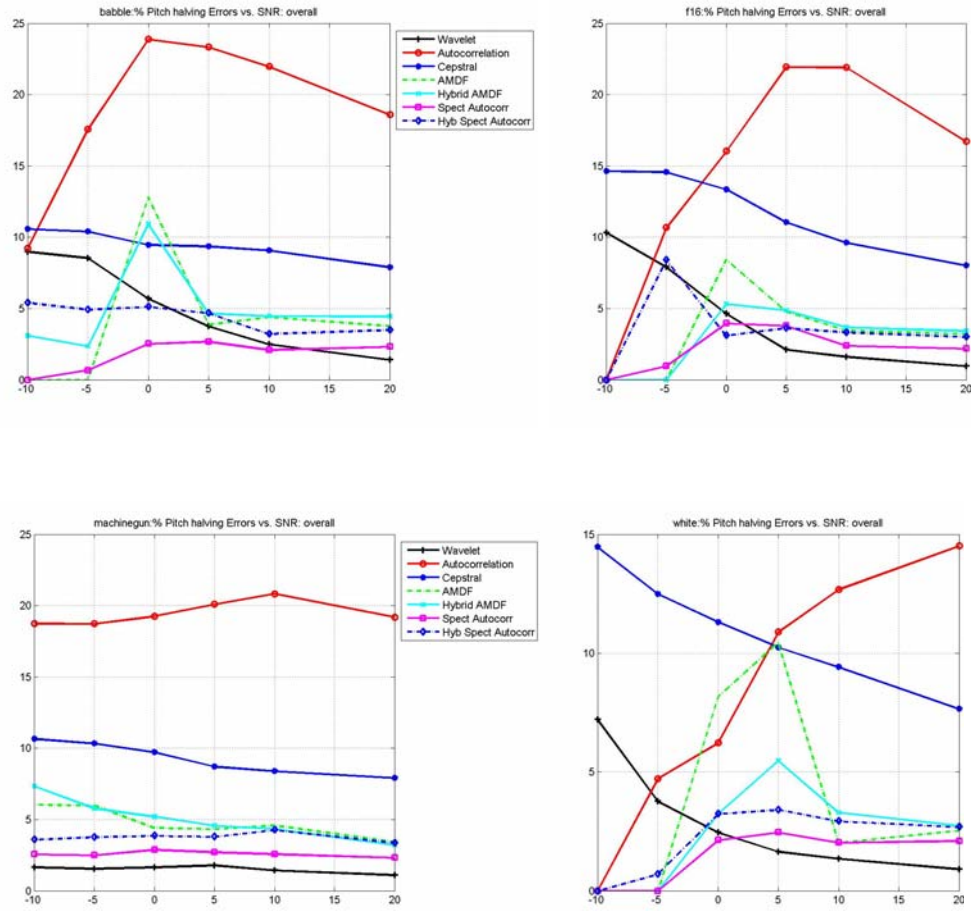

Figure 9: Pitch-halving errors vs. SNR of babble (top-left), f16 (top-right), machine gun (bottom-left) and white (bottom-right) noises

Annual Research Journal, Vol. IV
Electrical Engineering Research Experience for Undergraduates

ISBN 0-913260-06-1 (http://www.ee.psu.edu/reu/)

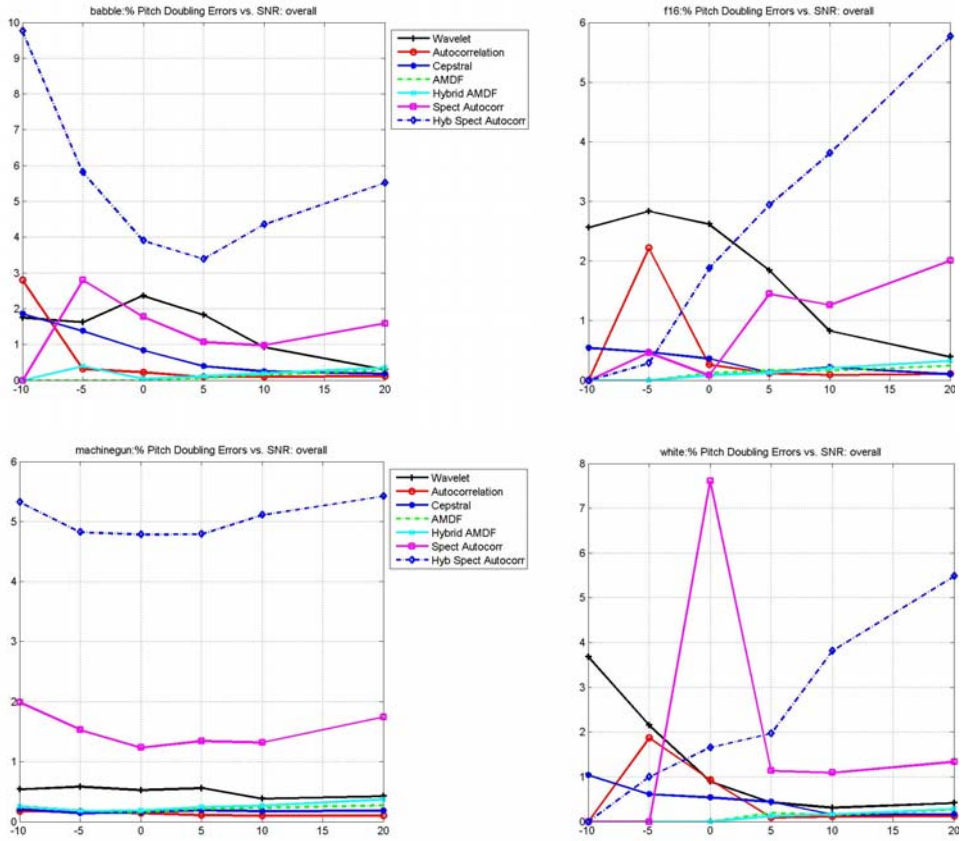

Figure 10: Pitch doubling errors vs SNR of babble (top-left), f16 (top-right), machine gun (bottom-left) and white (bottom-right) noise

As expected the autocorrelation method exhibits far more pitch-halving errors than any other method. One also may notice a peak at 0dB for AMDF-type and correlation estimators for all noises except machine gun noise. This is actually a bit deceiving. Below 0dB, the number of pitch estimates becomes so few (i.e. the number of unvoiced estimates in voiced sections increases) that very few pitch-halving errors remain

Not surprisingly, most of the pitch-doubling errors occur in the spectro-temporal estimators. In most cases, however, the error is quite small compared to other types of error. For the cepstral, correlation and AMDF functions rarely reach above 3%. Even the spectral ACF, which produce the highest error rate, average 6% and is bounded by a 10% error.

Stage 3

The pitch halving/doubling algorithm, for the most part, did not increase the overall percentage of correct estimates, since pitch halving and doubling

Annual Research Journal, Vol. IV
Electrical Engineering Research Experience for Undergraduates

ISBN 0-913260-06-1 (http://www.ee.psu.edu/reu/)

generally represented a small percentage of the total error. It did, however, help the autocorrelation function make much better estimates. Since the ACF is prone

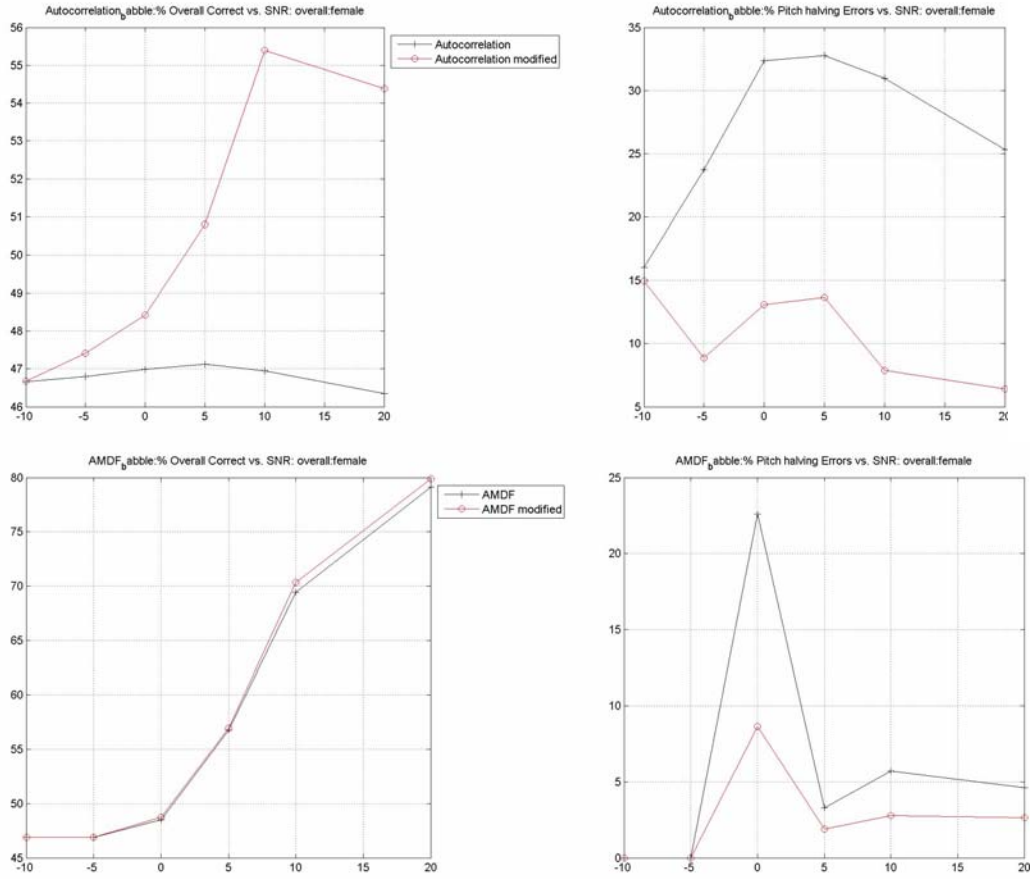

Figure 11: Autocorrelation and modified autocorrelation method (top) Overall correct estimate vs. babble SNR(left) and pitch halving errors(right) AMDF and modified AMDF version (bottom) Overall correct estimates (left) and pitch halving errors (right)

to pitch-halving errors, the autocorrelation function helped the percentage of correct estimates 10%. It achieves this feat by reducing pitch-halving errors by around 18%. In general, it also reduces AMDF-variant pitch-halving and doubling errors by 1-2%. It also improved AMDF-based estimators slightly. Other PDAs, however, showed a negligible improvement or even slight deterioration.

CONCLUSION

Seven different types of pitch estimators were compared using the Keele database. Four different types of noise were used and a pitch halving/doubling minimization algorithm was proposed. In the end, the TEMPO performed the best overall. This, however, was not surprising since it had been refined over a period

Annual Research Journal, Vol. IV
Electrical Engineering Research Experience for Undergraduates

ISBN 0-913260-06-1 (http://www.ee.psu.edu/reu/)

of 9 years.

On the other hand, what is exciting is that one type of pitch estimator did not work in every situation. The hybrid spectral autocorrelation seemed to work very well for noisy environments, although its inability to produce better F_0 estimates given better voicing data is somewhat troubling.

What is also interesting is that a hybrid approach did show some significant improvement. In the AMDF estimator, using the autocorrelation voicing estimation with the AMDF estimator allowed for a 5% gain in correct pitch estimates.

For a future outlook, what seems important is to get an independent algorithm to perform voicing estimation. A number of pitch estimators frequently produced the correct pitch estimate over truly voiced speech sections, but far too often the pitch estimators did not correctly identify a voiced section. The best voicing estimator was the autocorrelation method, but superior methods of voicing estimation exist and should be used.

Also, more investigation needs to be done with independent databases, since the number of signals used is quite few. Even though the speech segments are quite long, the number of speakers is quite small.

What is also not known is how an increasing number of pitch estimates affect the error rate. Kawahara et al. suggests that estimates should be made every 1ms instead of 5ms.[7]

Finally, the error profile is not exactly the same for every type of pitch estimator. It would be an interesting experiment to see if a weighting scheme could be used for different type of PDAs to create a truly hybrid robust pitch estimator.

ACKNOWLEDGEMENT

First and foremost I would like to thank my faculty mentors Prof. Nickel and Prof. Jenkins. I would like to thank Prof. Nickel for steering my ideas about speech into actual results and in the process save me a lot of frustration. I would also like to thank Prof. Jenkins, whose insight into an approach of research truly helped me throughout this summer program. Finally, I would like to thank the National Science Foundation for funding this great opportunity. The material is based upon work supported by the National Science Foundation under Grant No. EEC-0244030.

REFERENCES

[1] Kawahara, H., Masuda-Katsuse, I., de Cheveigne, A. "Restructuring speech representations using a pitch-adaptive time-frequency smoothing and an instantaneous-frequency-based F0 extraction: Possible role of a repetitive structure in sounds" *Speech Communication*, **27**, 3-4, pp.187-207. 1999.

[2] Deller, M., Hansen, J.H.L., Proakis, J.G. *Discrete-Time Processing of Speech*

Annual Research Journal, Vol. IV
Electrical Engineering Research Experience for Undergraduates

ISBN 0-913260-06-1 (http://www.ee.psu.edu/reu/)

Signals. New York: Institute of Electrical and Electronics Engineers. 2000.

[3] Quatieri, T.F. *Discrete-Time Speech Signal Processing.* Upper Saddle River: Prentice-Hall, Inc. 2001.

[4] Kondoz, A.M. *Digital Speech: Coding for Low Bit Rate Communications Systems.* New York: John Wiley and Sons. 1994.

[5] Noisex database. <http://spib.rice.edu/spib/select_noise.html>

[6] Kawahara, H., Masuda-Katsuse, I., de Cheveigne, A. "YIN, a fundamental frequency estimator for speech and music". Journal of The Acoustical Society of America. **111** (4): 1917-1930. Apr. 2002.

[7] Kawahara, H., Masuda-Katsuse, I., de Cheveigne. "Restructuring speech representations using a pitch-adaptive time-frequency smoothing and an instantaneous-frequency-based F0 extraction: Possible role of a repetitive structure in sounds" *Speech Communication*, **27**, 3-4, pp.187-207. 1999.

Annual Research Journal, Vol. IV
Electrical Engineering Research Experience for Undergraduates

ISBN 0-913260-06-1 (http://www.ee.psu.edu/reu/)

ELECTRICAL CHARACTERIZATION OF SILICON NANOWIRE FIELD EFFECT TRANSISTORS AND CORRELATION TO DEVICE PHYSICAL DIMENSIONS

Jason C. Mantey[1,*], Tsung-ta Ho[2,†], Theresa S. Mayer[2,‡] , and Joan M. Redwing[2,3,‡]

[1] Department of Electrical and Computer Engineering
Wayne State University, Detroit, MI 48202

[2] Department of Electrical Engineering
[3] Department of Materials Science and Engineering
The Pennsylvania State University, University Park, PA 16802

ABSTRACT

Silicon nanowire (SiNW) field effect transistors (FETs) are of interest for use in future nanoscale electronic devices and as a tool to investigate carrier transport in nanomaterials. In the current vapor-liquid-solid (VLS) method of producing SiNWs, physical dimensions of the grown SiNWs vary (based of the size of the starting catalyst, growing time lengths, oxidation time, etc.), and it is essential to understand the relationship between the variations in physical dimensions and electrical properties of SiNW FET devices. Using a Field Emission Scanning Electron Microscope (FE-SEM), the physical dimensions (notably the diameter and oxide thickness) of 8 SiNW FETs were determined. This data was correlated to electrical measurements made on the SiNW devices in order to effectively interpret measurement results. Even with similar device diameters, normalized on-state currents were found to vary, with a mean normalized value of 3.65 μA/μm and a standard deviation of 1.19 μA/μm. Despite this variation, the devices exhibited enough reproducibility to be of interest in the accurate extraction of device parameters, such as field-effect mobility.

---

[*] Undergraduate Student
[†] Graduate Mentor
[‡] Faculty Mentor

Annual Research Journal, Vol. IV
Electrical Engineering Research Experience for Undergraduates

ISBN 0-913260-06-1 (http://www.ee.psu.edu/reu/)

INTRODUCTION

Silicon Nanowires (SiNWs) are of interest for use as building blocks for future nanoelectronic devices due to their small dimensions, improved electrical properties, and ability to be grown from the ground up ("bottom-up")[1,2]. SiNWs can be grown using a vapor-liquid-solid (VLS) self-assembly technique to function as field effect transistors (FETs), and there is potential to create complimentary inverter-like devices using SiNWs[2]. Typical diameters for the examined SiNWs produced via the group's VLS method were between 50 and 100 nm, though some have achieved devices as small as 1.3 nm[3].

To grow the SiNWs, a ~1 nm layer of gold (Au) was sputtered on a silicon dioxide (SiO_2) coated wafer. When annealed at a high enough temperature (usually 450°C to 500°C)[4], the Au forms small droplets on the surface. The silane gas (SiH_4) decomposes on the Au catalyst surface, forming an Au-Si liquid alloy. Once the Au-Si liquid becomes supersaturated with Si, a Si crystal precipitates from the melt, and the SiNW begins to grow outward with the Au-Si liquid on the one end continuing to feed the NW growth. The SiNWs grown by this technique are typically uniform in diameter, which is defined by the initial size of the Au droplet[5].

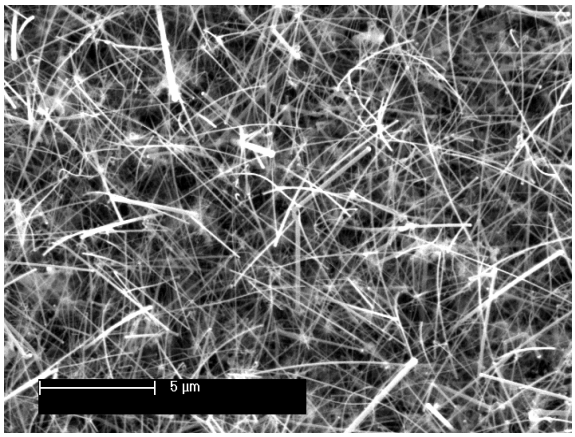

Fig. 1 -- SiNWs Grown Using VLS Growth

In addition to the SiH_4 gas, dopants such as phosphine[6] (PH_3) or tri-methyl boron[7] (TMB) ($B(CH_3)_3$) can be added to introduce donor or acceptor atoms (respectively) to the SiNWs. By adding these doping atoms at different times throughout the growth process, it is possible to create both n-type and p-type sections axially on the same NW. To fabricate n-channel FETs, as were utilized in our experiments, a SiNW is grown with n^+-p^--n^+ doping. The Au tip is then etched off to avoid the diffusion of Au into the n^+ region which might alter electrical properties. A diluted buffered-oxide etchant (BOE) is then used to remove any native oxide that may have developed during the growth process, and standard cleaning (SC1 and SC2) procedures clear the SiNWs of organic or metal

Annual Research Journal, Vol. IV
Electrical Engineering Research Experience for Undergraduates

ISBN 0-913260-06-1 (http://www.ee.psu.edu/reu/)

contaminants respectively. The SiNWs are then oxidized in an O_2 gas for 4 hours at 700°C to create a silicon dioxide (SiO_2) coating, which acts as the dielectric for the FET. After the oxidation, a ~8 nm oxide layer is present on the surface of the NWs.

The vapor-liquid-solid (VLS) self-assembly technique used to grow the SiNWs produces SiNWs of varying diameters[8], which is a concern when determining electrical characteristics of the SiNWs. The source-drain current in a FET is proportional to channel width, as shown in Eq. 1. By dividing each side by the channel width, a normalized current with respect to channel width can be obtained. Ignoring effects due to C_{ox}, it is possible to mathematically obtain reproducible results to aid in understanding the intrinsic variability that can occur experimentally.

$$I_D = \frac{W\mu_n C_{ox}}{2L}\left[2\left(V_{GS} - V_T\right)V_{DS} - V_{DS}2\right]$$

where $W = \pi d$

Eq. 1 -- MOSFET Source Drain Current

EXPERIMENTAL

After the SiNWs are fully grown to the desired length and prepared, they are detached from the SiO_2 wafer ultrasonically and placed into an ethanol solution. Using an electrofluidic alignment procedure[9], the SiNW ethanol solution is dropped onto a fabricated Si test structure that contains numerous electrical contact pairs. When an AC voltage is applied between the electrodes, an electric field occurs between them, attracting the SiNWs to align along the field. In the case where a SiNW becomes aligned between the contacts, the potential across the contacts becomes negligible, and typically no additional SiNWs will align in that location. Fig. 1 contains an SEM image of a NW aligned using the electrofluidic procedure.

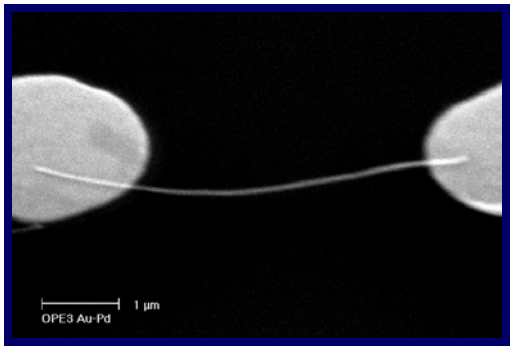

Fig. 1 -- Electrofluidic Alignment

Annual Research Journal, Vol. IV
Electrical Engineering Research Experience for Undergraduates

ISBN 0-913260-06-1 (http://www.ee.psu.edu/reu/)

After the alignment, the oxide is removed from the source and drain leads by utilizing a resist and a BOE solution. Using the resist, Ti and Au are applied to ensure a connection between the electrodes and the SiNW FET source and drain. Using electron beam (E-beam) lithography, a gate contact is constructed between the source and drain electrodes, connecting the test bed to the FET gate. This final NW structure is used for electrical and physical measurements.

I-V Measurements

To measure the I-V characteristics of the SiNWs, we placed probes on our test setup and used a LabView setup to controllably vary input voltages. For each successful NW alignment, a constant V_{DS} was established at 1.0 V, and the gate voltage V_{GS} was swept from -3 V to +3 V, and back to -3 V. Typical I_{DS}-V_{GS} curves are shown in Fig. 2a (linear scale) and Fig. 2b (log scale). From these measurements, the threshold voltage (V_T) can be extracted from Fig. 3a by linearly fitting the data where the device alternates from off-state to on-state, and finding where this linear fit crosses the X-axis. On-state currents are found by determining the current at a set point past the threshold voltage, known as the gate overdrive voltage. For these experiments, we used a constant overdrive voltage (V_{GS}-V_T) of 1.5 V.

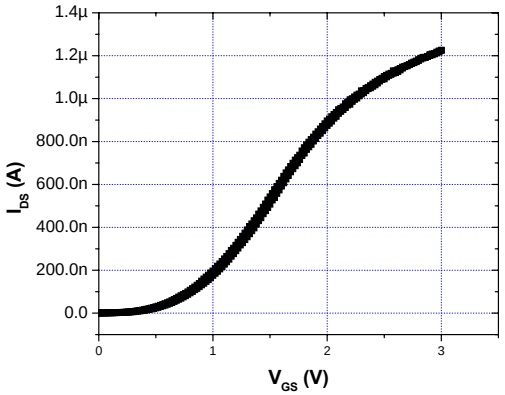

Fig. 2a.Typical I_{DS}-V_{GS} Curve (Linear)

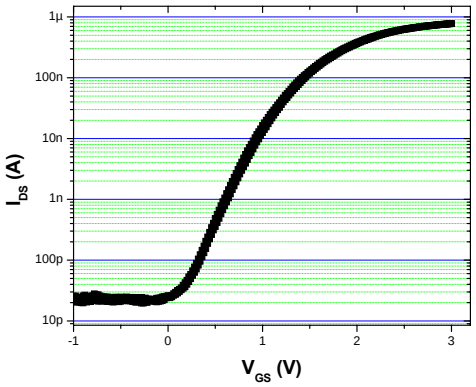

Fig. 2b. Typical I_{DS}-V_{GS} Curve (Log)

The high on-off ratio, as observed in Fig. 2b, makes SiNWs particularly attractive for nanoscale applications for the potential in developing low power devices. Another important characteristic of the FET log scale chart is the rate at which the devices changes from off-state to on-state, called the subthreshold slope, often measured in mV per decade. The theoretical lower limit for the subthreshold slope for silicon is approximately 60 mV per decade.

Physical Dimension Measurements

To measure the SiNW diameter and oxide thickness, the devices were observed under a Jeol 6700F field-emission scanning electron microscope (FE-SEM),

Annual Research Journal, Vol. IV
Electrical Engineering Research Experience for Undergraduates

ISBN 0-913260-06-1 (http://www.ee.psu.edu/reu/)

shown in Fig. 3. A standard SEM could not be used for the process. During the preparatory stages of an SEM session, the sample is sputter coated with Au to make surfaces conductive. This coat adds to the diameter of the NW and is thus unacceptable. The FE-SEM is able to view the sample without changing the physical dimensions of the specimen in any way.

Fig. 3 -- JEOL 6700 FE-SEM

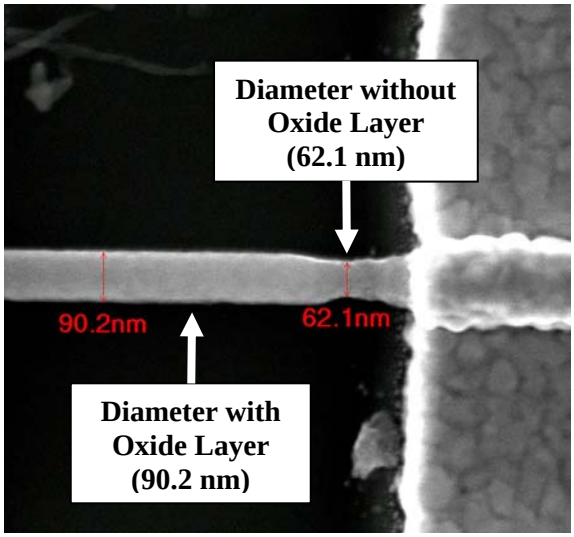

Fig. 4 -- Sample Diameter Measurement

Through the included JEOL software, accurate distances (diameters, etc.) can be determined once the NW is in focus. The diameter must be measured before the oxide layer begins (between the source or drain and the gate) to verify that the oxide thickness is not included in the diameter measurement. The oxide thickness is then determined by a simple calculation involving the difference between the diameter with the oxide and without, and dividing by two. Fig. 4 shows a typical FE-SEM image used to determine diameter and oxide thickness.

The JEOL 6700F also aids in determining the resistivity of a uniformly doped SiNW. A four-point test structure is shown below in Fig. 5. In such a setup, a known amount of current is passed between the outermost contacts, and a voltage drop is measured across the two inner contact points. From these values, resistance and resistivity are calculated, as shown in Fig. 5b. These resistivity values are crucial in determining the precise doping of the NWs for use in FETs. Fig. 6 shows the relationship between the dopant gas ratio and resistivity levels used in the creation of $n^+p^-n^+$ SiNW FETs.

Annual Research Journal, Vol. IV
Electrical Engineering Research Experience for Undergraduates

ISBN 0-913260-06-1 (http://www.ee.psu.edu/reu/)

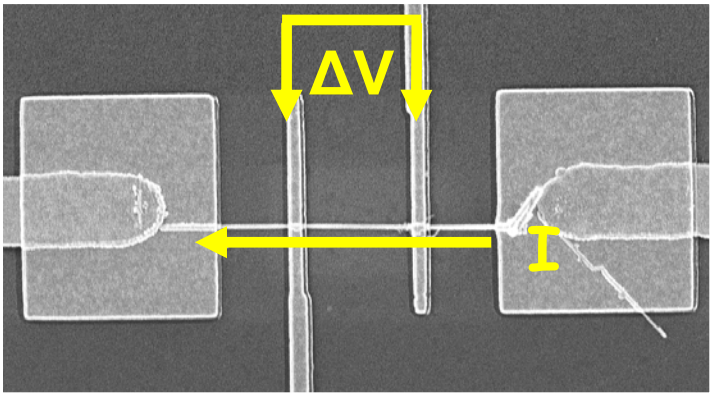

Fig. 5a. Four Point Test Structure

$$\rho = R\left(\frac{L}{A}\right)$$

Fig. 5b. Resistivity

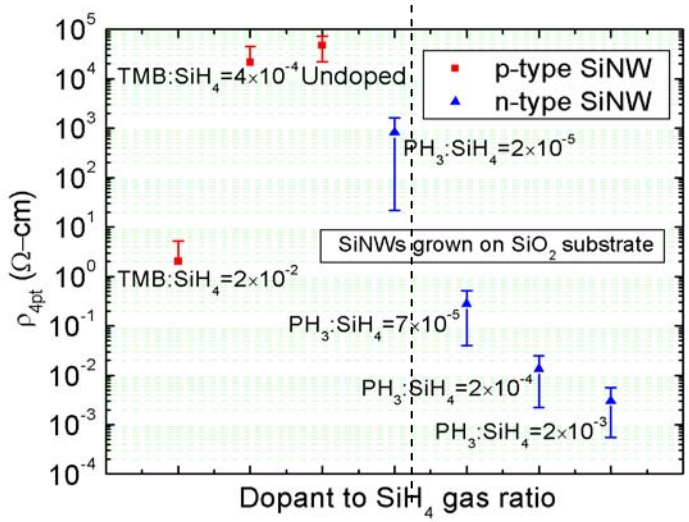

Fig. 6 -- Resistivity vs. Doping Concentrations

RESULTS AND DISCUSSION

Physical Dimension Measurement Results

The 8 SiNWs observed had diameters ranging between 66 and 83 nm and oxide thickness measurements between 8.0 and 13 nm. Table 1 lists the NWs and their equivalent channel width used in I_D calculations.

Because of the circular properties of the oxide, the channel width in conventional MOSFETs is related to the diameter of the SiNW by a factor of pi. A cross sectional view of the SiNWs indicates that the gate from the electron-beam lithography does not fully surround the oxide, so our model must be modified. From the cross sectional view in Fig. 7, approximately 60 degrees of the NW is not covered, leaving 83% of the SiNW with the electric field required to deplete

Annual Research Journal, Vol. IV
Electrical Engineering Research Experience for Undergraduates

ISBN 0-913260-06-1 (http://www.ee.psu.edu/reu/)

the NW. The adjusted channel width column in Table 1 compensates for the lack of a fully surrounded gate.

Table 1

SiNW Diameter (nm)	Channel Width (nm)	Adjusted Width (nm)
66	207.34	172.79
67	210.49	175.41
71	223.05	185.88
75	235.62	196.35
77	241.90	201.59
78	245.04	204.20
79	248.19	206.82
81	254.47	212.06
83	260.75	217.29

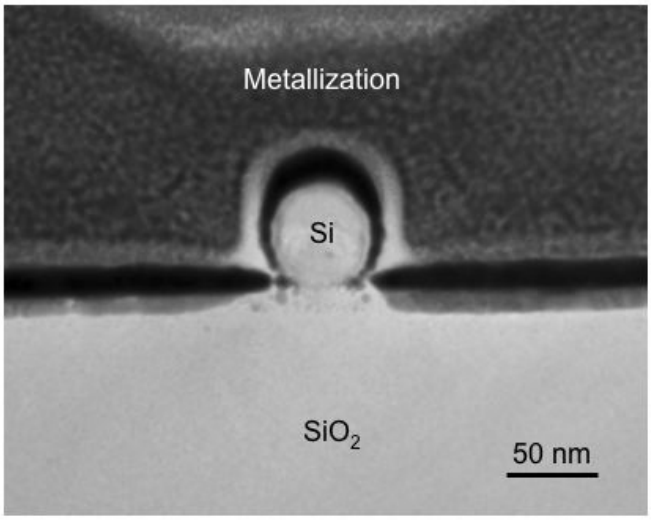

Fig. 7 -- Cross Sectional view of Measured SiNWs

While determining the diameter of the NWs with the FE-SEM, alignment errors were sometimes observed. These misaligned NWs were electrically tested prior to FE-SEM viewing, where they only received a brief viewing via an optical microscope, where it is difficult to tell if there is a problem. In Fig. 8a is a case where multiple wires were aligned on the same electrodes. Despite the ordinary appearing electrical curves (Fig. 8b), the results must be discarded in our efforts.

Annual Research Journal, Vol. IV
Electrical Engineering Research Experience for Undergraduates

ISBN 0-913260-06-1 (http://www.ee.psu.edu/reu/)

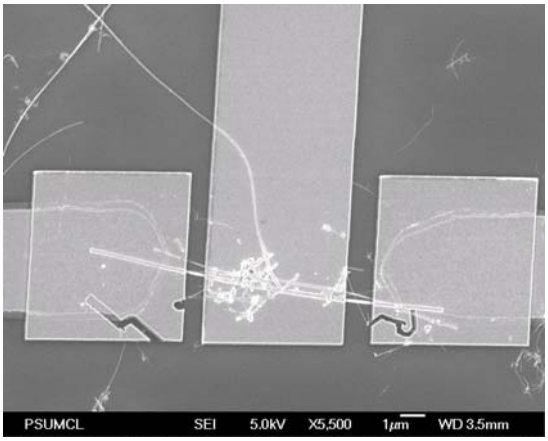

Fig. 8a -- 2 SiNWs aligned together

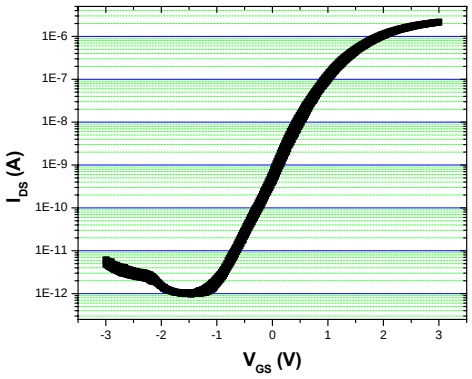

Fig. 8b -- 2 SiNWs aligned together

I-V Measurement Results

Each of the NWs were first analyzed to determine their respective threshold voltage (V_T). Fig. 9 shows an I-V relationship with the threshold voltage being determined in Fig. 9a. Our threshold voltages varied from 0.55 V to 1.37 V, with potential negative correlations between device diameters as shown in Fig 10.

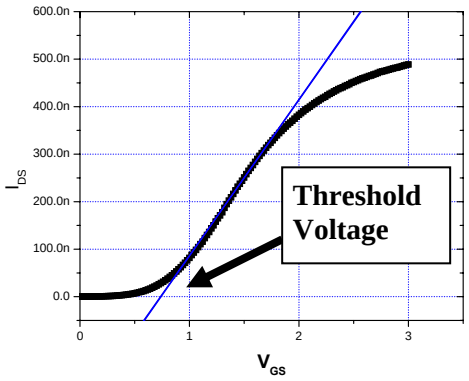

Fig. 9a -- V_T Extraction

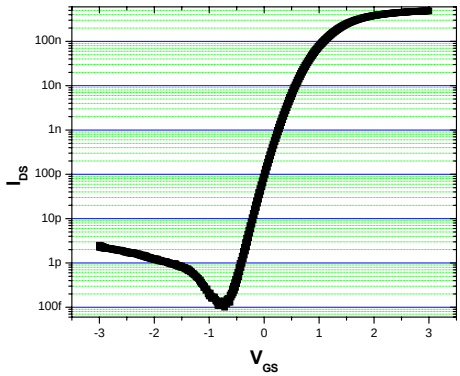

Fig. 9b -- On-Off Ratio

Annual Research Journal, Vol. IV
Electrical Engineering Research Experience for Undergraduates

ISBN 0-913260-06-1 (http://www.ee.psu.edu/reu/)

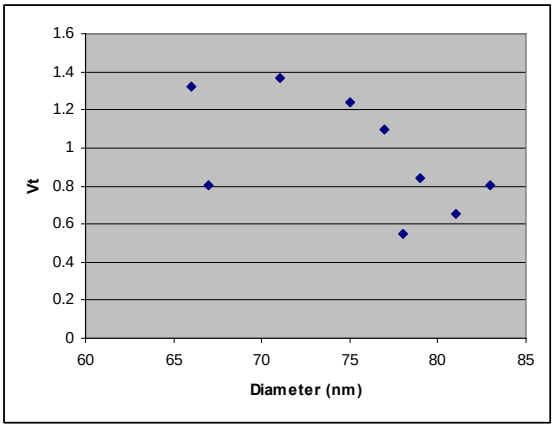

Fig. 10 -- Threshold Voltage vs. Diameter

The on-state current was determined by finding the current at the point where a constant gate overdrive voltage of 1.5 V was added to the threshold voltage. Our on-state currents varied from 0.26 μA to 1.0 μA, with a visible proportional relationship to device diameter. In Fig. 10a, after adding the V_T of approximately 0.6 V, you can find the on-state current in Fig. 10b by adding a constant 1.5 V overdrive voltage. In this case, the on-state current is over two orders of magnitude larger than at the threshold voltage. Our SiNW devices had typical sub-threshold slopes of ~250-300 mV per decade in the transition region between the off-state and on-state.

Diameter vs. On-state Current Results

Ideally, given two wires of equal diameter and other physical parameters, the wires should exhibit identical electrical characteristics and perform similarly. In order to show reproducibility, the diameter factor of the on-state current (adjusted channel width) was divided away. Eq. 2 shows an equation for source-drain current normalized for device diameter based on the adjusted channel width and neglecting effect due to C_{ox}.

$$I_{DS,normalized} = \frac{\mu_n C_{ox}}{2L}\left[2\left(V_{GS} - V_T\right)V_{DS} - {V_{DS}}^2\right]$$

Eq. 2 -- Normalized Current for Diameter

Before the channel width is taken out, we expect to see slight proportionality between device diameter and on-state current. Plotting the diameter against the on-state current of the 8 NWs provides indication that this is the case, as shown in Fig. 11.

Annual Research Journal, Vol. IV
Electrical Engineering Research Experience for Undergraduates

ISBN 0-913260-06-1 (http://www.ee.psu.edu/reu/)

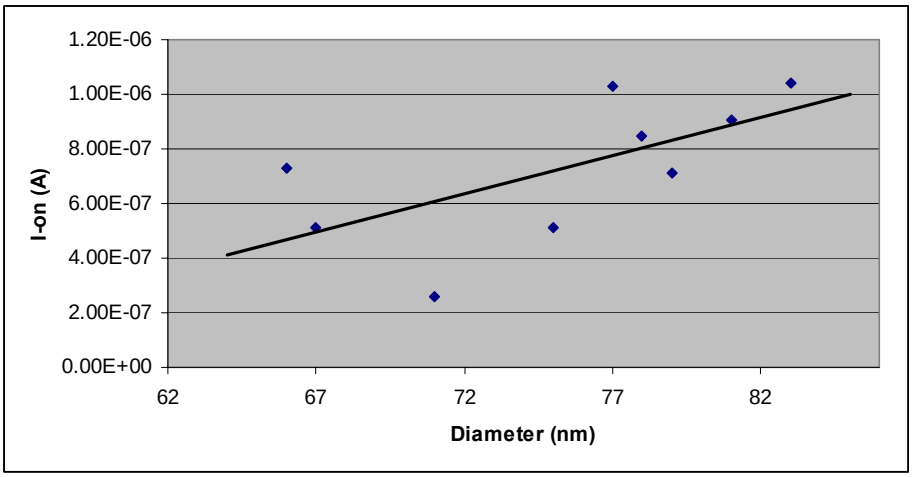

Fig. 11 -- Diameter vs. Current

To normalize the on-state currents with respect to the device diameter, the on-state currents were divided by their respective adjusted channel width. The corresponding on-state currents are listed in Table 2 and shown in Fig. 12. There is a mean normalized current of 3.65 μA/μm, and there exists variability from this value, despite the similarities in device diameters. The values vary by a standard deviation of 1.19 μA/μm. Accurate device parameters, such as field-effect mobility, can be determined if there is minimal device variation. More device data is needed to improve understanding of the variability of the NW on-state currents, and measurements such as channel length could aid in determining the variability.

Table 2

SiNW Diameter	On-State Current	Adjusted Width	Normalized Current
66 nm	7.31E-07 A	172.79 nm	4.23
67	5.10E-07	175.41	2.91
71	2.56E-07	185.88	1.38
75	5.09E-07	196.35	2.59
77	1.03E-06	201.59	5.11
78	8.46E-07	204.20	4.14
79	7.11E-07	206.82	3.44
81	9.03E-07	212.06	4.26
83	1.04E-06	217.29	4.79

Annual Research Journal, Vol. IV
Electrical Engineering Research Experience for Undergraduates

ISBN 0-913260-06-1 (http://www.ee.psu.edu/reu/)

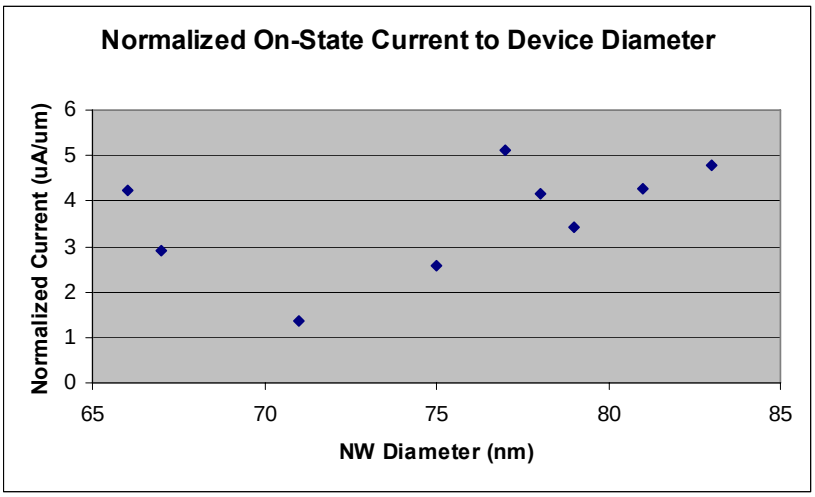

Fig. 12 -- Normalized On-State Currents

CONCLUSIONS

Silicon nanowire field-effect transistors were analyzed to compare device electrical properties (notably on-state source-drain current) to device physical dimensions. Despite the relatively close diameters of several of the NWs, the normalized on-state currents still varied and showed that other factors contribute. Future studies should be conducted with more NWs and measurements (such as channel length) to better understand the relationship. While there is a relationship between device diameter and on-state current, there are certainly other factors which affect the results. As these factors become better understood, it will be easier to reproduce experimental results and extract accurate device parameters from the NWs.

ACKNOWLEDGEMENTS

This research was funded and supported by grant number EEC-0244030 from the National Science Foundation.

ISBN 0-913260-06-1 (http://www.ee.psu.edu/reu/)

REFERENCES

[1] Y. Cul and C.M. Lieber, "Functional Nanoscale Electronic Devices Assembled Using Silicon Nanowire Building Blocks," *Scienc*e, Feb. 2001, pp. 851-853.

[2] Matthew M. Ziegle and Mircea R. Sta*n,* "CMOS/Nano Co-Design for Crossbar-Based
Molecular Electronic Systems," *IEEE Transactions on Nanotechnology Vol. 2 (4)*, Dec. 2003, pp. 217-230.

[3] Ma D. D. D., Lee C.S., Au F.C.K., Tong S.Y. and Lee S.T. "Small-Diameter Silicon Nanowire Surfaces," Science, Vol. 299 (5614), Mar. 2003, pp. 1874-1877.

[4] N. Ozaki, Y. Ohno, and S. Takeda, "Silicon nanowhiskers grown on a hydrogen-terminated silicon {111} surface," *Applied Physics Letters, Vol. 73 (25)*, Dec. 1998, pp. 3700-3702.

[5] Yi Cui, Lincoln J. Lauhon, Mark S. Gudiksen, Jianfang Wang, and Charles M. Lieber, "Diameter-controlled synthesis of single-crystal silicon nanowires," *Applied Physics Letters, Vol. 78 (15)*, April 2001, pp. 2214-2216.

[6] Y. Wang, K. Lew, T. Ho, L. Pan, S. Novak, E. Dickey, J. Redwing, and T. S. Mayer, "Use of Phosphine as an n-Type Dopant Source for Vapor-Liquid-Solid Growth of Silicon Nanowires," *Nano Letters, Vol. 5 (11)*, Oct. 2005, pp. 2139-2143.

[7] K. Lew, L. Pan, T. Bogart, S. Dilts, E. Dickey, J. Redwing, Y. Wang, M. Cabassi, T. S. Mayer, and S. Novak, "Structural and electrical properties of trimethylboron-doped silicon nanowires," *Applied Physics Letters, Vol. 85 (15)*, Oct. 2004, pp. 3101-3104.

[8] Yi Cui, Lincoln J., "Diameter-controlled synthesis of single-crystal silicon nanowires," *Applied Physics Letters Vol. 78 (15)*, Apr. 2001, pp. 2214–2216.

[9] P.A. Smith, C.D. Nordquist, T.N. Jackson, and T.S. Mayor, "Electric-field assisted assembly and alignment of metallic nanowires," *Applied Physics Letters Vol. 77 (9)*, Aug. 2000, pp. 1399-1401.

Annual Research Journal, Vol. IV
Electrical Engineering Research Experience for Undergraduates

ISBN 0-913260-06-1 (http://www.ee.psu.edu/reu/)

INVESTIGATION OF THE MORPHOLOGY AND STRUCTURE OF TIO_2 NANOTUBES FABRICATED IN HIGH DIELECTRIC CONSTANT ELECTROLYTES

Adriana Fitzgerald*, Karthik Shankar+, and Craig A. Grimes#

Department of Electrical Engineering
The Pennsylvania State University, University Park, PA 16802

*Undergraduate student of:
Department of Electrical and Computer Engineering
University of Minnesota, Twin Cities
Minneapolis, MN 55455

ABSTRACT

Highly-ordered TiO_2 nanotube-arrays have been extensively investigated due to their excellent charge transfer properties with applications including gas sensors [1], solar cells [2], and water photolysis for the solar production of hydrogen[3]. The length and aspect ratios (tube length to tube diameter) have a correlation to how well the nanotubes perform in the various applications. Growing the nanotubes by potentiostatic anodization in different electrolyte baths results in a range of length and aspect ratios [4-5]. For this experiment, the nanotubes were grown in amide-based baths with very high dielectric constants. With these anodization baths the tubes were substantially (x10) longer, and are in the process of being tested in the various applications to see if they indeed perform better in the mentioned applications.

+ Graduate Mentor
# Faculty Mentor

Annual Research Journal, Vol. IV
Electrical Engineering Research Experience for Undergraduates

ISBN 0-913260-06-1 (http://www.ee.psu.edu/reu/)

INTRODUCTION

Nanotubes, especially those made from carbon, have been the topic of research for decades. In 2001, highly-ordered titanium dioxide nanotube arrays via anodic oxidation was achieved by Grimes and co-workers [7]. This was accomplished using an HF based solution. With this method, a length of 500 nm was achieved [1]. By using KF as well, a maximum length of 4.4 μm was obtained. Research of TiO_2 nanotubes has continued because of their many applications. As a semiconductor, the nanotubes can be used for solar cells, hydrogen photolysis, and hydrogen sensing. Optimizing them for better, more efficient use is the focus of research for many labs working on alternative energy sources. Solar cells made from TiO_2 NT arrays have previously achieved conversion efficiencies of up to 2.9 percent [1].

The easiest form of optimization is varying anodization conditions. Anodization voltage, temperature, and bath chemicals/properties are easily varied. Grimes and co-workers have investigated the morphology [6], length [4], pore size [4], and wall thickness [3] changes associated with these variables. A length of 6.4 μm was achieved by varying the pH of the electrolyte bath [4].

However, as far as we know, there has been no research into the use of high dielectric constant electrolytes. Using these new baths, nanotubes have been grown with greater lengths and smaller aspect ratios. This is a major goal of titanium nanotube research. Improving the dimensions of the nanotubes may better the performance of dye-sensitized solar cells and hydrogen photolysis applications [1, 2, 3].

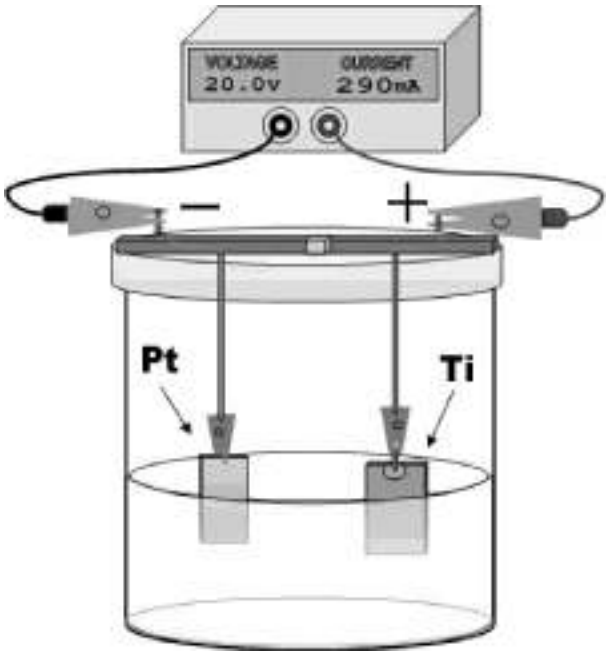

Figure 1 Anodic oxidation schematic

Annual Research Journal, Vol. IV
Electrical Engineering Research Experience for Undergraduates

ISBN 0-913260-06-1 (http://www.ee.psu.edu/reu/)

EXPERIMENTAL DESCRIPTION

Titanium dioxide nanotubes are grown using a process known as anodic oxidation or "anodization." As the name implies, a voltage is applied to a system where the titanium is the anode. The cathode is a piece of platinum foil. The titanium is then etched by the fluoride containing electrolyte solution, creating titanium dioxide nanotubes. This system, as seen in **Figure 1**, is the most common way of producing titanium nanotube-arrays.

After anodization, the platinum electrode (99% pure, Alfa-Aesar Corporation [9]) is rinsed and used again. The titanium foil (0.25 mm thick, 99.7% pure, Aldrich Corporation [8]) is rinsed and dried in preparation for annealing.

The titanium samples are annealed in an oxygen ambient tube furnace (see **Figure 2**). Before annealing, the nanotubes are amorphous. The heating process makes them crystalline, therefore making them stronger and easier to use. After annealing, SEM (scanning electron microscopy) is used to check the morphology and presence of nanotubes. Length, tube diameter, wall thickness, barrier layer thickness, and degree of clogging are observed. An indication of performance is obtained from the SEM images. The best tubes are then used in the dye-sensitized solar cells and hydrogen photolysis. The SEM images, coupled with the solar cell and photolysis results are then used to make decisions for new anodization situations and bath formulas.

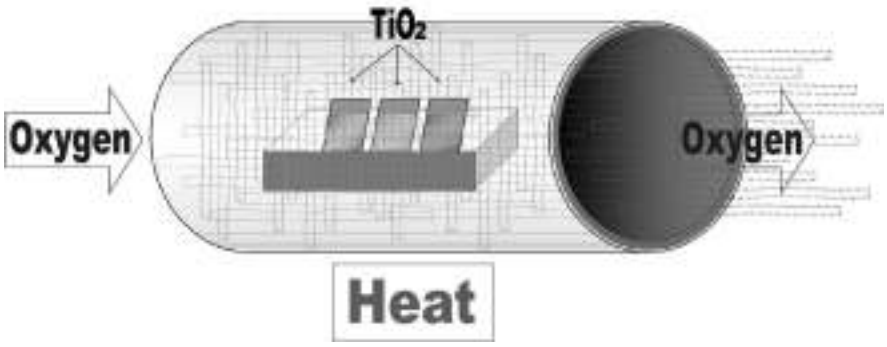

Figure 2 Oxygen annealing schematic

The chemistry of the bath, as it affects nanotube growth and composition, has been largely unstudied [13]. However, the mechanism for the formation of titania nanotubes is well known. In order for nanotubes to form via anodization, three key things must be present in the bath: An oxidizing agent for the titanium (O^{2-} or OH^-), a source of fluoride ions, and a source of H^+ ions (usually an acid or from dissolution of water) [13].

Annual Research Journal, Vol. IV
Electrical Engineering Research Experience for Undergraduates

ISBN 0-913260-06-1 (http://www.ee.psu.edu/reu/)

When the titanium is placed in the bath, an oxide layer forms. In the case of the water-containing baths used in this experiment, the oxidation agent is water. This reaction[13] is shown below.

$$2H_2O \rightarrow O_2 + 4e + 4H^+ \quad (1)$$

$$Ti + O_2 \rightarrow TiO_2 \quad (2)$$

Also, with the electric field, the titanium metal becomes ionized, making it Ti^{4+}. This dissolves in the bath.

The fluoride sources dissolve in water, creating F^- ions. Fluoride is incredibly reactive. The ions start etching the titania. This creates pits in the newly formed titanium dioxide surface. This reaction[13] is shown below.

$$TiO_2 + 6F^- + 4H^+ \rightarrow TiF_6^{2-} + 2H_2O \quad (3)$$

The oxygen gas then attacks the newly exposed titanium metal, which is again etched by the fluoride ions.

In order to get quality nanotubes, there must be a careful balance between these chemical reactions. Optimizing the voltage, time, amount of fluoride, and amount of water is essential. In this experiment, there is also another variable, the main chemical in which the nanotubes are grown.

RESULTS AND DISCUSSION

Overview

In the past, the major components of titania anodization baths were HF and water [1, 2, 3, 6, 7, 10, 13]. At room temperature, water has a dielectric constant of about 78.04 [15]. In baths chosen for a specifically high dielectric constant, we used Formamide (FA), N-Methylformamide (NMF). These have dielectric constants (at room temperature) of 109.52 and 182.61, respectively [16, 17]. These amides, along with water and ammonium fluoride, were used as the anodization baths in this experiment. The bath contents are in **Table I**.

Table I. Anodization Bath Details

Bath Name	NH_4F (g)	F^- (mol)	H20 (ml)	FA (ml)	NMF (ml)
N0:	.4	.01080	5	--	95
N1:	.56	.01512	5	--	95
N2:	.4	.01080	2.5	--	95
K1:	.56	.01512	5	100	--
K2:	.84	.02268	5	100	--
K3:	.4	.0180	2.5	95	--
K4:	1.04	.02808	5	100	--
K5:	1.5	.04050	5	100	--

Annual Research Journal, Vol. IV
Electrical Engineering Research Experience for Undergraduates

ISBN 0-913260-06-1 (http://www.ee.psu.edu/reu/)

The baths are very similar. Concentrations of F^- and amount of water are varied. As the names imply, the baths go in chronological order. For the K series, the concentration of F^- ions is increased with each bath. For the N series, the concentration of F^- and the amount of water is varied.

Using the aforementioned baths, titania nanotubes were grown under different voltage and time restrictions. Several samples were also monitored continuously, producing a current versus time graph. In brief, the results are presented in **Table II**. From the images in **Figure 3**, you can see the clearly defined tubes grown in these baths.

Table II. Anodization Results

Sample No.	Bath	Voltage (volts)	Time (hours)	Length (μm)	Diameter (nm)	Clogged	Picture
1	N0	20	48	12.9	109	no	--
2	N1	40	70	22	166	no	--
3	N2	20	50.5	16.6	85	yes	3a
4	K1	20	48	10.5	94	xx	3d
5	K1	35	75	18	203	no	--
6	K1	35	88	29.2	208	semi	3c
7	K2	20	60	11.8	xx	no	--
8	K3	35	28	17.4	173	no	3b
9	K4	20	24	19.6	90	xx	--
10	K4	20	30	19	87	xx	--
11	K4	35	30	36	159	xx	--
12	K5	35	26	21.1	130	xx	--

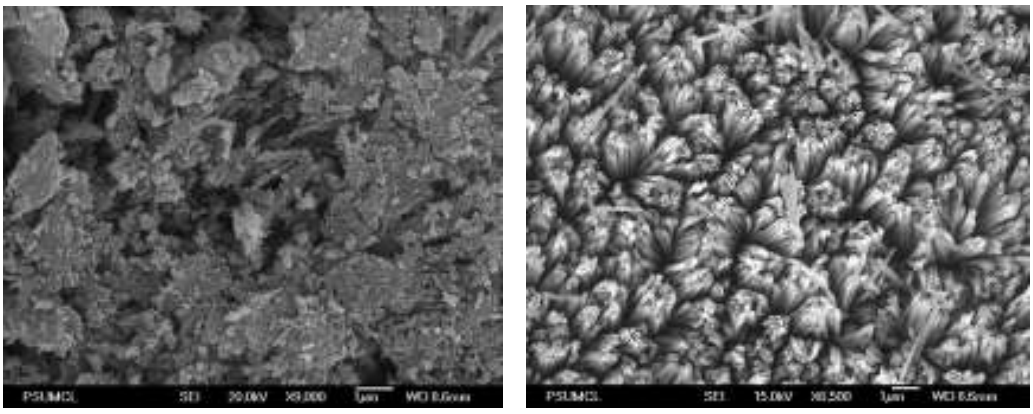

Figure 3.a (left) Picture of sample 3; example of clogged nanotubes.
Figure 3.b (right) Picture of sample 8; example of clean top view of nanotubes.

Annual Research Journal, Vol. IV
Electrical Engineering Research Experience for Undergraduates

ISBN 0-913260-06-1 (http://www.ee.psu.edu/reu/)

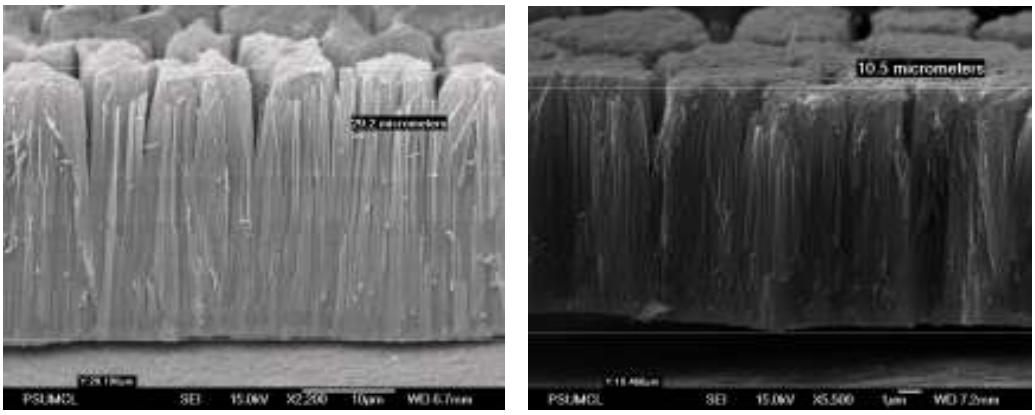

Figure 3.c (left) Picture of sample 6; example of very long nanotubes.
Figure 3.d (right) Picture of sample 4; example of shorter nanotubes.

Trends

There are several noticeable trends in the high dielectric constant baths. These involve fluoride concentration, water content, voltage, time, and the current density graphs.

Fluoride Concentration

As the concentration of F^- ions increases, the amount of time to grow equivalent nanotubes decreases. This indicates that with more fluoride ions, more etching occurs (see equation 3). Along with this comes the trend of longer nanotubes for comparable anodization situations. This is apparent when comparing the K baths.

Water Content

If the amount of water is raised in a bath, the current is lower. This, in essence, means the nanotubes will be shorter for other equivalent conditions. This is apparent when comparing N0 and N2. But, with less water there is more risk for clogged tubes

Voltage

Also, as voltage increases, the diameter of the tubes increases. This is consistent with previous research [18]. But, at very high voltages, the anodization system becomes unstable. Anodization is impossible above approximately 40 volts. With smaller voltages, there is a larger surface area. This is better for all applications. However, at the smaller voltages, the tubes aren't long enough. For each bath, there is an "ideal" voltage. Running an anodization at 20 volts seems to be ideal for most baths

Annual Research Journal, Vol. IV
Electrical Engineering Research Experience for Undergraduates

ISBN 0-913260-06-1 (http://www.ee.psu.edu/reu/)

Time

Time has an influence on the length of the nanotubes. There is a time threshold. After this time, the nanotubes actually become shorter and quality is influenced. Before this time, the nanotubes are only shorter. This is apparent when comparing samples 5 and 6 or samples 9 and 10 (see **Table II**).

Current Density Graphs

The current density versus time graphs (see **Figure 4**), show a distinct shape. There are also discrete differences in the N and K baths. The K baths reach their peak current sooner. Also, the shape is slightly different. These may be due to the unique properties of the high dielectric constant solvent.

With a higher concentration of F^-, the current density is much higher. This is coupled with the trend that higher concentrations produce longer nanotubes. Therefore, you can judge which tubes should be the longest from this graph. N2 should have tubes longer than N0 and K4 should have tubes longer than K2. From **Table II**, we can see that this is indeed the case.

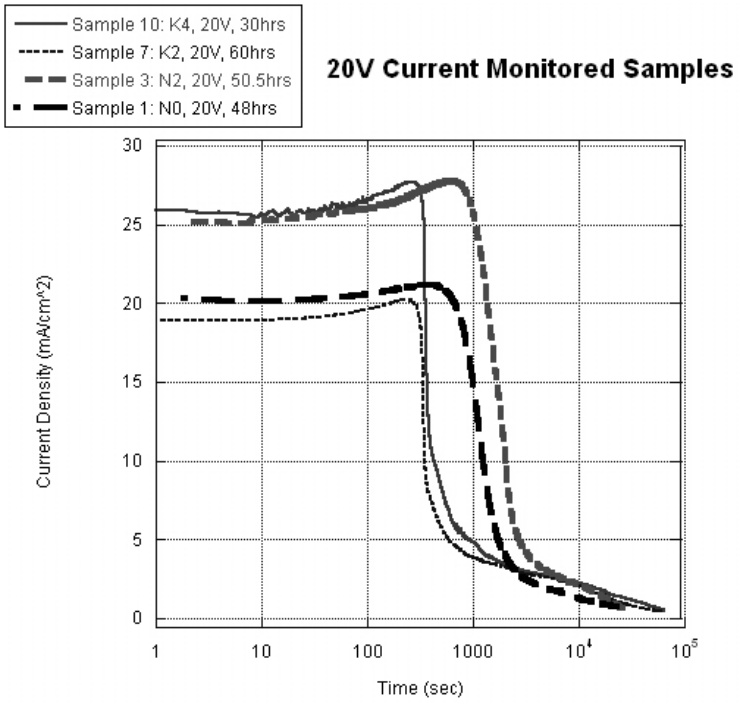

Figure 4 Current Density versus Time graph

CONCLUSION

Titania nanotubes were successfully grown in high dielectric constant anodization baths. These tubes have a greater length than baths grown in HF/water- based solutions. They also have a high aspect ratio, of typically

Annual Research Journal, Vol. IV
Electrical Engineering Research Experience for Undergraduates

ISBN 0-913260-06-1 (http://www.ee.psu.edu/reu/)

something greater than 500. This is important because it increases surface area, and allows for better performance in dye-sensitized solar cells and hydrogen photolysis.

Several trends were noticed in high dielectric constant anodization. The concentration of F^-, critical to the growth of nanotubes, changes the time required for anodization as well as the possible length of the nanotubes. The anodization time has a time threshold, after which deleterious changes in length and quality of tubes are observed. No matter the time frame, anodization becomes unstable at a voltage over approximately 40 volts. Also, the amount of water in the bath affects clogging and time required for anodization.

Whether or not the longer tubes show promise in improving titania nanotube applications is yet to be shown. However, the ability to grow the nanotubes to a greater length is a feat in itself. The longest tubes grown in the new anodization baths is 36 microns, with an aspect ratio of 3.5. In order to increase nanotube length and decrease aspect ratio, a different fluoride-containing solute may be needed. More research is being done on this topic.

ACKNOWLEDGEMENT

This material is based upon work supported by the National Science Foundation under Grant No. EEC-0244030.

REFERENCES

1. O. K. Varghese, D. Gong, M. Paulose, K. G. Ong, E. C. Dickey, C. A. Grimes, "Extreme Changes in the Electrical Resistance of Titania Nanotubes with Hydrogen Exposure," *Adv. Mater.* **15** (7-8) 624- 627 (2003).
2. G. Mor, K. Shankar, M. Paulose, O. Varghese, C. Grimes "Use of Highly-Ordered TiO_2 Nanotube Arrays in Dye-Sensitized Solar Cells," *Nano Letters*. **6** (2) 215-218 (2006)
3. G. Mor, K. Shankar, M. Paulose, O. Varghese, C. Grimes, "Enhanced Photocleavage Of Water Using Titania Nanotube Arrays," *Nano Letters* **5** (1) 191-195 (2005)
4. Q. Cai, M. Paulose, O. Varghese, C. Grimes, "The Effect Of Electrolyte Composition On The Fabrication Of Self-Organized Titanium Oxide Nanotube Arrays By Anodic Oxidation," *J. Materials Res.* **20** (1) 230-236 (2005)
5. J. M. Macak, L.V.T., H. Tsuchiya, K. Sirotna, J. Macak, P. Schmuki, "Influence of different fluoride containing electrolytes on the formation of self-organized titania nanotubes by Ti anodization," *Journal of Electroceramics*, **16** (1) 29-34 (2006)
6. O. K. Varghese, D. W. Gong, M. Paulose, C. A. Grimes, and E. C. Dickey, "Crystallization and high-temperature structural stability of

Annual Research Journal, Vol. IV
Electrical Engineering Research Experience for Undergraduates

ISBN 0-913260-06-1 (http://www.ee.psu.edu/reu/)

titanium oxide nanotube arrays," *J. Materials Res.* **18** (1) 230-236 (2003).
7. D. Gong, C. A. Grimes, O. K. Varghese, Z. Chen, W. Hu, E. C. Dickey, "Titanium oxide nanotube arrays prepared by anodic oxidation," *J. Materials Res.*, **16** (12) 3331-3334 (2001)
8. Aldrich Corporation: http://www.aldrich.com
9. Alfa-Aesar Corporation: http://www.alfa.com
10. V. Zwilling, M. Aucouturier, E. Darque-Ceretti, "Anodic oxidation of titanium and TA6V alloy in chromic media. An electrochemical approach," *Electrochim. Acta* **45** (6) 921-929 (1999)
11. J. M. Macak, H. Tsuchiya, L. Taveira, S. Aldabergerova, P. Schmuki, "Smooth anodic TiO2 nanotubes," *Angewandte Chemie-International Edition*, **44** (45) 7463-7465 (2005)
12. J. M. Macak, H. Tsuchiya, P. Schmuki, "High-aspect-ratio TiO2 nanotubes by anodization of titanium," *Angewandte Chemie-International Edition*, **44** (14) 2100-2102 (2005)
13. G. K. Mor, O. K. Varghese, M. Paulose, K. Shankar, C. A. Grimes, "A review on highly ordered, vertically oriented TiO2 nanotube arrays: Fabrication, material properties, and solar energy applications," *Solar Energy Materials and Solar Cells*, **90** (14) 2011-2075 (2006)
14. M. Paulose, G. K. Mor, O. K. Varghese, K. Shankar, C. A. Grimes, "Visible light photoelectrochemical and water-photoelectrolysis properties of titania nanotube arrays," *Journal of Photochemistry and Photobiology A: Chemistry*, **178** (1) 8-15 (2006)
15. J. Barthel, R. Neueder, Water and Deuterium Oxide, p11, *Electrolyte Data Collection Part 2: Dielectric Properties of Water and Aqueous Electrolyte Solutions,* DECHEMA, Frankfurt am Main, Germany, 1995
16. J. Barthel, R. Neueder, Formamide, p 8, *Electrolyte Data Collection Part 1g*: *Conductivities, Transference Numbers, and Limiting Ionic Conductivities of Protophilic H-Bond Donor and Aprotic Solvents I: Amides,* DECHEMA, Frankfurt am Main Germany, 2001
17. J. Barthel, R. Neueder, N-Methylformamide, p 84, *Electrolyte Data Collection Part 1g*: *Conductivities, Transference Numbers, and Limiting Ionic Conductivities of Protophilic H-Bond Donor and Aprotic Solvents I: Amides,* DECHEMA, Frankfurt am Main Germany, 2001
18. G. K. Mor, O. K. Varghese, M. Paulose, N. Mukherjee, C. A. Grimes, "Fabrication of tapered, conical-shaped titania nanotubes," *J. Materials Res.*, **18** (11) 2588-2593 (2003)

ISBN 0-913260-06-1 (http://www.ee.psu.edu/reu/)

STUDY OF ADSORPTION ISOTHERMS USING MICROMACHINED QUARTZ CRYSTAL GRAVIMETRIC SENSORS

Jay A. Mathews*, Abhijat Goyal[+], Ping Kao[+], and Srinivas A. Tadigadapa[#]

Department of Electrical Engineering
Department of Chemistry, and
Department of Physics
The Pennsylvania State University, University Park, PA 16802

*Undergraduate student of
Department of Physics
Colorado State University
Fort Collins, CO 80525

ABSTRACT

Using microfabrication techniques, it is possible to realize gravimetric sensor platforms which can resolve mass down to a few femtograms and are robust enough to operate even in aqueous ambient. In this study, an ultra-sensitive quartz crystal microbalance (QCM) was used to study the self-assembly of thiol-based alkyl molecules on the gold electrode of the QCM and subsequent specific adsorption of protein molecules on top of the grown Self Assembled Monolayers (SAMs). Specifically, isotherms for formation of monolayers of 1-hexadecanethiol were generated, as well as adsorption isotherms for proteins such as human serum albumin (HAS) on the grown monolayers. Such fundamental studies using gravimetric sensor platforms with unprecedented sensitivity are expected to result in better understanding of the biological processes in human body, better control over the self-assembly process, and possibly in realizing a System on a Chip (SOC) entirely through the self-assembly process.

[+] Graduate mentor

[#] Faculty mentor

Annual Research Journal, Vol. IV
Electrical Engineering Research Experience for Undergraduates

ISBN 0-913260-06-1 (http://www.ee.psu.edu/reu/)

INTRODUCTION

Motivation

Accurate and precise measurement of mass has been a human endeavor for centuries. In the early days, determination of the amount of matter present in a given sample of material was of importance for commerce. They used gravity to compare the mass of one object to that of another object whose mass was known beforehand. However, such measurements lacked accuracy and precision. Subsequently, people started using more sophisticated techniques, such as spring scales based on Hooke's law, capacitive measurement of mass, and measurement of mass of fundamental particles, for example, by using cyclotrons. However, while some techniques suffered from lack of accuracy and precision (spring balance and capacitive measurements), others suffered from lack of portability and high cost (for example, the cyclotron). What is required is a mass sensor which can measure mass accurately and precisely, and is portable and easy to operate. Mass sensors based on resonators satisfy all of these requirements. The most popular resonator-based mass sensors employed vibrating cantilevers, which greatly improved on the sensitivity and precision of the measurement. However, while they work great in controlled conditions in the laboratory, they are not robust and rugged enough for real world applications. Additionally, their sensitivity (ability to measure small amount of mass) is drastically reduced when operating in aqueous ambient. In this paper, we introduce a gravimetric based mass sensor (termed Quartz Crystal Microbalance), based on a resonating quartz crystal, whose sensitivity has been increased by six orders of magnitude from a few nanograms to a few femtograms using aggressive micromachining techniques. Additionally, we present preliminary results on the use of the robust and rugged device to study adsorption of thiol based alkyl molecules on the gold electrode of the QCM. Additionally, specific adsorption of protein molecules on the self assembled monolayers (SAMs) of thiol-based molecules is also presented.

The advent of quartz crystal resonators can be traced back to 1880, when Pierre and Jacques Curie performed a simple, yet historic, experiment on a small piece of AT-cut quartz crystal. They connected electrodes to two ends of the crystal, and then exerted a pressure on the quartz, causing a deformation. When they did this, they discovered that this deformation produced a potential difference across the ends of the quartz. It was also shown that the converse was true. Applying a voltage across the electrodes caused the crystal to deform. This is how the piezoelectric effect was discovered. Since that time, many other materials have been found to exhibit piezoelectric properties, but quartz is the most well known and widely used. This unique property of piezoelectricity in quartz allows it to be used as a resonator. If an AC voltage is applied to the two electrodes, the quartz crystal will vibrate with the frequency of the applied voltage.

Annual Research Journal, Vol. IV
Electrical Engineering Research Experience for Undergraduates

ISBN 0-913260-06-1 (http://www.ee.psu.edu/reu/)

The theory of the quartz crystal microbalance (QCM) was developed by Sauerbrey, who showed that the quartz crystal oscillator could be used as a sensor to measure the thickness of thin films. He showed that the change in resonant frequency of the crystal is directly proportional to the change in mass[1]. Thus, he could measure the deposition of thin films by looking at the frequency change of the quartz crystal. This was the first use of a QCM. Within a few years, QCM's became commercially available and were widely used in applications dealing with thin films and, later, used in other applications such as surface science and the study of self-assembled monolayers.

Study of Self-Assembled Monolayers

The study of organic thin films has been of interest for many years, and interest in the study of self-assembly in these two-dimensional systems has greatly increased in the past 25 years. In the early 1920's, Langmuir was the first to look at molecular films at the gas-liquid interface, and his work led to the Langmuir-Blodgett (LB) system of creating monolayers. Many years later, self-assembly was introduced as a possible alternative to the LB system for synthesizing organic monolayers[2].

With the advent of nanotechnology in the 21st century, scientists and technologists have realized that in order to realize nanostructures with excellent control over their physical, chemical and electrical properties, the self-assembly process can be developed as a tool for directing controlled assembly of nanostructures. Such directed growth using self-assembly of molecules and atoms may find applications, for example, to further shrink the size of electronic components and ultimately realize System on a Chip (SOC). The directed controlled growth process using self-assembly may also find applications in biology and medicine. Directed delivery of drug and control over the processes that result in cancerous tissue growth, for example, are some of useful applications that self-assembly process promises in the coming future.

It is possible to synthesize organic monolayers by immersing an appropriate substrate into a solution of an active surfactant in an organic solvent[2]. As the substrate is put into the solution, the molecules of the surfactant arrange themselves on the surface of the substrate. This process is completely spontaneous, where the molecules arrange themselves on the substrate. The molecular assemblies that are formed are called self-assembled monolayers (SAMs).

The experiment reported in this paper focuses on alkanethiol monolayers formed on gold substrates and specific protein adsorption on these monolayers. The alkanethiols bond with the surface of the gold through a Au-S covalent, but slightly polar, bond[2]. Since the alkanethiols terminate in a methyl (CH_4) group, it is possible to adsorb larger proteins to the surface created by the alkanethiols. This process was studied in detail, for example by Liu in 2005[3].

Annual Research Journal, Vol. IV
Electrical Engineering Research Experience for Undergraduates

ISBN 0-913260-06-1 (http://www.ee.psu.edu/reu/)

Theory of the Quartz Crystal Microbalance

When an AC field is applied to the electrodes on the QCM, it resonates with the resonant frequency, f_0, given by:

$$f_0 = \frac{\sqrt{\mu_q}}{\sqrt{\rho_q}} \frac{1}{2t_q} \tag{1}$$

where μ_q is the shear modulus of the quartz crystal (2.947×10^{11} g cm^{-1} s^{-2}), ρ_q is the density of the quartz crystal (2.648 g cm^{-3}), and t_q is the thickness of the quartz crystal. The change in resonant frequency, Δf_0, is then related to the change in mass, Δm, by the Sauerbrey equation:

$$\Delta f_0 = -S\Delta m \tag{2}$$

where S, the sensitivity of the device, is defined by:

$$S = \frac{2 f_0^{\,2}}{A\sqrt{\mu_q \rho_q}} \tag{3}$$

where A is the area of the overlapping electrodes on the QCM. Since the resonant frequency in inversely proportional to the thickness, the sensitivity of the QCM can be significantly increased by minimizing the thickness of the quartz. Additionally, since the sensitivity is inversely proportional to the area of the electrodes, it can be further increased by minimizing the size of the electrodes. This is how such high sensitivity to mass deposition was achieved.

EXPERIMENTAL DESCRIPTION

Apparatus and Overview

The experimental setup consists of the micro-machined QCM connected to an Agilent impedance analyzer, which is computer-controlled via Labview. The QCM, designed and built by graduate mentor Abhijat Goyal[4], consists of a circular disk of quartz approximately 500 μm in diameter, with a thickness of 60 μm. A thin layer of gold was deposited on both faces of the quartz, and then etched so that the gold formed two circular electrodes of diameter 250 μm, centered on the top and bottom of the quartz disk, as in Figure 1. Nine of these units were put in a 3x3 array with electrical connections to the electrodes made through wire bonds on the bond pads connected to each QCM pixel, as in Figure 2. The array was then packaged in a modified dual inline package (DIP). A square well was drilled into the DIP using water jet cutting, with sides 8 mm and

Annual Research Journal, Vol. IV
Electrical Engineering Research Experience for Undergraduates

ISBN 0-913260-06-1 (http://www.ee.psu.edu/reu/)

a depth of 200 μm. The QCM array was then mounted in the hole and sealed with GE Silicone RTV to make a watertight well of approximately 20 μL, with the QCM array at the bottom so that an aqueous solution could sit on top of the array. Figure 3 shows the array in the modified DIP. On the top of the DIP, the bond pads of the individual QCM's were connected to the DIP's leads using wire bonding. The top was then covered with a piece of glass to protect the bonds. Finally, the packaged device was encased in a watertight aluminum enclosure with BNC connectors on either end. (This enclosure was not used on the first data run, but was fabricated in order to prevent evaporation after this was determined to be a problem.) This enclosure was then connected directly to the impedance analyzer. Although there are nine QCM's available on the array, only one was used for this experiment.

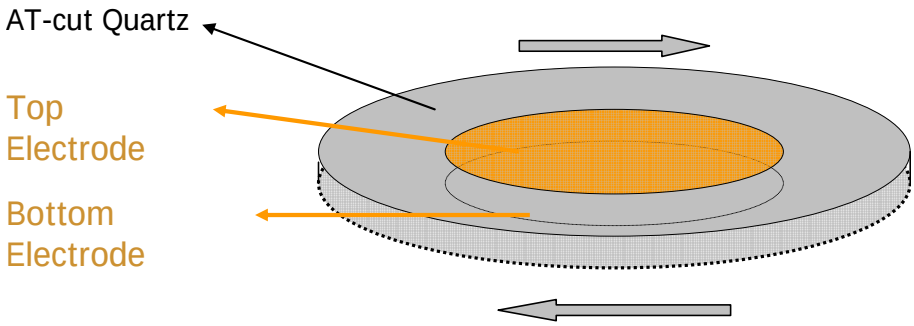

Figure 1: Picture of the quartz resonator with electrodes.

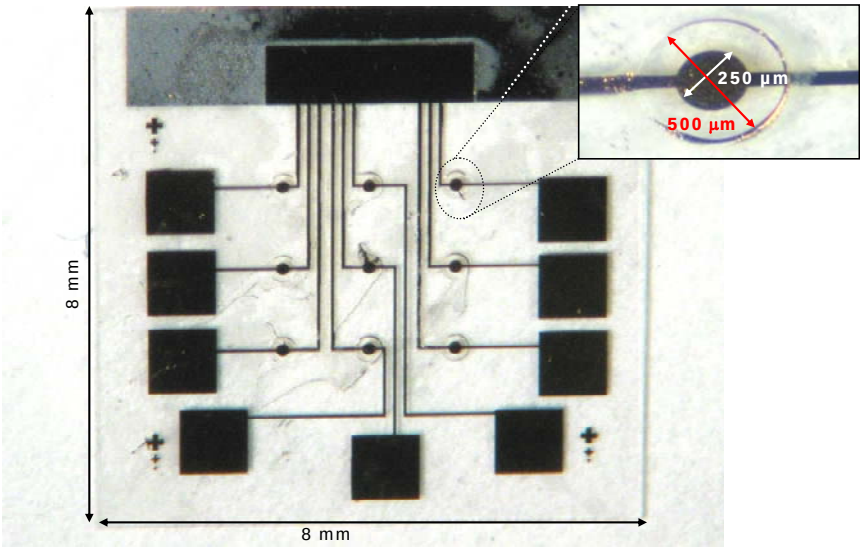

Figure 2: Picture of the 3x3 array of QCMs.

Annual Research Journal, Vol. IV
Electrical Engineering Research Experience for Undergraduates

ISBN 0-913260-06-1 (http://www.ee.psu.edu/reu/)

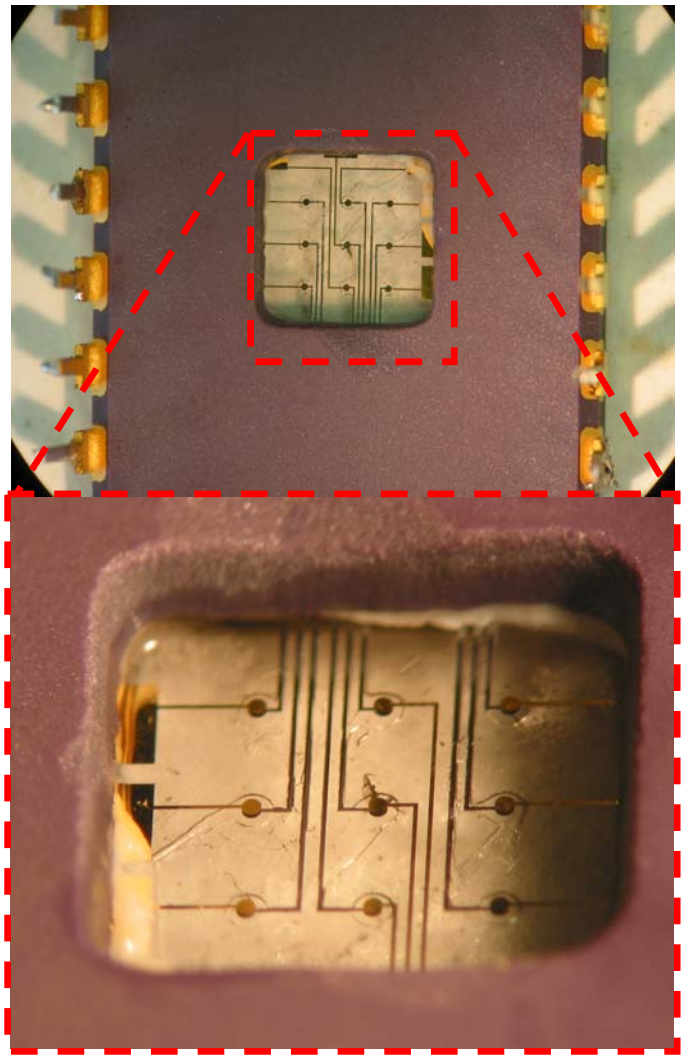

Figure 3: Picture of the QCM array in the modified DIP showing the watertight well.

Once the apparatus has been set up, the computer then controls the impedance analyzer via a GPIB connection. A Labview program was set up to automate the data acquisition process. The resonant frequency of the QCM is approximately 83 MHz, so this is used as a starting point. A 100 kHz sweep, centered at 83 MHz, is performed and the new resonant frequency is found. Next, the program centers the 100 kHz window on the new resonant frequency and performs the sweep again. This process is repeated every 27 seconds.

Preparation and Data Collection

Prior to performing the experiment, the device was cleaned by graduate mentor Ping Kao using a process involving exposure to UV and ozone[5]. In order

Annual Research Journal, Vol. IV
Electrical Engineering Research Experience for Undergraduates

ISBN 0-913260-06-1 (http://www.ee.psu.edu/reu/)

to get a baseline for the data, two preliminary data collection runs were performed. First, approximately 2 hours of data was taken with no solution on the device, with the device resonating in air. The resonant frequency of the QCM tends to drift a little higher linearly over time, and the above measurement enabled us to quantify the value of the drift. The solution used to grow a monolayer of SAM was a 1 mM solution of 1-hexadecanthiol ($CH_3(CH_2)15SH$) in ethanol, prepared prior to the experiment by Ping Kao. In the next run, a sample of pure ethanol was put on top of the device. This was done to quantify the change in resonance frequency due to mass loading and viscous damping in the presence of ethanol without the thiol molecules dissolved in it. Since the well in the device only holds about 20 μL of liquid, evaporation of the ethanol was of major concern. In order to prevent evaporation of the ethanol in the device, a layer of ethanol approximately 1 cm in depth was poutred in the bottom of the enclosure and the top was closed. Data was collected for approximately 2 hours and then the cover was removed in order to allow the ethanol to evaporate.

Once the ethanol was completely evaporated, leaving the QCM clean, the SAM's growth was started. Again, a 1 cm deep layer of ethanol was put in the bottom of the enclosure. The device was then filled with approximately 20 μL of the hexadecanethiol and ethanol mixture. Data was collected for approximately two hours.

Prior to the experiment, Ping Kao prepared 11 different protein solutions of varying concentration. Each solution consisted of human serum albumin in a phosphate buffered saline (PBS) solution. The protein concentrations ranged from 10^{-10}% to 1%. The excess SAM solution was collected from the device with special care so that the SAM would not be removed. Again, a 1 cm deep layer of liquid was put in the bottom of the enclosure. However, instead of ethanol, the PBS solution was used. Next, approximately 20 μL of the 10^{-10}% protein solution was put on top of the device. Data was then collected for approximately one hour. The excess protein solution was then wicked out from top of the device, so that the SAM, as well as the new layer of proteins, would not be removed. Then, the 10^{-9}% solution was added in the same manner. This process was repeated for all of the solutions, increasing in concentration each time.

In order to analyze the data, a Mathematica program, written by Abhijat Goyal, was used. The program looks at each 27 second sweep, fits a Gaussian curve to the peak, finds the resonant frequency and Q-factor, and then outputs the data to a file. The resulting file gives the resonant frequency and Q-factor, which can then be plotted as functions of time.

RESULTS AND DISCUSSION

During the first experiment, the device was not put in an enclosure. This led to rapid evaporation of the hexadecanethiol-ethanol solution. Thus, solution was added every 30 to 40 minutes. The data taken during this run is shown in Figure 4 as a plot of resonant frequency versus time. Note the large spikes in the data occurring when additional solution was added. The data should show an

Annual Research Journal, Vol. IV
Electrical Engineering Research Experience for Undergraduates

ISBN 0-913260-06-1 (http://www.ee.psu.edu/reu/)

exponential decay in resonant frequency as time increases. From this plot, it appears that there is a general exponential trend, but the addition of solution makes it unclear.

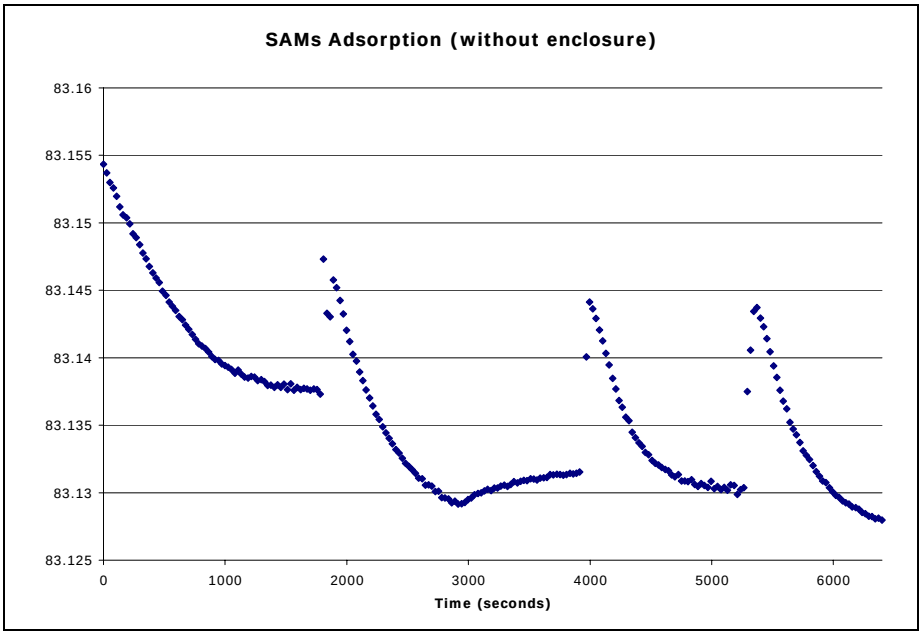

Figure 4: Plot of resonant frequency versus time for hexadecanethiol adsorption, performed without the enclosure.

The next experiment was done with the device enclosed in the enclosure described above. The results of this run are again plotted as resonant frequency versus time in Figure 5. Note that the large spikes present in the first run are no longer present, showing the process much more clearly. There is a clear exponential decay of the resonant frequency as time increases. This is can be explained by the process of adsorption. Initially, when the solution is applied to the QCM, there is nothing attached to the gold surface. Thus, the hexadecanethiol molecules are free to adsorb to the surface and do so very quickly. As more molecules adhere to the surface, there is less room for other molecules to adsorb. The rate of adsorption quickly decreases, eventually reaching an equilibrium when no more molecules can find sites on which to bond to the gold, which results in the stabilization of the resonant frequency.

The addition of the enclosure seems to have added a substantial amount of noise to the system. The data for the resonance curves is not as closely packed in the second set of data. Additionally, the Q-factor of the resonances has also decreased. Figures 6 and 7 show the Q-factor versus time for the two SAM adsorption experiments, while Figures 8 and 9 show two examples of the original resonant frequency curves with their fits from the Mathematica program. The Q-factor does seem to vary less with time in the experiment where the enclosure was

Annual Research Journal, Vol. IV
Electrical Engineering Research Experience for Undergraduates

ISBN 0-913260-06-1 (http://www.ee.psu.edu/reu/)

used, but overall the Q-factor is lower than in the experiment without the enclosure. These changes could be due to factors such as poor connections inside the box or changes in capacitance of the system due to the enclosure.

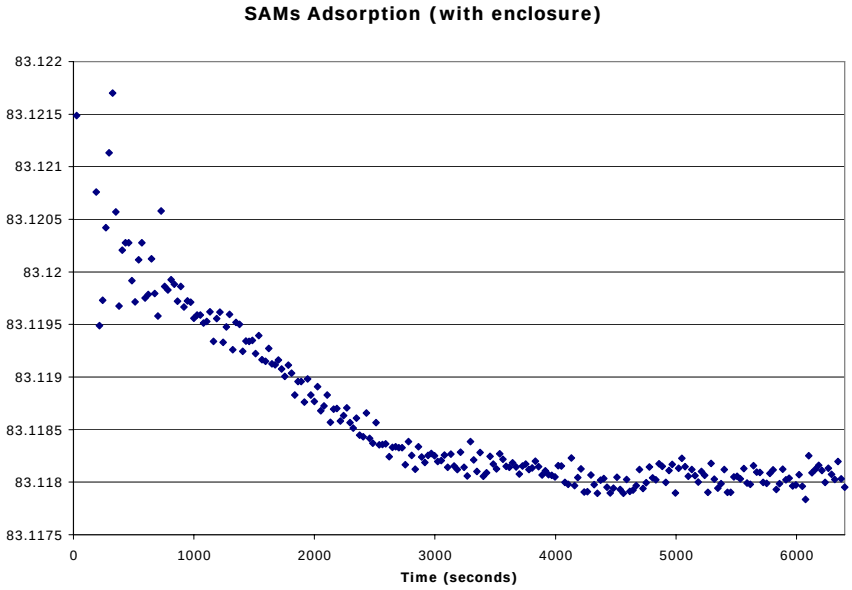

Figure 5: Plot of resonant frequency versus time for hexadecanethiol adsorption, performed with the enclosure.

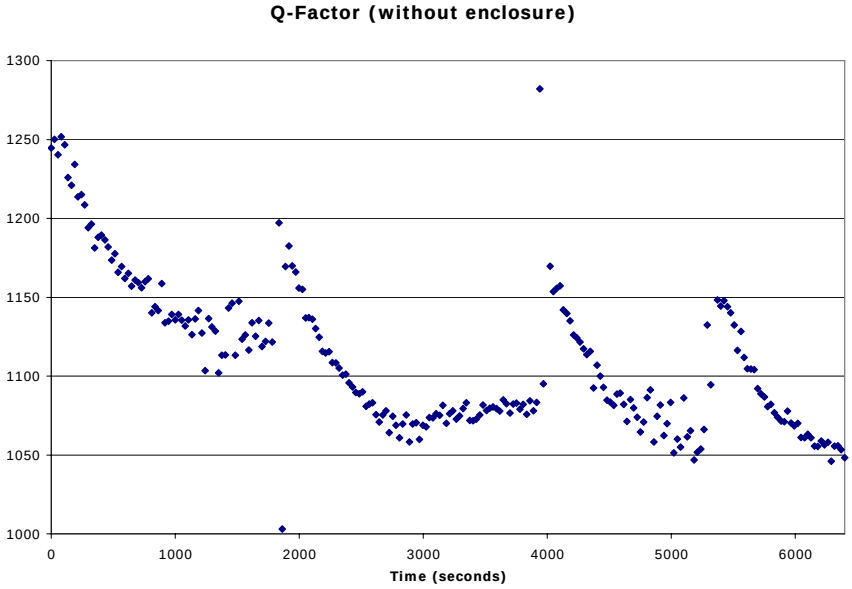

Figure 6: Plot of Q-factor versus time for SAMs adsorption experiment performed without enclosure.

Annual Research Journal, Vol. IV
Electrical Engineering Research Experience for Undergraduates

ISBN 0-913260-06-1 (http://www.ee.psu.edu/reu/)

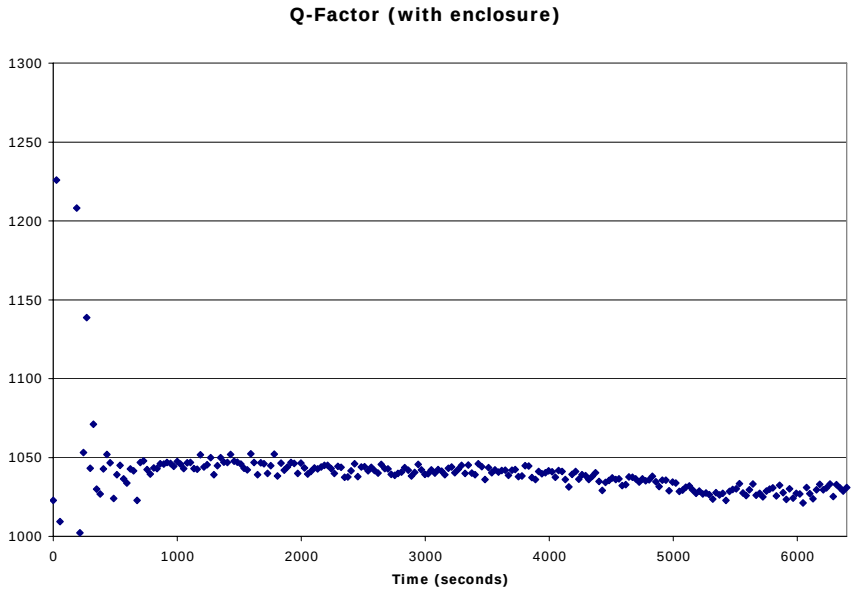

Figure 7: Plot of Q-factor versus time for SAMs adsorption experiment performed without enclosure.

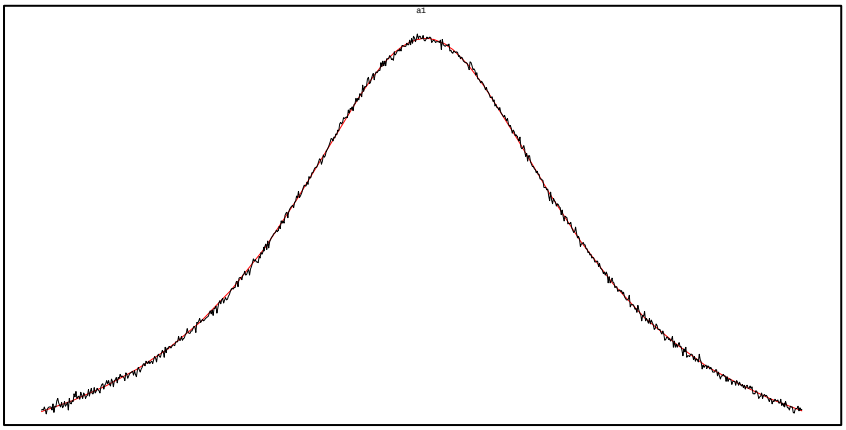

Figure 7: Typical resonance curve from first SAMs adsorption experiment with the curve fit. The data is in black and the fit is in red.

Annual Research Journal, Vol. IV
Electrical Engineering Research Experience for Undergraduates

ISBN 0-913260-06-1 (http://www.ee.psu.edu/reu/)

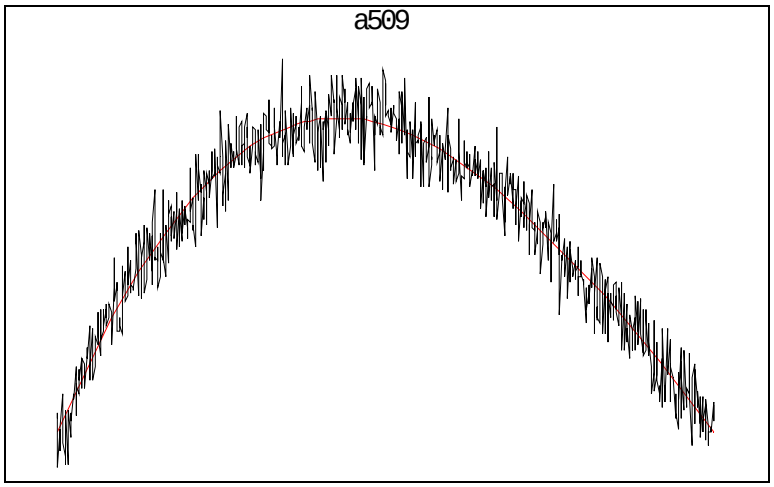

Figure 8: Typical resonance curve from second SAMs adsorption experiment with the curve fit. The data is in black and the fit is in red.

The data for both of the protein adsorption experiments did not turn out as well as the hexadecanethiol adsorption. The first protein adsorption experiment, performed without the enclosure, did not produce much usable data. Many of the plots did not show any significant change in resonant frequency, or actually showed an increase in the frequency. There were several that did turn out to be fairly good, however. Figure 9 shows the adsorption of the 10^{-8}% protein concentration. Again, we see the exponential decrease in resonant frequency, which stabilizes as the protein adsorption reaches equilibrium.

The protein adsorption experiment was performed with the second SAM of hexadecanethiol grown as described above. Again, there was an increase in the noise in the resonance curves, as well as a decrease in Q-factor. Figure 10 shows the adsorption of the 10^{-9}% protein concentration. Again, we see the expected exponential decay.

The data taken does show the adsorption of the different SAMs on the surface of the QCM. However, not all of the data supports this, as much of it was inconclusive. This experiment should be repeated, but with some modifications. First, only one experiment was run with the new enclosure. It may be possible to achieve better results by redesigning the enclosure and running subsequent experiments. It is possible that there are poor connections causing noise. Additionally, the enclosure is not completely airtight. It would be prudent to use some kind of sealant to make sure that the hexadecanethiol-ethanol mixture does not evaporate. Temperature is also of concern. All of the experiments were run at room temperature, but that may vary with the conditions of the building. More care should be taken to keep the temperature stable.

Annual Research Journal, Vol. IV
Electrical Engineering Research Experience for Undergraduates

ISBN 0-913260-06-1 (http://www.ee.psu.edu/reu/)

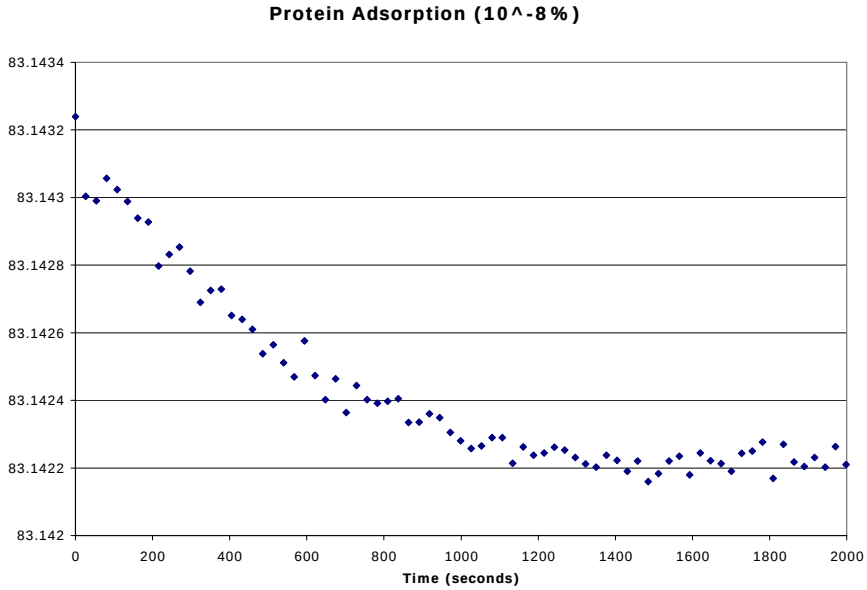

Figure 9: Plot of resonant frequency versus time for 10^{-8}% protein concentration in the first experiment.

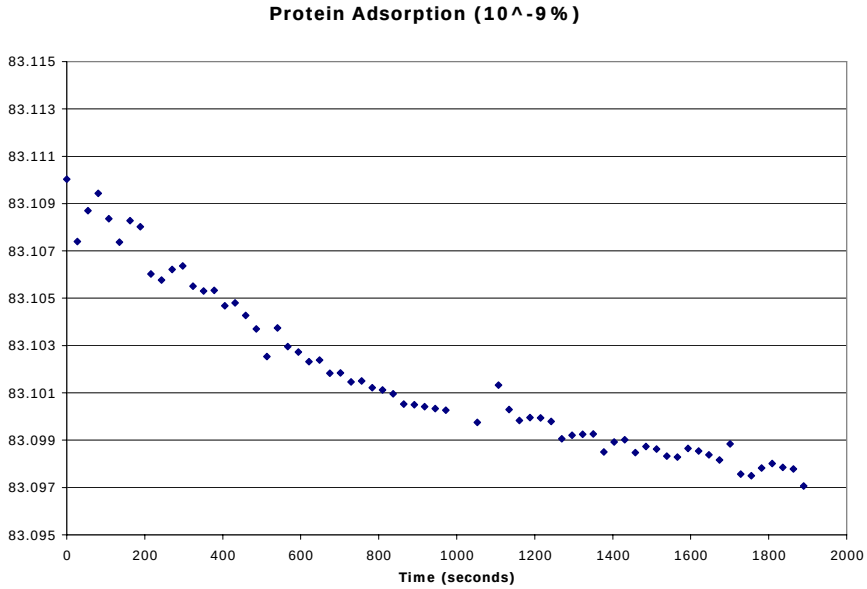

Figure 10: Plot of resonant frequency versus time for 10^{-9}% protein concentration in the second experiment.

Annual Research Journal, Vol. IV
Electrical Engineering Research Experience for Undergraduates

ISBN 0-913260-06-1 (http://www.ee.psu.edu/reu/)

Additionally, the computer taking the data seemed to be having problems. It shut down on its own several times, and at times it seemed to lose communication with the impedance analyzer. This could be due to the GPIB controller, but it seems more likely that it is the computer itself. The Labview program seemed to have problems, as well. The program is supposed to keep the frequency in the center of the 100 kHz window at all times, but this was not the case in many of the data sets. In fact, it is clear that the resonance peak drifts out of the window over time, adding uncertainty in the resonances, decreasing the Q-factor, and making subsequent sweeps useless. This problem could be in the program, or it could be a symptom of the computer losing connection with the impedance analyzer. This program and the computer itself should be looked at before performing further experiments.

One other source of uncertainty is in the compensations programmed into the impedance analyzer. Aside from the device itself, the connections and enclosure have some capacitance that must be accounted for. Several modified DIP's were used to program in compensations, but these were not the same type of DIP as used for the actual device. These compensations could be greatly improved by using devices similar to the actual package.

SUMMARY

The new micromachined quartz crystal microbalance described in this paper is much more sensitive than any QCM ever fabricated previously. It has a sensitivity of approximately 32 kHz/ng, which is 3 orders of magnitude better than any previous QCM. Much work needs to be done on testing this device and the fabrication process, but it is a very promising new gravimetric sensor. In the future, it may be applied in many different areas of thin film research and could possibly be used as a biosensor. The data taken shows the adsorption to the surface of the QCM of self-assembled monolayers of 1-hexadecanethiol, with further monolayers of human serum albumin on the surface created by the hexadecanethiol.

ACKNOWLEDGEMENT

This material is based upon work supported by the National Science Foundation under Grant Nos. EEC-0244030, DMR-0213623, and DMR-0305238, the John and Elizabeth Holmes TEAS Scholarship Fund, Penn State University, and the Pennsylvania Ben Franklin Technology Development Fund.

Annual Research Journal, Vol. IV
Electrical Engineering Research Experience for Undergraduates

ISBN 0-913260-06-1 (http://www.ee.psu.edu/reu/)

REFERENCES

[1] C. Lu and A. W. Czarderna, "Applications of Piezoelectric Quartz Crystal Microbalances," Elsevier, New York. 1984.

[2] Ulman, A. Self-Assembled Monolayers, 237-239, An Introduction to Ultrathin Organic Films, Academic Press. San Diego, CA. 1991.

[3] Liu, Y. "Determination of Protein Packing on Self-Assembled Monolayer Surfaces by Quartz Crystal Microbalance Measurements," Thesis (M.S.)--Pennsylvania State University, pp. 3-54 (2005).

[4] Goyal, A. "Ultrasensitive Quartz Crystal Microbalance Integrated with Carbon Nanotubes," Thesis (Ph.D.)--Pennsylvania State University (2006).

[5] Kao, P. "Applications of Self-Assembled Monolayers and the Micromachined Quartz Crystal Microbalance," Thesis (M.S.)--Pennsylvania State University (2006).

Annual Research Journal, Vol. IV
Electrical Engineering Research Experience for Undergraduates

ISBN 0-913260-06-1 (http://www.ee.psu.edu/reu/)

RESISTANCE AND FIELD EFFECT BEHAVIOR OF GRAPHENE FLAKES

David Gagnon*, Prasoon Joshi[+], and Srinivas Tadigadapa[#]

Department of Electrical Engineering
The Pennsylvania State University, University Park, PA 16802

*Undergraduate student of
Bradley Department of Electrical and Computer Engineering
Virginia Tech
Blacksburg, VA 24061

ABSTRACT

Graphene, a two dimensional hexagonal lattice of carbon atoms, is the constituent layer in graphite. As a nanomaterial it has gained prominence in recent times because of its unique electrical characteristics. Being a two dimensional material it offers the novel electronic properties of a two dimensional electron gas, as is manifested by heterojunctions. The factors that influence the electronic properties of graphene include: number of individual graphene layers, chirality, presence of edge states, etc. The present study seeks to improve understanding of graphene electrical characteristics, namely, resistance and its variation with an applied electric field.

A flake of graphene is deposited onto a silicon substrate with a silicon oxide layer and contacted to a grid of metallic contacts. These contacts permit the measurement of current-voltage characteristics and the application of external electric field. The results show that an applied voltage does have an appreciable effect on resistivity of graphene.

INTRODUCTION

Graphene appears in several different structures in nature, forming graphite when it is stacked and Carbon nanotubes(CNTs) when it is rolled. CNTs have

[+] Graduate Mentor
[#] Faculty Mentor

Annual Research Journal, Vol. IV
Electrical Engineering Research Experience for Undergraduates

ISBN 0-913260-06-1 (http://www.ee.psu.edu/reu/)

brought attention to this carbon lattice because of their unique electrical and mechanical properties. They are able to withstand considerable tension[1] and exhibit both semiconducting and metallic behavior[2]. Berger et al. have found a way to fabricate electronic devices out of graphene flakes using lithography, and the two-dimensional electron transport that they have observed may be useful in electronic devices. This hope is increased with the ability to modulate film conductance with a top-gate electrode[3]. Several researchers have studied the effect of magnetic field on graphene, especially in terms of the quantum Hall effect[4,5]. Banerjee et al. have studied the conductivity of highly oriented pyrolytic graphite (HOPG), which is essentially made of stacked sheets of graphene. They made maps of conductivity for multiple layers of graphite, and it was found that different layers exhibited different conductances, and the top layer was generally more conductive than the other layers. It was also found that the structure at the edge of a layer has an effect on the conductivity of that edge[6]. Conductivity has also been addressed theoretically with regard to small-scale defects like impurities, vacancies, and boundaries in graphene[7].

Although there has been research concerning graphene's resistivity with regard to shear displacement and impurities, this material has not been fully characterized. There has been some work on electric field in thin carbon films[8], which has been useful to the researchers at PennState who are trying to study different aspects of electronic transport in graphene flakes. In line with this motivation, the present paper is interested in the resistivity and electrical behavior of graphene flakes when an electric field is applied.

EXPERIMENTAL DESCRIPTION

The first step of the experiment involved fabrication of the graphene devices. These samples were prepared in Dr. Eklund's lab in the Dept of Physics at PennState University. Scotch tape was used to remove thin flakes off of HOPG. These flakes were transferred onto smooth Si substrates containg ~ 100nm of SiO_2 by rubbing. A thin film of Cr/Au 5nm/70nm was evaporated using a shadow mask in a thermal evaporator. The shadow mask would define a grid of metal pads 100μm by 100μm in size. Any graphene flake spanning across two such pads would serve as a potential graphene device.

To study the field effect on transport properties, a back gate using the underlying silicon substrate was fabricated by stripping the SiO_2 in HF. Drying silver was used to serve as a contact to the silicon.

The resulting devices were referenced by the metallic pads they contacted.

Measurements were carried out with a Keithley 4200 Semiconductor Characterization System in conjunction with a Karl - Suss probe station on a vibration isolation table. The 4200 enabled some degree of automation in data collection through the use of user-defined sweep parameters. The 4200 also permitted a stepping of one parameter in combination with sweeping of another parameter, thus streamlining the process of collecting three-terminal field-effect data. Voltage and current values were always initiated at very low levels to

Annual Research Journal, Vol. IV
Electrical Engineering Research Experience for Undergraduates

ISBN 0-913260-06-1 (http://www.ee.psu.edu/reu/)

prevent burn out of the devices due to resistive heating and then gradually increased to include more points in the interested range of data. The vibration isolation table served to protect the sample from any vibrations that would cause noise in the data and/or damage the sample.

The first set of measurements involved two-terminal IV characteristics for the viable graphene devices. Multiple graphene flakes were found on the sample. Eight such devices were chosen for testing, which consisted of multiple voltage sweeps across each one. The resistance for a given voltage sweep was determined by finding the slope of a linear fit through the data points, and the resistance values were averaged to find the overall resistance for each device.

The second set of measurements consisted of the application of an electric field, by applying a bias at the gate, to the graphene device. For each device tested, the Keithley 4200 was programmed to perform a voltage sweep for each step in gate voltage. The resulting curves were stored in spreadsheets for further analysis.

RESULTS

Two-Terminal Measurements

The measured devices and their corresponding resistances are shown to three significant figures in Table 1. The voltage was swept from -100 to 100 mV and the current compliance was set at 1nA to start with. Compliance was the parameter that the 4200 used to clip the current at a certain level, thus limiting the power through the device. It was found that to generate sufficient data points in the interested voltage range, the compliance had to be gradually increased. A satisfactory compliance was typically found around 1 mA, at which point the graph usually stopped clipping at the ends. In Table I, it can be seen that two different measurements were taken for device 6C-7C. The measurement was continued because of suspicion that the smaller compliance was insufficient. The result was a difference in resistance that spans nearly an order of magnitude. The cause of this change is not fully understood, and it is even possible that the smaller compliance was more accurate with respect to the three-terminal resistance.

Three-Terminal Measurements

To ensure good contact and consistency with the two-terminal measurements, the sweep sets included data at zero gate voltage. With no applied field, the devices were expected to perform as they had in the two-terminal tests. The results of these tests are shown in Table II.

The most thorough testing was conducted on device 6C-7C. One test was the sweeping of the gate voltage while the voltage across the device was held constant. Thus, only the current was permitted to change, and through Ohm's law, the resistance could be calculated. It was found that the resistance did vary with a change in gate voltage, with a peak resistance occurring at 5 V (Figure 1). The device was also tested with voltage sweeps across the device while the gate

Annual Research Journal, Vol. IV
Electrical Engineering Research Experience for Undergraduates

ISBN 0-913260-06-1 (http://www.ee.psu.edu/reu/)

voltage was gradually stepped. Sample curves from this process can be seen in Figure 2.

Table I. Resistances found for the two-terminal measurements

Device	Resistance (Ω)
1A-2A	382
2E-2F	90.5
6C-7C	662
6C-7C (higher compliance)	86.2
8B-9B	7660
6G-7G	3520
D-S	200
E-3D	1150
1G-3G	30.0

Device 6C-7C was tested twice with different compliances, which resulted in different resistance readings. Device 7G-7G showed good linearity in the IV curve, but most of the data points were clustered at the maximum and minimum voltages.

Table II. Resistances found for the three-terminal measurements with a gate voltage of 0V

Device	Three-Terminal Resistance (Ω)
6C-7C	658
6G-7G	1330
8B-9B	7700
Pattern 4	2130

Device 6G-7G showed erratic values, which may reduce the validity of the resistance shown.

Annual Research Journal, Vol. IV
Electrical Engineering Research Experience for Undergraduates

ISBN 0-913260-06-1 (http://www.ee.psu.edu/reu/)

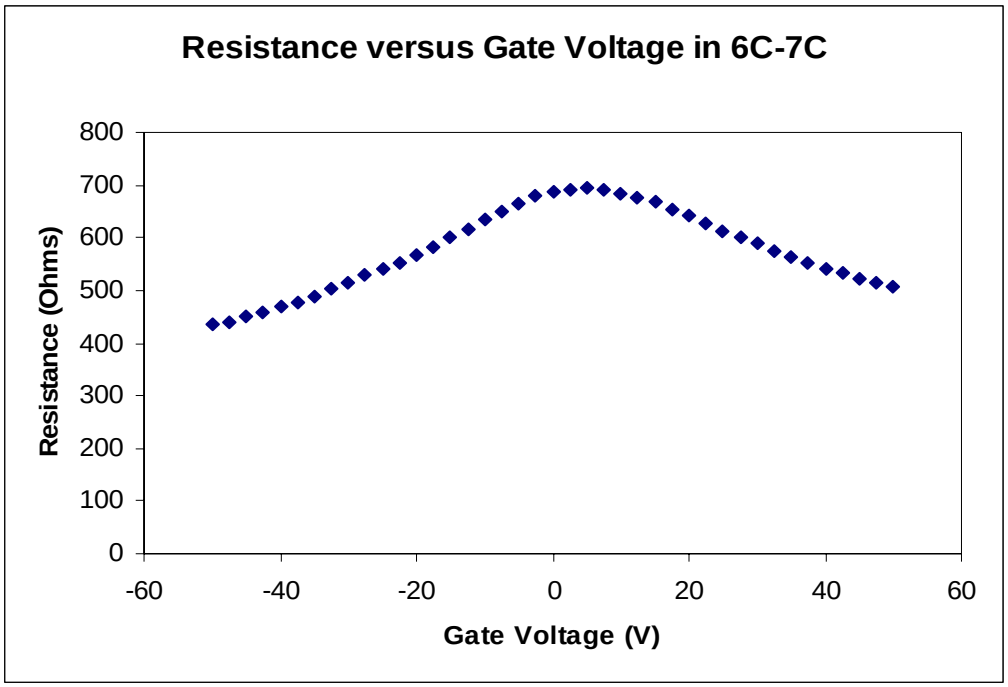

Figure 1. Graph of resistance in device 6C-7C for a constant 10mV across the device while the gate voltage was swept from -50V to 50V.

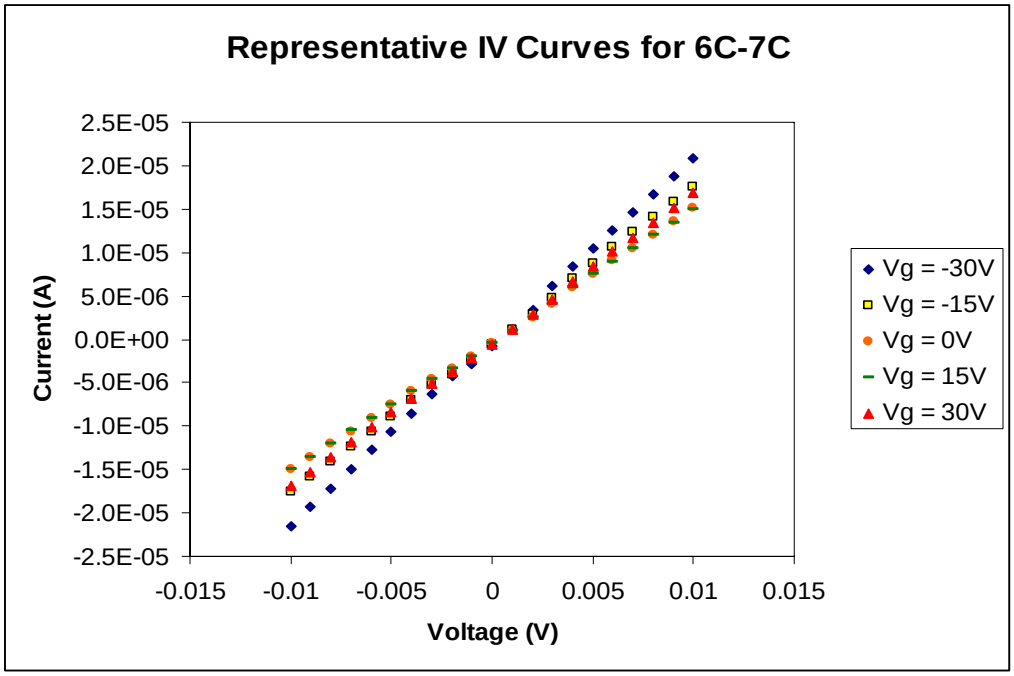

Figure 2: Graph of several IV curves collected for device 6C-7C. The voltage across the device was swept from -10mV to 10mV for every step in gate voltage.

Annual Research Journal, Vol. IV
Electrical Engineering Research Experience for Undergraduates

ISBN 0-913260-06-1 (http://www.ee.psu.edu/reu/)

The ±50V sweep shown in Figure 1 was the largest sweep obtained in the experiment. Afterward, a ±70V sweep was attempted, but the data differed significantly from the previous sweep. Upon further inspection, it was found that 70V resulted in dielectric breakdown. No photos were taken before the experiment, but the final state of device 6C-7C can be seen in Figure 3. A further consequence of having swept too far was damage to the dielectric for nearby devices. It is suspected that this dielectric breakdown is the source of the erratic data in device 6G-7G.

Device 6G-7G was the second piece of graphene to undergo three-terminal testing. Because of the breakdown problem with the previous device, the applied voltage was swept ±40V to prevent another loss. The results showed a widely varying resistance, as shown in Figure 4. It is suspected that the source of the erratic data could be the damaged dielectric caused by the destruction of 6C-7C. There is also a possibility that the device lacked sufficient contact with one of the metal pads. As shown in Figure 5, the device is somewhat triangular in shape, and the narrow end may have been burned by previous tests. Regardless of the resistivity data, the device is noteworthy for its thickness. Atomic force microscopy has shown that 6G-7G was an n = 1 flake, which means that the flake was made of a single layer of graphene.

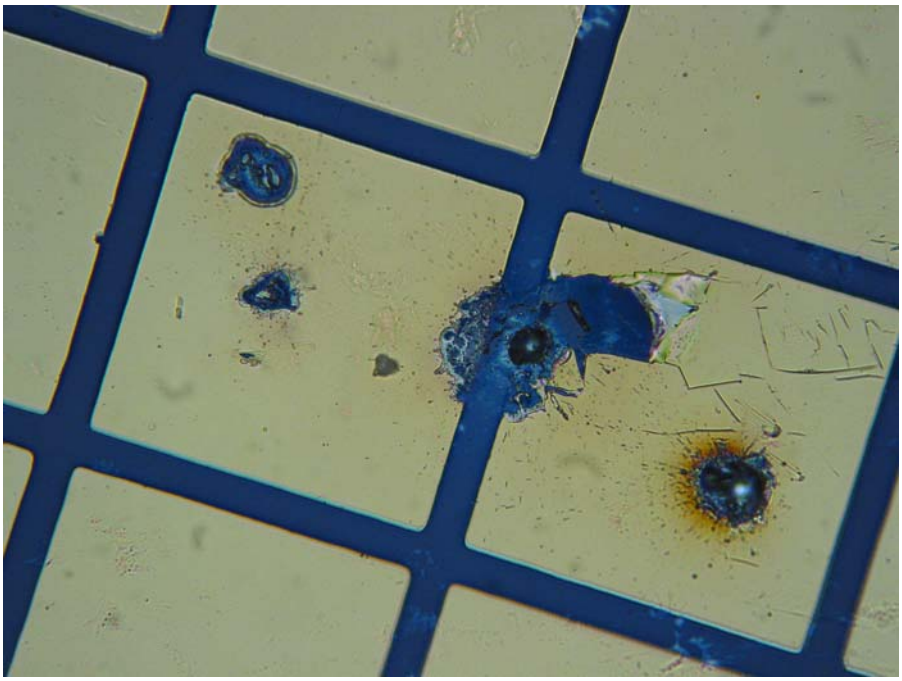

Figure 3. Device 6C-7C, destroyed. The small craters to the left and right show where the probes contacted the metal pads, and the central crater shows the previous location of the device.

Annual Research Journal, Vol. IV
Electrical Engineering Research Experience for Undergraduates

ISBN 0-913260-06-1 (http://www.ee.psu.edu/reu/)

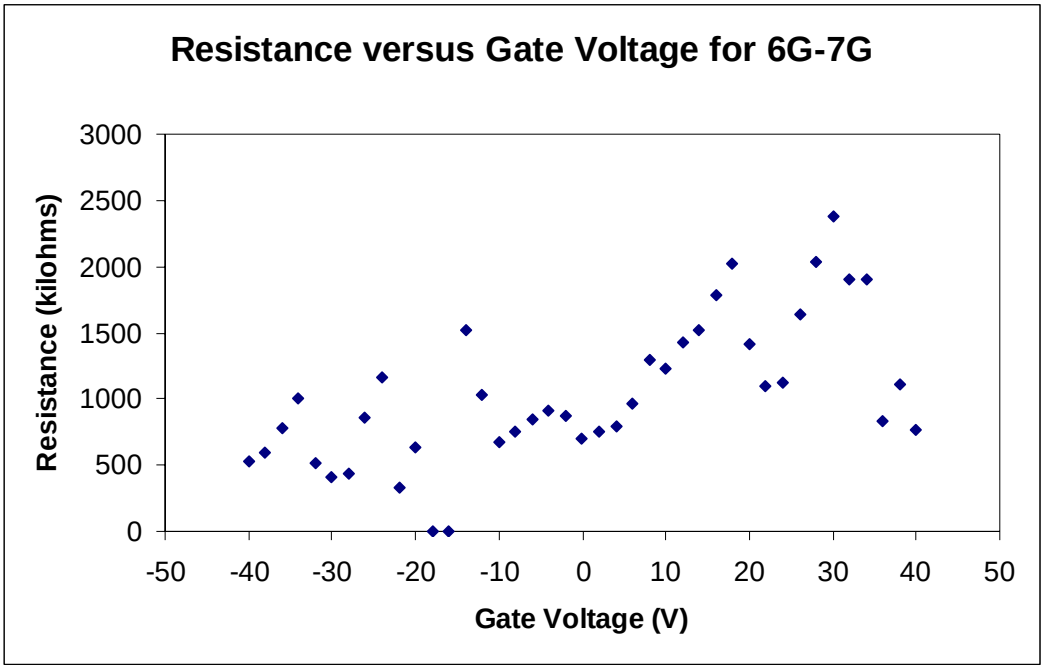

Figure 4. Graph of data points for the average resistance for each gate voltage sweep. Each average was found from a best-fit line of the IV curve.

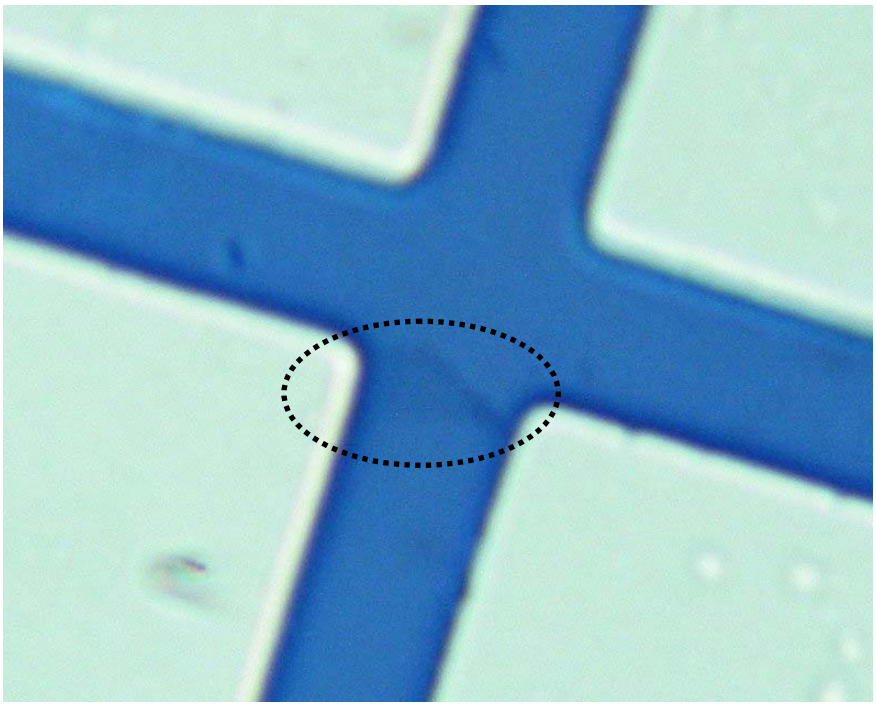

Figure 5. Photograph of 6G-7G, a potential single-layer graphene device. A dotted oval marks its location.

Annual Research Journal, Vol. IV
Electrical Engineering Research Experience for Undergraduates

ISBN 0-913260-06-1 (http://www.ee.psu.edu/reu/)

The third device, 8B-9B, showed a visible relationship between applied field and the corresponding resistance. This relationship is displayed in Figure 6. There is no point at which the resistance begins to descend again, but it is possible that the chosen sweep was too narrow to show the expected behavior. In its current form, the data appears similar in shape to the negative half of the 6C-7C data. The device itself, which was actually two graphene strips in close proximity, can be viewed in Figure 7.

The fourth device was referenced Pattern 4 because it was on the fourth pattern of the sample and had not previously been labeled. This device, like 8B-9B, showed a positive relationship between resistance and gate voltage. The graph of resistance data is available in Figure 8, and the captured image of the device is shown in Figure 9.

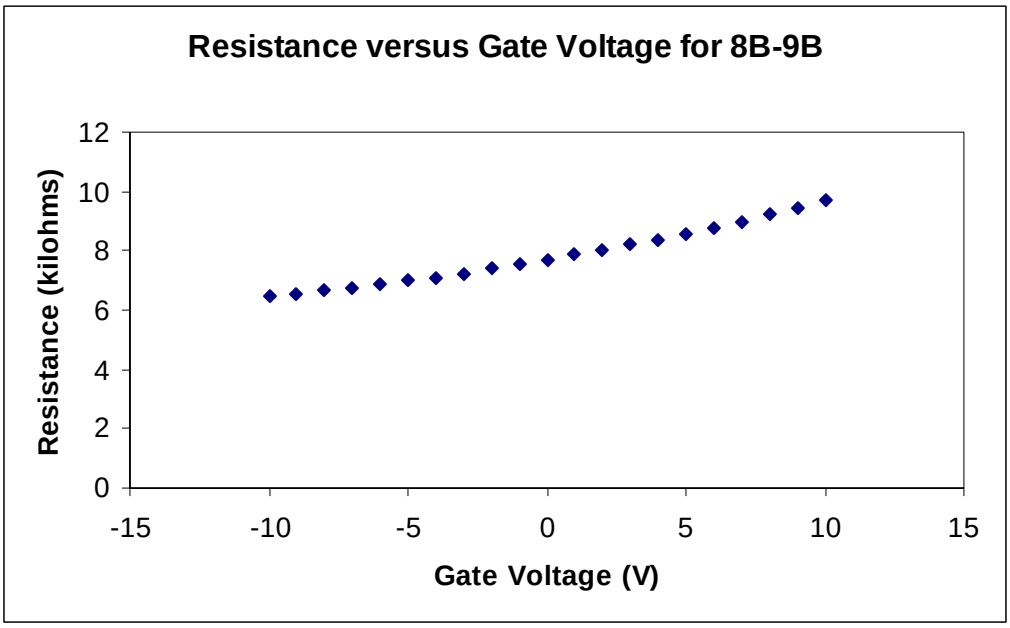

Figure 6. Graph of resistance versus gate voltage for 8B-9B. The voltage across the device was swept ±50mV for each gate voltage level, and each average resistance was found from a best fit line of the IV curve.

Annual Research Journal, Vol. IV
Electrical Engineering Research Experience for Undergraduates

ISBN 0-913260-06-1 (http://www.ee.psu.edu/reu/)

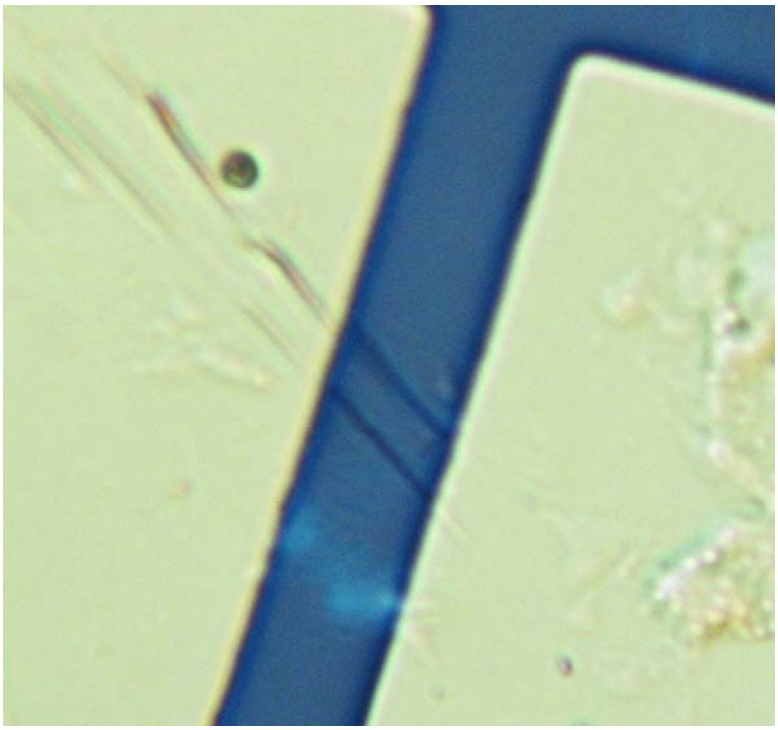

Figure 7. A photograph of 8B-9B. Note that device 8B-9B is actually two graphene devices near one another.

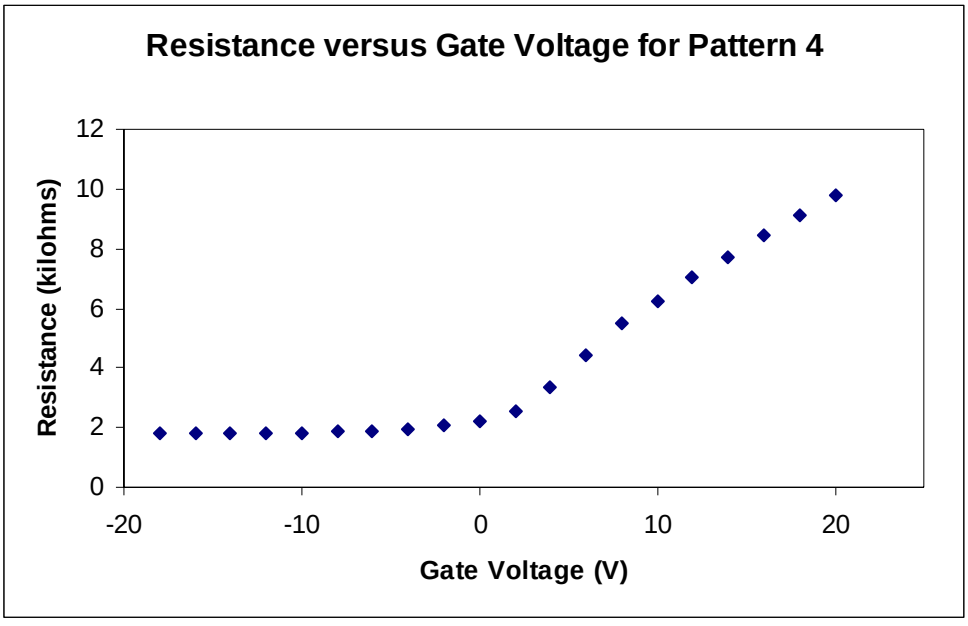

Figure 8. This data was obtained by stepping the gate voltage from -20V to 20V while sweeping the voltage across the device from -10mV to 10mV.

Annual Research Journal, Vol. IV
Electrical Engineering Research Experience for Undergraduates

ISBN 0-913260-06-1 (http://www.ee.psu.edu/reu/)

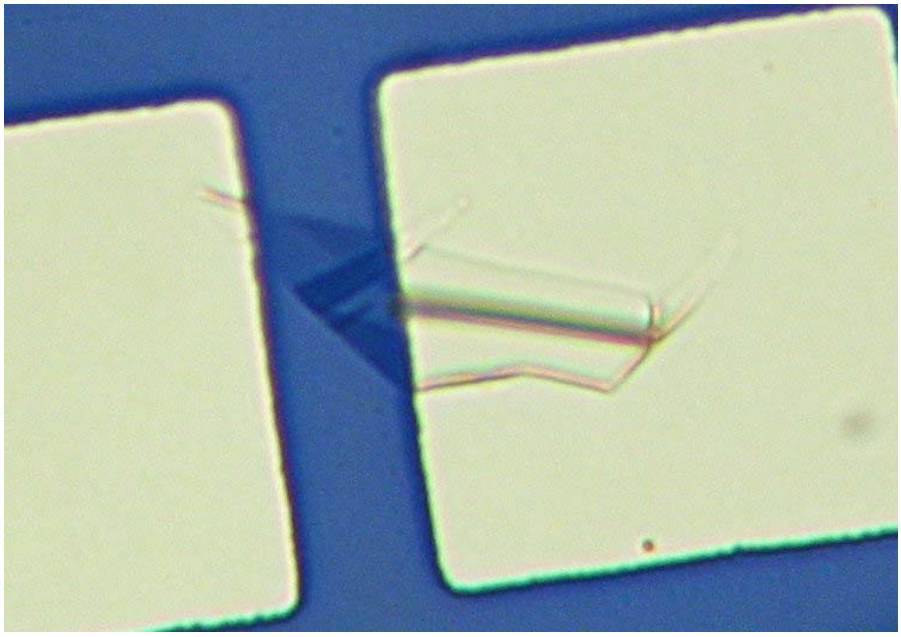

Figure 9. A photograph of Pattern 4. In this region of the sample, the metal pads were much smaller than those of the other devices.

DISCUSSION

From the data obtained in the two-terminal measurements, graphene appears to have a resistivity that is consistent with semimetals. Even thin layers have shown the ability to pass current, which indicates potential for electrical contacts at the microscopic scale. Furthermore, applied gate voltage did have an effect on the resistivity in three out of four tests. In the sample that did not show any relationship between resistance and gate voltage, it is suspected that the contact at the metal pads was insufficient. Even so, it has been shown that the method of graphene deposition in this experiment was successful in creating a monolayer of graphene. Perhaps the effect of gate resistance on resistance could still be observed with better alignment of the device to the metal pads. It is hoped that this element of resistivity control will be useful in further study of electrical properties in graphene.

Several challenges remain in the manipulation of graphene for practical purposes. Consistent thicknesses and accurate placement of the graphene would be necessary for its use as a reliable microelectronic device. The field-effect characteristics also require further study in order to ensure consistent behavior under different temperature conditions. It may be desirable to increase this field-dependent resistivity, perhaps by using thinner or narrower samples.

One topic for further investigation is the effect of confinement of the carriers through the graphene flakes. A narrow channel of carriers is desired. This can be accomplished by using a laser to cut inwards from the periphery towards the center, leaving a narrow channel in the middle.

Annual Research Journal, Vol. IV
Electrical Engineering Research Experience for Undergraduates

ISBN 0-913260-06-1 (http://www.ee.psu.edu/reu/)

A similar test would investigate the effect of edge states on graphene devices produced by burning holes with a laser. These edge states could be functionalized by a gas such as oxygen.

SUMMARY

Graphene has been noted for its potentially useful electronic properties. In nanotube form, it has been shown to behave as a metal or semiconductor depending on the orientation of the lattice relative to the tube. Physical strain has also had an influence on bandgap energies. The present study tested the resistances of several different graphene flakes and also observed changes in resistance according to an applied field. Such results are consistent with expected semimetallic behavior. As the properties of graphene are more thoroughly studied, we may be able to integrate them into truly functional microelectronic devices.

ACKNOWLEDGEMENT

This material is based upon work supported by the National Science Foundation under Grant No. EEC-0244030.

The author would also like to especially thank Prasoon Joshi, who provided guidance throughout the summer program and was integral in obtaining the graphene data. Dr. Srinivas Tadigadapa oversaw the direction of the project. Awnish Gupta and Dr. Peter Eklund helped with the graphene device samples. Dr. Ruyan Guo and Dr. Ken Jenkins made the summer Research Experience for Undergraduates possible, and Linda Becker provided significant logistical assistance.

REFERENCES

[1] J. P. Lu, "Elastic Properties of Carbon Nanotubes and Nanoropes," *Physical Review Letters*, **79**(7) 1297-3000 (1997).

[2] Ethan Davis Minot, "Tuning the band structure of carbon nanotubes," Dissertation to Cornell University, August 2004.

[3] Claire Berger, Zhimin Song, Tianbo Li, Xuebin Li, Asmerom Y. Ogbazghi, Rui Feng, Zhenting Dai, Alexei N. Marchenkov, Edward H. Conrad, Phillip N. First, and Walt A. de Heer, "Ultrathin Epitaxial Graphite: 2D Electron Gas Properties and a Route toward Graphene-based Nanoelectronics," *J. Phys. Chem. B*, **108** 19912-19916 (2004).

[4] Yuanbo Zhang, Yan-Wen Tan, Horst L. Stormer & Philip Kim, "Experimental observation of the quantum Hall effect and Berry's phase in graphene," *Nature*, **438** 201-204 (2005).

[5] Kikuo Harigaya, Atsushi Yamashiro, Yukihiro Shimoi, Katsunori Wakabayashi, Yousuke Kobayashi, Naoki Kawatsu, Kazuyuki Takai,

Annual Research Journal, Vol. IV
Electrical Engineering Research Experience for Undergraduates

ISBN 0-913260-06-1 (http://www.ee.psu.edu/reu/)

Hirohiko Sato, Jérôme Ravier, Toshiaki Enoki, Morinobu Endo, "Theoretical study on novel electronic properties in nanographite materials," *Journal of Physics and Chemistry of Solids*, **65** 123-126 (2004).

[6] S. Banerjee, M. Sardar, N. Gayathri, A. K. Tyagi, and Baldev Raj, "Conductivity landscape of highly oriented pyrolytic graphite surfaces containing ribbons and edges," *Physical Review B*, **72** 075418 (2005).

[7] N. M. R. Peres, F. Guinea, and A. H. Castro Neto, "Electronic properties of disordered two-dimensional carbon," *Physical Review B*, **73** 125411 (2006).

[8] K. S. Novoselov, A. K. Geim, S. V. Morozov, D. Jiang, Y. Zhang, S. V. Dubonos, I. V. Grigorieva, and A. A. Firsov, "Electric Field Effect in Atomically Thin Carbon Films," *Science*, **306** 666-669 (2004).

Annual Research Journal, Vol. IV
Electrical Engineering Research Experience for Undergraduates

ISBN 0-913260-06-1 (http://www.ee.psu.edu/reu/)

FEMTOSECOND FIBER LASER FOR CARS MICROSCOPY

Zhenyan Hua*, Kebin Shi+, and Zhiwen Liu#

Department of Electrical Engineering
The Pennsylvania State University, University Park, PA 16802

*Undergraduate student of
Department of Electrical Engineering
Pennsylvania State University
University Park, PA 16802

ABSTRACT

A femtosecond laser was constructed by using standard telecom fiber optical components. It uses a Erbium doped fiber as the gain medium, and utilizes passive mode-locking leading to ultra short pulses. An interferometric autocorrelator was built to characterize the pulse width. This laser can be potentially used for CARS imaging, a nonlinear optical imaging technique that permits visualization of a sample by detecting the vibration spectrum of molecules.

INTRODUCTION

In the 1960s, fiber gain medium were made possible by incorporation of trivalent rare-earth ions such as neodymium, erbium, and thulium into glass hosts.[1] Doping of silica fibers with Er^{3+} ions was not achieved until the 1980s.[2] Since then, Er-doped fiber lasers have received much attention. Due to its center gain wavelength at 1.55 μm that falls within the low loss range of the optical fibers, it's especially popular in the optical fiber communication field.[3] Potential applications for compact, diode-pumped, fiber-compatible optical sources at various wavelengths have motivated significant fiber laser research over the last 10 years. In addition to offering continuous-wave operation, fiber lasers can be mode-locked to generate femtosecond laser pulses. Compared with the

+ Graduate Mentor
# Faculty Mentor

Annual Research Journal, Vol. IV
Electrical Engineering Research Experience for Undergraduates

ISBN 0-913260-06-1 (http://www.ee.psu.edu/reu/)

Ti:Sapphire mode locked femtosecond laser, the fiber laser is compact, low cost, and can also potentially produce an average power of a few hundreds of milli-Watts. These advantages have potential for many applications, in particular for CARS imaging application.

EXPERIMENTAL DESCRIPTION

The construction of the fiber laser follows reference [4] very closely. Figure 1 shows the schematic of the fiber laser for this experiment. The 980nm light from a diode laser pumps the Er-doped fiber to achieve population inversion, and causes it to produce gain. Laser pulses grow exponentially as they travel down this fiber. Then the pulse travels to the wave plate/polarization controller, which changes its polarization state.

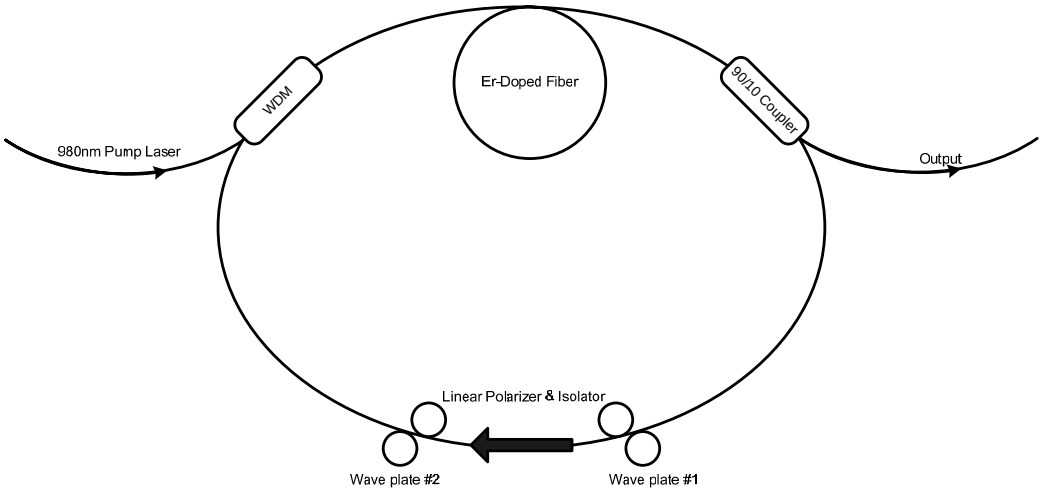

Figure 1 Fiber Laser Schematic modified from [5]

After the wave plate, the isolator acts as a valve, and permits light to pass through in one direction. By ensuring the direction of the light's travel, it negates interference between opposing light and reduces feedback. Now imagine a linearly polarized light leaving the linear polarizer, it will first enter wave plate 2 which transforms it to an elliptically polarized state.[5] If the light's intensity is high, e.g. pulse mode, the ellipse will rotate slightly as it travel through the cavity due to Kerr effect. Then wave plate 1 receives this Kerr-rotated state, and converts it back to the right linear polarization for the linear polarizer therefore results in a minimum loss. This is the basis of the passive mode-locking technique which causes the pulses to form and made ultra-short. The CW light has low intensity, thus does not rotate its ellipse enough after the wave plate, and dies off at the polarizer. Finally, the 90/10 output coupler will transfer 10% of the pulse energy to the output lead and 90% back to the cavity.

By tuning both of the wave plates, two modes of operation were obtained: CW mode and the pulse mode as shown in Figure 2 & 3. In time-domain, the pulse mode laser will look like a pulse train as shown in Figure 4.

Annual Research Journal, Vol. IV
Electrical Engineering Research Experience for Undergraduates

ISBN 0-913260-06-1 (http://www.ee.psu.edu/reu/)

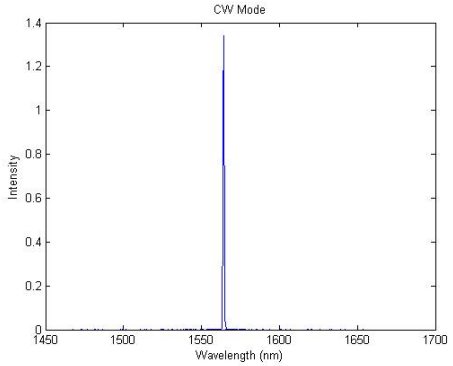

Figure 2 CW Mode Operation

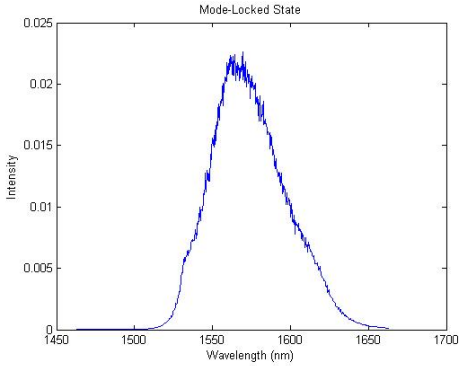

Figure 3 Mode-Locked Operation

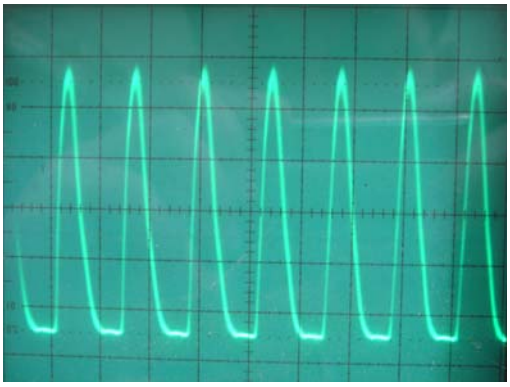

Figure 4 Time-Domain Pulse Train

In order to characterize the pulse from the fiber laser, interferometric autocorrelator was used as shown in Figure 5.

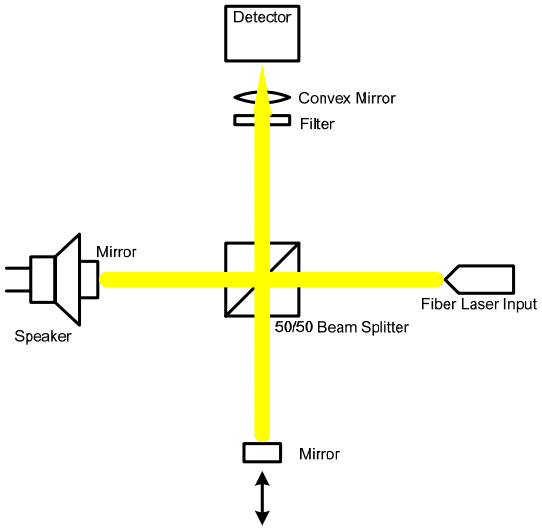

Figure 5 Interferometric Autocorrelator Schematic

Annual Research Journal, Vol. IV
Electrical Engineering Research Experience for Undergraduates

ISBN 0-913260-06-1 (http://www.ee.psu.edu/reu/)

The above interferometer has two arms; one is mounted on a translation stage, used for coarse alignment to make both arms of the interferometer of almost equal length. The other arm is mounted on an audio speaker driven by a sine wave from a function generator. Since one arm of the interferometer have a fixed path length and the other is constantly changing with respect to a fixed range, the phase between the two beams will differ at the detector where they recombine. Hence, resulting in an interference pattern.

A silicon photodiode detector was used to measure the pulse nonlinearly. Since silicon has a band gap of 1.3 μm,[4] the detector become transparent for any light with greater wavelength. However, if the light is in pulse mode, it will have enough energy to cause two photon absorptions at the detector. Based on this nonlinear effect, the autocorrelation pattern can be detected. The detected signal is a second order interferometric correlation, proportional to the function: [6]

$$G_2(\tau) = \int_{-\infty}^{\infty} \{[E_1(t-\tau) + E_2(t)]^2\}^2 dt \tag{1}$$

Substituting for the fields, the usual amplitude, and phase dependence, leads to the following decomposition for the second order correlation:

$$G_2(\tau) = A(\tau) + \mathrm{Re}\{4\tilde{B}(\tau)e^{i\omega_l\tau}\} + \mathrm{Re}\{2\tilde{C}(\tau)e^{2i\omega_l\tau}\} \tag{2}$$

Where

$$A(\tau) = \int_{-\infty}^{\infty} dt\{\varepsilon_1^4(t-\tau) + \varepsilon_2^4(t) + 4\varepsilon_1^2(t-\tau)\varepsilon_2^4(t)\} \tag{3}$$

$$\tilde{B}(\tau) = \int_{-\infty}^{\infty} dt\{\varepsilon_1(t-\tau)\varepsilon_2(t)[\varepsilon_1^2(t-\tau) + \varepsilon_2^2(t)]e^{i[\varphi_1(t-\tau)-\varphi_2(t)]}\} \tag{4}$$

$$\tilde{C}(\tau) = \int_{-\infty}^{\infty} dt\{\varepsilon_1^2(t-\tau)\varepsilon_2^2(t)e^{2i[\varphi_1(t-\tau)-\varphi_2(t)]}\} \tag{5}$$

When all terms of the autocorrelation are recorded, the peak to the background ratio for the interferometric autocorrelation is 8 to 1. [6] Due to the fiber dispersion, the output pulse might be chirped. Assuming the pulse is linearly chirped Gaussian pulse ($\varepsilon(t) = \exp[-(1+ia)(t/\tau_G)^2]$), now the interferometric autocorrelation can be determined exactly:

$$G_2(\tau) = \left\{1 + 2e^{-\left(\frac{\tau}{\tau_G}\right)^2} + 4e^{-\frac{a^2+3}{4}\left(\frac{\tau}{\tau_G}\right)^2}\cos\frac{a}{2}\left(\frac{\tau}{\tau_G}\right)^2\cos\omega_l\tau + 2e^{-(1+a^2)\left(\frac{\tau}{\tau_G}\right)^2}\cos 2\omega_l\tau\right\} \tag{6}$$

Annual Research Journal, Vol. IV
Electrical Engineering Research Experience for Undergraduates

ISBN 0-913260-06-1 (http://www.ee.psu.edu/reu/)

In Eq. (6), the parameter τ_G is the pulse duration and a is the chirp parameter.

RESULTS

The constructed interferometric autocorrelator is shown in Figure 6.

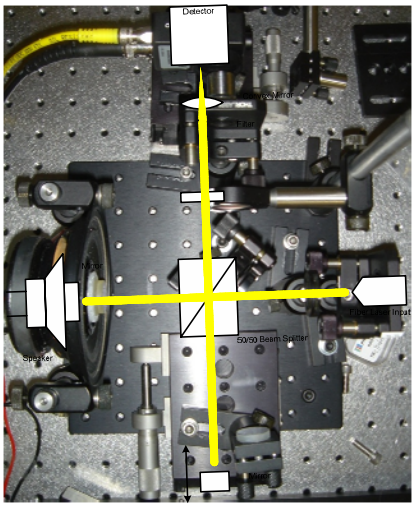

Figure 6 Interferometric Autocorrelator

Once the fiber laser is mode-locked, the following interferometric autocorrelation trace was obtained.

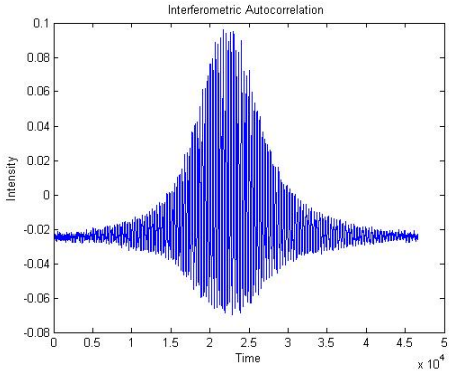

Figure 7 Interferometric Autocorrelation

Then by taking the Fourier transform of the above trace and apply a low pass filter, the DC component of the autocorrelation can be obtained.

Annual Research Journal, Vol. IV
Electrical Engineering Research Experience for Undergraduates

ISBN 0-913260-06-1 (http://www.ee.psu.edu/reu/)

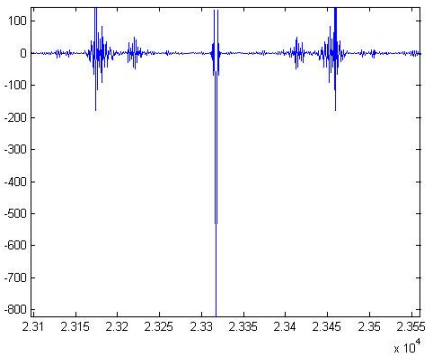

Figure 8 Fourier Transform of Autocorrelation

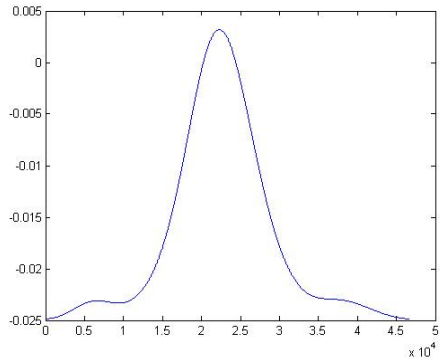

Figure 9 The DC Component

The DC Component shown above is represented by the first two terms of the Eq. 6.

$$G_2(\tau) = \left\{ 1 + 2e^{-\left(\frac{\tau}{\tau_G}\right)^2} \right\} \tag{7}$$

From the DC component trace, the constant term τ_G can be found. Once the τ_G value is known, the chirp value a can be found by solving Eq. 6.

CONCLUSION

As shown in Figure 2, the CW mode operation of the fiber laser has a center wavelength of 1564 nm and is a very narrow spike. The mode-locked operation of the fiber laser has a center wavelength of 1566 nm, and FWHM[1] of 60 nm as shown in Figure 3. The average power of the fiber laser in pulse mode was measured to be 15 mW. The spectrum of the pulse appears to be very noisy which requires further investigation. When mode-locked, the fiber laser is very stable. It will stay in the same mode-locked state after every restart of the pump laser. The τ_G constant was measured to be 151 fs.

ACKNOWLEDGEMENTS

This research journal could not have been written without Mr. Kebin Shi who not only served as my graduate mentor but also encouraged and challenged me throughout my EEREU program. Also I would like to thank Professor Zhiwen Liu for giving me the opportunity to participate in this program, moreover to be a part of his research group.

This material is based upon work supported by the National Science Foundation under Grant No. EEC-0244030.

[1] FWHM – **F**ull **W**idth **H**alf **M**aximum

Annual Research Journal, Vol. IV
Electrical Engineering Research Experience for Undergraduates

ISBN 0-913260-06-1 (http://www.ee.psu.edu/reu/)

REFERENCES

[1] E. Snitzer, "Optical Maser Action of Nd^{+3} in a Barium Crown Glass," *Physics Rev. Letter*, **1961**, 7, 444

[2] S. B. Poole, D. N. Payne; R. J. Mears, L. Reekie; M. E. Fermann; R. J. Laming, "Fabrication and characterization of low-loss optical fibers containing rare-earth ions," *J. Light wave Technology*, **1986**, 22, 159

[3] J. Y. Allain; M. Monerie; H. Poignant, "High-efficiency CW thulium-sensitized holmium-doped fluoride fiber laser operating at 2.04 μm," *Electron Letter*, **1991**, 27, 1513

[4] R.S. Marjoribanks, "A Primer on Ultrafast Fiber Lasers", **2003**, 1~10

[5] Nelson, L. E., D. J. Jones, "Ultrashort-pulse fiber ring lasers", *Applied Physics B*, **1997**, 277~294

[6] Jean-Claude Diels; Wolfgang Rudolph, "Interferometric Correlations", 369~373, *Ultrashort Laser Pulse Phenomena*, Paul F. Liao, Adademic Press, 1995

ISBN 0-913260-06-1 (http://www.ee.psu.edu/reu/)

TERAHERTZ WAVE GENERATION VIA OPTICAL RECTIFICATION

Jason M. Wishnov*, Peng Li[+], and Zhiwen Liu[#]

Department of Electrical Engineering
The Pennsylvania State University
University Park, PA 16802

*Undergraduate student of
Department of Electrical and Computer Engineering
University of Florida
Gainesville, FL 32607

ABSTRACT

Terahertz technology has found important applications in medical imaging, surveillance, materials research, and various other fields. In this paper we theoretically analyze terahertz wave generation by using a periodically poled electro-optic polymer waveguide (DR1-MMA) via optical rectification of femtosecond laser pulses. The periodic structure (induced via contact poling) of this polymer allows for quasi-phase-matching. The propagation modes of optical pump beam and terahertz radiation are studied in regards to various waveguide parameters; waveguide fabrication is also discussed in detail.

[+] Graduate Mentor
[#] Faculty Mentor

Annual Research Journal, Vol. IV
Electrical Engineering Research Experience for Undergraduates

ISBN 0-913260-06-1 (http://www.ee.psu.edu/reu/)

INTRODUCTION

Terahertz (THz) technology is continuing its expansion into numerous fields. As a penetrating, non-ionizing radiation, terahertz devices have applications in medical imaging, surveillance, and materials research. The simple approach of optical rectification is promising, yet previous implementations have been limited in usability and practicality. Here, we propose a design combining a waveguide structure with a non-linear, periodically-poled polymer core.

Optical rectification is a simple process that utilizes a femtosecond pulsed laser as an optical pump beam for the system. When directed through a material exhibiting a second-order non-linear effect, the induced polarization can be modeled as

$$P = \chi^{(2)} EE \tag{1}$$

where E is the electrical field of the femtosecond laser pulse, which can be written as

$$E = f(t)\cos(\omega_0 t) \tag{2}$$

as $f(t)$ is the pulse profile function, and ω_0 is the carrier frequency. Substitution yields

$$\mathrm{P} = \chi^{(2)} f^{(2)}(t)\cos^2(\omega_0 t)$$

$$= \frac{1}{2}\chi^{(2)} f^{(2)}(t)[1+\cos(2\omega_0 t)] \tag{3}$$

The DC component above is the pulse profile. The resulting radiation frequency is on the order of the inverse of pulse duration of the optical pump beam, thus creating a THz radiation pulse if femtosecond pulses are used. The final waveform is dependent on both the optical pump beam and the structure of the non-linear medium.

As described by Cao *et al.*[1], the waveguide structure geometry used allows for the generation of THz radiation over extended interaction lengths. This is accomplished by utilizing a nested waveguide design: a parallel-plate, dielectric-slab waveguide will be constructed and then embedded inside a larger, parallel-plate metal waveguide. The inner, dielectric-slab waveguide allows for propagation of the optical pump beam in its fundamental mode, while the outer metal waveguide allows for propagation of THz pulses in a TEM mode. This metal waveguide design has been demonstrated[2] to allow for distortionless propagation of THz pulses.

Annual Research Journal, Vol. IV
Electrical Engineering Research Experience for Undergraduates

ISBN 0-913260-06-1 (http://www.ee.psu.edu/reu/)

Of important consideration is the phase-matching condition, which must be satisfied for efficient THz radiation. The phase matching condition for the optical rectification process (collinear difference frequency mixing) is given by

$$\Delta k = k(\omega_{opt} + \omega_{THz}) - k(\omega_{opt}) - k(\omega_{THz}) = 0 \qquad (4)$$

where ω_{opt} and ω_{THz} are the optical an THz frequencies, respectively, and ω_{opt} and $(\omega_{opt}+\omega_{THz})$ lie within the spectrum of the optical pulse. This equation can also be rewritten as

$$\frac{k(\omega_{THz})}{\omega_{THz}} \approx \left(\frac{\partial k}{\partial \omega}\right)_{opt} \qquad (5)$$

implying that the group velocity of the optical beam and phase velocity of the THz wave must be matched as they propagate through the non-linear polymer. This increases the interaction length of the pulses, yet is generally difficult to achieve in a uniform media. Here, we introduce a quasi-phase-matching condition by using a periodically poled structure in the electro-optic polymer. This allows for tunable frequencies of the resulting terahertz waveforms, determined by the domain length.

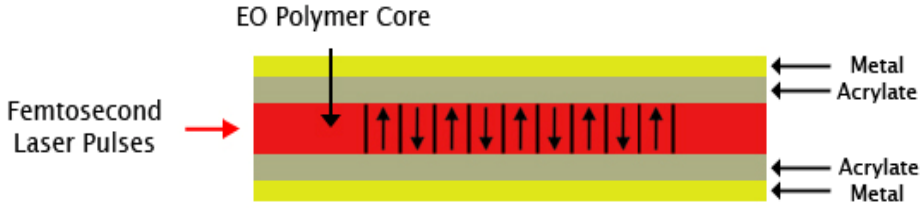

Fig. 1. A diagram of the proposed periodic poling structure. The EO polymer core is alternately poled with a uniform period over the entire length of the waveguide.

EXPERIMENTAL PROCEDURE

Construction

The proper construction of the waveguide is of great importance. The device is to be fabricated on a wafer of silica glass. A layer of metal will be deposited on the wafer (either gold or aluminum) using a DC sputtering technique. Upon that, a layer of acrylate substrate, made up of a UV-curable acrylate (Norland optical adhesive NOA 81), will be applied using a spin-coating

Annual Research Journal, Vol. IV
Electrical Engineering Research Experience for Undergraduates

ISBN 0-913260-06-1 (http://www.ee.psu.edu/reu/)

technique. The non-linear core was chosen to be the copolymer Disperse Red 1-methyl methacyrlate (DR1-MMA) at 10% molar mass. Properties of this material have been described in detail elsewhere[3].

The copolymer must also be applied using spin-coating. After applied the desired thickness, the sample must be baked at high temperatures to achieve a solid formation. First, the sample is pre-baked for several hours at 1 ATM at approximately 121 C (Tg – 10 C). Then the sample is placed in a vacuum oven and baked at approximately 151 C (Tg + 20 C) overnight. Great care must be taken to avoid any air bubbles in the polymer, as they will result in a non-uniform field within the waveguide.

To pole the polymer, a mask is applied with the appropriate domain length. A technique of contact poling[4] is used: voltage is applied at about 50-60V/μm.

The waveguide is then completed by fabricating another half (silica glass, metal poling later, and UV-curable acrylate) with the procedures outlined above, then pressing the two halves together.

Parameter Analysis

Both analytic and numerical methods will be used to calculate the optimal parameters for THz waveform generation in the proposed structure. Specifically, the finite-element analysis technique within FEMLAB 3.1 will be used to obtain appropriate results for various configurations of poling domain length, material type, and layer thickness within the structure.

RESULTS & DISCUSSION

It should be noted that for the purposes of simulation, the metallic layers in the waveguide are assumed to be perfect conductors, and therefore create a boundary condition of E = 0. In an actual setup, this cannot be assumed for optical frequencies.

The waveguide itself should be modeled so that not only do both the optical pump beam and resulting THz waveform propagate in their fundamental modes, but so that the maximum amount of energy is contained within the waveguide and transmitted. The basic equations modeling a symmetric parallel-plate waveguide are

$$\frac{\partial^2}{\partial x^2}E(x,y)+(k_0^2 n_1^2-\beta^2)E(x,y)=0 \quad \text{(inside core region)} \tag{6.1}$$

$$\frac{\partial^2}{\partial x^2}E(x,y)+(k_0^2 n_2^2-\beta^2)E(x,y)=0 \quad \text{(outside core region)} \tag{6.2}$$

implying a sinusoidal or exponentially decaying solution[7]. In our case, the solution is sinusoidal in the core region, resulting in a basic solution of

Annual Research Journal, Vol. IV
Electrical Engineering Research Experience for Undergraduates

ISBN 0-913260-06-1 (http://www.ee.psu.edu/reu/)

$$E \propto \sin(hx + \alpha)\exp(-i\beta z) \tag{7}$$

where the constant h obeys the relation

$$h^2 = k_0^2 n_1^2 - \beta^2 \tag{8}$$

to satisfy the wave equation in (9.1). The solution in the cladding regions imply exponential decay.

Of important consideration is the coherence length of the waveguide in question. For difference-frequency generation within the waveguide, the coherence length can be approximately written as[1]

$$L_c = \frac{\pi c}{\omega_{THz}\left|n_g - n_{THz}^{eff}\right|} \tag{9}$$

where n_g is the optical group velocity, and n_{THz}^{eff} is the effective refractive index of the waveguide structure in THz frequency conditions. In the case of our particular waveguide, the following graph is presented with various thicknesses of the cladding.

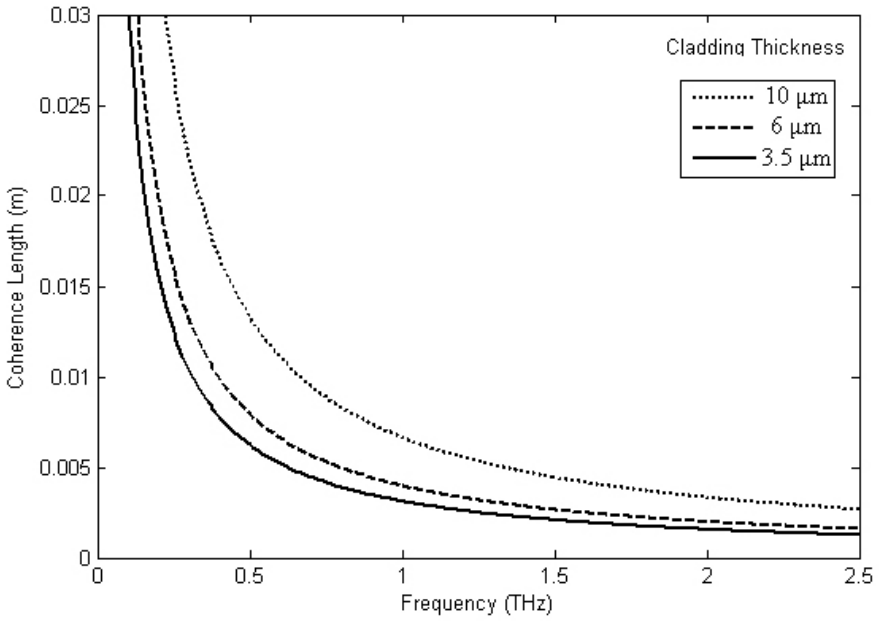

Fig. 2. Frequency versus coherence length for optical rectification with various thicknesses of the cladding acrylate.

Annual Research Journal, Vol. IV
Electrical Engineering Research Experience for Undergraduates

ISBN 0-913260-06-1 (http://www.ee.psu.edu/reu/)

While a smaller cladding layer will allow for increased coherence length, one must take into the account the difficulty of practically manufacturing such a layer. As stated earlier, we will work with a 3.5 μm thick cladding layer.

Work has been done[5, 6] regarding periodically poled structures tuning the output terahertz wave to a specific frequency. Specifically, the equation

$$v_{THz} = c / 2d(n_T - n_O) \tag{10}$$

will govern the output THz frequency, where d is the domain length and n_T and n_0 are the THz and optical refractive indices, respectively. The relative bandwidth Δv/v is given by 2/N, where N is the number of domain lengths over the length of the sample waveguide.

Modeling the waveguide using the proposed measurements of Cao *et al.*[1] (3 μm core thickness, 3.5 μm cladding thickness) the following numerical solution is obtained.

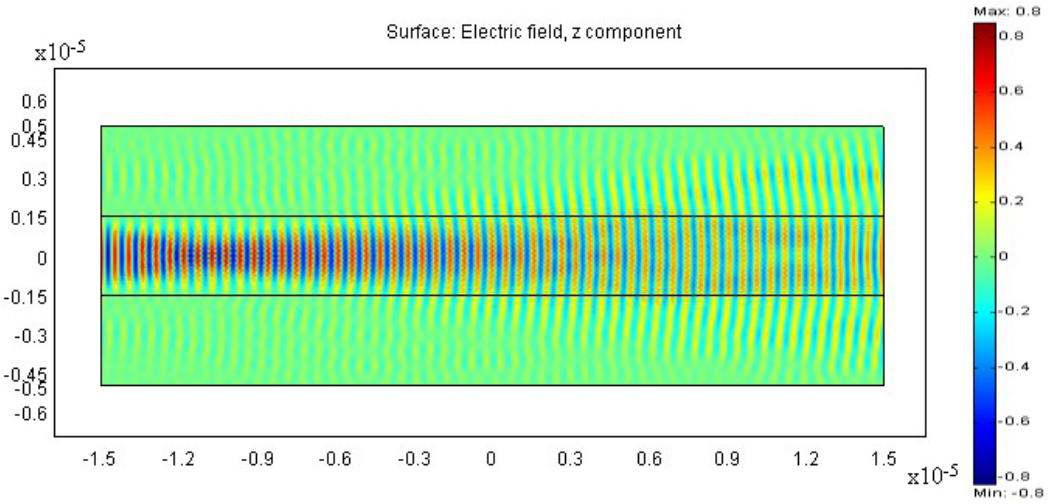

Fig. 3. The numerical solution of the optical pump beam in the proposed waveguide structure.

Three subdomains were initiated that modeled the respective materials of which they consisted. The top and bottom of the waveguide used boundary settings to model metal layers, while other edges were set up as matched boundary conditions. On entry (left side of the core region), the electric field was modeled as sin(pi*(a-y)/(2*a)), where a is half the thickness of the core. This is the known shape of the TE10 mode in an infinitely long rectangular waveguide.

Here, we can see the propagation of the optical pump beam. The loss of energy is due to the small difference between layer indices of refraction (1.557 for

Annual Research Journal, Vol. IV
Electrical Engineering Research Experience for Undergraduates

ISBN 0-913260-06-1 (http://www.ee.psu.edu/reu/)

the cladding, and 1.5667 for the core). Taking a cross-sectional plot of the center line, we see the following:

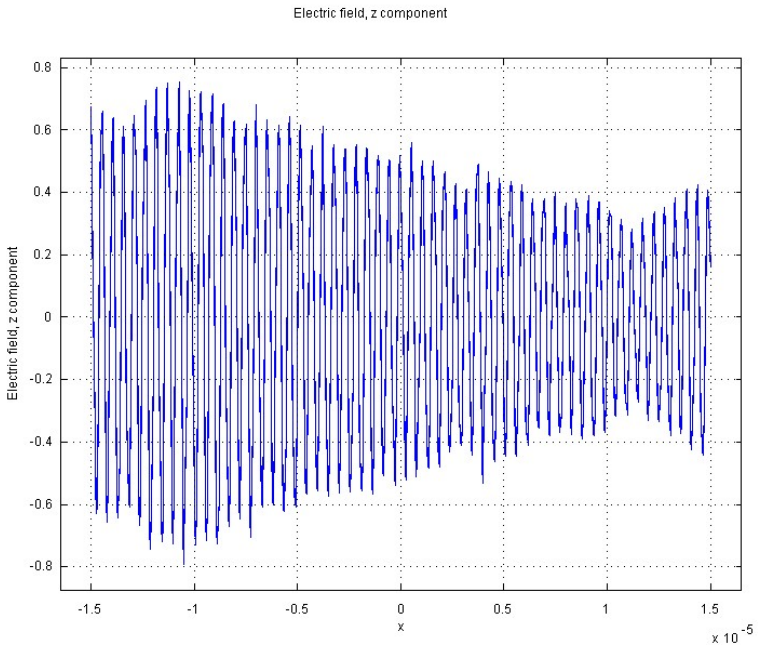

Fig. 4. A cross-sectional plot of the waveguide, showing the strength of the electric field down the center of the core.

The propagation period is measured as 0.5283 μm. The propagation constant is defined as

$$\beta = \frac{2\pi}{\lambda_m} \tag{12}$$

where λ_m is the propagation period. Thus, the propagation constant is measured to be 1.189×10^7. The following table presents the results for varying optical pump wavelengths.

Table I. A table compiling the results of various optical pump beam wavelengths.

Optical Pump λ_0 (nm)	Propagation Period λ_m (μm)	Frequency ω (Hz)	Propagation Constant β
800	0.51165	2.3562×10^{15}	1.228×10^7
810	0.51945	2.3271×10^{15}	1.2096×10^7
820	0.52711	2.2987×10^{15}	1.192×10^7
830	0.53465	2.2710×10^{15}	1.1752×10^7

Annual Research Journal, Vol. IV
Electrical Engineering Research Experience for Undergraduates

ISBN 0-913260-06-1 (http://www.ee.psu.edu/reu/)

To find v_g, the group velocity of the optical beam, we must use the equation

$$v_g = \frac{d\omega}{d\beta} \tag{13}$$

And so, we obtain the following three approximations for v_g:

Table II. The group velocities of the optical pump beam at slightly varying wavelengths.

1.5815×10^8
1.61364×10^8
1.64881×10^8

The average group velocity is 1.61465×10^8 m/s. The changes in group velocity appear to be larger than expected, but this is most likely due to a limited number of sample points and the non-differential approximation technique.

Future Work

Future work on this project includes the actual fabrication and experimental testing of the proposed waveguide structure, as described in the experimental procedure section. Power output must be optimized, and implementing a "tunable" frequency structure[6] for specific applications.

CONCLUSION

In conclusion, we have proposed and theoretically modeled an optical rectification device for terahertz wave generation. By using a periodically poled structure inside a waveguide, power levels are expected to exceed previously implemented devices. The structure allows for fundamental propagation of both the optical pump beam and THz wave, satisfying a quasi-phase-matching condition. This device is an excellent tool in advancing THz technology.

ACKNOWLEDGEMENTS

This material is based upon work supported by the National Science Foundation under Grant No. EEC-0244030.

Annual Research Journal, Vol. IV
Electrical Engineering Research Experience for Undergraduates

ISBN 0-913260-06-1 (http://www.ee.psu.edu/reu/)

REFERENCES

1. H. Cao, R. A. Linke, and A. Nahata, "*Broadband Generation of Terahertz Radiation in a Waveguide*", Optics Letters **27** (15), 1751 (2004).
2. R. Mendis and D. Grischowsky, J Appl. Phys. **88,** 4449 (2000).
3. A. Nahata, J. Shan, J. T. Yardley, and C. Wu, J. Opt. Soc. Am. B **10**, 1553 (1993)
4. X. Zhang, X. Lu, L. Wu, R. Chen, "*Contact poling of the nonlinear optical film for polymer-based electro-optic modulator*", Proc. SPIE, **4653** (2002).
5. Y.S. Lee, T. Maede, H. Winful, and T.B. Norris, "*Generation of narrow-band terahertz radiation via optical rectification of femtosecond pulses in periodically poled lithium niobate*", Applied Physics Letters **76** (18), 2505 (2000).
6. Y.S. Lee, T. Maede, and T.B. Norris, "*Tunable narrow-band terahertz generation from periodically poled lithium niobate*", Applied Physics Letters **78** (23), 3583 (2001)
7. A. Yariv, Propagation and Coupling of Modes in Optical Dielectric Waveguides – Periodic Waveguides, p. 491-499, *Optical Electronics in Modern Communications*, Fifth Edition, J. Mercado & M .E. Johnson, Oxford University Press, Oxford, England, 1997.

ISBN 0-913260-06-1 (http://www.ee.psu.edu/reu/)

MICROWAVE CHARACTARIZATION OF METAMATERIALS

Lana H. Carnel[*], Khalid Z. Rajab[+], Steven E. Perini[†], Michael T. Lanagan[#]

Department of Electrical Engineering
Department of Engineering Science and Mechanics
The Pennsylvania State University, University Park, PA 16802

[*]Undergraduate student of
Department of Electrical and Computer Engineering
University of Tennessee, Knoxville, TN 37996

ABSTRACT

Metamaterials research is a rapidly growing field for electrical engineers, physicists, and material scientists because of the unusual properties they possess, such as negative refractive index. Metamaterials are comprised of individual resonators, the fundamental building blocks for metamaterials, which are arranged in a periodic array. Resonators were studied at microwave frequency (18 to 26 GHz). Simple rectangular and cylindrical cavity resonators with metal walls were explored and then dielectric resonators with a range of permittivity values were evaluated. It was found that dielectric resonators with low dielectric permittivity had very high radiation loss, which is unsuitable for metamaterials in the microwave frequency range. Materials with dielectric permittivity greater than 10 were found to be the most promising for metamaterial resonators.

INTRODUCTION

Metamaterials are artificial materials that exhibit properties that are different from those of its individual components, and may not be found in nature. They were initially proposed by Veselago in 1968 [1] and were later developed by Shelby, Smith, and Schultz in 2000 [2].

[+] Graduate Mentor
[†] Technical Mentor
[#] Faculty Mentor

Annual Research Journal, Vol. IV
Electrical Engineering Research Experience for Undergraduates

ISBN 0-913260-06-1 (http://www.ee.psu.edu/reu/)

Metamaterials are studied through examination of resonant frequencies of individual cylindrical elements. Resonance occurs when the oscillating electric and magnetic fields maintain themselves within a cavity structure. This occurs when the electromagnetic fields form standing waves within the metal or dielectric boundaries of the cavity. The resonator shape may be cylindrical or rectangular, and the resonant frequency is affected by the resonator size and material within the resonator. Generally, the resonant frequency decreases as the cavity size increases and the dielectric permittivity increases.

In this study, several resonator structures were explored. First, a rectangular cavity, which has metal walls and air as the dielectric, was studied. Next, cylindrical cavities with metal walls were investigated, and then cylindrical dielectric resonators were explored. Metamaterials comprised of dielectric resonator arrays have been investigated earlier [3]. An example of a dielectric resonator array is shown in Figure 1.

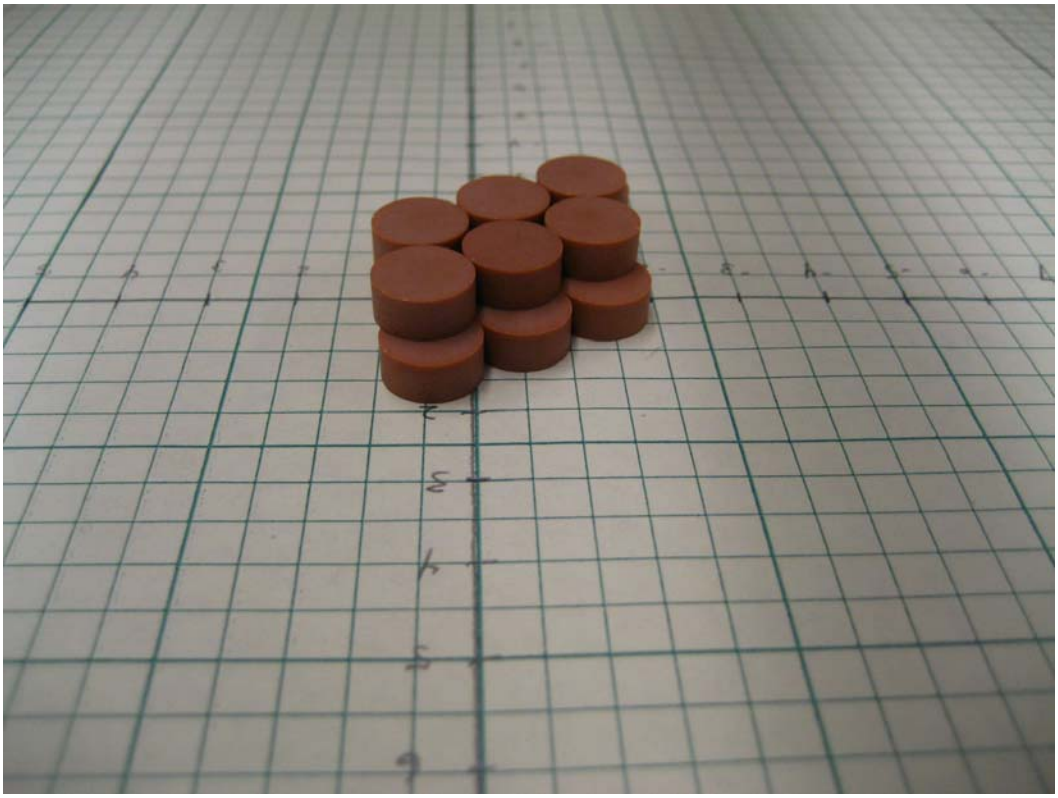

Figure 1: Ceramic dielectric resonator array

It was found that the resonators interacted with one another to scatter microwaves in unusual ways. In order to better understand the properties of the metamaterial array, individual resonator properties were investigated.

Annual Research Journal, Vol. IV
Electrical Engineering Research Experience for Undergraduates

ISBN 0-913260-06-1 (http://www.ee.psu.edu/reu/)

Resonant frequencies in rectangular cavities are a function of the cavity geometry, relative permeability, and permittivity. Two primary types of resonant modes are defined as transverse electric (TE) and transverse magnetic (TM) modes, which define the electromagnetic fields in the microwave propagation direction. Interpretation of these TE_{mnl} or TM_{mnl} modes, given in [4] are made using the following:

$$f_{mnl} = \frac{c}{2\pi\sqrt{\mu_r \varepsilon_r}} \sqrt{\left(\frac{m\pi}{a}\right)^2 + \left(\frac{n\pi}{b}\right)^2 + \left(\frac{l\pi}{d}\right)^2} \qquad (1)$$

where: a is interior waveguide width
b is interior waveguide height
d is the length of the cavity
f_{mnl} is resonant frequency of the mode
m,n,l correspond to the number of variations in the standing wave pattern in the x,y,z directions respectively

Modes are distinguished by the values of m,n,l as shown in Figure 2. Red curves represent the maxima and minima of the electric field vector along the x, y, z directions in the cavity. Integers representing m,n,l indicate maxima in the electric field corresponding to the number of half wavelengths of the standing wave. The electric field's polarity alternates with each half wavelength.

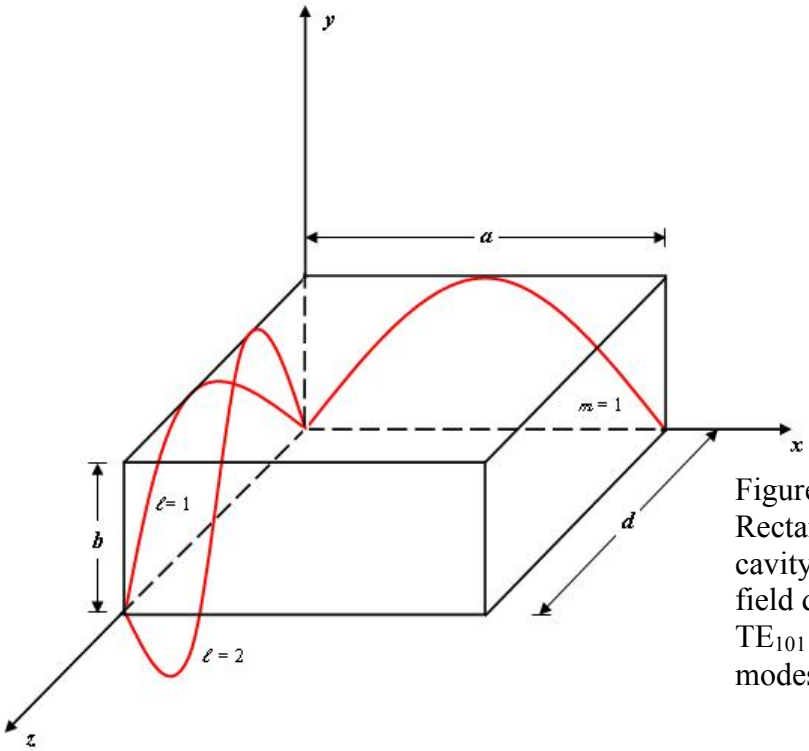

Figure 2: Rectangular resonant cavity with electric field distribution for TE_{101} and TE_{102} modes.

Annual Research Journal, Vol. IV
Electrical Engineering Research Experience for Undergraduates

ISBN 0-913260-06-1 (http://www.ee.psu.edu/reu/)

This was demonstrated using a thin copper plate (with a small center hole) that was attached to each end of a rectangular waveguide before connecting to the network analyzer to create the standing wave inside the waveguide's cavity. The waveguide used is shown in Figure 3 and has dimensions a = 34.90mm, b = 15.67mm, and d = 470mm.

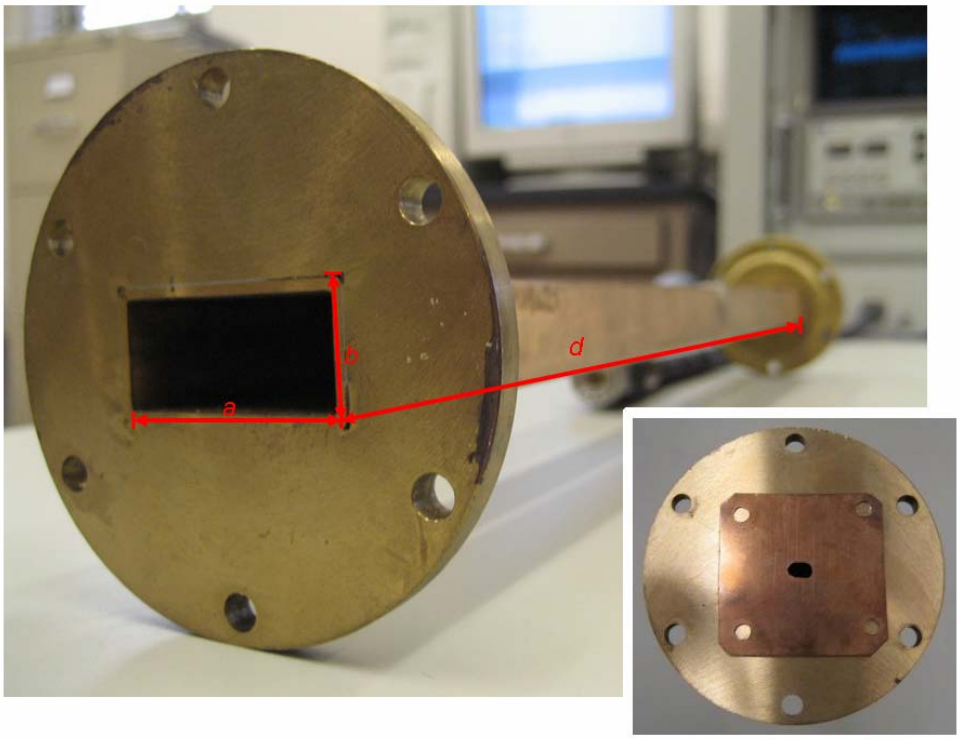

Figure 3: C-Band Waveguide with Inset of Waveguide with Copper Plate Covering

The air filled cavity has both relative permittivity (ε_r) and permeability (μ_r) of 1. Also, as $b < a < d$, the dominant resonant mode (lowest resonant frequency) is the TE_{101} mode. It is then possible to examine the l variations of the standing wave as a function of frequency by using the simplified equation:

$$f_{mnl} = \frac{c}{2\pi}\sqrt{\left(\frac{\pi}{a}\right)^2 + \left(\frac{l\pi}{d}\right)^2} \qquad (2)$$

Consulting a Standard Rectangular Waveguide Data sheet, these dimensions indicate operation in the C band, with a Cutoff Frequency of 4.301GHz, justifying network analyzer trace boundaries of 4.68-8.2GHz. The simplified equation was then used with each observed peak. Near integer, consecutively increasing, numbers for the resulting l values were expected.

Annual Research Journal, Vol. IV
Electrical Engineering Research Experience for Undergraduates

ISBN 0-913260-06-1 (http://www.ee.psu.edu/reu/)

The rectangular cavity was characterized by a network analyzer in which the magnitude of the transmitted power through the cavity was measured. Resonant frequencies are indicated by peaks in transmitted power (Figure 4). Using peak values from the transmitted power data and inserting into the simplified equation above, calculated *l* values are as follows:

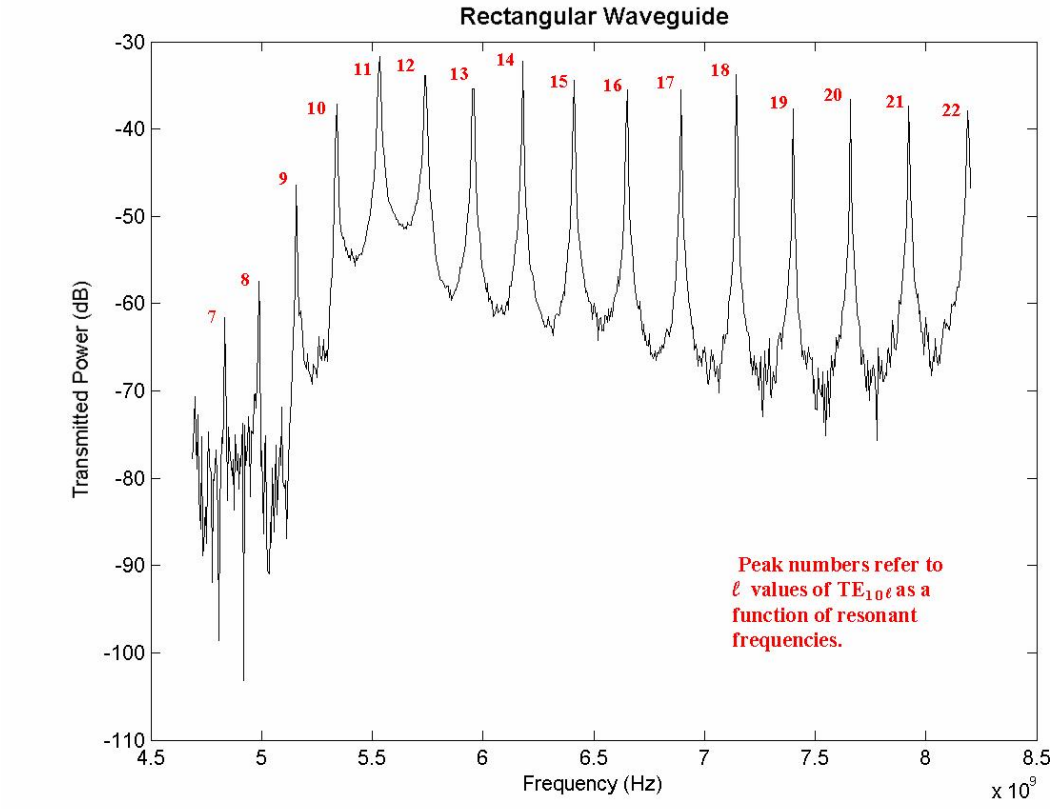

Figure 4: Graphical representation of calculated *l* values with forward transmission measurements

CYLINDRICAL CAVITIES

As indicated by Balanis [4], cylindrical cavities are similar to rectangular cavities, except that the boundary conditions use Bessel function solutions instead of sinusoidal solutions to Maxwell's equation. Transverse electric and magnetic propagation are similarly described for cylindrical cavities by the equation:

$$f_{mnl} = \frac{c}{2\pi\sqrt{\mu_r \varepsilon_r}} \sqrt{\left(\frac{p'_{mn}}{a}\right)^2 + \left(\frac{l\pi}{d}\right)^2} \qquad (3)$$

Annual Research Journal, Vol. IV
Electrical Engineering Research Experience for Undergraduates

ISBN 0-913260-06-1 (http://www.ee.psu.edu/reu/)

where: a is cavity radius
d is the height of the cylinder
p' is the m^{th} root of J'n (solutions to the Bessel functions)
f_{mnl} is resonant frequency of the mode
l is the number of half-wavelengths in the z- direction

Mode distinctions are made by values of m,n,l as shown in Figure 5. Red curves represent the magnitude of the electric field vector along the r and z directions of the cylinder. The electric field in the d direction falls to negligible magnitudes at the top and bottom of the cavity due to the conductivity of the metal walls.

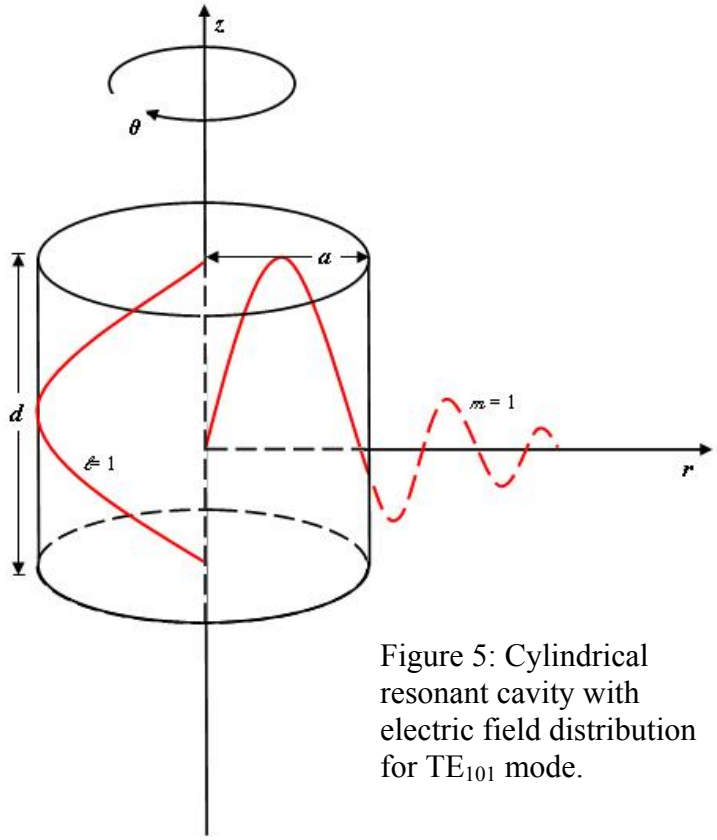

Figure 5: Cylindrical resonant cavity with electric field distribution for TE_{101} mode.

A cylindrical cavity of radius of 86.5mm and height 76mm. The cavity used for experimentation can be seen in Figure 6.

Annual Research Journal, Vol. IV
Electrical Engineering Research Experience for Undergraduates

ISBN 0-913260-06-1 (http://www.ee.psu.edu/reu/)

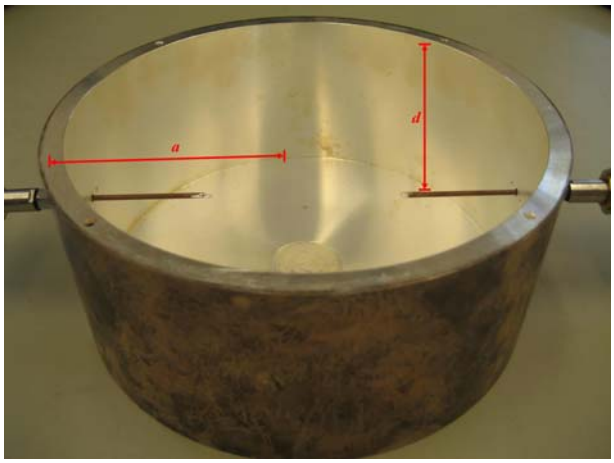

Figure 6:
Cylindrical resonant cavity with top metal plate removed.

Cutoff frequency is found as 1.3762GHz and appropriate trace boundaries are chosen as 1GHz-3.26GHz. The above equation is then used to determine modes corresponding with peak values. The complex geometry requires consideration of several different modes to determine *l* values for consecutively occurring peaks. Using peak values from the transmitted power data and inserting into the simplified equation above, calculated TE modes are as follows:

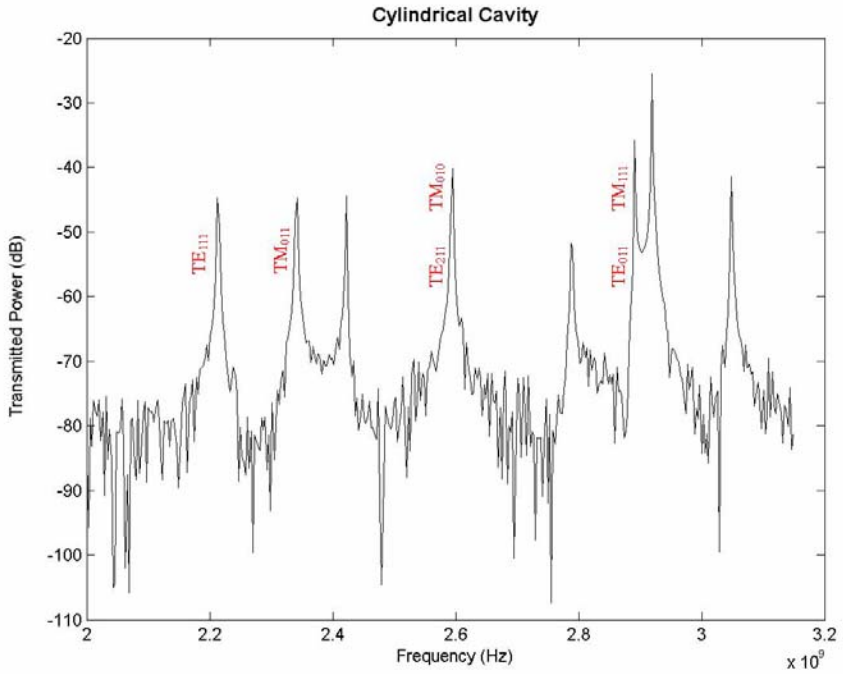

Figure 7: Graphical representation of calculated TE/TM modes with forward transmission measurements

ISBN 0-913260-06-1 (http://www.ee.psu.edu/reu/)

DIELECTRIC RESONATORS

Dielectric resonators, described in [5], behave similarly to the air filled cylindrical cavity. However, electric field waves do not reach zero values at the top and bottom of the cylinder, and instead asymptotically approach the *z*-axis at some point outside the resonator.

This difference between the cylindrical cavity and dielectric resonator is noted in the preceding section's nomenclature by replacing the variable *l* with δ to indicate the extension of the electric field along the *z*-direction and is illustrated in Figure 8.

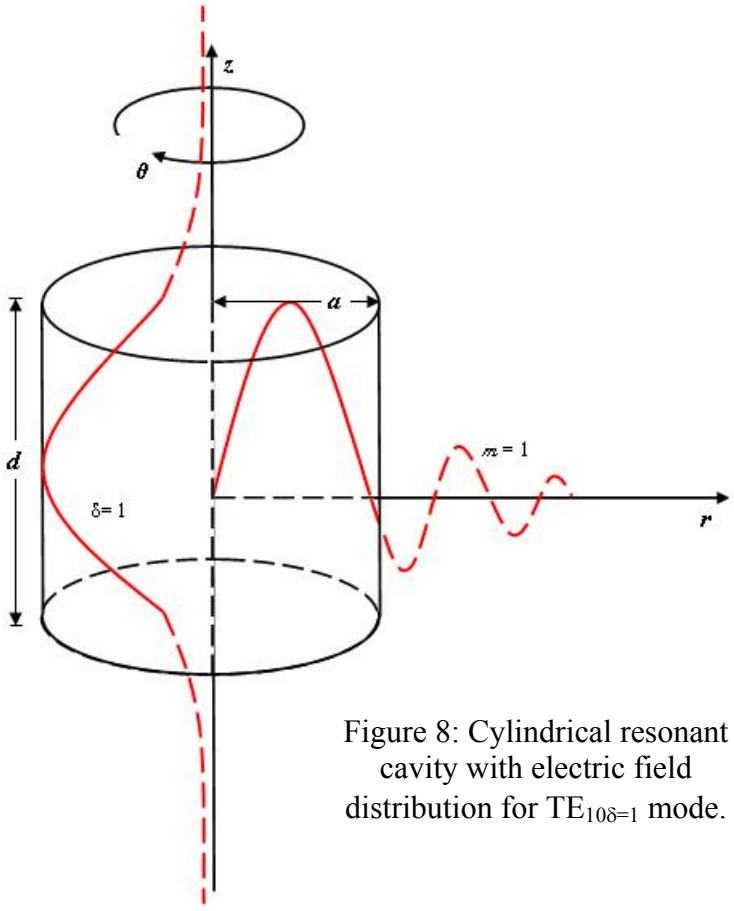

Figure 8: Cylindrical resonant cavity with electric field distribution for $TE_{10\delta=1}$ mode.

It is this phenomenon that allows dielectric resonators to couple with one another if the trailing wavelengths are in close enough proximity to interact with one another. We choose three materials: Teflon, alumina, and ceramic, whose permittivities are 2, 9, and 37, respectively, to provide a range of results.

Annual Research Journal, Vol. IV
Electrical Engineering Research Experience for Undergraduates

ISBN 0-913260-06-1 (http://www.ee.psu.edu/reu/)

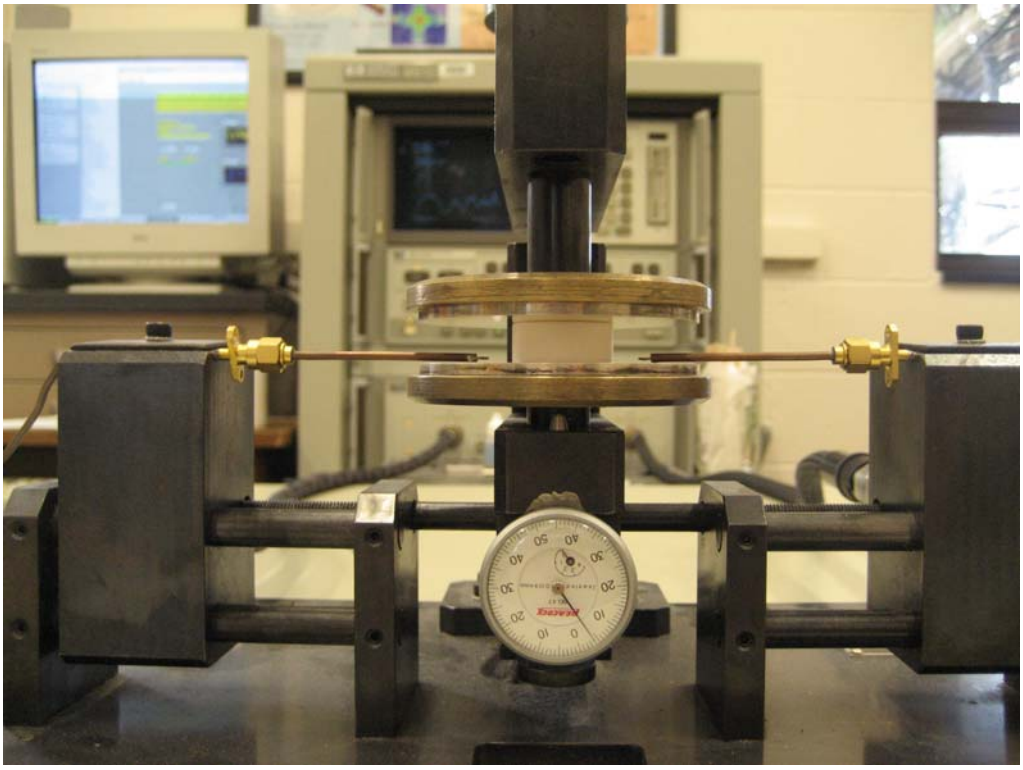

Figure 9: Hakki-Coleman apparatus with Upper Plate Touching Teflon Sample

In order to investigate the electric field extension outside the dielectric resonator, the top plate of resonant post experiment was moved above the cylinder (Figure 9). The resonant frequency will decrease as the top plate is raised and the frequency change is proportional to the electric field outside the resonator. In addition, the loss of the resonator was quantified by the Q factor which is defined as the inverse of the resonator loss.

Both changing Q values and peak location are measured. Q value is calculated as:

$$Q_{loaded} = \frac{f_o}{f_2 - f_1} \qquad (4)$$

where: f_0 is fundamental resonant peak
f_2-f_1 is half power bandwidth

Q is presented as a function of the separation of the metal plates as a percent of sample height as seen in Figure 10.

ISBN 0-913260-06-1 (http://www.ee.psu.edu/reu/)

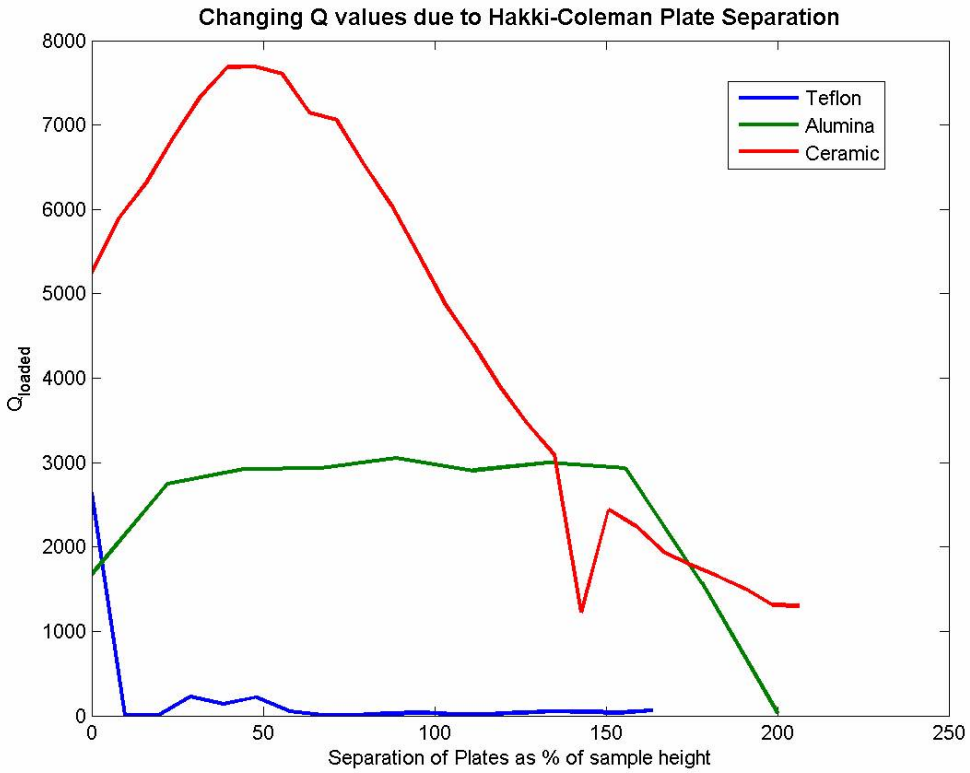

Figure 10: Cylindrical resonant cavity with electric field distribution for $TE_{10\delta=1}$ mode.

The Q increases initially for the alumina and ceramic samples due to the decreased effect of resistive losses from the metal plate. For all of the dielectric resonator materials the Q drops as sample height is increased beyond a threshold value, which was attributed to radiation losses. The degree and speed with which the decrease in Q occurs is due to the extension of the electric field outside of the dielectric resonator. The low permittivity of Teflon indicates a minimal reaction to conduction and great sensitivity to radiation loss, which suggests that the electric field extends very far outside of the Teflon resonator. The effect is proportionately less pronounced as the permittivity of the sample increases; more of the electric field energy is concentrated within high permittivity materials. Materials with higher permittivity exhibit wave δ oriented electric field values more closely equal to zero at the resonator boundaries as illustrated in Figure 11.

Annual Research Journal, Vol. IV
Electrical Engineering Research Experience for Undergraduates

ISBN 0-913260-06-1 (http://www.ee.psu.edu/reu/)

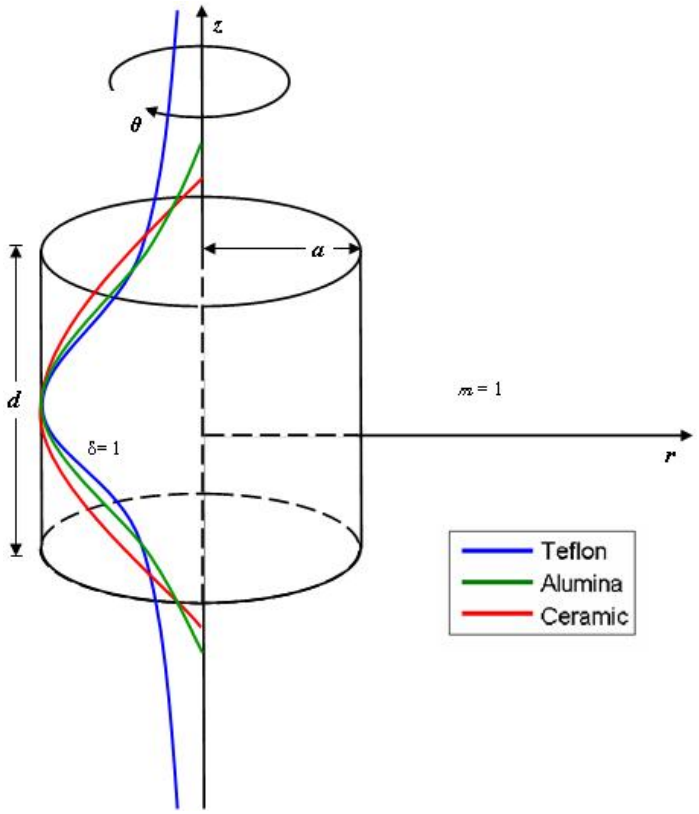

Figure 11: δ direction radiation of varying materials

The relative frequency shift as a function of separation of plates provides the basis for extrapolation into much larger distances. Frequency shift is normalized as:

$$fshiftnorm = 1 - \left(\frac{f_{0c} - f_o}{f_{0c}} \right) \qquad (5)$$

While the data as shown in Figure 12 indicates that the magnitude of frequency shift is inversely proportional to the amount of plate separation; frequency shift is proportional to electric field extension beyond the resonator. The color-coded equations indicate exponential curves fitted to the corresponding data points. The third Teflon data point is omitted during curve fitting to provide a curve that is more representative of the overall data trend.

ISBN 0-913260-06-1 (http://www.ee.psu.edu/reu/)

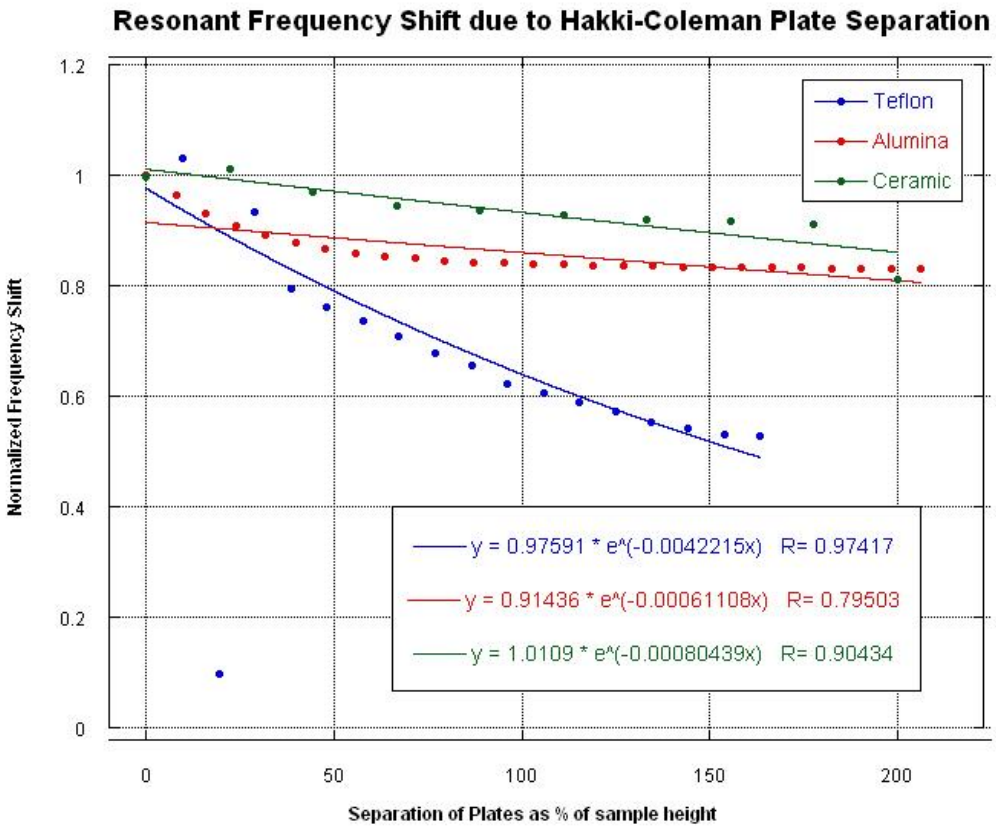

Figure 12: Frequency shift magnitude as a function of plate separation

CONCLUSIONS

Cavity and dielectric resonators were systematically investigated by measuring the microwave response and determining the resonant frequencies from the cavity dimensions. Individual dielectric resonators that comprise metamaterial structures were investigated. In addition, the electrical properties of the dielectric materials were characterized. Through this work, we have determined that dielectrics exhibit Q loss inversely proportional to permittivity. We also find that normalized frequency shift becomes larger for lower permittivity samples, indicating that the electric field extends beyond the dielectric walls into free space. The permittivity must also be low enough to exhibit distinct TE/TM modes at the desired frequency range (18-26 GHz). Further experimentation is necessary to determine the effects of resonator volume in addition to relative height. It is also necessary to examine several other dielectrics with an even greater range of permittivities to further establish Q loss relationships. The results of these experiments imply that materials used for the construction of metamaterials must have permittivities of greater than 10. While some radiation must occur outside the resonator to allow for coupling, the overall

Annual Research Journal, Vol. IV
Electrical Engineering Research Experience for Undergraduates

ISBN 0-913260-06-1 (http://www.ee.psu.edu/reu/)

radiation loss and frequency shift must be less than that observed in Teflon and Alumina samples.

ACKNOWLEDGEMENT
This material is based upon work supported by the National Science Foundation under Grant No. EEC-0244030.

REFERENCES

[1] V. Veselago, "The electrodynamics of substances with simultaneously negative values of ε and μ," *Soviet Physics Uspekhi*, vol. 10, no.4, pp509-514, 1968.

[2] R.A. Shelby, D.R. Smith, and S. Schultz, "Experimental verification of a negative index of refraction," *Science*, vol.292, no. 5514, pp.77-79, 2001.

[3] M. Iwasaki, E. Semouchkina, G. Semouchkin, K. Rajab, C. Randall, M. Lanagan, "Symmetry Matching of Hybrid Modes for Dielectric Metamaterials," *Japanese Journal of Applied Physics Part 1-Regular Papers Brief Communications & Review Papers*, 45(4a): 2835-2841 (Apr 2006).

[4] C. Balanis, *Advanced Engineering Electromagnetics*, New York: Wiley, 1989.

[5] B.W. Hakki and P.D. Coleman, "A Dielectric Resonator Method of Measuring Inductive Capacities in the Millimeter Range," *IRE Trans. Microwave Theory Tech*., vol. 8, pp. 401-410, July 1960.

ISBN 0-913260-06-1 (http://www.ee.psu.edu/reu/)

PHASE LOCKED OPTICAL SENSING OF TWO-D PIEZOELECTRIC STRAIN

Matthew Blaisse* and Amar S. Bhalla#

Department of Electrical Engineering and Materials Research Institute
The Pennsylvania State University, University Park, PA 16802

*Undergraduate student of
Department of Physics
Lebanon Valley College
Annville, PA 17003

ABSTRACT

The purpose of this study is to demonstrate the advantages of a non-contact method of piezoelectric strain measurement. To this aim, the experiment utilizes a phase-sensitive optical technique for measuring small amounts of strain in $Pb(ZrTi)O_3$ – PZT bulk samples.

Small displacements in an AC-driven sample are detected by the MTI 2000 Fotonic™ fiber optic sensor. The output signal is then processed through the SR830 lock-in amplifier that locks in on that AC frequency, effectively ignoring the noise caused by external vibrations. In addition to providing a high degree of precision in displacement measurements, this non-contact method allows for the sample to be isolated and exposed to low temperatures. The experimental design therefore permits the exploration of some of the less well-known properties of PZT, including low field and low temperature effects. The mapping of the d_{33} piezoelectric coefficients at various points on two-dimensional surfaces was performed. The values obtained are close to reported values found using other measurement techniques. This method has great potential for future devices requiring the non-contact evaluation of sensing elements.

Future technology may also require the use of more environmentally friendly materials in piezoelectric devices. In this context, the measurements have been extended to the sensing elements of composition $Ba(ZrTi)O_3$ – BZT.

Faculty Mentor

Annual Research Journal, Vol. IV
Electrical Engineering Research Experience for Undergraduates

ISBN 0-913260-06-1 (http://www.ee.psu.edu/reu/)

INTRODUCTION

Of the 32 crystal groups, 20 exhibit the physical property known as piezoelectricity. The non-centro-symmetric structure of these crystals is such that a mechanical stress applied to a piezoelectric material results in an electric charge (and a measurable voltage/current). This is known as the direct piezoelectric effect. Conversely, an applied voltage/electric field will result in a measurable mechanical strain within the material.

The relationship between the mechanical/electrical input and the electrical/mechanical output is linear (at least for low fields). In particular, the converse piezoelectric effect is expressed by:

$$x_3 = d_{33} E_3 \tag{1}$$

where E_3 is the applied electric field and x_3 is the strain, or the ratio between the resultant displacement Δx and the sample thickness x_0. This linear relationship is defined by the coefficient d, known as the piezoelectric coefficient (units of picometers per volt). The subscripts represent the axes on which the strain or field are being measured or applied. In this case we are interested in measuring the strain along the 3-axis (or z-axis; the thickness of the sample) as a result of an electric field applied in that same direction.

To complicate matters, the d_{33} itself is also dependent on the strength of the applied electric field, as well as on frequency, temperature, geometry, boundary conditions, and other factors related to the chemical composition and molecular alignment of the sample. In addition, the d_{33} of a given sample cannot only change over time (such as with temperature), but can actually vary throughout the sample itself! Traditional contact methods of piezoelectric strain measurement leave these factors unexplored. Here we present a non-contact method of strain determination and experimentally demonstrate the advantages of such a system.

The experiment itself serves as an extension of the work done by Skrabut at the Pennsylvania State University as part of her Master's Thesis.[1] In her thesis, Skrabut discusses the difficulties she faced and how they were overcome. Here we do our best to make use of those findings. Like Skrabut, we continue to explore (albeit minimally) the low-temperature effect on the piezoelectric coefficient, however we also expand that research to investigate the variance of the piezoelectric coefficient throughout a given sample. Initial measurements were performed on $Pb(ZrTi)O_3$ – PZT samples and have been extended to the environmentally friendly composition $Ba(ZrTi)O_3$ – BZT.

EXPERIMENTAL DESIGN

By applying an electric field of known strength and accurately measuring the strain, one can make observations as to the nature of that strain, as well as determine the piezoelectric coefficient for the material. Unless a sample displaces uniformly (which a bulk disc or thin film is not likely to do), the d_{33} piezoelectric coefficient will not be the same throughout the sample. This experiment deals

Annual Research Journal, Vol. IV
Electrical Engineering Research Experience for Undergraduates

ISBN 0-913260-06-1 (http://www.ee.psu.edu/reu/)

with strain measurements and mapping of d_{33} piezoelectric coefficients on two-dimensional surfaces of samples through the application of the following procedure at various points.

The design of this experiment is best understood through the idea of signal flow (see Figure 1 below). We begin by using the SRS SR830 lock-in amplifier to generate an AC signal of variable amplitude and constant frequency (500Hz). The need for an AC voltage (as opposed to DC) will be explained in the following text. The signal is then amplified and offset before being applied to the sample, so as to avoid any unintended reverse poling of the pre-poled sample. We define the applied electric field as simply the peak-to-peak voltage per centimeter thickness. This oscillating electric field causes the sample to vibrate at the frequency of the AC signal. The sample itself is isolated in a temperature-controlled vacuum chamber.

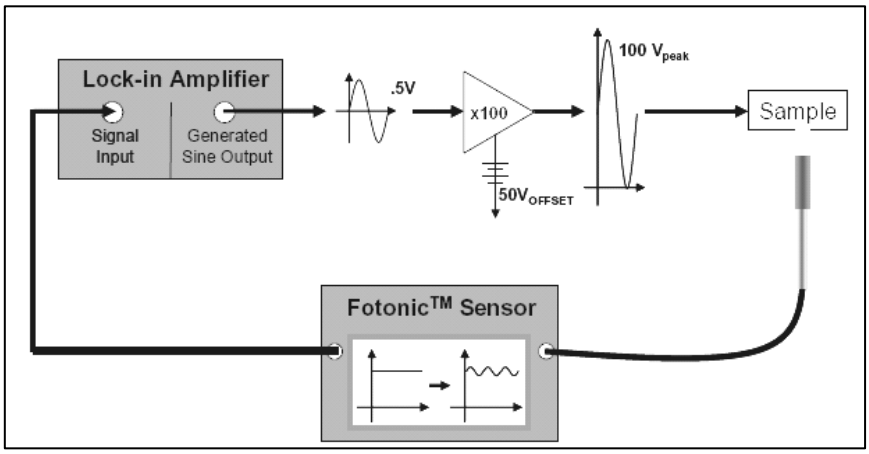

Figure 1: Block diagram of the measurement system design.[1]

The MTI 2000 Fotonic™ sensor detects small displacements in the sample and expresses this information as a voltage signal. These displacements, however, are insignificant compared to room noise and other external sources of vibration. For this reason, the signal is actually sent back to the lock-in amplifier. By comparing this signal to the AC signal it itself is generating, the lock-in can single out the frequency of interest, effectively ignoring the external noise. The resultant reading can then be related to a displacement in the sample, and the d_{33} piezoelectric coefficient can be determined. The basic design is simple enough, however the real uniqueness of this technique is in the use of the optical sensor in conjunction with the lock-in amplifier. They both deserve a closer look.

Phase Locked Optical Sensing

The MTI 2000 Fotonic™ sensor probe is an array of pairs of fiber optic cables. Each pair consists of one cable designed to emit light, and one designed to collect any reflections of that light from the sample surface (see Figure 2). Each probe "sees" some area of the surface, and it is only when those areas

Annual Research Journal, Vol. IV
Electrical Engineering Research Experience for Undergraduates

ISBN 0-913260-06-1 (http://www.ee.psu.edu/reu/)

overlap that reflection is detected. This overlapping varies with the probe to surface distance. For example, if the probe was in direct contact with the surface, one would expect there to be no reflection picked up, as the "seeing" areas of each cable are simply side-by-side. As the probe is moved further away from the sample, however, one would expect the areas to overlap, resulting in more reflection being picked up by the second cable, and therefore resulting in an increasing output reading. At some point the two areas should completely overlap. This is called the optical peak. As the probe continues to move further away, the areas should overlap less and less, and so the output reading should decrease. This trend is called the calibration curve of the probe (see Figure 2).

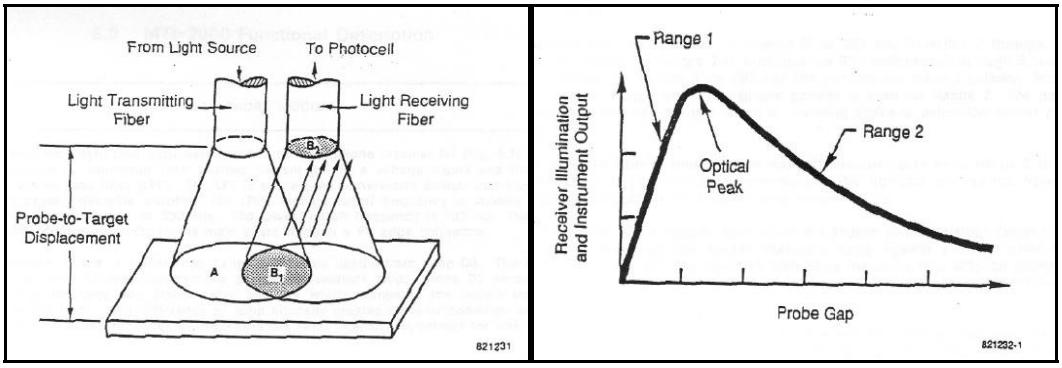

Figure 2: Inner workings (left) and calibration curve (right) of the MTI 2000 Fotonic™ sensor.[2]

Because this experiment aims in part to map the surface of the sample, it is necessary for the light to be as finely focused as possible. Also, the desire to isolate the sample (so that it may be exposed to low temperatures) creates the need for a greater standoff distance between the probe and sample. For these reasons it was necessary to employ an optical extender. The optics of the MTI KD-LS-1A optical extender are such that the calibration curve contains a null in place of where the optical peak should be (see Figure 3).

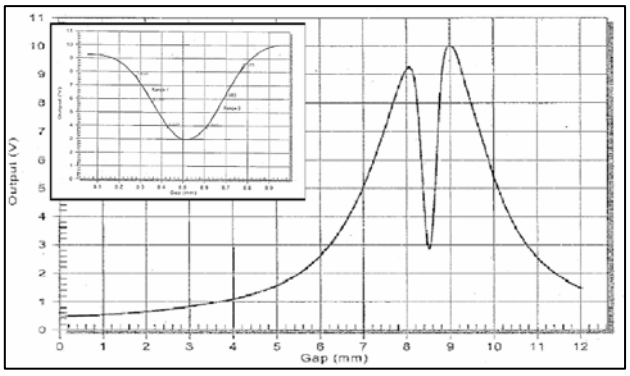

Figure 3: Calibration curve of the KD-LS-1A optical extender.[3]

Annual Research Journal, Vol. IV
Electrical Engineering Research Experience for Undergraduates

ISBN 0-913260-06-1 (http://www.ee.psu.edu/reu/)

The main idea behind using the MTI 2000 Fotonic™ sensor is to work within a region of the calibration curve such that the output voltage signal received from the sensor can be translated into a displacement value. As can be seen above, the curve of the probe alone (Figure 2) has two workable regions, whereas the probe with the extender (Figure 3) results in four. The best idea is to choose a linear region in which to work. For example, in this experiment we have chosen to work within the steep region of positive slope just to the right of the null. The slope of this linear region (units of V/mm) provides a conversion factor between the output voltage and the actual sample displacement.

It would be convenient if, at this point, the Fotonic™ sensor could just give us a number and thus the required values. Unfortunately the displacement signal we are interested in is overshadowed by external vibration and other sources of noise. There are two types of noise with which we need to be concerned: periodic and broadband. Broadband noise, which is essentially any part of the signal that is not periodic, is primarily reduced/eliminated using the filters found on both the lock-in and the Fotonic™ sensor. The broadband noise that is not filtered out is typically smoothed out through the integration and averaging process used to eliminate the periodic noise.

This process of integration and averaging essentially exploits the Fourier series, or the idea that any periodic signal can be thought of as a summation of sine functions at various frequencies and amplitudes. (See Figure 4.) The lock-in amplifier multiples the input signal by a square wave of amplitude one whose frequency is the same as the frequency being used to drive the sample. When multiplied by the square wave, the part of the signal whose frequency matches the reference frequency will be fully rectified such that when it is averaged the result will be a constant DC voltage. Any part of the signal whose frequency differs from the reference frequency will continue to be symmetric about the x-axis and thus will result in an average value of zero.

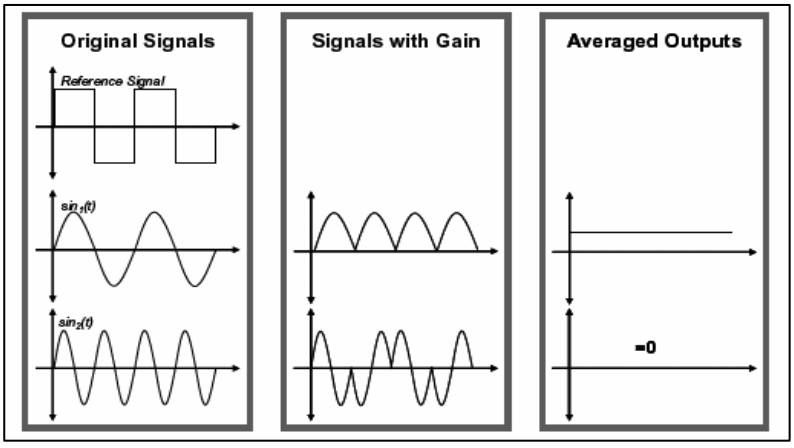

Figure 4: Operating principle of the lock-in amplifier.[1]

Annual Research Journal, Vol. IV
Electrical Engineering Research Experience for Undergraduates

ISBN 0-913260-06-1 (http://www.ee.psu.edu/reu/)

RESULTS AND DISCUSSION

The data collection process for each point on each sample involved the following procedure: once the Fotonic™ sensor was properly calibrated and the working zone determined, a computer was used to increase the strength of the applied electric field by step, while the output values given by the lock-in were recorded and averaged. Using these average values, the necessary calculations were performed, the data plotted, and the d_{33} piezoelectric coefficient found. Figure 5a shows a sample plot consisting of data gathered from the upper region of a $Pb(Zr_{0.48}Ti_{0.52})O_3$ – PZT 48/52 sample:

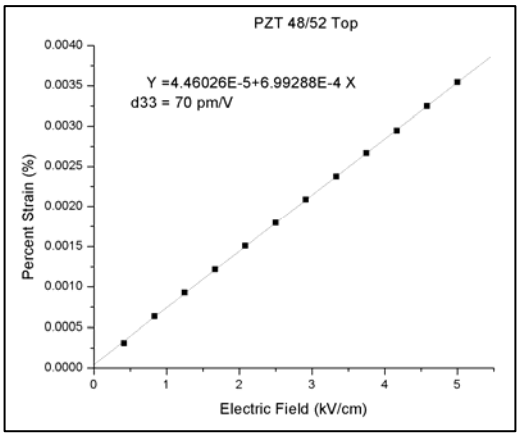

Figure 5a: Sample plot of Percent Strain vs. Electric Field.

The slope of the graph yields a d_{33} value of 70 pm/V. By repeating the above procedure for each point of interest on the surface (three total for this sample), the d_{33} piezoelectric coefficients can be mapped as shown in Figure 5b:

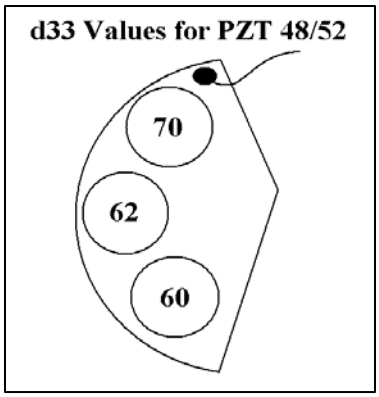

Figure 5b: d_{33} Values for PZT 48/52 at various points

In this case, all three points chosen were along the left (curved) edge. Because of their similar boundary conditions, it is of no surprise that the results show only minor discrepancies with respect to one another. Still, the differences do suggest that the idea of d_{33} mapping has potential.

Annual Research Journal, Vol. IV
Electrical Engineering Research Experience for Undergraduates

ISBN 0-913260-06-1 (http://www.ee.psu.edu/reu/)

Mapping of d33 Piezoelectric Coefficients

The dependency of the d_{33} on the geometry and boundary conditions of a sample suggests that a greater variety in point selection might yield more diverse results. A slightly larger sample of composition $Pb(Zr_{0.64}Ti_{0.36})O_3$ – PZT 64/36 allows us to probe five points instead of the previous three. The results (Figure 6) show much more significant differences between the measured d_{33} values:

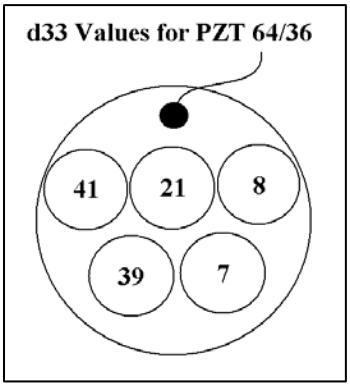

Figure 6: d_{33} Values for PZT 64/32 at various points

Strain measurements on the left side of the sample appeared significantly greater than those on the right, with the middle splitting the difference. The result is a set of d_{33} values ranging from 7 to 41. This makes it very difficult to state definitively the piezoelectric coefficient of this material, let alone of this sample. Unfortunately no specific conclusion can be immediately drawn as to the reason for this variance; there are countless factors that could have contributed to it. The simple fact this sample behaves in this manner, however, is evidence enough that the mapping done by this system is of great benefit.

Piezoelectric Response at Low Temperatures

Another advantage of this non-contact measurement system is its ability to perform strain measurements on a sample that has been isolated in a temperature-controlled chamber. Figure 7 presents the mapping of d_{33} values along the edges of a sample of composition $Pb(Zr_{0.53}Ti_{0.47})O_3$ – PZT 53/47 at two temperatures:

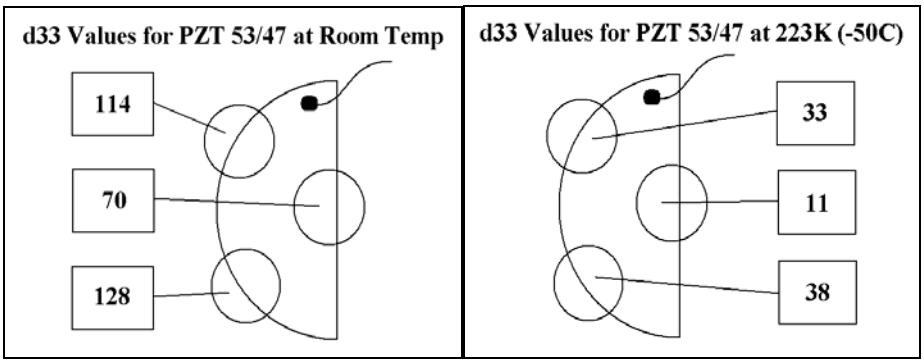

Figure 7: d_{33} Values for PZT 53/47 at various points at room temp and -50ºC

Annual Research Journal, Vol. IV
Electrical Engineering Research Experience for Undergraduates

ISBN 0-913260-06-1 (http://www.ee.psu.edu/reu/)

The variance between the two points on the curved edge is minimal, however the middle right edge shows significantly less strain. Regardless, all the room temperature results are within the range of expected values for PZT 53/47. The important thing to notice is the difference between the d_{33} values of the sample at room temperature compared to those at -50ºC. For example, the lower region at room temperature yields a d_{33} value of 128 pm/V, while at -50ºC the value is only 38. Clearly PZT 53/47 has a greater piezoelectric response at room temperature.

Not all piezoelectric materials, however, behave in this manner. For example, Figure 8 shows the results of measurements at the same two temperatures for the environmentally friendly composition $Ba(Zr_{0.15}Ti_{0.85})O_3$ – BZT:

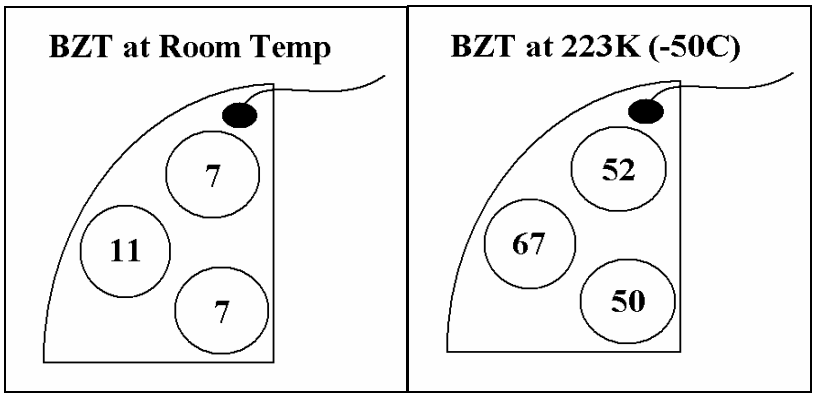

Figure 8: d_{33} Values for BZT at various points at room temp and -50ºC

Unlike PZT, BZT has a greater piezoelectric response at the low temperature. In particular, the room temperature measurements for the middle region resulted in a d_{33} value of only 11 pm/V, whereas the d_{33} at -50ºC was a much higher 67. Actually, BZT exhibits an even greater response at even lower temperatures. The only way to successfully measure the strain at these low-temperatures is with a non-contact method such as this.

Future Improvements

In order for this method to provide reproducible data, it is necessary for the sample surfaces (as well as any surfaces touching the sample) to be as flat as possible. In addition, the measurements are most reliable when the surface is highly reflective and the probe is completely perpendicular to the surface. It is recommended that future developments of this system take these factors into account more seriously. There also exists the potential for the construction of a set of probes working in this manner such that the strain (and hence the d_{33} piezoelectric coefficients) throughout a sample could be mapped all at once, with a computer program taking care of the necessary calibrations and calculations. Such an approach could be useful for testing array structure devices like ultrasonic transducers and for other experimental and commercial applications.

Annual Research Journal, Vol. IV
Electrical Engineering Research Experience for Undergraduates

ISBN 0-913260-06-1 (http://www.ee.psu.edu/reu/)

SUMMARY

1) A non-contact optical method has successfully been used to measure the piezoelectric strain on various surfaces.
2) The d_{33} piezoelectric coefficients 70 pm/V (for PZT 48/52) and 128 pm/V (for PZT 53/47) at frequency 500Hz were obtained. These values are close to the expected values (using a d_{33} meter at 60Hz).
3) The technique has been employed for the mapping of piezoelectric strain over the sample surfaces. In some cases the d_{33} values appeared to be different at various locations on the samples. Such results need to be correlated with the possible compositional heterogeneity of the samples, such as differences in the local poling (electrical state) of the samples.
4) The approach has also been used to measure the temperature dependence of the piezoelectric coefficient of the various samples.
5) A sample of the environmentally friendly composition BZT has been studied both at room temperature and at -50ºC (closer to its ferroelectric state). A reasonable d_{33} piezoelectric coefficient of 67 pm/V was measured.
6) The technique has great potential as a non-contact characterization tool for studying piezoelectric array structure devices.

ACKNOWLEDGEMENTS

Special thanks to Tanmoy Maiti, Dr. Ruyan Guo and Amanda Skrabut for their technical assistance with the instrumentation used in this experiment. Thanks also to Hongbo Liu and Gabriel Reyes who wrote the computer program used for data collection. This material is based upon work supported by the National Science Foundation under Grant No. EEC-0244030.

REFERENCES

[1] Skrabut, Amanda Ann. "High Precision Strain Determination Optimized for Cryogenic Temperatures by Phase Locked Optical Sensing." MS Thesis. The Pennsylvania State University, 2006.

[2] "MTI 2000 Fotonic™ Sensor User's Manual." Revision 2.3. MTI Instruments, Inc. Apr 2002. p. 37.

[3] "KS-LS-1A Optical Extender Operating Instruction Manual." Revision 1.1. MTI Instruments, Inc. 25 Aug 2004. pp. 5-6.

ISBN 0-913260-06-1 (http://www.ee.psu.edu/reu/)

DYNAMIC MEASUREMENT AND NUMERICAL SIMULATION IN STUDYING FREQUENCY DEPENDENCIES OF ELECTROOPTIC (EO) EFFECTS

Gabriel Reyes*, Hongbo Liu[+], and Ruyan Guo[#]

Department of Electrical Engineering and Materials Research Institute
The Pennsylvania State University, University Park, PA 16802

* Undergraduate student of
Department of Electrical & Computer Engineering
University of Florida
Gainesville, FL 32601

ABSTRACT

The electrooptic (EO) effect (at λ=633nm) in piezoelectric single crystals was investigated as a function of dynamic modulating frequencies. A dynamic optical measurement method, known as the Sénarmont compensation method, was utilized to determine frequency dependence of the electrooptic coefficient in anisotropic electrooptic single crystals under electric fields of low to medium range (10-10^6 Hz) frequency. Piezoelectric resonance measurements were also conducted to determine the influence of piezoelectric lattice vibrations on the electrooptic behavior. The crystals investigated were Lead Zinc Niobate-Lead Titanate ($0.92Pb(Zn_{1/3}Nb_{2/3})O_3$-$0.08PbTiO_3$ or PZN-8%PT) and periodically poled Lithium Niobate ($LiNbO_3$). Finally, to better understand the effects of an applied electric field and optical wave propagation across the crystals, the strain field distribution of the different materials was simulated using a finite element modeling (FEM) software package called ATILA™. It is found that the electrooptic coefficients showed a generally decreasing trend with increasing frequency of the modulating electric field; whilst anisotropic enhancement arises near piezoelectric resonance frequencies.

[+] Graduate Mentor
[#] Faculty Mentor

Annual Research Journal, Vol. IV
Electrical Engineering Research Experience for Undergraduates

ISBN 0-913260-06-1 (http://www.ee.psu.edu/reu/)

INTRODUCTION

Over the past few decades, the field of optics has become increasingly important. The invention of optical fibers dates back to the 1920's, but practical applications did not appear until the 1970's with the development of high purity silicon (Si) glass fibers and the availability of single frequency lasers. Fiber optics have introduced technologies that through the manipulation and transport of coherent light have provided an increasing ability to transmit more information, at greater speeds, and over longer distances. This has expanded the boundaries of developments and applications in various medical, communications, and industrial fields. For example, optical systems are used in telecommunications, computer networking, cable TV, and scientific measurements.

Fiber optic communications systems can also increase the capacity of wireless systems, if one can impress radio signals onto light signals and vice versa. Current research is focused on the integration of wireless and optical networks as a potential solution for increasing capacity and mobility, as well as decreasing costs in the access network. This technique is often termed radio over fiber (RoF).

In military applications, radio over fiber technology can be used onboard ships replacing numerous heavy copper cables with fibers, delivering a lighter, more rapidly installed low maintenance means to link computers and various other communication devices. [1]

Efficient laser pulse modulation may be accomplished, with a piezoelectric single crystal used to modulate a laser beam, utilizing the electrooptic effect of the crystal under an applied electric field. The induced optical index of refraction, for linear approximation, is proportional to the amplitude of the modulating electric field. This facilitates the task of pulse width modulation, utilizing solely the crystal with an applied electric field.

The Sénarmont compensator method is the chosen technique used to obtain low frequency measurements for the electrooptic coefficient of piezoelectric single crystals, and will be used in this experiment. Future research will expand upon this method to understand high frequency dependences, by using microwave technology.

This research paper will focus specifically on the electrooptic properties of PZN8%-PT and $LiNbO_3$ crystals, and the frequency dependence of their electrooptic coefficients, including low frequencies and near piezoelectric resonance frequencies.

EXPERIMENTAL DESCRIPTION

Piezoelectricity

The ability of crystals to generate a voltage in response to applied mechanical stress is termed "piezoelectricity". The word is derived from the Greek *piezein*, which means to squeeze or press. One can readily observe the magnitude of the polarization set-up in the piezoelectric if electrodes are applied to the material on the appropriate faces. This action of stress-induced polarization is termed the

Annual Research Journal, Vol. IV
Electrical Engineering Research Experience for Undergraduates

ISBN 0-913260-06-1 (http://www.ee.psu.edu/reu/)

direct effect. In contrast, the converse effect describes the change in dimensions or strain, when the piezoelectric is subject to an applied field. The converse effect will be utilized in this research experiment.

Crystal Growth

The two crystal samples used in this experiment were PZN-8%PT and $LiNbO_3$. The PZN-8%PT sample was cut from a single crystal bulk, grown using the seeded flux growth technique. The polar c-axis of the crystal sample was determined by back reflection X-ray Laue method. After careful orientation, the surfaces were polished to optical finish using 1/4 μm diamond paste. The $LiNbO_3$ crystal sample was cut from a Czochralski grown crystal, with periodically poled domains. Parallel electrodes were applied on both crystals, using air-dry silver (Ag) paint. The PZN-8%PT crystal was poled along the [001] c-axis direction to reduce the population of domain walls, and to minimize the scattering of light. In the experiment, both samples were measured with the electric field parallel to their polar axes, and with incident light propagating perpendicular to it. In such a configuration, the effective EO coefficient, r_C, is measured.

Piezoelectric Resonance Measurement

The electromechanical coupling of a piezoelectric crystal influences the impedance or admittance as a function of frequency. Piezoelectric resonance measurements were obtained using the HP Impedance/Gain-Phase Analyzer 4194A, which operates from DC to 30 MHz. However, for our purposes, impedance measurements were taken from 50 kHz to 2 MHz. The c-axis electroded crystal (longitudinal resonator) was used in these measurements. The impedance data collected was used to locate piezoelectric resonances, and to facilitate comparison with electrooptic measurements and the finite element simulations at similar frequencies.

Dynamic Electrooptic Measurement

The Sénarmont compensator technique was utilized to measure dynamic electrooptic frequency variation in the linear region of the transmittance curve for our crystals. This linear region occurs at the 50% point on the transmittance curve. To achieve maximum modulation depth it is essential to operate in the linear region to avoid distortion effects that would occur if operating near the non-linear parts of the curve (Figure 1).

The Sénarmont compensation method consists of an optical system of two polarizers, attenuator, beam reflector, light filter, quarter-wave plate (λ/4-plate), focal lens, and a photo-detector. The laser utilized in this experiment is a high quality HeNe red laser (λ=633nm). A graphical representation of the Sénarmont optical portion of the experimental system is shown (Figure 2).

The laser is the starting point for the Sénarmont method. The light emitted by the laser passes through an attenuator to control its intensity, hence the power, passing through the system. The attenuated light is redirected 90°, by a beam

Annual Research Journal, Vol. IV
Electrical Engineering Research Experience for Undergraduates

ISBN 0-913260-06-1 (http://www.ee.psu.edu/reu/)

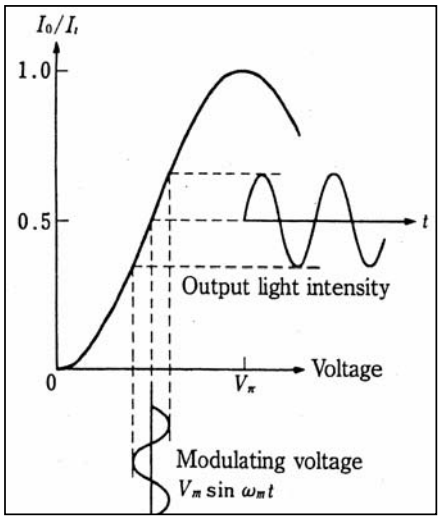

Figure 1 Transmittance of a crossed-polarized electrooptic modulator as a function of applied voltage. Modulator bias is at the point $\Gamma = \pi/2$, resulting in 50 percent intensity transmission. A small-applied sinusoidal voltage modulates the transmitted intensity about the bias point. [2]

reflector, towards the crystal location. The reflected light is filtered and polarized before passing through the crystal sample, which is being held under a constant electric field. The effect of the electric field, causing the crystal to strain, will affect the passing of light, which will later provide an accurate means of calculating the electrooptic coefficient of the crystal. The light passing through the crystal then reaches the quarter wave ($\lambda/4$) plate, set at 45° from the angle that allows minimum light to reach the photo-detector when no modulating electric field is applied. Finally, the remaining light passes through the second polarizer, also referred to as the analyzer, which is set at 90° from the first polarizer. The polarized light is focused onto the photo-detector input, using a focal lens. The signal seen by the photo-detector is sent to the input of our measuring device, a lock-in amplifier.

In order to conduct electrooptic measurements over a wide range of frequencies and to collect any given number of data points for a given frequency, a LabView™ control program was developed. Using the GPIB-USB interface capabilities of the lab equipment, an intricate feedback system was developed to accomplish three main functions. Firstly, automatically set and sweep any frequency range of the applied electric field signal, provided by the HP33120A function generator. Secondly, use the HP Infinium 1.5 GHz oscilloscope to monitor and feedback the amplitude of the function generator signal, which is being amplified using a TREK610D voltage amplifier. The feedback signal provided by the oscilloscope will adjust the amplitude of the function generator

Annual Research Journal, Vol. IV
Electrical Engineering Research Experience for Undergraduates

ISBN 0-913260-06-1 (http://www.ee.psu.edu/reu/)

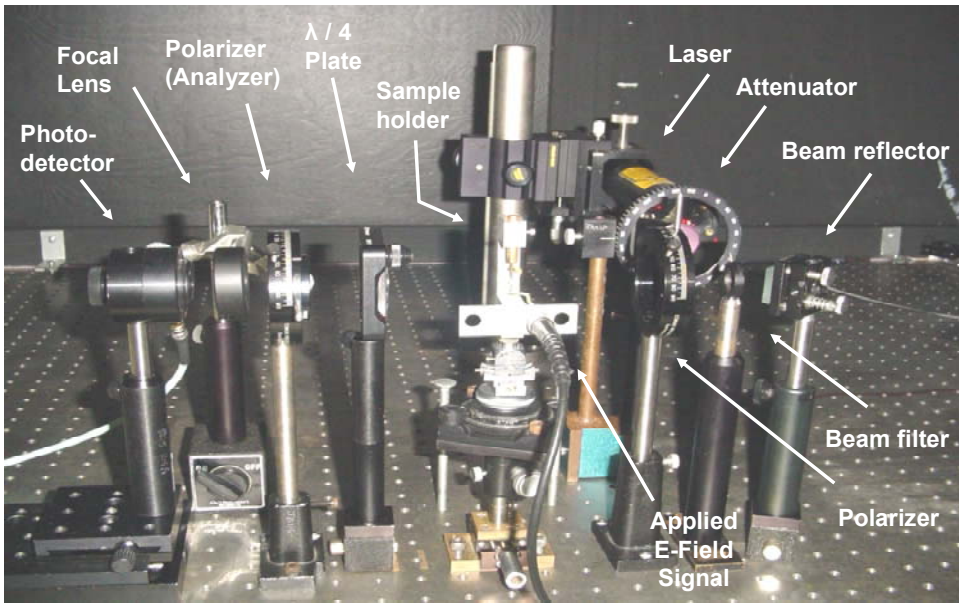

Figure 2 Experimental Sénarmont compensation set-up used to collect electrooptic frequency plots for the piezoelectric crystals.

signal to within ±0.01V of the desired voltage to be applied on the crystal. Finally, the system will interface with the SR830 lock-in amplifier to collect all data measured from the output of the photo-detector. The lock-in amplifier is such that it is able to detect and measure very small AC signals.

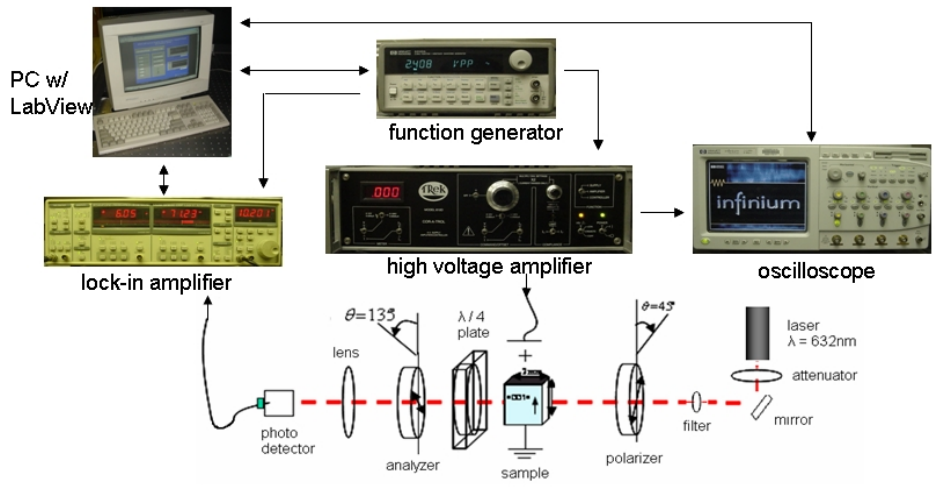

Figure 3 Schematic illustration of the dynamic electrooptic frequency measurement apparatus used to measure the electrooptic coefficient for PZN-8%PT and $LiNbO_3$ samples.

Annual Research Journal, Vol. IV
Electrical Engineering Research Experience for Undergraduates

ISBN 0-913260-06-1 (http://www.ee.psu.edu/reu/)

The lock-in amplifier uses a technique known as phase-sensitive detection to single out the component of the signal at a specific reference frequency. This external reference frequency is provided as a sync output from the function generator. This will cause noise signals at frequencies other than the reference frequency to be rejected and therefore, will not affect the measurements. A flow diagram of the entire feedback system used in this experiment is shown (Figure 3).

Measurement Theory

In the dynamic Sénarmont compensator method, when an electric field is applied to the crystal sample, this causes changes in the index of refraction of the crystal. This electrooptic effect is better known as the Pockels effect:

$$\Delta n \cong -\frac{1}{2} n_e^3 r_C E \tag{1}$$

Where Δn is the induced index change, n_e is the extraordinary index of refraction under zero field, r_C is the effective electrooptic coefficient ($r_C = r_{33} - \left(\frac{n_o}{n_e}\right)^3 r_{13}$), and E is the modulating field. This causes phase retardation (Γ) of the light, which can be recorded according to the equation:

$$\frac{I_{out}}{I_{in}} = \sin^2 \frac{\Gamma}{2} \tag{2}$$

where I_{out} and I_{in} are the output and input intensities. It is known that $\Gamma = \pi V_{app}/V_\pi$, where V_{app} is the electric field applied to the crystal, and V_π is the voltage at which Γ is equal to π. Substituting into the above equation and using trigonometric identities, the following equation is obtained:

$$\frac{I_{out}}{I_{in}} \approx \frac{1}{2}\left[1 + \Gamma_m \sin \omega t\right] \tag{3}$$

Thus, I_{out} / I_{in} is proportional to $\pi V_{app}/V_\pi$, but only when the retardation is close to $\pi/4$, or when I_{out} is approximately its maximum value. When this is the case, the following is true:

$$V_\pi = -\frac{\lambda t}{n_e^3 r_C L} \tag{4}$$

Annual Research Journal, Vol. IV
Electrical Engineering Research Experience for Undergraduates

ISBN 0-913260-06-1 (http://www.ee.psu.edu/reu/)

Therefore, our final result for the electrooptic coefficient, r_C, is given by:

$$r_C = -\frac{4\lambda}{\pi n_e^3}\left(\frac{t}{L}\right)\left(\frac{\Delta V_{out}}{V_{pp}\,\Delta V_{app}}\right) \tag{5}$$

where V_{out} refers to the RMS value of small signal output voltage measured by the SR830 lock-in amplifier, V_{app} is the RMS modulation voltage, V_{pp} corresponds to the transmittance voltage, t is the crystal thickness (parallel to the electric field), and L is the length of the optical passage through the crystal.

Principle of Simulation

ATILA™ is a commercially developed, finite element, software package specifically designed for the analysis of two or three-dimensional structures that contain piezoelectric, magnetostrictive, electrostrictive or shape memory materials. Because its formulation is organized around a strong electrical/mechanical coupling, ATILA™ is a very efficient design tool for all types of active materials applications: actuators, motors, transducers, sensors, and transformers. For this research, ATILA™ has been utilized to provide accurate simulations of the piezoelectric properties of the PZN-8%PT and $LiNbO_3$ crystals, under a sinusoidal electric field. Impedance and admittance graphs, generated along with the simulations, were also used to further understand crystal behavior near piezoelectric resonance frequencies.

RESULTS AND DISCUSSION

Dynamic Electrooptic Measurement

Sénarmont optical measurements were conducted multiple times for both crystals, in a frequency range from 10 Hz to 30 kHz. The capabilities of the TREK610D voltage amplifier and the amplitude of the HP33120A function generator at high frequencies limited this frequency range. Using the data collected by the lock-in amplifier and the LabView™ feedback system, the electrooptic coefficient, r_C, was calculated for both PZN-8%PT and the periodically poled $LiNbO_3$ crystals.

The frequency dependence of the effective EO coefficient may be explained by the nature of piezoelectricity and the electrooptic coefficient at various frequencies, contributing to the so called primary and secondary effects, which can be expressed as:

$$r_{ijk}^{X} = r_{ijk}^{x} + \pi_{ijlm} d_{lmk} \tag{6}$$

Annual Research Journal, Vol. IV
Electrical Engineering Research Experience for Undergraduates

ISBN 0-913260-06-1 (http://www.ee.psu.edu/reu/)

where r_{ijk}^{X} is the effective electrooptic coefficient at low frequency with constant stress, r_{ijk}^{x} is the effective electrooptic coefficient at high frequency with constant strain, π_{ijlm} is the elastooptic coefficient, and d_{lmk} denotes the piezoelectric coefficient. Further analysis on the primary and secondary contributions to our experimental results will be discussed.

The apparent electrooptic coefficient, r_C, calculated for PZN-8%PT presents strong frequency dependence and is decreasing with increasing frequency (up to 30 kHz) of the applied AC electric field (Figure 4). High values of the electrooptic coefficient were obtained at frequencies from 1 kHz to 30 kHz (i.e., r_C ~100pm/V at 15 kHz). A polynomial fit has been plotted along with the data results to show the decreasing trend.

It is important to mention that the electrooptic coefficient measurement is not only dependent on the intrinsic properties of the crystals, but it is also minimally dependent on external factors, such as temperature fluctuations, humidity in the air, electrical coupling, and even possible power surges, etc.

The measurement of the peak-to-peak DC voltage required for the electrooptic coefficient calculation (Equation 5) was measured using a low frequency light chopping device. It is believed that this measurement technique requires further exploration, and therefore, an apparent electrooptic coefficient is presented.

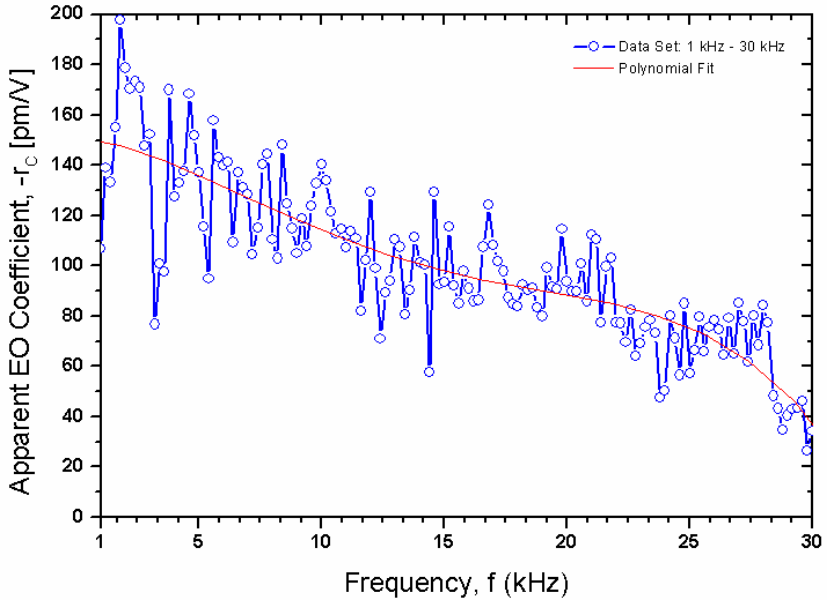

Figure 4 Apparent EO coefficient, r_C, measurements for PZN-8%PT.

At low frequencies or frequencies below resonance, the ionic displacement in the crystal is free to respond to the applied electric field. In this case, the values of the effective EO coefficient will contain both the primary and secondary contribution terms. Therefore, the frequency dependent behavior is expected, as

Annual Research Journal, Vol. IV
Electrical Engineering Research Experience for Undergraduates

ISBN 0-913260-06-1 (http://www.ee.psu.edu/reu/)

the dielectric permittivity and the ionic polarization decrease with increasing frequency.

The apparent electrooptic coefficient, r_C, calculated for the periodically poled $LiNbO_3$ also presents frequency dependence and appears to be decreasing with increasing frequency (up to 30 kHz) of the applied AC electric field (Figure 5). However, the values of the electrooptic coefficient seem to be decreasing much slower than those of the PZN-8%PT sample. Highest values of the electrooptic coefficient were obtained at frequencies from 1 kHz to 30 kHz (i.e., r_C ~16pm/V at 10 kHz). Most electrooptic guided-wave devices using $LiNbO_3$ utilize an r_{33} electrooptic coefficient value of 30.8pm/V.[3] The measured value is somewhat lower than the reported values in literature for which r_C is ~21 pm/V (taking r_{33}=30.8, r_{13}=8.6, n_o=2.286, and n_e=2.20, respectively). However, r_C value in literature is generally reported for a single domain crystal of $LiNbO_3$. In this experiment, it is believed that the relative distribution of the domain walls within the periodically poled $LiNbO_3$ crystal may have contributed to a lower electrooptic coefficient result. Therefore, an apparent electrooptic coefficient has been plotted, along with a polynomial approximation to fit the overall trend of the data.

The frequency dependence of the electrooptic coefficient may also be attributed to time dependent charge distributions that cause dynamic changes in the effective index of refraction. At the low frequency range, space charges (due to oxygen vacancies or imperfections in the crystal) may contribute to the electrooptic frequency dependence, through a reverse process of photo-refraction, where charges transported and trapped under incident light become mobile and destabilize the photo-refractive local field. The space charge effect is a slow process (millisecond scale) and is unable to stabilize at high frequencies. Lastly, another process (covering a wider frequency range) that may contribute to the EO frequency dependence is the dipole reorientation (such as $[Ti^{4+}$ -$O^{2-}]$) in response to the applied electric field.

Piezoelectric Resonance Measurement vs. ATILA™ Simulation

The piezoelectric resonance measurements for both PZN-8%PT and $LiNbO_3$ crystals were obtained using the HP Impedance/Gain-Phase Analyzer 4194A at the Penn State Materials Research Laboratory. Using the impedance analyzer it was found that PZN-8%PT presented resonance peaks in the 50 kHz to 250 kHz range. An image from the impedance analyzer of this result is shown (Figure 6).

In general, it is not possible to separate the contribution of the elastooptic and piezoelectric effects explicitly due to the lack of independent elastooptic coefficient measurements (Equation 6). Since limitations with the experimental equipment prevented the completion of dynamic electrooptic measurements near resonance frequencies for either crystal, the capabilities of computer simulations were used to further understand the contribution of the primary and secondary effects on the electrooptic coefficient, and the crystal behavior near resonance frequencies.

Annual Research Journal, Vol. IV
Electrical Engineering Research Experience for Undergraduates

ISBN 0-913260-06-1 (http://www.ee.psu.edu/reu/)

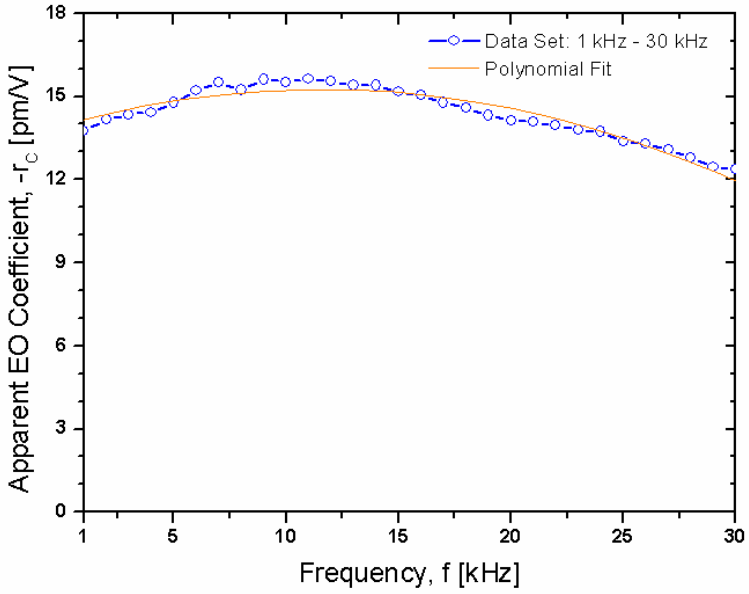

Figure 5 Apparent EO coefficient, r_C, measurements for $LiNbO_3$ crystal with periodically poled domain structures.

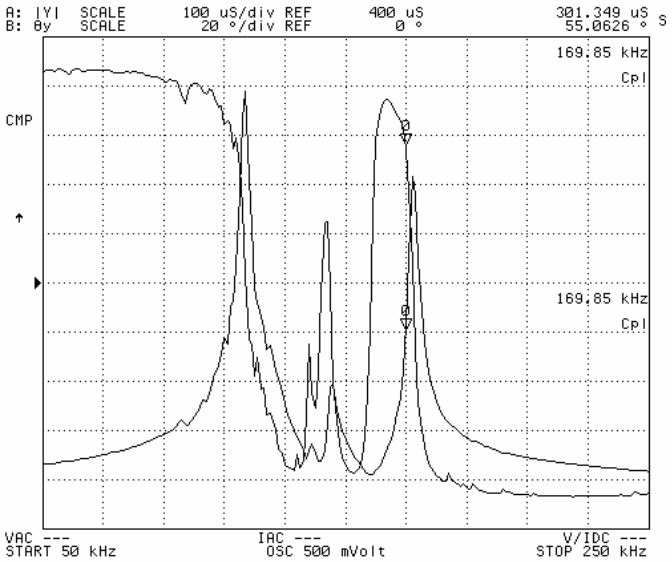

Figure 6 HP Impedance Analyzer 4194A image of PZN-8%PT crystal resonance modes in the 50 kHz to 250 kHz range.

It is anticipated that near resonance frequencies, the secondary effects scale with the resonant behavior of the dielectric constant, causing the EO coefficient to

Annual Research Journal, Vol. IV
Electrical Engineering Research Experience for Undergraduates

ISBN 0-913260-06-1 (http://www.ee.psu.edu/reu/)

experience anomalous values as a function of the resonance frequency. It is also worthwhile to mention that near piezoelectric resonance, crystal lattices experience a standing wave vibration at resonance frequency, represented by:

$$f_r = \frac{v}{2d} = \frac{1}{2d}\sqrt{\frac{1}{\rho s_{kl}^{D}}} \tag{7}$$

where υ is the phase velocity of the acoustic wave, ρ is the density of the vibrator, S_{kl}^{D} is the compliance coefficient at constant dielectric displacement, and d is the length in the vibration direction. Therefore, each elemental unit cell may be regarded as containing a dipole. When the wavelength of lattice vibration is in harmony with piezoelectric resonance frequencies, it is found that the electrooptic coefficient is greatly amplified. [4]

Optical measurements near piezoelectric resonance frequencies previously completed by Hongbo Liu for the PZN-8%PT crystal, using a spectrum analyzer, are presented below in comparison to the data obtained from the impedance analyzer (Figure 7).

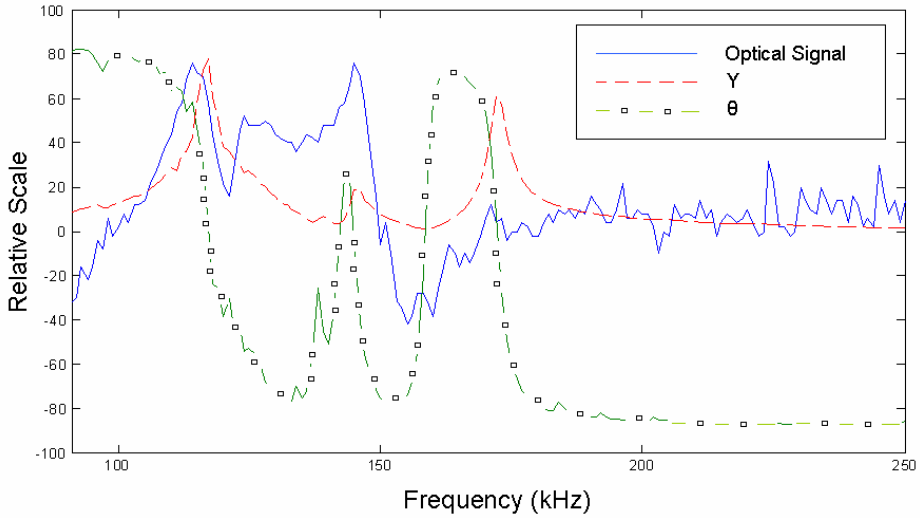

Figure 7 Measured modulated optical output intensity (solid line) for PZN-8%PT crystal, in comparison to the data obtained from the impedance analyzer.

The finite element modeling software ATILA™ requires the input of the dimensions of the crystals, as well as various mechanical, dielectric, and coupling constants, in order to properly simulate their behavior. Sample dimensions were measured using a Mitutoyo Digimatic Caliper. The PZN-8%PT crystal used was

Annual Research Journal, Vol. IV
Electrical Engineering Research Experience for Undergraduates

ISBN 0-913260-06-1 (http://www.ee.psu.edu/reu/)

measured to be 4.07mm in length (along electroded surface), 2.15mm in width, and 4.15mm in height. Similarly, the $LiNbO_3$ crystal was measured to be 5.09mm in length (along electroded surface), 2.10mm in width, and 2.35mm in height. Hence, for ease of simulation reproducibility, a table containing the principal constants used for PZN-8%PT and $LiNbO_3$ is presented below (Table I).

Table I – ATILA™ Simulation: crystal properties

Crystal Sample	Temperature (°C)	Density (kg/cm^3)	s_{11}^E ($10^{-12}\ m^2/N$)	d_{31}^E (10^{-12} C/N)	d_{33}^E (10^{-12} C/N)
PZN-8%PT [5]	25	8315	87	-1455	2890
$LiNbO_3$ [6]	25	4640	5.78	-0.85	6

ATILA™ simulation results for PZN-8%PT are presented in comparison with the data obtained from the impedance analyzer, in the frequency range from 50 kHz to 250 kHz. The obtained results are shown (Figure 8) in a relative scale for admittance values, since the simulation does not take into consideration any external factors such as temperature variations, differences in the material property constants, etc. Materials parameters for PZN-8PT are not yet well defined which are needed to improve the agreement between measured and simulated results.

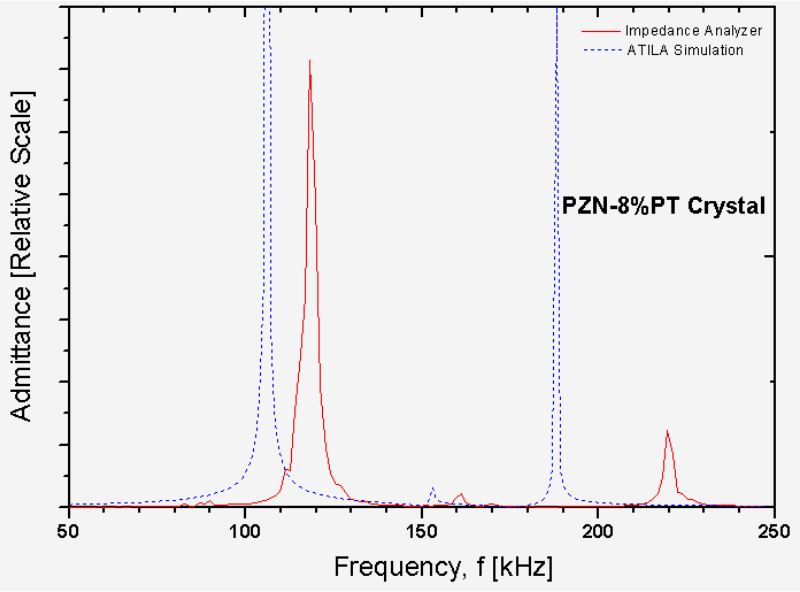

Figure 8 Impedance analyzer measurements obtained (solid line), in comparison to the simulated results (dotted line) for the PZN-8%PT crystal.

Annual Research Journal, Vol. IV
Electrical Engineering Research Experience for Undergraduates

ISBN 0-913260-06-1 (http://www.ee.psu.edu/reu/)

ATILA™ simulation results for $LiNbO_3$ are presented in comparison with data from the impedance analyzer, from 1.1 MHz to 1.9 MHz. The results for the periodically poled crystal are shown (Figure 9) in a relative scale for values of admittance. The correspondence between measured and the simulated results are evident; however, adjustment of simulation parameters and considerations of periodically poled domains structures are needed to improve their numerical agreement.

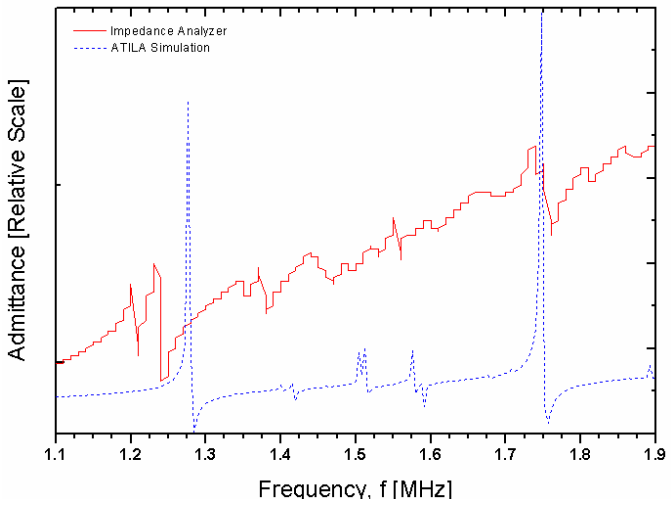

Figure 9 Impedance analyzer measurements obtained (solid line), in comparison to the simulated results (dotted line) for the $LiNbO_3$ crystal.

SUMMARY

The Sénarmont compensation method was used to measure the effective electrooptic coefficient of PZN-8%PT and $LiNbO_3$, and to explore frequency dependencies. The electrooptic coefficients in both crystals are, in general, decreasing with increasing frequency. The apparent electrooptic coefficient, r_C, was estimated in PZN-8%PT to be about 120pm/V at 10 kHz, and estimated in $LiNbO_3$ to be about 15pm/V at 10 kHz. Through numerical simulation and comparison with impedance analyses near resonance frequencies, it has been shown that anisotropic enhancement arises near piezoelectric resonance frequencies. It is suggested that with more suitable equipment, optical measurements used to obtain the electrooptic coefficient could be completed at much higher frequencies, allowing us to further understand the piezoelectric properties of these and other crystals. Lastly, the finite element modeling software ATILA™ proved to be a valuable tool to simulate the behavior of the piezoelectric crystals near their resonance frequencies.

Annual Research Journal, Vol. IV
Electrical Engineering Research Experience for Undergraduates

ISBN 0-913260-06-1 (http://www.ee.psu.edu/reu/)

ACKNOWLEDGEMENTS

This material is based upon work supported by the National Science Foundation under Grant No. EEC-0244030. Special thanks are given to the National Science Foundation and Penn State University for this research opportunity.

REFERENCES

[1] M. Fujise, "Radio over Fiber Transmission Technology for ITS and Mobile Communications", invited paper *Special IEICE Transactions on Fundamentals of Electronics, Communications, and Computer Sciences*, Vol. **E84-A**, 8. pp. 1808-1814, 2001

[2] A. Yariv, Electrooptic Modulation of Laser Beams, p. 326-371, *Optical Electronics in Modern Communications*, Fifth Edition, Oxford University Press, Oxford, England, 1997.

[3] I. Savatinova, S. Tonchev, R. Todorov, M. N. Armenise, V.M.N. Passaro, and C.C. Ziling, "Electro-optic effect in proton exchanged LiNbO3 and LiTaO3 waveguides," *J. Lightwave Technol.*, vol. **14**, no. 3, pp. 403-409, Mar. 1996.

[4] S. Johnson, K. Reichard, R. Guo, *Developments in Dielectric Materials & Electronic Devices*, Ceramic Transactions, 277-287 Am. Soc. Westville, OH, 2000.

[5] R. Zhang, B. Jiang, W. Jiang, W. Cao, *Complete set of properties of* $0.92Pb(Zn_{1/3}Nb_{2/3})O_3$-$0.08PbTiO_3$, Materials Letters, **57**, 1305-1308, Elsevier Science B.V., 2003.

[6] *Landolt-Börnstein: Ternary Elements and Compounds*, **III-11**, p. 52, 390, 341, Springer-Verlag, New York, USA, 1982.

Annual Research Journal, Vol. IV
Electrical Engineering Research Experience for Undergraduates

ISBN 0-913260-06-1 (http://www.ee.psu.edu/reu/)

ENERGY HARVESTING WITH POLYVINYLIDENE DIFLUORIDE (PVDF) PIEZOELECTRIC POLYMER FILM

Haig Norian*, Seung-Ho Park[+], and Kenji Uchino[#]

International Center for Actuators and Transducers
Materials Research Institute
The Pennsylvania State University, University Park, PA 16802

*Undergraduate Student of
Department of Electrical and Computer Engineering
Villanova University
Villanova, PA 19085

ABSTRACT

This paper documents an analysis of the energy harvesting capability of PVDF piezoelectric film. Computer simulations and in-lab experimentation were performed to examine the performance of this material. Emphasis was placed on acquiring mechanical excitation from the human stride, thus testing the feasibility of wearable piezoelectrics. In order to increase the output voltage of the piezoelectric material, the PVDF sheet was bonded to aluminum foil, thus forming a unimorph configuration. Using FEM simulations, the voltage outputs of the PVDF film (thickness = 40 microns) were obtained for varying thicknesses of the aluminum substrate. For the PVDF under investigation, the optimum thickness of the aluminum shim was determined to be 50 microns. Thus, we adopted a 54 micron aluminum foil, manufactured by Reynolds Consumer Products. The PVDF/aluminum combination (dimensions = 2cm x 10cm) was then attached to a circuit designed to effectively harness the piezoelectrically induced voltage. Test simulations sought to examine the power output as the PVDF/aluminum was subjected to harmonic mechanical excitation associated with the average human stretch motion. Output of 2.5 V DC was measured with output power in 1 ~ 2 mW range.

[+] Graduate Mentor
[#] Faculty Mentor

Annual Research Journal, Vol. IV
Electrical Engineering Research Experience for Undergraduates

ISBN 0-913260-06-1 (http://www.ee.psu.edu/reu/)

1. INTRODUCTION

1.1 Piezoelectric Materials

The piezoelectric effect is a property exhibited by certain materials by which an electric surface charge is generated as a result of the application of mechanical stress. (The Greek prefix *piezo-* roughly translates to pressure. Piezoelectricity is a very fitting name, as it precisely describes the effect inducing charge via mechanical pressure.) In such materials, the converse piezoelectric effect is also observed. An applied voltage will cause geometric strain on the material. This phenomenon has been observed in several materials, including ceramics (barium titanate, lead zirconate titanate), single crystals (quartz, lithium niobate, lithium tantalate), thin films (zinc oxide, aluminum nitride), and polymers (PVDF). [1]
The following equations summarize the fundamental property of all piezoelectric devices.

$$E = g \cdot X \tag{1}$$

$$x = d \cdot E \tag{2}$$

Equation 1 states that induced electric field E is directly proportional to applied stress X by the piezoelectric voltage constant g. Conversely, equation 2 states that induced strain x is directly proportional to the applied electric field by piezoelectric strain constant d. Combined, these equations describe nearly all observed behavior of piezoelectric behavior. [1]
Piezoelectric materials have found extensive use in transducer and actuator applications due to their intrinsic electromechanical properties. Examples include stress/strain meters, mechanical filters, underwater acoustic devices, and ultrasonic motors. [1]

1.2 Background of Piezoelectric Energy Harvesting

Despite the success and increasing effectiveness of the mobile electronic industry, the problem of efficiently powering these devices still remains. Lithium ion batteries can supply suitable power but require a stationary power outlet in order to recharge. Piezoelectric materials can transform electronics into fully mobile and independent systems. Ideally, mobile electronics will be powered by motion, i.e. the human stretch motion, eliminating the need for plug-in socket recharging. And so, the field of piezoelectric energy harvesting seeks to transform mechanical energy into electrical output capable of powering an electronic device. The flexible piezoelectric polymer PVDF, for example, can be easily incorporated into a garment, thus allowing for a wearable power supply.

1.3 PVDF: Structure and Properties

Figure 1 displays the molecular structure of polyvinylidene difluoride, or PVDF.

Annual Research Journal, Vol. IV
Electrical Engineering Research Experience for Undergraduates

ISBN 0-913260-06-1 (http://www.ee.psu.edu/reu/)

Although this material is a polymer, it does in fact exhibit piezoelectric properties. During the manufacturing process, the cast polymer is transformed to its microscopically polar phase, meaning a unique piezoelectric symmetry is established. This is accomplished by stretching the PVDF along the y-axis and, as is also common, along the z-axis (refer to Fig. 1). Once the geometric necessities for piezoelectricity have been met, the dipoles can be reoriented through standard electric poling in which a voltage in the kilovolt range is passed though the material. [1] Due to the tendency of fluorine atoms to attract electric density, very strong dipoles are formed in the C-F bonds. [2]

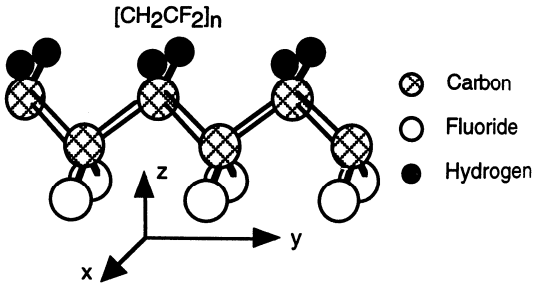

Figure 1: Molecular Structure of PVDF [1]

Following the poling process, PVDF is transformed from the α-phase(anti-parallel dipoles) to the β-phase (piezoelectric). Note the dipole orientation. Consider a mechanical vibration on the β-phase (Figure 2a). Because all of the molecules share the same dipole orientation, a net electric charge will be generated. However, in the case of the α-phase (Figure 2) , mechanical stress will not generate any electrical output. Although molecular motion is still observed, due to the anti-parallel orientation of the molecules, no net electrical charge is generated. Thus, poling and subsequent uniform unidirectional poling is absolutely necessary for generating the piezoelectric effect. [3]

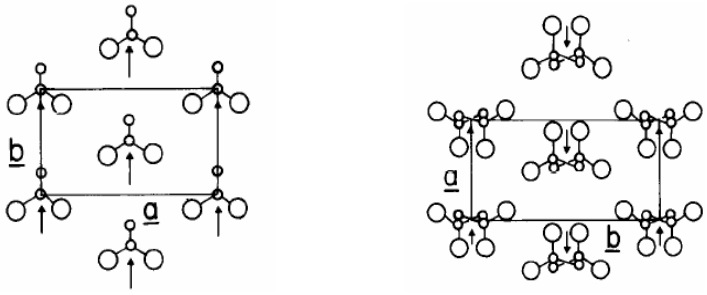

(a) *(b)*

Figure 2: Phases of the PVDF: (a) β-phase and (b) α-phase [2]

The molecular structure described above gives PVDF mm2 orthorhombic crystal properties. In other words, the lattice structure is fundamentally pyramidal. Stemming from this, we see that the material is chemically inert. Furthermore, PVDF is very durable as it possesses a high elastic compliance. The material is

Annual Research Journal, Vol. IV
Electrical Engineering Research Experience for Undergraduates

ISBN 0-913260-06-1 (http://www.ee.psu.edu/reu/)

also known to display the pyroelectric effect, in which an increase in temperature yields an induced voltage. [1]
The following table displays fundamental PVDF properties [4] used in all test simulations:

Table 1: PVDF properties

PVDF constants	
s_{11}^E	$335\frac{m^2}{N}$
d_{31}	$25\frac{pC}{N}$
d_{32}	$2.3\frac{pC}{N}$
d_{33}	$-30\frac{pC}{N}$
T_C	$90°C$
k_p	0.15

Although PVDF is not the most efficient piezoelectric material due to its low coupling coefficient, its unique attributes are perfectly suited for energy harvesting for mobile electronics. Consider the standard human stretch motion. This involves both leg and arm extension/contraction. Much of this movement is transferred to the clothing. Due to the flexibility of PVDF, clothing and piezoelectric materials can be joined to produce energy harvesting clothing, or Intelligent Clothing (IC). [5] Ideally, mobile electronics will be recharged solely by human movement, without any external power source.

2. EXPERIMENTAL DESCRIPTION

2.1 FEM Simulation: Sample Model Geometry

In order to increase the output voltage, an aluminum shim was bonded to the PVDF film, thus creating a PVDF/aluminum unimorph. Without the added aluminum, a standard bending motion will not produce a harvestable voltage. The compression strain will negatively compliment the extension strain in such a way that the piezoelectric effect will be minimized. In other words, a minimum voltage will be generated due to an effective contraction/extension cancellation effect. However, this cancellation can be offset by bonding an aluminum substrate to the PVDF sheet. This effectively shifts the neutral line of the contraction/extension forces into the aluminum. Because the neutral line of the contraction/extension is no longer within the piezoelectric material, a greater voltage output is generated. However, as the substrate thickness is increased, the rigidity of the composite increases, thus decreasing the voltage output. Thus, we

Annual Research Journal, Vol. IV
Electrical Engineering Research Experience for Undergraduates

ISBN 0-913260-06-1 (http://www.ee.psu.edu/reu/)

see that an optimal substrate thickness will both minimize rigidity and minimize the effect of contraction/extension voltage cancellation. Prior research has shown that aluminum is most suitable as the substrate material due its ability to effectively shift the neutral line out of the piezoelectric. [5]

Initial experimentation dealt with the optimization of the PVDF/aluminum composite. Computer simulations were run utilizing the ATILA FEM software package (Micromechatronics Inc., State College, PA). To simulate the human stretch motion, a low force (0.1 N) and very low frequency (1-5Hz) bending motion was simulated on the clamped unimorph. This bending motion is illustrated in Figure 3, a screen shot from the FEM simulation. Each simulation (two dimensional) tested a different thickness of aluminum substrate. Ultimately, voltage analysis was performed for each simulation in order to determine the optimum aluminum thickness.

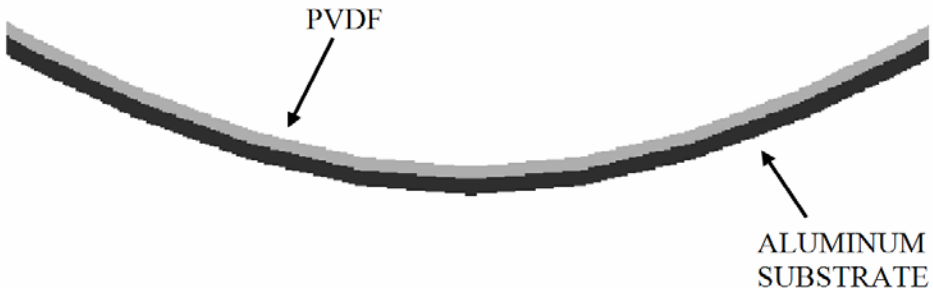

Figure 3: FEM simulation 'bending' motion of PVDF/Aluminum unimorph

2.2 Sample Fabrication

Each 40 μm PVDF sample (factory treated with a conductive Aluminum coating) was bonded to a 50 μm aluminum shim. The PVDF film used in the experiment was supplied by Kureha Chemical Industries Co., Ltd., Tokyo, Japan.

The dimensions of the PVDF/Al sample were as 2 cm x 10 cm. The bonding adhesive used was TRA-DUCT BA-2902, a silver based conductive epoxy manufactured by Tra-Con. In order to minimize the epoxy thickness, a drop of ethanol was added, allowing for smoother application. The final epoxy coat contributed roughly 2~3 microns of thickness. Copper wire electrodes were attached with conductive silver epoxy, sealed with silicon rubber and electrical tape. Such an insulated electrode configuration ensured that the electrode would remain stationary during experimental testing.

2.3 Experimental Set-up

Prior to the start of the primary experiment, the pyroelectric properties were tested in order to ensure no interference in the experiment. Using a standard hair dryer, an electroded PVDF sample was heated from room temperature to roughly 28 degrees Celsius. The voltage output transient was observed on an oscilloscope. The induced voltage was in the 15 ~ 45mV range. For this reason, the

Annual Research Journal, Vol. IV
Electrical Engineering Research Experience for Undergraduates

ISBN 0-913260-06-1 (http://www.ee.psu.edu/reu/)

pyroelectric properties of PVDF, although far from insignificant, will not dampen the piezoelectric output at approximately room temperature.
Each electroded sample was connected to the energy harvesting circuit under investigation (See Section 2.4). The sample was then subjected to various forces focused at the center, ultimately generating a bending motion. This bending motion, seen in Figure 4, simulates the bending displacement that would be observed if the sample were attached to the human elbow during walking stride. The mechanical excitation was on the order of 3~5 Hz with force in the 1~4 N range. Oscilloscope readings (Agilent MSO6014A Mixed Signal Oscilloscope) were obtained, analyzing input and output voltages simultaneously.

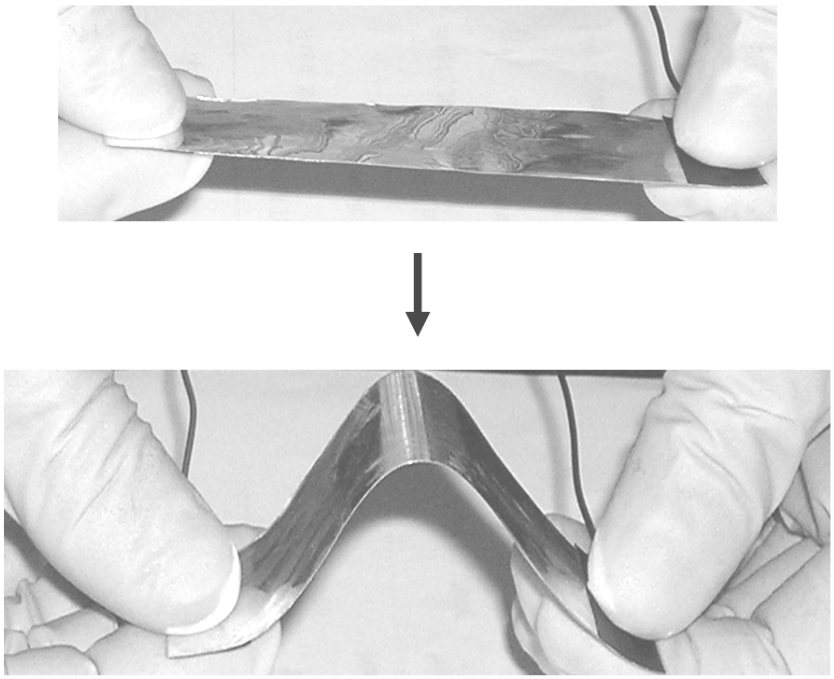

Figure 4: PVDF/Aluminum Unimorph Testing Method

2.4 Energy Harvesting Circuit Design

Circuit Theory
The circuit below is intended to take a piezoelectric PVDF voltage input and output a harness able DC output. Let us consider the theoretical output from a sinusoidal input voltage. As the voltage is applied, C1 begins to charge. During the C1 charging phase, there is no voltage drop across C2. Once C1 is fully charged, we observe the charging phase of C2. Once C2 is fully charged, output voltage must equal twice the voltage of the input in order to satisfy Kirchhoff's Voltage Law. Note that due to the diode configuration, this output voltage will be

Annual Research Journal, Vol. IV
Electrical Engineering Research Experience for Undergraduates

ISBN 0-913260-06-1 (http://www.ee.psu.edu/reu/)

a DC signal. This circuit is commonly referred to as a Voltage Doubler.[6]

Figure 5: Energy Harvesting Circuit

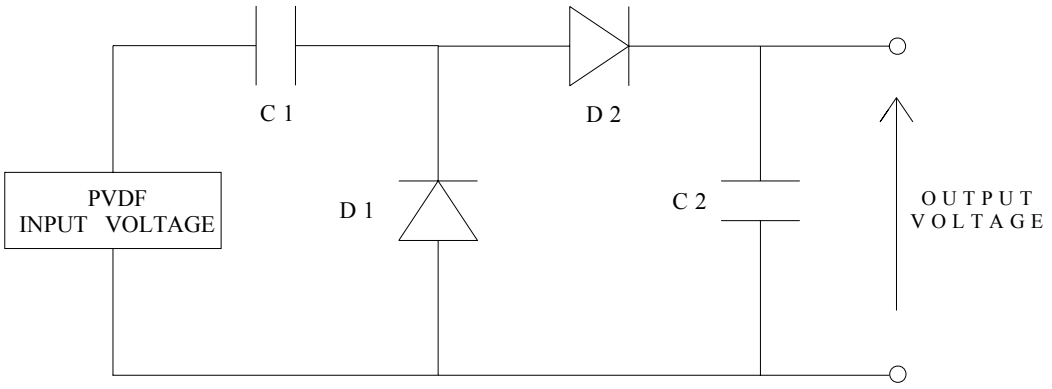

Table 2: Circuit Component Specifications

Circuit Component	***Component Specs***
C1, C2	Electrolytic Capacitor C = 22μF
D1, D2	Germanium Diode Model = 1N270 Minimum Forward Voltage Drop = 0.21 V

This circuit is ideally suited for the PVDF energy harvesting due to the low power consumption of each component. All circuit components are passive. The circuit components, listed in Table 2, combine for a very compact circuit and can be easily integrated as part of a mobile energy harvesting unit with negligible power consumption. The assembled circuit can be seen in Figure 6. Looking in from the input terminals, the circuit has an equivalent capacitance of $4.42\,\mu F$ while the PVDF / Aluminum has capacitance of $68.5\,nF$. Although the impedances are not ideally matched, the input signal will still run through the circuit with minimal "reflection" interference.

Annual Research Journal, Vol. IV
Electrical Engineering Research Experience for Undergraduates

ISBN 0-913260-06-1 (http://www.ee.psu.edu/reu/)

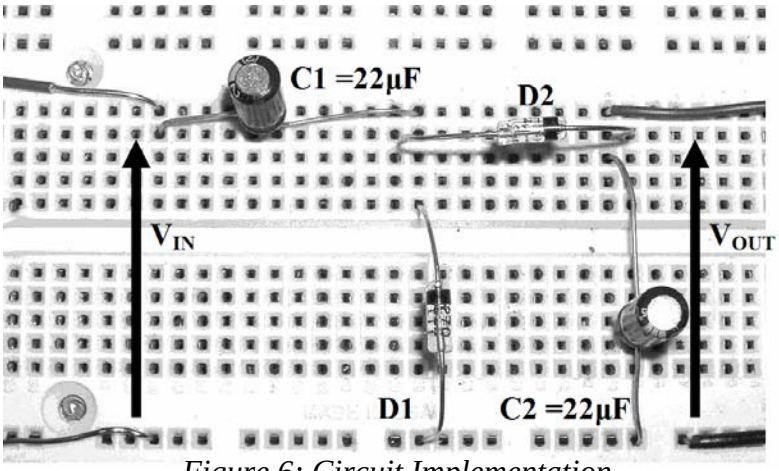

Figure 6: Circuit Implementation

3. RESULTS

3.1 FEM Results

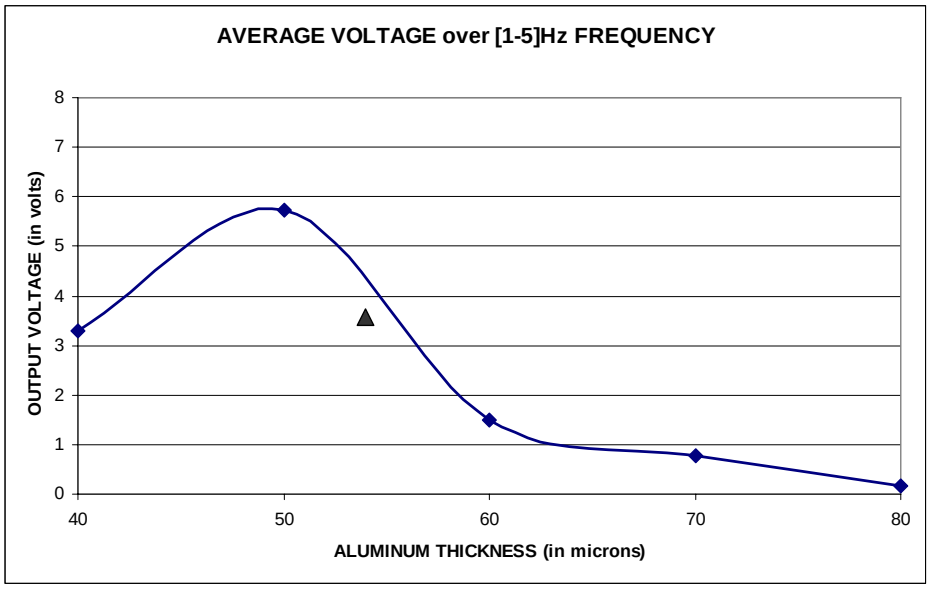

Figure 7. Output Voltage as a function of Aluminum Substrate Thickness [FEM]
[▲ *is an experimental result from our sample*]

Figure 7 was generated using Excel with data exported from FEM simulations. As seen above, maximum voltage is obtained when the aluminum substrate thickness is equal to 50 microns. The triangle (▲) data point denotes experimentally determined voltage (See Section 3.2).

Annual Research Journal, Vol. IV
Electrical Engineering Research Experience for Undergraduates

ISBN 0-913260-06-1 (http://www.ee.psu.edu/reu/)

3.2 Experimental Results

As seen in Figure 8a, the output voltage takes 60 seconds to reach DC steady state. Although this charge-up time is significant, the circuit does so with negligible power consumption as the DC output is obtained without the use of a silicon bridge rectifier.

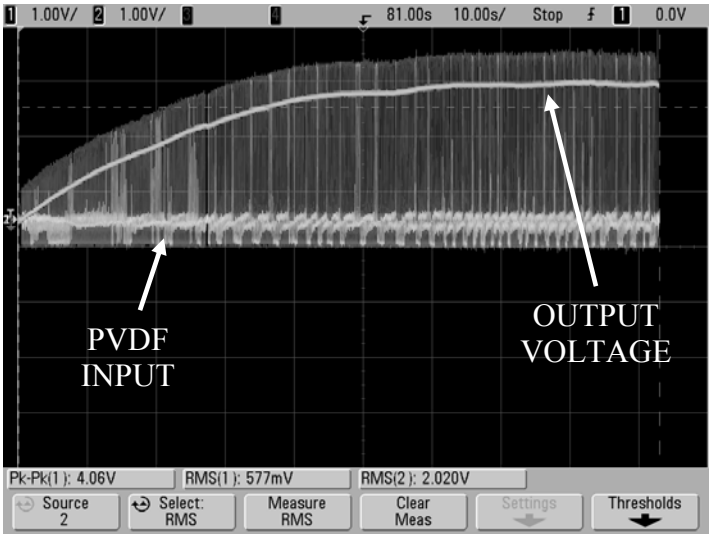

Figure 8a:
PVDF Energy Harvesting Circuit Input and Output Voltages

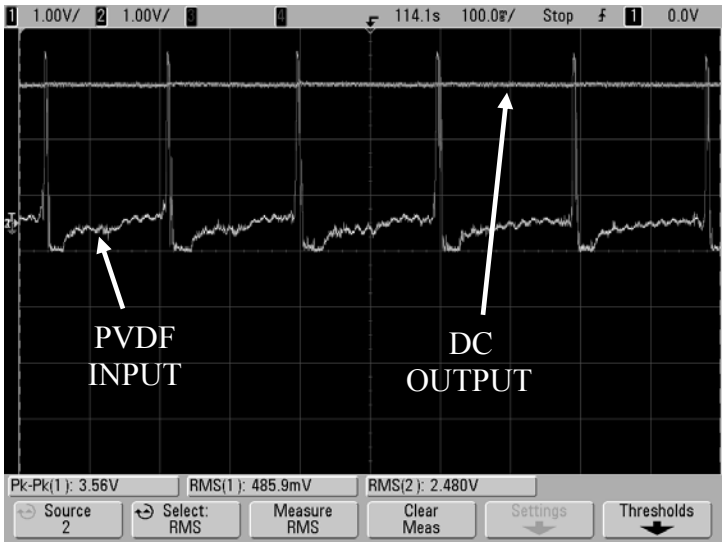

Figure 8b:
Zoomed Plot of PVDF Energy Harvesting Circuit Input and Output Voltages

From Figure 8b, we see that the PVDF piezoelectric input wave took the form of a pulse signal graphically determined to be a roughly 10% duty cycle. The

Annual Research Journal, Vol. IV
Electrical Engineering Research Experience for Undergraduates

ISBN 0-913260-06-1 (http://www.ee.psu.edu/reu/)

frequency of this oscillation was 5 hertz. Although the peak to peak voltage was found to be roughly 3.56 volts, the root mean square of the input voltage was only 485mV. This low RMS value severely limits the output power potential of the pulse signal. The output of the energy harvesting circuit outputs a 2.48 V DC signal. The RMS value has been increased by a multiple of FIVE. Using voltage and current probes, the power of the output signal was measured to be in 1 ~ 2 mW range. Note that the amplitude of the input voltage is within 15% of the voltage from the FEM analysis seen in Figure 7. This correlation verifies the computer simulation.

SUMMARY

Using FEM simulation, a PVDF / Aluminum unimorph was optimized. A 50 micron aluminum shim was bonded to the PVDF using conductive silver epoxy. This composite was hooked up to a passive energy harvesting circuit and subjected to a 5 Hz bending motion of 1 ~ 4 Newtons. Output power was in the range of 1 ~ 2 mW.

The energy harvesting circuit utilized in this project was found to be very effective in that it outputs a rectified DC output voltage in the 1 ~ 2 mW range with negligible circuit power dissipation.

Future research will seek to further optimize the passive energy harvesting circuit and obtain increased output power.

In consideration that output power is expected to increase in proportion to the sample size/area, 50 mW electrical energy harvesting is easily anticipated by covering a larger area of the human body via IC (Intelligent Clothing) jacket or trousers.

ACKNOWLEDGEMENT

This material is based upon work supported by the National Science Foundation under Grant No. EEC-0244030. Special thanks go to Jiro Masuko of Kureha for supplying the PVDF sample utilized in all experimentation.

Annual Research Journal, Vol. IV
Electrical Engineering Research Experience for Undergraduates

ISBN 0-913260-06-1 (http://www.ee.psu.edu/reu/)

REFERENCES

[1] Uchino, Kenji. *Ferroelectric Devices*. New York: Marcel Dekker, Inc., 2000.

[2] Jenket, Don. Li, Kathy. Stone, Peter. *Eelectric: Energy Harvesting through Piezoelectric Polymers.* ONLINE POWERPOINT FILE located at web.mit.edu/3.082/www/team4/FinalPresentation.ppt

[3] Davis, G.T., McKinney, J.E., Broadhurst, M.G.,Roth, S.C. Electric-field-induced phase changes in poly(vinylidene fluoride). *Journal of Applied Physics* **49**(10) pp.4998-5002. (1978).

[4] PVDF. Landolt-Börnstein: *Ferroelectric and Related Substances*. **16**(b), pp. 305-306, 709. New York: Springer-Verlag, 1982.

[5] Kim, Hyeoungwoo. Uchino, Kenji. Daue, Thomas. *Energy Harvesting with Flexible Piezo-Composites.* Proc. CD 9th Japan Internation SAMPE Symp. and Exhibition, SIT Session 05, Nov. 29 – Dec 2 (2005).

[6] Jones, Martin Hartley. *A Practical Introduction to Electronic Circuits. New York: Cambridge University Press, 1985.*

ISBN 0-913260-06-1 (http://www.ee.psu.edu/reu/)

DEVELOPMENT OF UNDERGRADUATE LABORATORY MODULES IN CONTINUOUS-WAVE QUADRUPOLE RESONANCE SPECTROSCOPY

Thomas Tyson* and Jeffrey L. Schiano[#]

Department of Electrical Engineering
The Pennsylvania State University, University Park, PA 16802

*Undergraduate Student of
Department of Physics and Engineering
West Virginia Wesleyan College
Buckhannon, WV 26201

ABSTRACT

This paper outlines a series of experiments that introduce undergraduate chemistry and physics majors to continuous-wave (CW) quadrupole resonance (QR) spectroscopy. In addition to obtaining absorption spectra, the students also determine the inverse-linewidth parameter, the spin-lattice relaxation time, and the effect of sample size on the spectra. The experiments require two one-hour and one six-hour laboratory sessions in order to complete. In addition to describing the experiments, this paper shows representative data for nitrogen-14 nuclei in hexamethylenetetramine and provides a description of the CW QR spectrometer. Although tailored for use in a series of laboratory courses at West Virginia Wesleyan College, the laboratory exercises described in this paper can be easily incorporated into other curriculums.

INTRODUCTION

Concepts in Magnetic Resonance Spectroscopy

Spectroscopy is a valuable tool in chemistry and physics for determining molecular structure and material parameters. Magnetic resonance spectroscopy involves the magnetic and electric properties of nuclei. Two types of spectroscopy

[#] Faculty mentor

Annual Research Journal, Vol. IV
Electrical Engineering Research Experience for Undergraduates

ISBN 0-913260-06-1 (http://www.ee.psu.edu/reu/)

are of particular relevance to this work, nuclear magnetic resonance (NMR) and quadrupole resonance (QR) spectroscopy NMR spectroscopy techniques involve the interaction of the nuclear magnetic moment with two externally applied magnetic fields: a static magnetic field whose amplitude determines the resonant frequency and a radio frequency (RF) magnetic field that perturbs the nuclear moments from a thermal equilibrium state. Typical NMR spectrometers utilize Faraday induction to observe the RF magnetic field produced by hydrogen-1 nuclei within a sample after they have absorbed energy from an excitation RF pulse. The amplitude and frequency of the detected signal relates to the amplitude of the static magnetic field and the chemical environment of the hydrogen nuclei. NMR spectroscopy reveals information on molecular structure as variations in the chemical environment of hydrogen nuclei produce shifts in resonant frequencies that are measured on the order of parts per million. NMR spectroscopy has a significant advantage in that the signal-to-noise ratio (SNR) of a magnetic resonance measurement may be improved by increasing the strength of the static magnetic field. This feature results from two aspects of the NMR spectroscopy. First, the resonant frequency is proportional to the strength of the applied static magnetic field. Second, because a coil detects the RF magnetic field produced by the hydrogen nuclei, Faraday's law reveals that the magnitude of the induced signal is proportional to resonant frequency. However, there is a significant disadvantage associated with improving the SNR by increasing the magnetic field strength as this method increases the cost of the magnet system. In addition, as most NMR systems utilize superconducting magnets to generate the static magnetic field, increasing the field strength also increases the long term costs associated with cryogens.

QR is another type of nuclear magnetic resonance wherein the resonant frequency is determined by the electrostatic interaction between the nuclear charge density and the electric field from surrounding electronic charges. In comparison to NMR, QR does not require a static magnetic field to obtain spectral data thereby significantly reducing the spectrometer operating costs. More importantly, as the resonant frequency in QR spectroscopy is extraordinarily sensitivity to chemical environment, chemical shifts are typically measured in parts per thousand, and so QR spectroscopy is orders of magnitude more sensitive to chemical structure than NMR. The primary disadvantage of QR spectroscopy is that the SNR can not be increased by raising the strength of an externally applied static magnetic field. Whereas state-of-the-art NMR spectrometers utilize resonant frequencies on the order of GHz for hydrogen nuclei, QR spectrometers typically operate in the MHz region, and so the resulting RF magnetic field measurements are three orders of magnitude smaller that those for NMR measurements. Another disadvantage is that the large sensitivity of resonant frequency to chemical structure requires that QR spectrometers operate over a proportionately much larger bandwidth than NMR spectrometers.

Annual Research Journal, Vol. IV
Electrical Engineering Research Experience for Undergraduates

ISBN 0-913260-06-1 (http://www.ee.psu.edu/reu/)

The Physical Basis for QR Spectroscopy

The physical basis for QR spectroscopy is the interaction between the electric field gradient (EFG) tensor produced by electronic charges surrounding the nucleus and the electric quadrupole moment of the nuclear charge[1]. Nuclei with spin angular momentum have a magnetic moment proportional to the spin quantum number I. The positive charge distribution of a nucleus is symmetric about the axis of spin momentum, or equivalently, the magnetic moment of the nucleus. However, the nuclear charge density is not necessarily spherically symmetric. Along the axis of the magnetic moment, the charge density may be either contracted (Frsibee-shaped), or elongated (cigar-shaped). The electric quadrupole moment, eQ, describes the shape of the nuclear charge distribution. The nuclear charge density is spherically symmetric when eQ = 0, elongated when eQ > 0, and contracted when eQ < 0. The electronic charges surrounding the nucleus produces an electric field at the nucleus. The electric field of the nuclear charge distribution and surrounding electronic charges can interact to produce a torque on the nucleus. In particular, if the nucleus is not spherically symmetric, than the nuclear charge density will experience a torque in the presence of an electric field gradient from the surrounding electron charges. Although the EFG tensor has nine components (dE_i / dx_j for i, j = x, y, z), it can be described by two parameters that are the largest gradient

$$eq = \frac{dE_z}{dz}, \tag{1}$$

and the asymmetry parameter

$$\eta = \frac{dE_x/dx - dE_y/dy}{dE_z/dz}, \tag{2}$$

that is a measure of the axial symmetry of the electric field gradient tensor around the z-axis. These parameters are defined in the coordinate frame for which the EFG tensor is a diagonal matrix.

The electrostatic interaction between the EFG tensor and the electric quadrupole moment of the nucleus yield preferred orientations of the nucleus defined by the axis of the magnetic moment. This paper presents QR spectra for nitrogen-14 nuclei for which the spin angular momentum quantum number is I=1. In this case there are three preferred nuclear orientations, and Figure 1 shows the three corresponding energy states. A transition from one energy state to another requires a RF magnetic field with a frequency determined by the difference between energy levels.

Annual Research Journal, Vol. IV
Electrical Engineering Research Experience for Undergraduates

ISBN 0-913260-06-1 (http://www.ee.psu.edu/reu/)

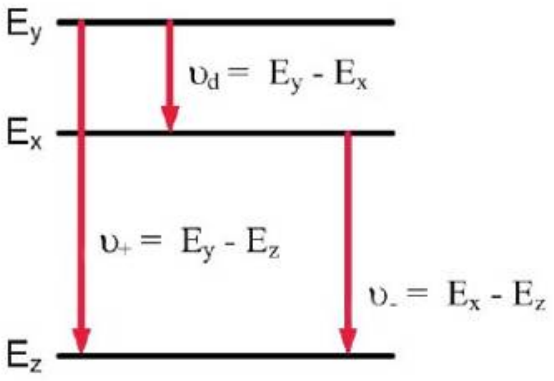

Figure 1: Energy levels and transition frequencies for nuclei with I = 1.

Figure 1 shows that for nuclei with spin quantum number I=1 there are three transition frequencies expressed as

$$\upsilon_{\pm} = \frac{3}{4} e^2 qQ \left(1 \pm \frac{1}{3} \eta \right)$$
$$\upsilon_d = \frac{1}{2} e^2 qQ \eta \qquad (3)$$

The electric quadrupole moment eQ is a property of the nuclei, and is a constant across different compounds. In contrast, the parameters eq and η describing the EFG tensor are significantly affected by molecular structure. For this reason, different compounds containing a given nuclei of interest, for example, nitrogen-14, have distinct transition frequencies.

The preferred energy states for a spin quantum number are not sharp as in Figure 1 because of variations in the EFG tensor across a material that may arise, for example, from impurities, mechanical strains, or temperature variations. Figure 2 shows the normalized Lorentzian distribution

$$\Lambda(\omega) = \frac{1}{1 + [T_2^*(\omega - \omega_*)]^2} \qquad (4)$$

that is typically used to approximate the distribution in the resonant frequencies between two energy levels[2]. The center frequency of the QR transition is ω_* while the inverse-linewidth parameter T_2^* describes the full-width half-maximum (FWHM) of the normalized Lorentzian lineshape

$$FWHM = 2/T_2^* . \qquad (5)$$

Annual Research Journal, Vol. IV
Electrical Engineering Research Experience for Undergraduates

ISBN 0-913260-06-1 (http://www.ee.psu.edu/reu/)

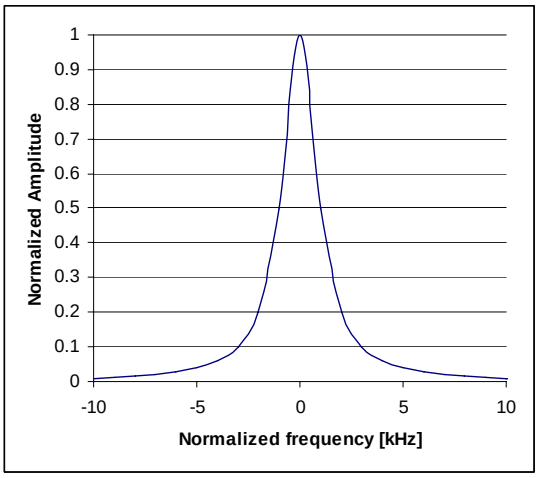

Figure 2: The normalized Lorentzian lineshape.

For a given sample, thermal equilibrium exists when generally more nuclei are in the lower energy states than the higher energy states. Application of a RF magnetic field tends to equalize out the population of the three states[1]. When the RF field is removed, the population at a given energy level returns to its thermal equilibrium value with a time constant T_1 is known as the spin-lattice relaxation time. A correlation exists between the amplitude of the applied RF magnetic field and the energy absorbed by the nuclei. The maximum absorption occurs when the RF amplitude H_1 satisfies the constraint

$$\gamma^2 H_1^2 T_1 T_2 = 1 \qquad (6)$$

where γ is the gyromagnetic ratio, and T_2 is the spin-spin relaxation time[2]. If the applied magnetic field exceeds the optimal value specified by equation (6), the nuclei are equally distributed between energy states and the system is said to be saturated and the energy absorbed by the nuclei decreases. The gyromagnetic ratio is a constant for the nuclei of interest. For example, for nitrogen-14 the value of γ is 1933 rad/sec/Gauss.

Continuous-Wave Spectroscopy

Continuous-wave (CW) spectroscopy is a technique for providing a measure of Lorentzian lineshape. Once transition frequencies are identified, it is possible to back calculate the EFG tensor parameters eq and η that in turn provide information on the structure of chemical bonds. The CW spectrometer measures the absorption of energy by the nuclei at a QR transition frequency.

ISBN 0-913260-06-1 (http://www.ee.psu.edu/reu/)

The CW spectrometer detects the absorption of power by nuclei using the tuned RLC circuit shown in Figure 3. The sample is placed in a vial over which a coil with self-inductance L_o and resistance R_o is wound. The parallel capacitor is used to set the frequency at which the maximum response of the LRC circuit to a RF magnetic field occurs.

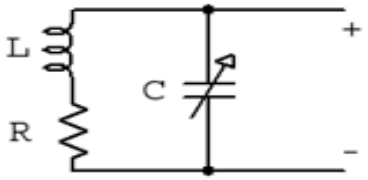

Figure 3: Model of the probe circuit for CW QR spectrometer.

The effect of the sample on the tuned probe coil is revealed by considering the Quality-factor (Q) of the probe coil that is defined as

$$Q = 2\pi \frac{\text{max energy stored per cycle}}{\text{Energy disipated per cycle}}. \tag{7}$$

The Q-factor of the probe coil at a specified frequency ω_o is

$$Q = \frac{\omega_o L}{R}. \tag{8}$$

In a CW QR spectrometer, the tuned circuit in Figure 3 determines the frequency of an oscillator. The frequency of the oscillation is approximately

$$\omega_o = \frac{1}{2\pi\sqrt{LC}} \tag{9}$$

while the amplitude of the oscillation is directly proportional to the probe coil Q-factor given by equation (8). As the frequency ω_o of the oscillator is swept through a QR transition, the magnetic susceptibility of the material changes altering both the resistance and inductance seen looking into the probe coil, thereby changing both frequency and amplitude of the oscillator.

The complex magnetic susceptibility

$$\chi(\omega) = \chi_R(\omega) - j\chi_I(\omega) \tag{10}$$

Annual Research Journal, Vol. IV
Electrical Engineering Research Experience for Undergraduates

ISBN 0-913260-06-1 (http://www.ee.psu.edu/reu/)

of the sample within the coil affects both the inductance and resistance of the probe coil as

$$\begin{aligned} L &= L_o\left(1+\chi_R(\omega)\right) \\ R &= R_o + \omega_o L \chi_I(\omega) \end{aligned}, \tag{11}$$

where the real component χ_R is called the dispersion term while the imaginary component χ_I is called the absorption term. From first principles, the real and imaginary components of the magnetic susceptibility are related to the Lorentzian line shape of the QR transition as

$$\begin{aligned} \chi_R(\omega) &= K_1(\omega-\omega_*)T_2^*\Lambda(\omega) \\ \chi_I(\omega) &= K_1\Lambda(\omega) \end{aligned}, \tag{12}$$

where K_1 is a proportionality constant.
When the frequency ω is outside the Lorentzian lineshape the magnetic susceptibility is zero. As ω approaches the transition frequency there is a peak in the absorption term, while the dispersion term passes through zero. As a result, at the QR transition frequency the Q-factor of the probe decreases as the value of R increases, and when the oscillator frequency ω_o matches the QR transition frequency ω_*,

$$Q(\omega_o)\big|_{\omega_o=\omega_*} = \left.\frac{\omega_o L_o\left[1+K_1(\omega_o-\omega_*)\Lambda(\omega_o)\right]}{R_o+K_1\Lambda(\omega_o)}\right|_{\omega_o=\omega_*} = \frac{\omega_* L_o}{R_o+K_1}. \tag{13}$$

The reduction in Q-factor is observed as a decrease in the amplitude of the oscillator.

As the change in probe resistance is small, a lock-in amplifier measures the change in oscillator amplitude. The output of the CW spectrometer is the envelope of the waveform across the tuned circuit in Figure 3 and is given by

$$v_{en} = \frac{K_2}{R_o+K_1\Lambda(\omega_o)} \tag{14}$$

where K_2 is a constant parameter. For lock-in detection, the amplitude of the envelope is modulated by electrically varying the capacitance in Figure (3) so that

$$\omega_o(t) = \omega_c + \omega_d\cos\left(\omega_m t\right), \tag{15}$$

Annual Research Journal, Vol. IV
Electrical Engineering Research Experience for Undergraduates

ISBN 0-913260-06-1 (http://www.ee.psu.edu/reu/)

where ω_c is the center frequency of the oscillator, ω_d is the peak change in oscillator frequency, and ω_m is the reference frequency for lock-in amplification. The time-varying oscillator frequency produces a time-varying envelope amplitude. As the change in oscillator frequency ω_d is orders of magnitude smaller than ω_c, the envelope amplitude can be approximated by the truncated Taylor series

$$\begin{aligned} v_{en}\left(\omega_c + \omega_d \cos\left(\omega_m t\right)\right) &= v_{en}(\omega_c) + \left.\frac{\partial v_{en}}{\partial \omega_o}\right|_{\omega_d = 0} \omega_d \cos\left(\omega_m t\right) \\ &= v_{en}(\omega_o) + K_3 \frac{\partial \Lambda(\omega)}{\partial \omega} \omega_d \cos\left(\omega_m t\right) \end{aligned}, \qquad (16)$$

where K_3 is a constant parameter. Within the Lock-in amplifier, the signal $v_{en}(t)$ is multiplied by $\cos\left(\omega_m t\right)$ and lowpass filtered to produce the lock-in amplifier output

$$V_o(\omega_c) = K_4 \left.\frac{\partial \Lambda(\omega)}{\partial \omega}\right|_{\omega=\omega_c}, \qquad (17)$$

where K_4 is a constant parameter.

In a CW spectroscopy experiment, the output voltage V_o is recorded as a function of the center oscillator frequency ω_c. By sweeping the oscillator frequency ω_c through a QR transition, the output voltage of the lock-in amplifier sweeps out the derivative of the QR Lorentzian lineshape, thereby revealing the QR transition frequency ω_* as well as the inverse-linewidth parameter T_2^*.

EXPERIMENTAL DESCRIPTION

Instrumentation

Figure 4 shows a block diagram the CW spectrometer less the lock-in amplifier. The oscillator frequency ω_c is varied by electronically adjusting the tuning capacitor. The center frequency of the oscillator is modulated as given by equation (15) using the varactor diode C1. Unfortunately, a time varying voltage across the varactor also modulates the amplitude of the envelope and leads to a DC offset at the lock-in amplifier output. To overcome this limitation, Robinson showed that the bridge circuit consisting of C1, C2, R1 and R2 can be used to null the alternating voltage component across the varactor C1 as long as the relationships R1 C1 = R2 C2 holds[3]. The amplifier presents a high impedance to the tuned circuit to avoid lowering the Q-factor and provides a voltage gain of

Annual Research Journal, Vol. IV
Electrical Engineering Research Experience for Undergraduates

ISBN 0-913260-06-1 (http://www.ee.psu.edu/reu/)

several dB. The limiter produces a feedback signal of fixed amplitude, regardless of the amplitude of the voltage across the tuned circuit. The feedback signal is coupled back into the tuned circuit to produce a self-sustained oscillation. Because of the limiter, as the frequency of the oscillation passes through a QR transition, the envelope of the voltage across the oscillator will decrease. The Detector block in Figure 4 represents the envelope detector. The CW spectrometer in Figure 4 is known as a Robinson marginal oscillator, where the term marginal refers to the fact that the feedback signal is limited so that the absorption of energy by the nuclei will reduce the amplitude of the oscillation.

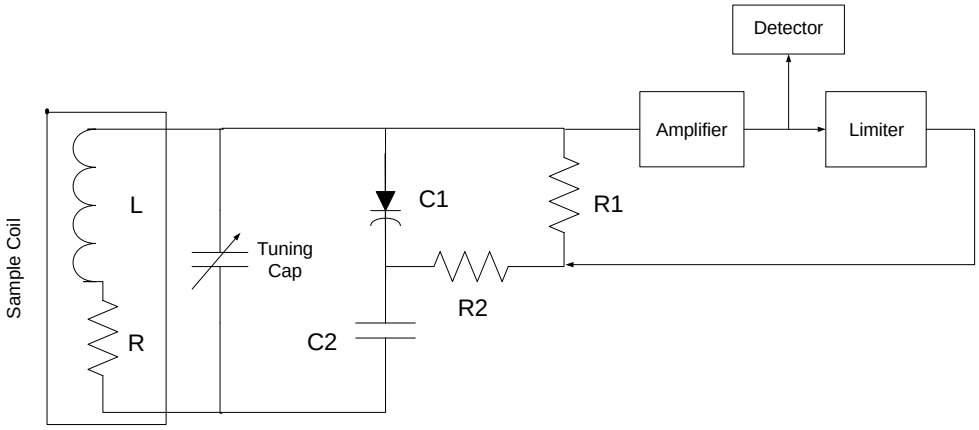

Figure 4: Block diagram of the Robinson marginal oscillator.

Figure 5 shows the complete system for detecting a QR transition. The system consists of a Robinson marginal oscillator, a data acquisition (DAQ) board controlled by a personal computer, and a lock-in amplifier. The Robinson marginal oscillator has three inputs. The center frequency ω_c of the oscillator is set by an 8-bit digital bus and a DC voltage (CF). The third input is a time-varying waveform for modulating the frequency of the oscillator according to equation (8). The parameters ω_d and ω_m in equation (8) are set by the amplitude and frequency of the controlling voltage (FM), respectively. These inputs allow the computer to control the spectrometer through the DAQ board.

The Robinson marginal oscillator also has four outputs. In addition to the output of the envelop detector, there are three additional signals. One signal is a square-wave reference signal for the lock-in amplifier, another is a square-wave whose frequency matches that of the oscillator, and the third is a DC voltage that is proportional to the root-mean-square (rms) value of the limiter output voltage. The square-wave signal is used to measure the center frequency ω_c of oscillation while the rms output provides a measure of the RF magnetic field amplitude H_1 seen by the nuclei.

Annual Research Journal, Vol. IV
Electrical Engineering Research Experience for Undergraduates

ISBN 0-913260-06-1 (http://www.ee.psu.edu/reu/)

In addition to generating analog and digital control signals for the Robinson marginal oscillator, the DAQ board also has an internal counter that is used for measuring the frequency of the oscillator and an analog input for recording the output voltage of the lock-in amplifier. Operation of the CW spectrometer is controlled by a LabView interface that enables the user to set experiment parameters including the range of values for ω_c as well as all the parameters ω_d and ω_m. The LabView interface also displays a graph of the lock-in amplifier output voltage as function of ω_c and saves this data to a text file that can be read by another program such as MATLAB or EXCEL for additional data processing.

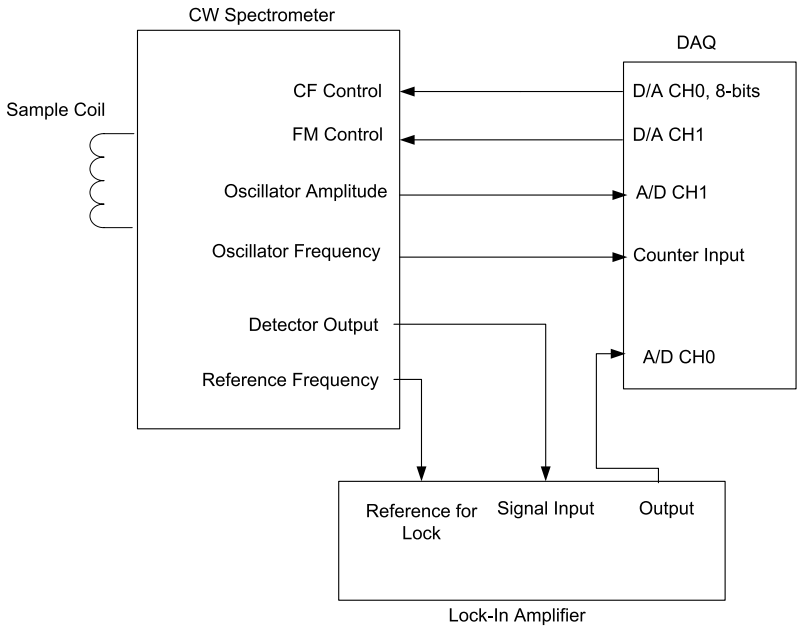

Figure 5: Block diagram of the complete QR spectrometer.

Laboratory Modules

The experiments introduce the technique of CW QR spectroscopy and the relationship between spectroscopic data and chemical structure. The experiments also demonstrate the use of a lock-in amplifier in absorption spectroscopy. Experiments include locating QR transitions, studying the effect of temperature on the QR line-shape, and measuring the inverse-linewidth parameter, and the spin-lattice relaxation time for several different materials. The chief product of this work is a laboratory manual for guiding students through the experiments.

Annual Research Journal, Vol. IV
Electrical Engineering Research Experience for Undergraduates

ISBN 0-913260-06-1 (http://www.ee.psu.edu/reu/)

The first experiment introduces students to CW QR spectroscopy of nitrogen-14 nuclei in hexamethylenetetramine (HMT). The students obtain the absorption line estimate the inverse-linewidth parameter for HMT.

In the second experiment students observe the effect of sample mass on the absorption spectra. In particular, they learn that the inverse-linewidth parameter is unaffected by sample mass whereas the amplitude of the absorption spectra varies linearly with sample mass. In order to account for the inhomogeneity of the magnetic field in the solenoidal probe used for the experiments, the HMT is dispersed uniformly throughout the probe coil by using sodium bicarbonate as a diluent.

The goal of the third experiment is to estimate the value of the spin-relaxation time using equation (6). In this experiment students record the absorption spectra for several different values of the RF magnetic field amplitude H_1. This data, along with their previous measurement of the inverse-linewidth parameter, is required for estimating the value of T1.

Representative Data

Figures 6 through 13 show representative data for nitrogen-14 nuclei in HMT. The room temperature transition frequency is approximately 3.308 MHz and the values of T_1 and T_2^* are approximately 190 ms and 540 μs respectively. From equation 6, the RF amplitude H_1 maximizing the absorption signal is 50 mG. The modulation frequency ω_m is set to 100 Hz and a time constant of 10 seconds is used for all experiments.

Figures 6 shows the lock-in output voltage as function oscillator frequency for various values ω_d and H_1 = 45.9 mG. The horizontal axis represents the deviation of oscillator frequency from the nominal QR transition frequency of 3.308 MHz. However, as the QR transition frequency is temperature sensitive, the location of resonance varies with changes in room temperature. As expected from the Taylor series expansion, the shape of the curve is the derivative of the Lorentzian lineshape and the amplitude of the signal increases with ω_d. Figures 7 and 8 show similar experimental data for H_1 values of 40.3 mG and 36.4 mG. Figure 9 compresses the results from Figures 6 to 8 into a single plot. The vertical axis represents the peak-to-peak voltage of the absorption signal obtained in a single sweep of the absorption spectra as a function of ω_d for the three different values of H_1. The key feature of this plot is that the amplitude of the absorption spectra increases with the value of ω_d.

Figures 10 and 11 provide further data on the relationship between the RF field amplitude $H_1$and the peak-to-peak value of the absorption spectra. Figure 10 shows the lock-in amplifier output voltage as a function of oscillator frequency ω_c for several different values of H_1; while Figure 11 shows the peak-to-peak value of the absorption spectra for a single sweep as a function of H_1. Figure 11 show that a H_1 value of approximately 22 mG maximizes the

Annual Research Journal, Vol. IV
Electrical Engineering Research Experience for Undergraduates

ISBN 0-913260-06-1 (http://www.ee.psu.edu/reu/)

absorption. In contrast, using the approximate values of T_1 and T_2^* found in the literature equation (6) predicts a value of 50 mG. Further work is required to reconcile this discrepancy.

The data presented in Figures 12 to 13 shows that the amplitude of the line spectra is linearly proportional to sample mass. Figure 12 shows the lock-in amplifier output voltage as function of oscillator frequency for several different quantities of HMT. Figure 13 shows that the peak to peak value of the absorption spectra for a single sweep is proportional to the HMT mass. This result is expected as the area of the Lorentzian lineshape is proportional to the number of nuclei within the sample[2].

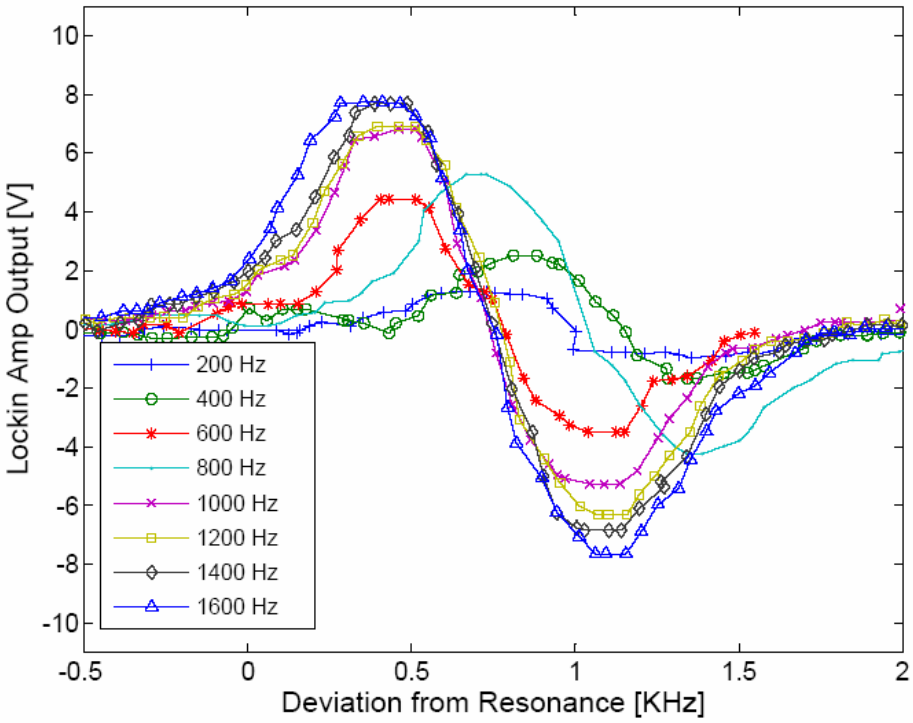

Figure 6: HMT spectra for H_1 = 45.9 mG and various values of ω_d .

Annual Research Journal, Vol. IV
Electrical Engineering Research Experience for Undergraduates

ISBN 0-913260-06-1 (http://www.ee.psu.edu/reu/)

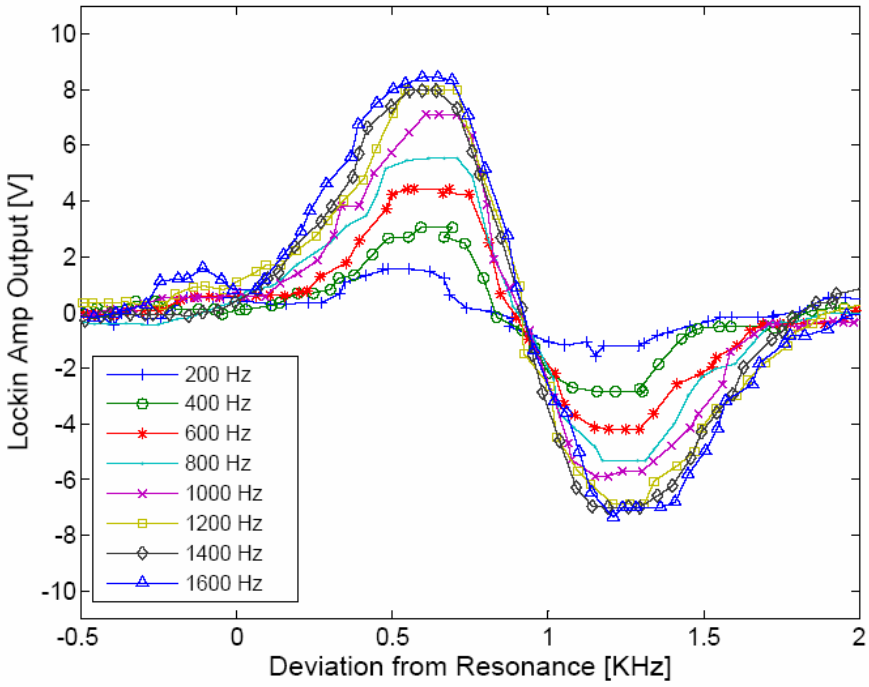

Figure 7: HMT spectra for H_1 = 40.3 mG and various values of ω_d .

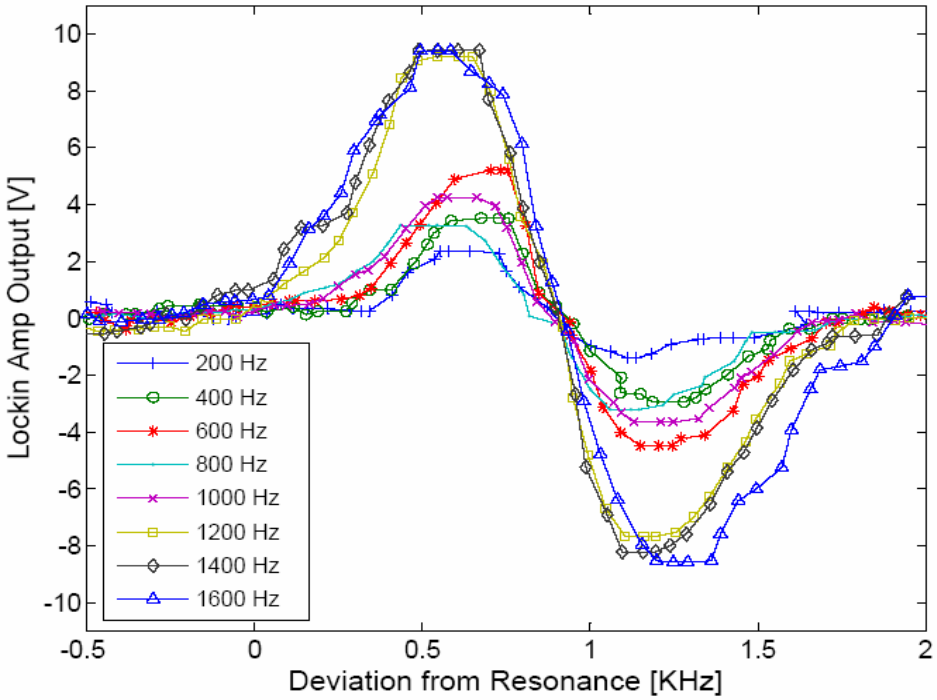

Figure 8: HMT spectra for H_1 = 36.4mG and various values of ω_d .

Annual Research Journal, Vol. IV
Electrical Engineering Research Experience for Undergraduates

ISBN 0-913260-06-1 (http://www.ee.psu.edu/reu/)

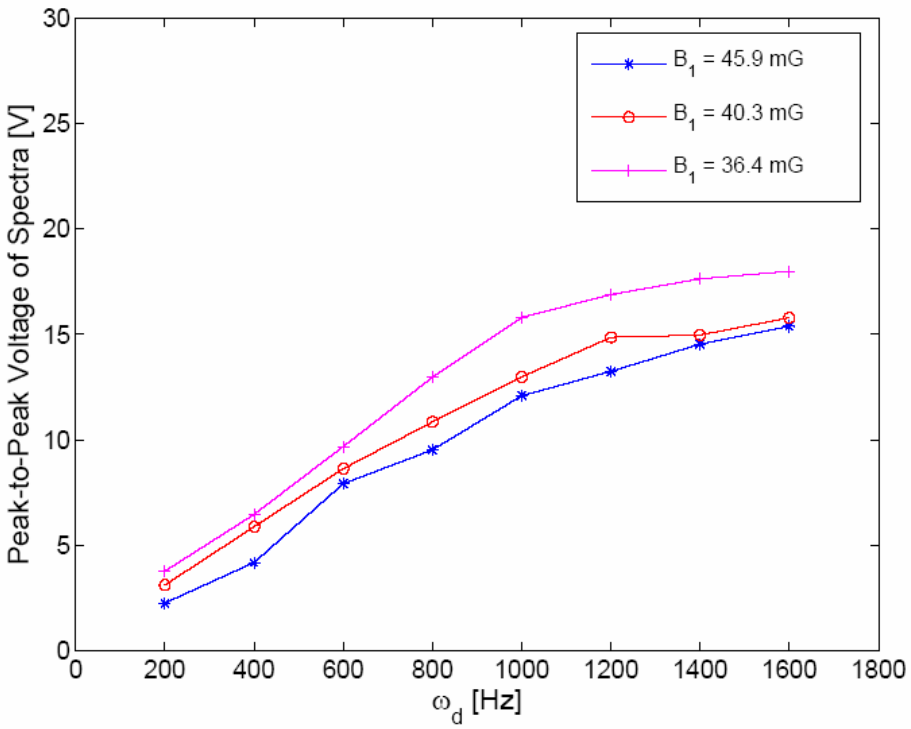

Figure 9: Peak-to-peak voltage of HMT spectra as a function of ω_d for three magnetic field amplitudes.

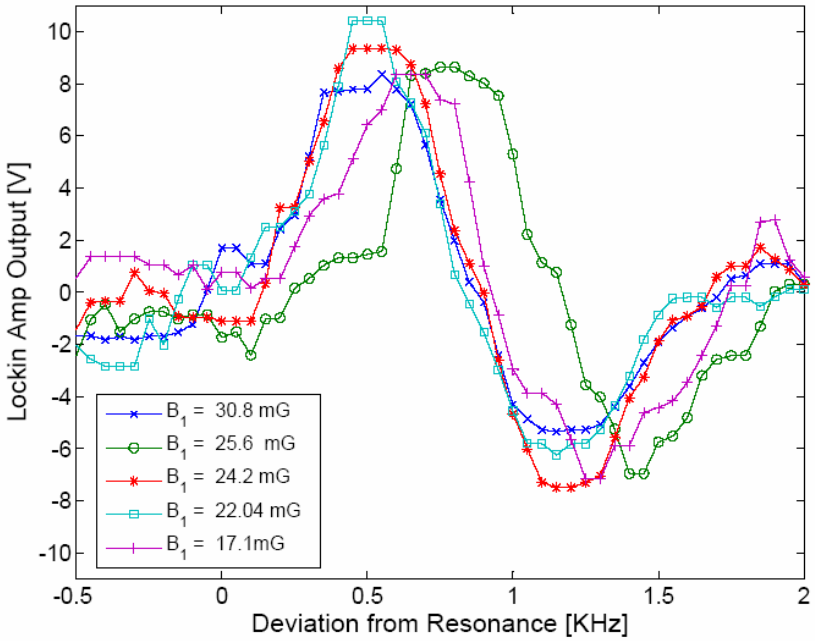

Figure 10: HMT spectra for several different values of RF magnetic field amplitude.

Annual Research Journal, Vol. IV
Electrical Engineering Research Experience for Undergraduates

ISBN 0-913260-06-1 (http://www.ee.psu.edu/reu/)

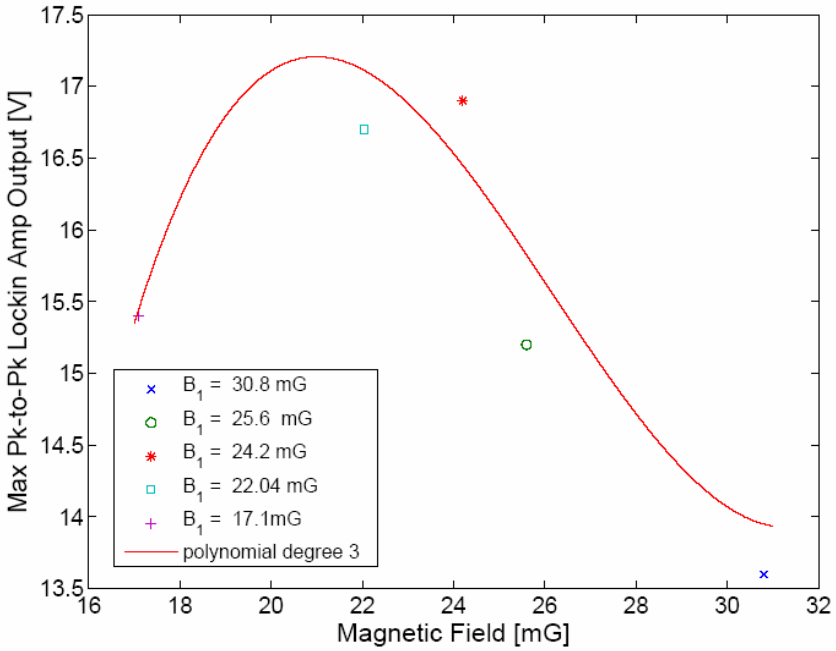

Figure 11: Peak-to-peak voltage of HMT spectra as a function of RF magnetic field amplitude.

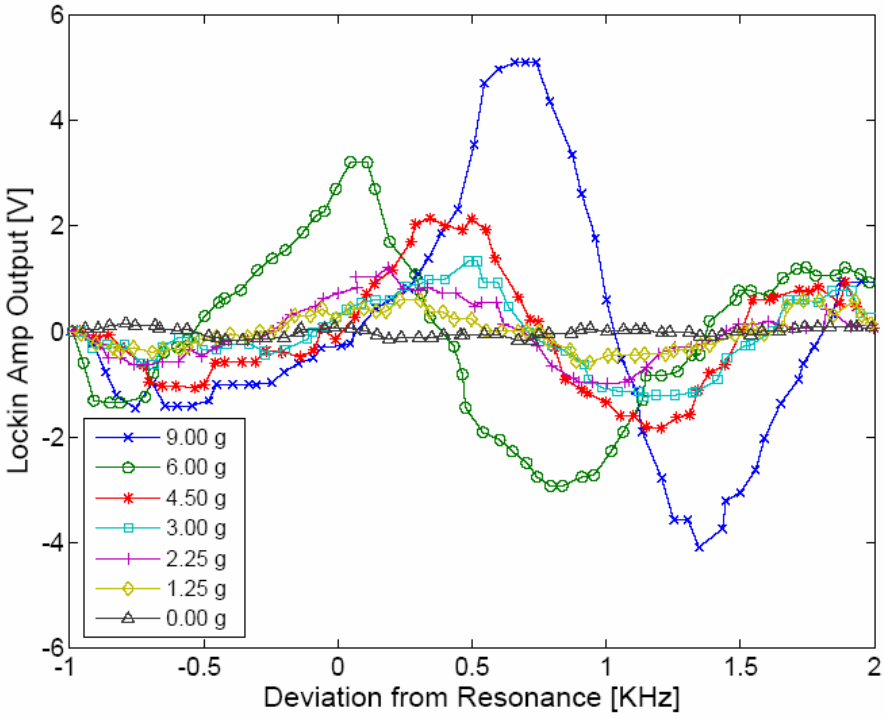

Figure 12: Absorption spectra of HMT for various sample sizes.

Annual Research Journal, Vol. IV
Electrical Engineering Research Experience for Undergraduates

ISBN 0-913260-06-1 (http://www.ee.psu.edu/reu/)

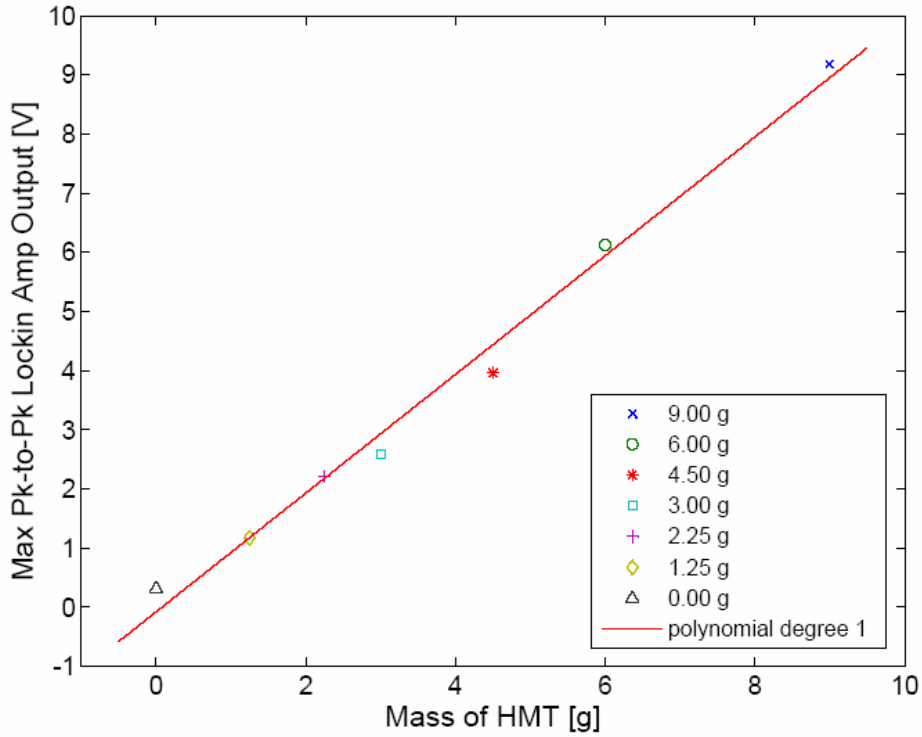

Figure 13: Peak-to-peak voltage of HMT spectra as a function of sample mass.

ACKNOWLEDGEMENTS

First, I would to thank Dr. Schiano for all the knowledge and experience I have gain in the nine weeks here at Penn State. Secondly, I want to thank the National Science Foundation and Penn State for allowing me to gain research experience with the REU program. Lastly, I would like to acknowledge all the teachers, family, and friends who helped me to get to this point in my life.

REFERENCES

[1]J. A. S., "Nuclear Quadrupole Resonance Spectroscopy: General Principles," *Journal of Chemical Education*, **48** (1) 39-48 (1971).

[2]Abragam, A. The Principles of Nuclear Magnetism. Oxford University Press Inc., New York, 1961.

[3]F.N.H. Robinson, "Frequency Modulated NMR Oscillator without Amplitude Modulation," *The Review of Scientific Instruments* **34** (11) 1260 (1963).

Annual Research Journal, Vol. IV
Electrical Engineering Research Experience for Undergraduates

ISBN 0-913260-06-1 (http://www.ee.psu.edu/reu/)